Dynamics and Control of Very High Altitude Tethered Balloons

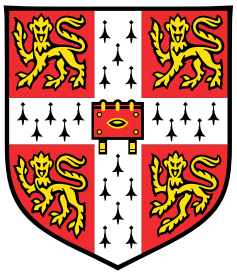

Marianna Sykopetritou

Department of Engineering
University of Cambridge

This dissertation is submitted for the degree of
Doctor of Philosophy

St Edmund's College

May 2020

To my loving parents, brother and late grandfather ...

Declaration

I hereby declare that except where specific reference is made to the work of others, the contents of this dissertation are original and have not been submitted in whole or in part for consideration for any other degree or qualification in this, or any other university. This dissertation is my own work and contains nothing which is the outcome of work done in collaboration with others, except as specified in the text and Acknowledgements. This dissertation contains fewer than 65,000 words including appendices, footnotes, tables and equations and has fewer than 150 figures.

Marianna Sykopetritou
May 2020

Acknowledgements

I would like to thank my supervisor, Dr Hugh Hunt, for his constant support and guidance over the past four years and for inspiring me to do a PhD in the first place. I know that the knowledge and ways of thinking that I have learnt from working with him will be invaluable in my future. I would also like to thank Professor Robin Langley for his advice regarding the control aspect of the research which ultimately determined the direction of the work. I am grateful to the entire Division C for the positive environment and useful discussions. I would like to thank the EPSRC for funding the research and therefore making this possible.

I am so grateful for the people who have supported me in different ways over the last four years. My amazing parents, Stelios and Mirvat, and brother Adam for providing moral support and love at every step in my academic career. My late grandfather Adamos who believed in me more than anyone. My amazing partner Jeremy Amez-Droz for his daily encouragement and love. My best friend Christina Razouk for being my listening ear whenever I needed it and for helping me with my organisation. My friends at St Edmund's College, for providing me with a sense of community and becoming like my second family.

Abstract

This research involves the development of a full 3-dimensional nonlinear model of a tethered aerostat, with the aim of conducting a preliminary feasibility assessment of Very High Altitude Tethered Balloons (VHATBs) under both steady-state and extreme operational conditions. A discretized lumped-parameter model is used to represent the tether.

HATBs have a variety of potential applications ranging from telecommunications to solar power harvesting, but none have been practically implemented to date. The application considered in this research is Stratospheric Particle Injection for Climate Engineering for which the setup comprises of several unique features that are expected to have an impact on the system's dynamics and therefore its technical feasibility. An operational altitude of 20km is recommended for this application, which makes it the largest scale tethered aerostat considered to date. A hollow pipe-like tether is required for the transportation of the high-pressure fluid to the stratosphere where it is expected to scatter radiation.

In order to qualify for long-duration operation, HATBs must be able to withstand extreme weather conditions on top of the harsh steady-state winds the tether would be subjected to. In this research, a series of dynamic simulations are conducted to assess the system's safety in the face of a range of potential 3-dimensional disturbances. The balloon's altitude deviation and the tether's maximum longitudinal stress relative to that of the system's equilibrium are considered the critical parameters that are used to quantify the system's response, as these are considered the primary risks of failure.

The use of optimal control methods to minimise these is proposed and introduced into the dynamic simulations. Previous methods proposed for the altitude stabilization of tethered aerostats are not practical for the scales considered in this research, and so the horizontal motion of the ship the tether is mounted to is suggested as an alternative control input. A preliminary assessment of the potential use of this type of control to reduce failure risks in the face of extreme wind disturbances is provided. The closed-loop performance, practicality and robustness of the controller are considered in this analysis. The critical parameters are found to be reduced by $\sim 65\%$ for in-plane disturbances and $\sim 90\%$ for out of plane disturbances through the implementation of controllers that are deemed both practically feasible and sufficiently robust.

Table of contents

List of figures

List of tables

Nomenclature

Greek Symbols

$\beta_{0,j}$	Equilibrium β_j
β_j	Angle between adjacent links (3D)
β'_j	Deviation from equilibrium $\beta_{0,j}$
Δ	Logarithmic Decrement
δ	Delta Function
λ_b	Bending Damping Coefficient
λ_e	Element Damping Coefficient
λ_s	Sample Damping Coefficient
μ	Mass per Unit Length
μ_b	Dynamic Viscosity of Air Surrounding Balloon
ω	Frequency in rad/s
ω_d	Damped Natural Frequency
ω_j	Element Angular Velocity
ω_n	Undamped Natural Frequency
$\phi_{0,j}$	Equilibrium ϕ_j
ϕ_j	Element Angle from x-axis about K (Euler)
ψ_j	Element Twist Angle (Euler)

$\rho_{a,j}$ Density of Air at jth Element

ρ_b Balloon Skin Density

σ Stress

$\sigma_{L,max}$ Maximum Longitudinal Stress in Tether

σ_L Longitudinal Stress

θ' Relative angle between two links (2D)

$\theta_{0,j}$ Equilibrium θ_j

θ_j Element Angle from Vertical (Euler)

ζ Damping Ratio

ζ_s Sample Damping Ratio

π $\simeq 3.142\ldots$

Other Symbols

$\mathbf{D}_b$ Balloon Drag

$\mathbf{e}_j$ Unit Direction Vector of jth Element

$\mathbf{F}_{td}$ Time-Delayed Input Force Vector

$\mathbf{i}$, $\mathbf{j}$, $\mathbf{k}$ Cartesian Direction Vectors

$\mathbf{K}$ Feedback Gain Matrix

$\mathbf{n}_j$ Element Bending Moment Direction Vector

$\mathbf{Q}$ State Cost Matrix

$\mathbf{q}$ State Cost Parameter

$\mathbf{R}$ Input Cost Matrix

$\mathbf{r}$ Reference Vector

$\mathbf{r}_j$ Position Vector of jth Element

$\mathbf{u}$ Input Vector

$\mathbf{u}_{td}$	Time-Delayed Input Vector
$\mathbf{v}_{w,j}$	Wind Velocity Acting on jth Element
$\mathbf{v}_{w,ss}$	Steady-State Wind Velocity Profile
$\mathbf{x}$	State Vector
$\mathbf{y}$	Output Vector
ρ	Density
σ_h	Hoop Stress
A_{CS}	Cross-sectional Area
A_r	Reference Area
A_{SA}	Balloon Surface Area
b	Base Damping
c	Wave Speed
$C_{d,b}$	Balloon Damping Coefficient
$C_{d,t}$	Tether Damping Coefficient
C_D	Drag Coefficient
D	Damping Matrix
d	Diameter
d_b	Balloon Diameter
d_i	Inner Diameter
D_j	Element Drag Force
d_o	Outer Diameter
d_t	Tether Diameter
EI	Flexural Rigidity
f	Frequency

F_D Drag Force

$F_{H,j}$ External Horizontal Force on jth Element

F_{IN} Input Force

F_{lift} Balloon Lift Force

f_M Mth Natural Frequency

f_{pen} Pendulum Mode Natural Frequency

f_{string} Stretched String Mode Natural Frequency

$F_{V,j}$ External Vertical Force on jth Element

$F_{x,j}$ External Force on jth Element in x-Direction

F_x Input Force in x-Direction

$F_{y,j}$ External Force on jth Element in y-Direction

F_y Input Force in y-Direction

$F_{z,j}$ External Force on jth Element in z-Direction

g Acceleration due to Gravity

H Gust Gradient Length

I Impulse

I Moment of Inertia

I Second Moment of Area

I_{bal} Balloon Impulse

$I_{G,cp} =$ Moment of Inertia of a Compound Pendulum

$I_{G,sp} =$ Moment of Inertia of a Simple Pendulum

I_{inf} Impulse Applied to a Semi-Infinite String

I_{xx} Moment of Inertia about x

I_{yy} Moment of Inertia about y

J_0, Y_0 Zero Order Bessel Functions

K Stiffness Matrix

k_e Element Axial Stiffness

k_s Sample Axial Stiffness

l Element Length

$l_{0,j}$ Equilibrium l_j

L_e Element Length

L_j Unstretched Length of jth Element

l_j Element Length

L_s Sample Length

L_T Temperature Lapse Rate

M Bending Moment

M Mass Matrix

$m_{a,cyl}$ Added Mass for a Cylinder

$m_{a,sphere}$ Added mass of a sphere

m_a Added mass

m_{base} Mass of Base

m_b Balloon Mass

m_{fl} Mass of Fluid

M_j Element Bending Moment

m_j Element Mass

m_s Sample Mass

$N_{1,j}$ Element Shear Force

$N_{2,j}$ Element Shear Force

P Beam Tension

p Pressure

p_0 Atmospheric Pressure at Sea-Level

P_{CR} Beam Buckling Load

p_{in} Internal Pressure

P_j Element Generalised Force

p_{out} External Pressure

q_j Element Generalised Coordinate

R Radius

r_b Balloon Radius

r_i Inner Radius

r_M Mth root of J_0

r_o Outer Radius

Re Reynolds Number

Re_b Reynolds Number for Flow Around Balloon

T Kinetic Energy

T Temperature

t Time

T_0 Sea-Level Standard Temperature

t_b Balloon Skin Thickness

t_d Time Delay

$T_{j,dashpot}$ Element Tension Component due to Dashpot

$T_{j,spring}$ Element Tension Component due to Spring

T_j Element Tension

T_{max} Maximum Tether Tension

T_{min} Minimum Tether Tension

u_j Deviation from Equilibrium $\theta_{0,j}$

V Potential Energy

$v_{0,j}$ Element Initial Velocity

$v_{g,max}$ Peak Gust Velocity

v_g Gust Velocity

v_j Deviation from Equilibrium $l_{0,j}$

$v_{x,SS}$ Steady-State Wind Velocity Profile in x-direction

$v_{y,SS}$ Steady-State Wind Velocity Profile in y-direction

w_j Deviation from Equilibrium $\phi_{0,j}$

$x_{0,j}$, $y_{0,j}$, $z_{0,j}$ Equilibrium Cartesian Coordinates of jth Element

x_0 Base Displacement in x-Direction

x_j, y_j, z_j Element Cartesian Coordinates

y_0 Base Displacement in y-Direction

E Young's Modulus

F Force

k Axial Stiffness

k_b Rotational Spring Stiffness

L Cable Length

N Number of Discretized Cable Elements

Acronyms / Abbreviations

CDR Carbon Dioxide Removal

CL Closed Loop

FEM Finite Element Model

FFT Fast Fourier Transform

GGR Greenhouse Gas Removal

HAP High Altitude Platform

HATB High Altitude Tethered Balloon

LQR Linear Quadratic Regulator

MIMO Multiple-Input-Multiple-Output

ODE Ordinary Differential Equation

OL Open Loop

PID Proportional-Integral-Derivative

ROV Remotely Operated Vehicle

SISO Single-Input-Single-Output

SPICE Stratospheric Particle Injection for Climate Engineering

SRM Solar Radiation Management

VHATB Very High Altitude Tethered Balloon

Chapter 1

Introduction

1.1 Motivation for the Research

High Altitude Platforms have a variety of potential applications that have lead to a growing interest in developing methods of obtaining these. While high altitude free balloons have successfully been used for such applications, the potential benefits brought about by the more versatile and longer duration platforms of high altitude tethered balloons make these an exciting prospect in a range of fields. These fields include but are not limited to communications, solar power harvesting, surveillance and the application that motivated this research, geoengineering through stratospheric particle injection.

While geoengineering is considered an absolute last resort method of fighting the devastating consequences of climate change due to its risky nature and political implications, the availability of thorough research into every aspect of the proposed methods is crucial if it is to ever be considered in a climate emergency. The particular branch of climate engineering considered in this research is not a solution to global warming; unlike Greenhouse Gas Removal methods, Solar Radiation Management does nothing in the way of reducing the high concentration of greenhouse gases that are the cause of the rapidly increasing global temperatures. It is therefore not a solution to climate change in any way; it is merely a way of delaying the consequences to buy us some time to implement the changes necessary to mitigate climate change.

Stratospheric Particle Injection is a process which mimics a naturally occurring phenomenon in which sulphate aerosol particles emitted as a result of volcanic eruptions behave like a layer of fine dust in the stratosphere and reflect a portion of the incoming sun rays. This in turn reduces the amount of heat that enters and gets trapped in the atmosphere, which results in a cooling effect. When Mount Pinatubo erupted in 1991, its effect on the aerosol

optical depth resulted in a drop in the average global temperature of about 0.4°C for about a year. With stratospheric particle injection being such an extreme method of combating rising temperatures, it is once again emphasized that the use of this method is only considered in a very worst case scenario. If such a case were to arise in the future, every aspect of the process and its possible risks would need to have been extensively researched and deemed feasible, and it would have to have been decided that the potential benefits outweigh the risks. This may well not be the case, but this research is intended as a step towards a better understanding of the process and its technical feasibility.

This research focuses on the mechanical aspect of what is believed to be the most feasible delivery method to transport the aerosol particles to stratospheric altitudes; the Very High Altitude Tethered Balloon. For this specific application, the tether is not only used as an anchor for the high altitude platform, but also doubles as a pipe that the fluid would be pumped through at a high pressure. This introduces a variety of parameter constraints that are unique to this application, the feasibility of which must be assessed. The tether's cross-sectional area must be sufficiently large to endure the longitudinal stresses it would be subjected to, while also being hollow to allow for the passage of fluid for example. A thicker outer diameter makes the tether more susceptible to aerodynamic drag, and with steady-state wind conditions with expected peak velocities of over $50 m/s$ this poses a risk to the system's structural integrity. Since the system would need to be in operation for long durations, it must also be able to endure more short term and extreme weather conditions.

Before HATBs can be used for this application or any others, a thorough analysis of the system's expected behaviour under realistic operational conditions is required.

1.2 Research Objectives

This research focuses on developing methods to accurately simulate the dynamics of 3-dimensional tethered balloon systems. Upon validating the model using theory and experimentation, the aim is to then use the model to assess the feasibility of Very High Altitude Tethered Balloons ($\approx 20 km$) under both steady-state operational conditions and more extreme weather. The specific system parameters used are to be based on the proposed design of the VHATB for the stratospheric particle injection application.

This research quantifies the system's response to disturbances using the balloon's deviation from its operational altitude as well as the maximum longitudinal stress experienced by the tether, as these are considered the largest risk factors for the system's mechanical failure. This research also proposes the use of feedback control to improve the stability of these parameters and therefore the system's safety during operation. A preliminary assessment

of the feasibility of the use of optimal control with a base motion input to achieve this is conducted. The improvement of the response to a variety of disturbances and the robustness of the closed loop system are considered, as well as the practical limitations of the selected input.

1.3 Thesis Outline

This thesis begins by covering the existing literature surrounding Stratospheric Particle Injection and explores a variety of other potential applications for the research. The literature review then provides a more technical summary of the work done on the dynamic modelling of cable structures and tethered balloons.

In Chapter 3, a nonlinear 3-dimensional model of the tethered balloon system is produced and partially validated through the use of two methods to produce the system's equations of motion. A lumped parameter model is used to represent the cable structure and two types of cable models are considered; a chain-like inextensible cable with no bending stiffness and an extensible cable with non-zero bending stiffness.

In Chapter 4, available theory which is relevant in the validation of the model and its sub-systems is provided. Equations that are to be used to quantitatively validate both the time and frequency domain response of the system model are derived. Hanging chain dynamics and wave propagation theory are used to verify the cable model and estimates of the expected frequency response of a tethered balloon system are made in order to validate the combined system.

In Chapter 5, experimental data on hanging chain and tethered balloon motion collected by Richard Andrews in 2016 [7] is used to validate the 3-dimensional nonlinear system model. The responses of the two cable models are also compared for the case in which the extensible model is given a very high axial stiffness.

Chapter 6 introduces the methods used to both produce and implement a suitable feedback controller to improve the dynamic responses of such systems. Two methods for the linearization of a simplified tethered balloon model subjected to wind loading are applied as a form of partially validating the resulting linearized model. The general robustness of LQR is explored, and the effects of the controller's design on stability margins are also investigated.

The derivation of the system's state space form using the linearization methods used in Chapter 6 is found to be highly computationally demanding for a 3-dimensional system discretized into many elements. In Chapter 7, general equations for the entries of the mass, stiffness and damping matrices of tethered balloon systems under steady-state wind loading

are derived. This allows for a much faster computation of a HATB system's state space form which can then be used for the deduction of an optimal gain matrix using LQR methods.

Chapter 8 provides detailed theoretical validations for several aspects of the system's dynamics. The nonlinear and linear models are initially compared for small amplitude motion. The theory derived in Chapter 4 is then used to quantitatively validate various aspects of the system's behaviour. In addition to this, the system's bending properties are validated using Euler-Bernoulli Beam Theory, both for zero and non-zero axial tension.

Chapter 9 applies the derived methods to the full-scale VHATB model for the application of Stratospheric Particle Injection. The system's parameter selection is discussed, and methods of incorporating the expected external conditions are described. The system's resulting steady-state position is derived and discussed. The system's open and closed loop responses to a variety of disturbances are discussed in the Case Studies. The effects of the LQR cost function selection on the system's closed loop response and robustness are investigated and discussed.

Finally, Chapter 10 summarises the overall findings and contributions of the research in the conclusion. Recommendations of further work that would improve and build on this research are also suggested.

Chapter 2

Literature Review

In this section, the existing literature on various aspects of the research is described. To start with, some aspects of the background of this research are covered. A variety of existing or proposed potential applications for high altitude tethered balloons are discussed, as they provide a purpose for this research. Other types of high altitude platforms are briefly mentioned. Next, the specific application that this research focuses on, i.e. stratospheric particle injection is explained in more detail. For completeness, other methods of climate engineering are briefly described. The potential need for climate engineering research as well as the controversy surrounding this is discussed.

Having provided a summary of the existing research on the areas surrounding this research as well as the motivation behind it, the existing literature on the more technical aspects of the research is described. This includes work done on modelling cables in general as well research conducted on models of tethered balloons in the past, what they have shown, and what remains to be done. Existing literature on the control of cable structures is also summarised.

2.1 High Altitude Platforms

While this research focuses on stratospheric particle injection as the motivation behind the feasibility assessment of HATB and thus uses parameters suitable for this application specifically, there are a variety of potential applications of long duration high altitude platforms for which the methods used are applicable and useful.

High altitude balloons have a wide range of applications – their stratospheric positioning allows for a number of tasks to be undertaken that prove difficult if the equipment is not positioned above the atmosphere. Having a platform in the stratosphere where any tasks that

are normally hindered by the earth's atmosphere can be undertaken is the main drive for research into high altitude balloons. In most of the research conducted on HABs, the balloon and any equipment it's carrying are positioned at an altitude of 20km, where stratospheric winds are at a minimum, reducing the aerodynamic forces that may need to be opposed to avoid undesired motion. Their payload often includes a satellite navigation system such as GPS, and a radio transmitter and whatever scientific equipment is needed for their specific purpose. There are two main kinds of high altitude balloons that have been considered in the literature, which work in very different ways and each pose their own flaws and challenges; the high altitude tethered balloon and the high altitude free balloon. Experimentally, a lot more work has been done on the free balloons, with several successful stratospheric balloon missions having been conducted over the last 4 decades. A high altitude tethered balloon is yet to have been flown successfully, but the potential benefits it may bring over the free balloon has driven interest in its development as a potential high altitude platform.

Stratospheric imaging was the earliest drive behind research into high altitude balloons – an observing platform located above the majority of the earth's atmosphere is known to produce images of a very high clarity, comparable even to those taken from space while being executed much more cheaply. The atmosphere greatly diminishes the quality of images, by attenuating and distorting electromagnetic rays that travel through it. This desire for high resolution solar studies initiated the first research to be conducted on high altitude balloons that started in the late 1950s [29], during which balloons were used to transport telescopes (Stratoscope I and II) at a height of 24km, above the distortion of the atmosphere, and images of the Sun, planets, stars and galaxies were taken with a high resolution of 0.2 arcseconds [103][117][13]. In addition to this, the stratospheric balloon allows for the exploration of the sun in near ultraviolet radiation, which is greatly reduced as it passes into through the earth's atmosphere. In 1970 a balloon-borne telescope was flown twice at altitudes exceeding 30km for submillimetre astronomy, and in the process captured high-resolution photographs of the sun, ranging from 200nm to 460nm [58]. Some more recent high altitude balloon missions include BOOMERanG and GLAST. BOOMERanG consisted of a balloon-borne telescope which floated though the stratosphere at an altitude of 36km for 10.5 days, circling the South Pole in 1998 [27][82]. NASA has been using balloons as high altitude platforms for scientific payload since 2015. In July of 2018, NASA's PMC Turbo mission [91] released a balloon which floated through the stratosphere to study polar mesospheric clouds (seasonal electric blue clouds that form over the poles in summer, located at altitudes of 80km) for 5 days across the Arctic. Another potential application of HATB is for solar power harvesting [4]; the elevation of the solar panels to altitudes above the earth's atmosphere eliminates the

issue of clouds blocking and attenuating the sun's rays. The use of HATB for this application was described and evaluated by Redi et al in 2010 [97].

High altitude platforms can be used for telecommunications [9][31] – their high altitude allowing for signals to travel to a wider area. Compared to satellites which average an altitude of 36,000km and a minimum of about 1,000km, their relative closeness to the earth's surface at an altitude of 20km mean's a much stronger signal is received at the earth's surface. The use of HATBs for coastal surveillance has also been considered [22].

For the SPICE project application [106], the high altitude balloon must be tethered to the earth's surface in order to hold up the pipe required for the transmission of the sulfate aerosols from the ground to the stratosphere. In the cases mentioned above the stratospheric balloons were not tethered to the earth's surface, they were simply released into the stratosphere and allowed to travel through it. A high altitude tethered balloon could also be used for the applications described above however, and may offer certain advantages over a free balloon, such as a reliable, relatively cheap and long duration stratospheric platform that can be used for telecommunications, the study of space, or the transport of particles into the stratosphere as is required by the SPICE project. The HATB's suitability for any one of these applications must be carefully assessed, but the high altitude tethered balloon has the potential to be very useful. The physical attachment of the balloon to the earth's surface, along with research into potential 'cheap' methods of controlling the location of the balloon potentially eliminates the need for a propeller, which is necessary in some free balloon cases. The lack of a propeller, solar panels to power it, and a battery for nighttime use means a lighter payload for the balloon, allowing for more scientific equipment. High altitude tethered balloons should theoretically be able to stay in the stratosphere for longer periods of time, which could also be very useful.

In 2015, Fesen and Brown [43] introduced another alternative to the two types of stratospheric balloon discussed. This type of stratospheric balloon also makes use of a tether, but in this case the tether does not go all the way down to the earth's surface. At certain points in the year, winds at the higher end of the stratosphere move in the opposite direction to winds in the lower end of the stratosphere. This is called stratospheric wind shear and occurs at low latitudes. This method makes use of this by tethering the balloon at the top end of the stratosphere to a glider tug positioned at the lower end of the stratosphere, where the wind velocity is in the opposite direction. By tweaking the aerodynamics of the tug, the force acting on it can be made to oppose that on the balloon and therefore maintain the balloon's position.

In this research, the high altitude tethered balloon is investigated, primarily because it is necessary for the application that drove this research, and also because less research has

been done into stratospheric tethered balloons than free balloons and this method has the potential to yield great benefits. Though many examples of free balloons flown successfully were already mentioned, a high altitude tethered balloons has yet to be flown successfully to this date, despite several attempts made by French atmospheric scientists in the 1970s [41].

2.2 SPICE Project: Stratospheric Particle Injection for Climate Engineering

This section provides background information on the SPICE project, which is the application of VHATBs that this research focuses on. Some background information on climate change introduces the subject, followed by a brief summary of the history of the project, alternative delivery methods that were considered and finally the VHATB setup suggested for the process.

2.2.1 Climate Change and its Potential Solutions

Due to the continuous burning of fossil fuels, the amount of greenhouse gases present in the atmosphere is continually on the rise and unless drastic changes are made, the changing climate will inevitably and unfortunately lead to disastrous consequences. One of the biggest concerns is that once a tipping point is reached, the climate situation will escalate chaotically and return from this will not be possible. At a certain global temperature, a series of self-enforcing feedback loops are expected to be triggered and the current state of the earth will become unstable and change exponentially, for the worse.

The white and shiny surface of the polar ice caps acts as a good reflector, sending a significant portion of the sun's radiation back out into space. As more of it melts away, even more heat will be retained by the planet. In addition to this, as the ice melts, there is the risk that permafrost, a layer of the ice that has large stores of methane trapped in it, will be exposed, resulting in the release of large volumes of methane into the atmosphere. With methane being a greenhouse gas that is 30 times more potent than carbon dioxide, this will greatly exacerbate the global warming problem. The worry is that the effect of one tipping point will trigger another, and that this could lead to a cascading effect of tipping points, many of which are unknown, accelerating global warming to an uncontrollable rate and leading the planet to becoming uninhabitable.

The primary solution to this is for all nations to work together to mitigate climate change through natural means, such as a large reduction in the global greenhouse emissions and increased forest cover. This is the safest and most long-term solution to global warming.

Though nothing should detract from working towards this goal, there is a worry that the collective action being taken is not occurring at a fast enough rate to sufficiently decelerate global warming, and that other, more drastic and risky solutions should be investigated, for the unfortunate case that they become necessary in the future.

In 2016 the Paris Agreement was signed by the parties of the UNFCCC to officially state their intention to unite and work towards the mitigation of climate change and to take necessary actions to sustain a low carbon future. The main aim of the agreement is to prevent the global temperature from increasing more than 1.5 degrees Celsius above pre-industrial levels in this century. All parties are expected to put their best efforts into achieving this goal and report back with their emission levels and the methods of reduction implemented. While this remains the ideal solution and the primary method of action, there is some concern that the targets set are not achievable [102] and even worse, that the rate of reduction of greenhouse gases will be insufficient to prevent the tipping point from being reached without climate intervention, exacerbated by the long lifetime of the greenhouse gases in the atmosphere [8]. For this reason, though controversial, research exists on methods of engineering the climate for the unfortunate case of a climate emergency.

There are two main methods of climate engineering: Greenhouse Gas Removal and Solar Radiation Management, both of which are expected to decelerate the rise of global temperatures [111]. As implied by the name, the former involves the removal of greenhouse gases, often carbon dioxide, from the atmosphere to reduce the greenhouse effect. The latter involves the reduction in the amount of solar radiation absorbed by the planet through other means, to cancel out the warming caused by the greenhouse effect. SRM doesn't reduce the amount of carbon dioxide in the atmosphere or the rate at which is it is being produced and released into the atmosphere, and so is a method that is purely intended to be used alongside the mitigation of global warming through greenhouse gas reduction to buy time if necessary. It also does not reduce ocean acidification.

GGR requires two main steps: extracting the greenhouse gas from the atmosphere (most of the research has been on carbon dioxide) and storing it for long periods of time. Within GGR, the most widely studied area is Carbon Dioxide Removal (CDR), which includes a number of negative emission methods in which CO2 is removed from the atmosphere at a large scale [45][102][86]. The first step can be done using either biological methods or through chemical reactions, and the carbon produced then needs to be stored either underground or in the ocean. None of the possible methods have been developed and researched extensively enough to be applied to the huge scales required to make a significant difference yet, and each pose their own problems and limitations. Many of these issues relate

to the huge scale required, as well as cost, resources and space. There are also several ethical issues that arise [95], as well as practical and environmental issues and limitations [105][20].

SRM mostly involves methods of reflecting the sun's rays back out into space i.e. increase the earth's albedo and therefore reduce the amount of heat absorbed by the planet. Proposed methods of doing this including cloud brightening, space sunshades, space mirrors, oceanic foams, the placement of reflective sheeting in deserts, 'cool roof' technologies, reflective balloons, and, the method that has received the most attention and that is the focus of this research, stratospheric particle injection.

The main method of SRM present in research is Stratospheric Aerosol Injection (SAI). Sulfate aerosols are released naturally into the stratosphere when volcanoes erupt and are known to reflect light and reduce global temperatures [99]. Studies specifically looking at the ways in which the eruption of Mount Pinatubo in the Philippines in 1991 impacted the climate have been conducted in detail [34][50], and it is known that global temperatures fell by approximately half a degree Celsius for approximately 2 years following the eruption. The objective of SAI is to mimic this process.

Over the years there have been debates over whether climate engineering should even be considered, with some opposing it completely [61] and some defending its use as a last resort in the case of a climate emergency if extensive research points to its feasibility [71]. Some believe that further research into SAI is necessary in order to make an informed decision on whether or not it should be implemented [28][100][64], and therefore encourage it. As with CDR, there are ethical and political issues to be considered [14][53][109], and there is a lot of opposition to climate engineering [94], which has resulted in very limited research going into these technologies.

2.2.2 SPICE Project History

The government funded SPICE project [106] began in October of 2010 with the aim of investigating the feasibility of this type of climate engineering as well as to gain a better understanding of the potential risks associated with it. The research was divided into 3 areas: the candidate particles to be injected into the stratosphere, the delivery method used and modeling the climatic response. The primary delivery method considered in this project was the high altitude tethered balloon due to its potential as being a relatively cheap and effective method, and also due to the fact that no such structure has ever been used before and so little is known about how it would behave under such conditions. Plans were made to conduct a small-scale practical test in October 2012, in which a 1km tethered balloon would be flown and its behavior observed. The data collected from this was to be compared to software models in attempt to validate them so that they could then be used to predict the dynamics of

the full-scale model with more confidence. Due to the controversy, the test was first delayed and then cancelled completely.

The project received funding by the EPSRC for 4 years and ran until March 2014 after which it was terminated. The opposition to this research stemming from the fear that implementing the particle injection system may result in unexpected adverse effects on the planet or may result in ozone depletion has stunted further research into this particular temporary solution for global warming and little work has been done on it since. If the reduction of the emission of greenhouse gases proves to be taking place at an insufficient rate and the climate situation continues to get worse, research into this area may pick up again. In the mean time, the research conducted in this PhD aims to build on the existing understanding of the dynamics of the tethered balloon delivery method. The aim is to write and validate an accurate model of the entire system in its external condition, and predict its behaviour. Through this model the stability of the system can be assessed and methods of controlling the system investigated.

2.2.3 Particle Delivery Method

In 2009, the Royal Society report [104] assessed the feasibility of a range of geoengineering options and concluded that solar radiation management using aerosols injected into the stratosphere would be the most feasible and cost-effective method, but did not include much detail about potential delivery systems. In March 2010, at an Engineering and Physical Sciences Research Council workshop, ideas were discussed and a number of proposals for research into potential ways of engineering the climate were suggested, including the idea of a VHATB supporting a high pressure pipe as a delivery method. During these early discussions, the potential advantages of this method over other delivery methods began to emerge. The potential delivery methods considered and compared in the literature are aircraft, airships, rockets, naval guns, free balloons, tethered balloons and towers. Several papers compare their relative cost and practicality. In 2009, Battisti et al. [15] produced a technical review of possible methods of stratospheric aerosol injection and evaluated their practicality to provide both sides of the climate engineering debate with a clearer understanding of how it may be done, but did not consider their relative costs. Some literature evaluates potential costs of some possible delivery methods such as aircraft [84][101], but these are limited to batch delivery systems and do not discuss continuous delivery systems in which a pipe is suspended into the stratosphere such as the tethered balloons or towers.

In 2012, Davidson et al. [30] produced a more detailed discussion of the different ways in which the particles could be delivered to the stratosphere. Batch delivery processes were considered, but more focus was placed on continuous delivery systems in which the particles

are pumped through pipes leading from the earth's surface to the stratosphere. To hold the pipe up where it needs to be, the option of the use of a tower was eliminated as being impractical, and a high altitude tethered balloon system was deemed the most viable delivery method due to its simplicity and relatively low cost. A summary of the delivery system comparison was presented in the form of graph below which shows the cost and development time of each method considered. In 2017, Moriyama et al. [87] revised the costs of the methods presented in previous literature.

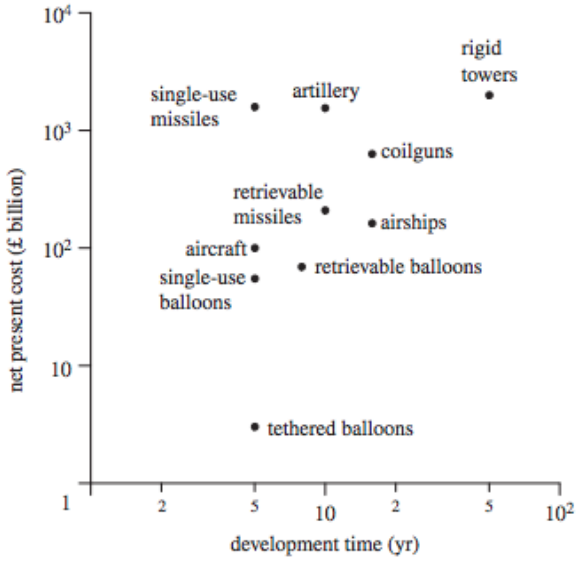

Fig. 2.1 Development time and cost estimations of potential delivery methods for stratospheric particle injection [30]

2.2.4 VHATB for SPICE Application

With the VHATB appearing to be the most economically and practically feasible delivery method for the particles from ground level to the stratosphere, work has been done on establishing the specific system parameters that would be required for the application.

In 2012, Davidson et al. [30] provided a detailed analysis of suggested system parameters and materials. The parameters used in the system model in this research are based on these, and a summary of the selected parameters and the reasoning behind them is provided in Section 9.2.

This delivery method involves the suspension of a very large pipe using a Helium balloon of diameter 315m. The system is designed such that the operational altitude of the top end of the tether/pipe is around 20km, as this places the balloon in a region of lower wind speeds

and is also an appropriate altitude for the placement of the particles to serve their purpose. Figure 2.2 displays a schematic of the proposed system.

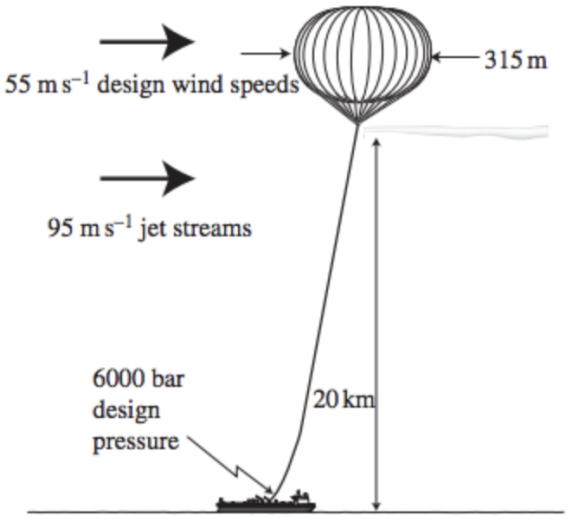

Fig. 2.2 VHATB for the SPICE application [30]

In 2015, Kuo et al. [73] researched the process of pumping fluid through the tether of HATBs, with the feasibility of pumping sulphur dioxide for this application considered as an example.

2.3 High Altitude Tethered Balloons

The earliest work found on the feasibility of high altitude tethered balloons was conducted by the US navy in the 1960s and published in 1965 [39]. They conducted several small-scale experiments, ascending tethered balloons to heights of up to 4km. In this publication, plans to attempt a full-scale stratospheric tethered balloon launch later that year were discussed and planned. No information was found about this. Between 1969 and 1976, the French government conducted several unsuccessful experiments [41], though limited information can be found on the details of these. As far as is known by the author, tethered aerostats have reached maximum altitude of 4.5km to this date [66][67][110]. It is believed [16] that existing aerostats can reach altitudes of up to 8km safely.

Before the potential applications of high altitude tethered balloons became apparent, more research was conducted on the dynamics of smaller scale tethered balloon systems. In 1972, DeLaurier et al. [33] conducted a stability analysis of tethered aerodynamically shaped balloons in which a tether length of around 1.2km was considered. Jones et al. [67] built

on this research in 1982 by incorporating nonlinearities into the system and predicting the system's response to turbulence. A lumped parameter extensible cable model was used.

In 1995, Euler et al. [41] extended existing research investigating the feasibility of very high altitude tethered balloons (20km altitudes) by considering not only the steady-state behavior of the balloon at operational altitude, but also the required balloon specifications in order for it to survive conditions during its ascent and decent. They proved that steady-state analysis on its own was inadequate, producing balloon specifications that would fail during its ascent. With peak winds occurring at an altitude of 12km and not at the operational altitude of 20km, the peak tether tension will occur when the balloon ascends through this region at the balloon-tether interface; the strength of the tether would therefore need to withstand this maximum tension which in turn affected the minimum tether diameter and therefore the size of the balloon needed to hold this increased mass. They concluded that very high altitude tethered balloons are feasible using existing materials and tools, but that further work and design optimisation was required.

In 1996, Badesha et al. [11] conducted a parametric sensitivity analysis on VHATBs to gain a deeper understanding into the way in which selected critical design parameters of the system affected the required balloon size. These included the selected drag coefficient, the tether length and the tether's weight among others. It was concluded that the parameter that had the greatest influence of the required balloon size by a long way, was the operational wind profile applied to the system model. Badesha et al. [12] conducted another study in 1996 on the potential problems associated with the system's descent, and suggested potential solutions. Grant et al. [48] also conducted a feasibility assessment of the ascent of VHATBs using dynamic simulations of the launching process. Both studies concluded that the process of ascending and descending the VHATB system is critical in determining suitable system parameters.

In 2001, Jones et al. [66] produced a nonlinear dynamic simulation of a tethered streamlined aerostat, which was compared to real data from flight tests of a TCOM 71M tethered aerostats. The dynamic responses were compared and were found to be qualitatively similar, following similar patterns of motion and values of the same order of magnitude.

In 2002, the Johns Hopkins University Applied Physics Laboratory [10] conducted a feasibility assessment on Very High Altitude Tethered Balloons with an operational altitude of 20km for the context of collecting intelligence data. In this study, 2-dimensional dynamic simulations were conducted in response to a thunderstorm and other environmental stimuli to assess the system's safety under extreme weather conditions. A discretized lumped parameter was used to model the tether.

In 2009, Aglietti [3] expanded this into a 3D model and also incorporated bending stiffness into the model in addition to axial stiffness. The application for which the analysis was conducted was High Altitude Electrical Power Generation [4], for which an operational altitude of 7.5km was used. The reduced scale of the system allows for a significantly smaller balloon of 60m diameter. A Finite Element Model (FEM) was used in this study, and the discretized beam elements with distributed mass were used. This model was used to investigate the system's 3-dimensional dynamic response to wind gusts acting in line with the wind as well as laterally. Some theoretical validations were made by comparing the model's response to a simplified inverted pendulum with equivalent characteristics. This research was continued by Redi et al. in 2011 [98] when the model was extended to more completely analyze the behavior of high altitude tethered balloons by taking into account gusts in all 3 directions, vortex-induced vibrations and simulated continuous turbulence. In this study the selected tether length was 6km. The aim was to simulate realistic operational conditions as a preliminary assessment of the system's feasibility. There are multiple other studies that investigate the feasibility of tethered aerostats in the face of turbulence for smaller scale systems [70][108].

2.4 Modelling Cable Structures

In this section, a summary of the methods in which cables have been modelled in literature is given. Cables are either modelled as being continuous or they are discretized, and a compromise must be made between achieving the highest possible model accuracy and maintaining a software model that is computationally efficient. Within the discretization category, there are number of ways to represent tether elements. This section summarises the findings from previous research with the aim of identifying a suitable way of representing the tether.

Over the last 4 decades, a large amount of research has been conducted in order to develop numerical cable models, which can accurately and efficiently predict the shape, amplitude and internal tension within cables over many future time steps. Almost all the research that was done on cable systems either looked at horizontally suspended cables that are pinned at both ends [62][63], or undersea cables towed by ships [18][37][49][59][77], the latter of which has initiated a great amount of research into marine cables and their dynamics. In these cases, the cables are assumed to be either towed or tethered in a marine environment, which besides the effects of the external fluid, is similar to the high altitude tethered balloon case, and parallels can be drawn from the motions of these cases. At the cable extremities there is often a body with significant mass/inertia. This is analogous to the large inertia due

to the balloon having to force its way through surrounding fluid. Also, the other end of the cable is connected to a ship whose motion is known and controlled. It is expected that these marine models will portray a larger similarity to the one being investigated than other cable models that were reviewed.

Intuitively, the most accurate way to model a cable structure is through the use of a continuous model in which a two-point boundary value problem is used. An alternative, simplified method is to discretize the cable into physical segments, for which the equilibrium of forces or solving Lagrangian equations yields a series of nonlinear equations of motion, which has the obvious advantage of model order reduction; the reduced computational complexity and running time. In 1999, Dreyer and Van Vuuren [36] compared the use of continuous and discrete modeling of cables and established that although using a continuous model yields more accurate results than using a discrete model as expected, this improvement is not dramatic and is not worth the vast increase in cost and effort associated with the solution of a continuous model. In addition to the fact that the continuous model entails solving 24 nonlinear differential equations simultaneously, they discovered that the continuous model is very sensitive to perturbations of the initial conditions, requiring a very small time step length in the numerical integration process. With the computational effort increasing roughly a 1000-fold, they concluded that the slight gain in accuracy cannot be justified. In addition to this, continuous models are only valid and usable if the tether is taut and it is very difficult to solve the differential equations governing a tether when hydrodynamic forces and the tether's properties change along the tether's length [37]. Discretization also makes it easier to accommodate intermediate forces or material discontinuities. For these reasons, the vast majority of research on modeling cables has incorporated a discrete system model.

There are several ways in which a tether model can be discretized, and upon choosing one of these, the accuracy, computational cost and the reliability of the model must be considered. In 2001, Haan et al. [52] studied the accuracy of implementing damping into discretized models using the Standard Linear visco-elastic model specifically. In 2016, Hembree et al. [57] compared three of these, discussing the advantages and disadvantages of each model and providing guidelines on the applications most suitable to each. The types of segments discussed and compared in this publication are rigid link models (which are the most computationally efficient [55][56]), Kevin-Voigt visco-elastic models and Standard Linear visco-elastic models.

In the majority of work in which cables are modelled discretely, there are two main ways in which this has been done. Some of the conducted research used a finite-segment model [68][116] in which the cable is modeled as a series of rod-like links which are connected by spherical ball-and-socket joints (i.e. pin joints), and some used a lumped-mass model

[19][37][68][107][75][96] which consists of a series of point masses connected by massless links that transmit only cable tensions (these may be rigid or may have elasticity and damping properties depending on the specific cable's material properties). The lumped mass model is also referred to as a lumped parameter model, since all parameters such as the hydrodynamic forces are also modeled as being concentrated at the nodes of the elements. Dreyer et al. [35] conducted a comparison of these two ways of spatially discretizing cable models and concluded that for the same physical system the two methods of discretization are equivalent provided certain conditions are met. So long as these conditions are met for a particular problem, either model can be used to obtain a numerical solution. These require that the force acting on a particular lumped mass be equal to half the sum of the distributed loads acting through the centers of the adjacent rods in the equivalent rod model plus any point loads. For the case in question as well as the majority of marine cable cases, either of these models would be a good approximation of the physical system, and the lumped-mass model is selected due to its relative simplicity.

Lumping both the mass of the element (essentially shifting the total inertia of the element to a single point) and all the forces acting on it into a point allows for the motion of each node to be described independently by a series of ordinary differential equations, the number of which depends on the number of degrees of freedom used in the particular model. The internal forces in the elastic links between the nodes impose a constraint on the motion of the nodes.

In conclusion, the literature established that a lumped mass model greatly simplifies the analysis of the continuous nonlinear physical system and results in a potentially hugely complex mathematical model collapsing into a relatively compact, efficient one, with a minimal compromise on accuracy.

Such models have been used and validated to a great extent over the last few decades. In 1960, Walton et al. [115] conducted some of the earliest research in which a lumped parameter model was used. In 1999, Kamman et al. [68] established that the lumped parameter model produces accurate and computationally efficient results. Driscoll et al. [37], Huang [60] and Buckham et al. [18] accounted for the extensibility of the cable by using springs in parallel with dashpots to connect the lumped parameter nodes rather than rigid links.

The research conducted on the nonlinear free vibration of suspended cables is vast, but some of the assumptions and simplifications that have been made in some of these models would be unsuitable and may result in inaccurate results produced for the VHATB tether. Some models [68][69] produced for similar cable systems considered the extensibility of the cable negligible. While this may produce accurate results [1] for some small-scale systems

or cases with relatively high axial stiffness, care must be taken if the model is meant to represent a cable with elasticity, as in some cases axial deformation may have large effect on its dynamic response, as illustrated by several studies [112][21]. For cables such as the one that is the focus of this research, even a very large stiffness would result in significant axial motion due to the great length of the cable and magnitude of the forces acting on the system.

Another simplification made in some of the literature was to limit cable motion to only one or two dimensions. Driscoll et al. (2000) [37] used a lumped mass model to represent the tether in a deep-sea ROV system. This model only included vertical motion and was therefore simplified as being one-dimensional, which is sufficient for this specific application in which the tether is almost perfectly vertically taut and any horizontal motion is insignificant. This simplification would be insufficient however for the high altitude tethered balloon to be modeled, and a 3-dimensional model would be required in order to accurately capture and display the complex axial, in-plane and out-of-plane motion exhibited by the tether and the balloon. This is because while in the undersea model the only significant external excitation is the unsteady vertical motion of the ship due to the waves, the harsh conditions of the stratosphere produce much more complicated external conditions. In 1999, Koh et al. [72] studied the low-tension large amplitude dynamics of cables by considering a vertically hanging cable.

In addition to cables, research also exists on the discretization of beam systems using lumped mass models. Belytschko et al. [17] investigated the use of these approximations to model flexural wave propagation.

2.5 Modelling a Body Moving Through a Fluid

This section provides a summary of the available literature on the ways in which the drag components of bodies travelling through a fluid can be incorporated into the model. The drag coefficient values used in a few studies of tethered aerostats are also included.

2.5.1 Added Mass Approach

In order to model a body moving through fluid, the ‘added mass’ approach was used and described in the majority of research. For the under-sea ROV case modeled by Driscoll et al. [37] for example, the cage and ROV that are tethered by the cable are represented by a point mass with a slight alteration. Though a point mass in itself accurately accounts for the weight of the cage and ROV, it doesn’t account for the large drag force opposing its motion due to the large volume of fluid that needs to be displaced as the body moves through the

water. In this model, this drag is accounted for using the 'added mass' approach, where the body's inertia is increased by a specific value to represent the increased resistance to its motion. This extra mass is only added to the body's inertia and not its weight, as is intuitive. When applying Newton's second law of motion to the body in order to obtain its equation of motion, the virtual mass which includes the added and entrained mass is used rather than the actual mass on the right hand side of the equation. For a sphere, this virtual mass is equal to:

$$m_{a,sphere} = \frac{2}{3}\rho\pi R^3 \tag{2.1}$$

Using the added mass approach is a well-known method of modeling a body flowing through a fluid and equations for the value of the added mass are readily available for simple shapes such as cylinders and spheres. For more complicated scenarios, Tuveri et al. [113] computed the added mass for a range of unconventional airships and scientific balloons (more than 20), for which simply assuming a spherical or ellipsoidal shape is inaccurate, using analysis on CAD models of several aerostats/balloons.

2.5.2 Drag Equation and Drag Coefficient Selection

In the cases the fluid the is moving, e.g. in the presence of wind the added mass approach is insufficient, as it does not include the drag component that is due to the motion of the fluid. In these cases, the drag equation is used for the balloon as well as the tether.

When applying the drag equation to calculate the instantaneous drag force the balloon is subjected to, the selection of the drag coefficient is crucial in accurately representing the system's behaviour. In the existing research on tethered aerostats, there is a range of selected drag coefficients.

The drag coefficient selected would be dependent on the Reynolds number and is therefore affected by the balloon's design altitude. In addition to this, it has been suggested that the drag coefficients of tethered aerostats differ to those of equivalent fixed spheres. The presence of vortex-induced vibrations is also expected to increase the expected drag coefficient.

For the system in question, the Reynolds number is expected to be in the supercritical region, i.e. greater than 3.5e5 (this is shown in Section 9.2). For a smooth fixed sphere with a Reynolds number in the supercritical region, several studies have suggested a drag coefficient of around 0.15 [83][2][23]. Redi et al. [98] raised this value to 0.2 to account for the fact that the balloon is not fixed. Coulombe-Pontbriand et al. [26][25] experimentally estimated a drag coefficient of around 0.56 for a tethered aerostat, that they explained by the large amount of upstream turbulence, the system's oscillations and the roughness of the balloon's skin. Miller et al. [85] assumed a conservative value of 0.7 for the drag coefficient - this value was

found by Govardhan et al. [47] for subcritical flow, which involves a larger drag coefficient than supercritical flow. Due to the uncertainty in the drag coefficient of tethered spherical aerostats, the effects of a range of possible drag coefficients on the system are considered in this research.

2.6 Feedback Control of Cable Structures

This research proposes the use of feedback control to stabilise the VHATB to improve its safety and durability. Existing work on the use of control on general cable structures is initially discussed, before summarising the more specific and limited research on the control of tethered balloons in the next section.

In 1999, Kamman et al. [68] conducted research on tethered marine systems, in which the cable was modeled as having a variable length to simulate reel-in/pay-out maneuvers, a mechanism which is applicable in the control of tethered balloons. In this model, the number of discretized elements of the link is held constant throughout a simulation, so in order to model the reeling in or paying out of the cable a change of element length is required. To reel the cable in, the link towards the towed end is shortened until it reaches a minimum length, after which the adjacent link may be shortened up to that length, etc. An equivalent element extension method is used for pay-out.

In order to develop methods of controlling the motion of the balloon through controlled inputs at the base of the tether, it is important to not only accurately model the dynamic behavior of cables, but also accurately model the way in which the vehicle at the base, the tether cable and the balloon all interact with each other. This 3-component system is quite similar to the under-sea marine systems studied in a lot of the literature, with the ground-level vehicle appearing in both, the cable appearing in both, and the balloon being analogous to the towed vehicle. In almost all the literature, the motion of the ground vehicle is simply modeled using a kinematic boundary condition on the first node of the cable model. This implies that the tension force imposed by the tether onto the ground vehicle has a negligible effect on the vehicle's motion, which is a valid assumption for most cases, with the exception of models in which the ground level vehicle is small and unmanned [19]. For the case of the VHATB system with the ship's motion being the control input, the effect of the tension on the ship is significant and this simplification is not made. In some models, the towed body (i.e. the ROV) was modeled as a spherical or cylindrical body, which could easily be coupled to the cable model by treating it as an extra node at the tether's end. This node would be positioned at the center of mass of the towed body, i.e. for a spherical body of radius *r,* the final node representing the body would be positioned at a distance *r* from the final node of the

cable. The lumped parameters associated with this node would be very different from those of the cable, and the final rigid link would likely have a much larger stiffness. This was used by Huang (1994) [60], Palo et al (1983) [93] and many others. Some more recent models incorporated a more accurate model of the towed body, but these complex representations are irrelevant for this research in which the tethered body is a balloon and relatively simple to model.

2.7 Control of Tethered Aerostats

Available literature on the use of feedback control to stabilise tethered balloons is limited. Two main control inputs have been considered; the use of actuated wenches to reel-in and pay-out cable length and the use of actuated fins. The work conducted on these is summarized in this section.

2.7.1 Actuated Wench Cable Control

In 1999, Nahon [88] produced computer models on the potential use of multiple tethers connected to computer-controlled actuated winches as a control system for a tethered aerostat. Starting from 2002, Lambert et al. [78][81][79][80][74][76][89] a series of papers were published on the continuation of this work in which smaller scale (1/3 of the intended full-scale system) experiments were conducted along with ongoing simulations on the proposed feedback system. In this setup, the controller acts to change the lengths of the tethers in order to stabilize the position of the HAP in the face of wind disturbances. This was done with the aim of assessing the feasibility of using such a control method to stabilize the altitude of a radio telescope with a design altitude of 500m, for which a stable position is important. Both PID and optimal control methods were used, and while both resulted in a significant improvement to the system's stability the response of the latter was found to be 50% better [79].

In 2019, Gupta et al. [51] also investigated the use of actuated winches as a control method for tethered aerostats, for the application of solar power harvesting. In this case, wind disturbances result in the oscillation of the photo voltaic modules that are mounted onto the aerostat, which has a significant negative impact on power generation. This was investigated for both single tether and tri-tether control. In this research, a tether length of 1km is considered.

2.7.2 Actuated Fin Control

In 2007, Nahon et al. [90] conducted a series of experimental tests to investigate the use of movable tail fins to stabilise tethered aerostats under a variety of wind disturbances. PID control was used in these tests. In 2017, Azevedo et al. [32] conducted further studies on this using dynamic simulations and LQR control.

2.8 Contributions of Current Research

While dynamic models of tethered balloon systems do exist, feasibility assessments on VHATBs specifically (20km+ altitude) are very limited. The larger scale of these along with the greatly altered system parameters that are needed to account for this pose their own unique challenges. The vast majority of the work on VHATBs to date was done at the Johns Hopkins University as described previously [10][12]. The dynamic simulations conducted in these studies were purely 2-dimensional however, and there is scope to analyze the system's behaviour in full 3-dimensional space. To the author's knowledge, no work has been done on the dynamic analysis of VHATBs of such large scales in response to out-of-plane gusts and other 3-dimensional disturbances.

In addition to this, the VHATBs that would be used for the SPICE application have unique features that are expected to have a significant impact on their behaviour. There have been no studies done which use dynamic simulations to assess the system's response to harsh weather conditions using the geometry and materials specific to stratospheric particle injection. For this application, the tether must be hollow like a pipe to allow for the transport of the fluid to the stratosphere from ground level. To maintain a surface area large enough to withstand the huge axial tensions that result from the system's scale, the system's outer diameter will be significantly larger than those of VHATBs proposed for other applications. This is expected to have a significant impact on tether drag. In addition to this, the tether will contain a large amount of high pressure fluid during operation, which contributes to the tether's weight and also exerts large hoop stresses onto the tether's wall. These are all challenges that are unique to the application and are likely to affect the system's dynamics significantly. This research aims to conduct a preliminary assessment on the system required for this application.

While research has been done on the implementation of feedback control to stabilize tethered balloon systems primarily using reel-in pay-out cable control, these systems were of significantly smaller scale than the VHATB considered in this research. The extensive work done on the control of tethered aerostats by Lambert et al. [78][81][79][80][74][76][89] considers a system with an operational altitude of only 500m. The cross-sectional tether

diameter required for this case is 18.5mm [81]. For this tether geometry, the use of a winch to reel-in and pay-out cable length is feasible and works well. For the case of the VHATB for the SPICE application, a tether outer diameter of 200mm is suggested [30]. The bulkier cable body, along with the much greater bending stiffness as a result of this, makes the use of a winch impractical for this case. The use of multiple tethers would also not be feasible for a system of this scale in which the tether is also transporting fluid. The potential use of actuated fins was also disregarded due to the amount of power that would be required to move a system of this scale against harsh wind conditions. The horizontal motion of the ship to which the base is constrained is therefore selected as the most practical control input for a VHATB. To the author's knowledge, no work has been done on the altitude control of VHATBs, and the selected control input has not been considered for tethered aerostats in general. This research aims to conduct a preliminary assessment of whether or not this is feasible and effective under the practical limitations of such a system.

Chapter 3

Nonlinear Model of the Tethered Balloon System

In this section, a 3-dimensional nonlinear model of a tethered balloon system is derived and developed. The system is comprised of two subsystems; a cable and a balloon. Each system is considered separately in detail before the subsystems are combined to produce the tethered balloon system model. While modelling a balloon is relatively straight-forward, modelling a cable structure is more complex and this is therefore the main focus of this section. In this research, two different cable models are considered; an extensible cable with bending stiffness, and a chain-like inextensible cable with no bending stiffness. In both of these cases, a discrete lumped-parameter model of the cable is used for computational efficiency. As the number of elements in the cable increases, the behaviour of the system is expected to approach that of a continuous model. Force and energy methods are both used to obtain the equations of motion for each case as a method of validating the expressions obtained.

3.1 3-Dimensional Extensible Tether Model

In this section, the extensible 3-dimensional cable model with bending stiffness is considered. In this model, the cable is discretized into N elements, with the elements' masses lumped at nodes. The massless links connecting these nodes comprise of a spring in parallel with a dashpot to represent the tether's stiffness and material damping. Since the forces acting on the tether such as the weight and the drag are also concentrated at the nodes, the model is referred to as a 'lumped parameter model'.

In order to use a lumped parameter approach to model a continuous cable, the cable's axial and bending properties must be discretized. The cables axial and bending stiffness are

incorporated into the model using axial and rotational springs that link each pair of adjacent lumped masses, as can be seen in Figure 3.1. The cable's axial damping is incorporated into the model using axial dashpots positioned in parallel to the axial springs. Expressions that relate the discretized stiffness and damping coefficients to the system's known parameters must first be derived in order to accurately represent the continuous system. Following this, the nonlinear equations of motion for the cable elements are derived in this section.

3.1.1 Discretizing the Cable's Axial Properties

The system's axial properties are represented by a spring and a dashpot in parallel to each other that link adjacent element masses. The spring's stiffness and dashpot's damping coefficient are dependent on the cable's material, geometry and the number of discrete elements chosen to represent the system, N.

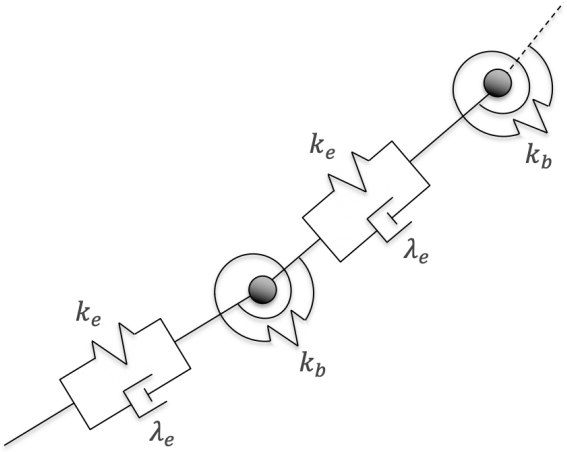

Fig. 3.1 Discretized Tether Elements for the Extensible Cable Model

Discretizing the Cable's Axial Stiffness

For a general length of continuous cable, L, the following expression for the Young's Modulus E holds:

$$E = \frac{FL}{A_{CS}x} \tag{3.1}$$

Here, F is the axial force acting on the cable, A_{CS} is the cross-sectional area and x is the resulting extension of the cable. While the Young's Modulus is a material property, the stiffness k is specific to a selected cable sample and is dependent on the cable's geometry in addition to its material. Since the axial force also relates to the cable's extension with $F = kx$,

this can be substituted into Equation 3.1 to produce the following relationship:

$$k = \frac{EA_{CS}}{L} \tag{3.2}$$

Discretizing a cable into elements has no effect on its material or cross-sectional area, but reduces the length of the segment for which the stiffness is being found, by a factor that is dependant on the number of elements chosen, N. For an element length l, the elemental axial stiffness can therefore be found using:

$$k_e = \frac{EA_{CS}}{l} = \frac{EA_{CS}N}{L} \tag{3.3}$$

The elemental spring stiffness for the system in question is therefore obtained using this expression.

Discretizing the Cable's Axial Damping

For a particular cable, its damping properties can be found through experimentation. By applying an initial non-zero axial displacement, free axial vibration of the system can be initiated and observed. For a cable sample of length L_s that has non-zero material damping, the amplitude of vibration is expected to decrease exponentially with time. The logarithmic decrement, Δ, can be calculated by recording the peak amplitudes of more than one vibration period, using the following expression:

$$\Delta = \frac{1}{n} \ln \frac{x(t)}{x(t+nT)} \tag{3.4}$$

Here, $x(t)$ is the peak amplitude at time t and $x(t+nT)$ is the peak amplitude n periods after t. The damping ratio of the sample, ζ, can then be calculated from the logarithmic decrement using the following relationship:

$$\zeta = \frac{1}{1+(2\pi/\Delta)^2} \tag{3.5}$$

The equivalent damping coefficient of the sample λ_s can then be found using the following relationship with the damping ratio of the sample ζ_s:

$$\lambda_s = 2\zeta_s \sqrt{k_s m_s} \tag{3.6}$$

Since the damping coefficient is expected to be inversely proportional to length like the stiffness, the damping coefficient multiplied by the sample length is expected to be constant for any sample length (assuming the other properties are unchanged). The element damping coefficient λ_e can therefore be calculated using the following expression:

$$\lambda_e = \frac{\lambda_s L_s}{L_e} \tag{3.7}$$

By experimenting on a sample of the cable, the elemental dashpot damping coefficient can therefore be calculated and applied to the model.

3.1.2 Discretizing the Cable's Bending Properties

In discretizing the system spatially into a lumped mass model, its continuous bending stiffness is replaced by a series of rotational springs, which act to oppose the beam's curving. For a continuous cable structure with non-zero bending stiffness, the system's bending properties are defined by the cable's flexural rigidity EI which depends on both the material the cable is made of as well as its cross-sectional shape. For the discretized software cable model, the bending stiffness is accounted for through the use of a set of rotational springs that connect each pair of adjacent elemental links and act towards holding them such that they are parallel to one another. The stiffness parameter in this case is the stiffness of these rotational springs k_b, which is the constant of proportionality relating the internal bending moment to the relative rotation between the adjacent links.

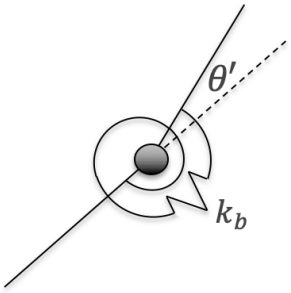

Fig. 3.2 Elemental Rotational Spring

For a relative angle θ' the expression for the elemental bending moment is:

$$M = k_b \theta' \tag{3.8}$$

In order to accurately model the balloon's tether in a spatially discretized manner, a relationship between the two bending stiffness parameters must be established. In this section, a relationship between a system's flexural rigidity EI and its equivalent discretized bending stiffness k_b is established. The discretization of the system's axial and bending properties are validated in Chapter 8.3.

A cantilever beam is considered. By comparing the relationships between a force applied to the end of the beam and the beam's deflection for the continuous and discrete systems, a relationship can be obtained that relates the elemental rotational spring stiffness k_b to the continuous system's flexural rigidity EI. Figure 3.3 shows diagrams of the two systems side by side.

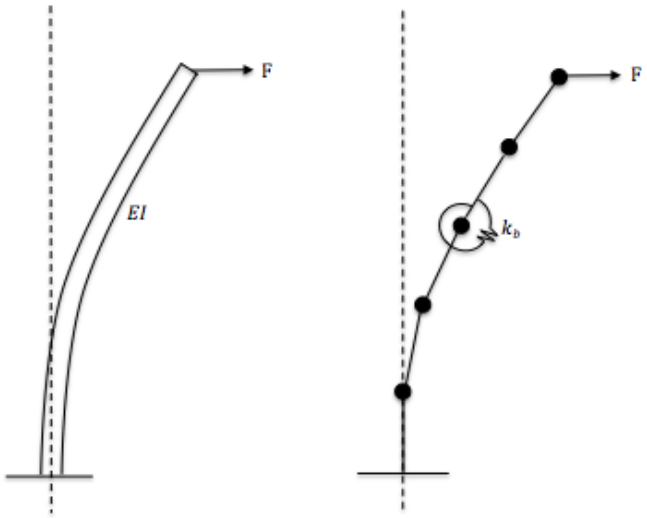

Fig. 3.3 Relating the flexural rigidity EI to the bending stiffness of the elemental rotational spring k_b of the discretized model

According to theory, the lateral displacement of the end of a cantilever due to the force applied to the end, F, can be found using the following equation:

$$x = \frac{FL^3}{3EI} = \frac{FN^3l^3}{3EI} \tag{3.9}$$

Here, L is the length of the cantilever, and l is the length of the N discrete elements. By deriving an expression for the end displacement of the equivalent discretized system in terms of the rotational spring stiffness k_b, the two values can be equated and their relationship found.

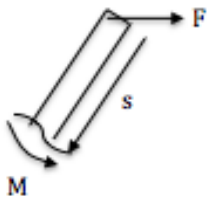

Fig. 3.4 Free body diagram for a cut section from the end of the beam

Assuming small lateral displacement, the internal moment at an arbitrary distance s from the cantilever's end is:

$$M(s) = Fs \tag{3.10}$$

In the discrete case, the equivalent equation for the i*th* element starting from the discrete cantilever's end is:

$$M(i) = F(i-1)l \tag{3.11}$$

This can be equated to the expression for the internal bending moment in 3.8:

$$M(i) = F(i-1)l = k_b\theta_i' \tag{3.12}$$

Here θ' is the angle extended by the rotational spring, i.e. the link's angle relative to the previous link. This equation holds for $i = 1 : N-1$, since the rotational stiffness of the element at the cantilever's fixed end is infinite to mimic a clamped end. The rotation of this element is taken as 0, and it therefore does not contribute to the end displacement of the discrete cantilever model. Rearranging equation 3.12, the general magnitudes of the springs' extended angles are:

$$\theta_i' = \frac{F(i-1)l}{k_b} \tag{3.13}$$

To remain consistent with the remainder of this research, this expression is altered such that the element number j starts from the cantilever's fixed end. In this case, the following expression is valid for $j = 2 : N$, since the rotation of the first element is 0.

$$\theta_j' = \frac{F(N-(j-1))l}{k_b} \tag{3.14}$$

The absolute angle from the vertical for an arbitrary link is the sum of all the previous relative rotations between adjacent links and is therefore:

$$\theta_j = \theta_j' + \theta_{j-1}' + \ldots + \theta_2' + \theta_1' = \theta_j' + \theta_{j-1}' + \ldots + \theta_2' \tag{3.15}$$

The term θ_1' is omitted from the expression since its magnitude is 0. Substituting the expressions for the relative rotations between the links produces the following general expression for the elements' absolute rotation:

$$\theta_j = \frac{Fl}{k_b}\left(N-(j-1)+N-(j-2)+N-(j-3)+\ldots+N-2+N-1\right) \tag{3.16}$$

Combining the expressions together produces the following expression for the absolute angle from the vertical of an arbitrary jth element.

$$\theta_j = \frac{Fl}{k_b}\left((j-1)N-\frac{j(j-1)}{2}\right) \tag{3.17}$$

The lateral displacement of the jth element for small deviations from the vertical is approximated by the following expression.

$$x_j = l\left(\theta_j+\theta_{j-1}+\ldots+\theta_2+\theta_1\right) = l\left(\theta_j+\theta_{j-1}+\ldots+\theta_2\right) \tag{3.18}$$

The lateral displacement at the cantilever's end due to the force F is therefore approximately equal to the following summation:

$$x(N) = l\sum_{j=1}^{N}\theta_j = \frac{Fl^2}{2k_b}\sum_{j=1}^{N}(j-1)(2N-j) \tag{3.19}$$

Equating the expressions for the end deflection of the continuous and discrete cantilevers and simplifying produces a relationship between the flexural rigidity of a beam and the rotational spring stiffness of its equivalent discrete model.

$$k_b = \frac{3EI}{2N^3 l}\sum_{j=1}^{N}(j-1)(2N-j) \tag{3.20}$$

The elemental rotational spring stiffness can therefore be calculated for any system and applied to the discrete model.

3.1.3 Newtonian Derivation of Equations of Motion

In this section, the nonlinear equations of motion for the discretized elements of the extensible cable model are derived. 3-Dimensional Cartesian coordinates are used in this section, making it a $3N$ degree of freedom system. At each time instant, the instantaneous internal and external forces of each element must be calculated and Newton's second law can be

applied to each point mass in the system individually, by using vector form. This leaves us with 3N second order differential equations that describe the system's dynamic behaviour.

Calculating the Internal Tension along the Tether

To start with the method for obtaining the elemental tension is described. The figure below shows the components of the tension of an element that must be considered.

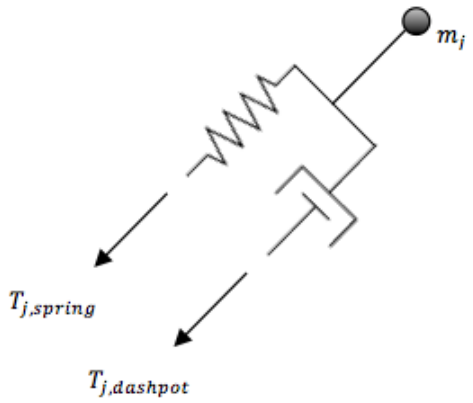

Fig. 3.5 Elemental internal tension components

The internal tension of an element contains components due to its spring and its dashpot. From the current state vector, the program uses the coordinates of every pair of adjacent nodes to determine the instantaneous extension of each spring/link and therefore calculate the magnitude of the tension in each link due to the spring. The instantaneous spring tension is calculated for each element as follows:

$$T_{j,spring} = k\left(|\mathbf{r}_j - \mathbf{r}_{j-1}| - L_j\right) \tag{3.21}$$

Here, L_j is the unstretched length of the jth element and $\mathbf{r}_j$ is the position vector of the jth point mass. The second contribution to the elemental tension is due to the dashpot that is modelled as being in parallel with the spring. The value of this is proportional to the rate of the extension of the link, i.e. the relative velocity of the two nodes resolved into the direction parallel to the link that connects them (hence the dot product with the unit vector representing the instantaneous direction of the jth link, $\mathbf{e}_j$), with a constant of proportionality equal to the damping factor λ.

$$T_{j,dashpot} = \lambda\left(\left(\dot{\mathbf{r}}_j - \dot{\mathbf{r}}_{j-1}\right).\mathbf{e}_j\right) \tag{3.22}$$

The total magnitude of the elemental tension is simply a sum of these.

$$T_j = T_{j,spring} + T_{j,dashpot} = k\left(|\mathbf{r}_j - \mathbf{r}_{j-1}| - l_0\right) + \lambda\left(\left(\dot{\mathbf{r}}_j - \dot{\mathbf{r}}_{j-1}\right).\mathbf{e}_j\right) \tag{3.23}$$

The magnitudes of the tensions in the links can therefore be calculated using the entries of the state vector which are known at each time step. Since the tension acts along a link, the tension force in each link can be written as a vector by multiplying each scalar tension magnitude with the corresponding unit vector. In this way the tension is expressed as components in the x, y and z directions, for easy application of Newton's second law later.

$$\mathbf{T}_j = T_j \mathbf{e}_j \tag{3.24}$$

The unit direction vector of an arbitrary jth element can be found using the following expression:

$$\mathbf{e}_j = \frac{\mathbf{r}_j - \mathbf{r}_{j-1}}{|\mathbf{r}_j - \mathbf{r}_{j-1}|} \tag{3.25}$$

Calculating the Internal Bending Moment Along the Tether

The bending stiffness of the tether is accounted for in the model through the use of rotational springs that create bending moments that act to oppose misalignments between adjacent element links. The spring bending moment is proportional to the angular deviation from parallel of the two adjacent links, and the constant of proportionality, or the spring stiffness, is k_b. Another possible component of the internal bending moment is rotational damping which acts to oppose relative rotational motion between adjacent elements. Figure 3.6 shows a schematic of the bending moment components of an element.

Here, β_j is the 3-dimensional relative angle between the adjacent elemental links, and $\mathbf{e}_j$ and $\mathbf{e}_{j+1}$ are the unit vectors of the respective links, as in the previous section. It is important to remember that the internal bending moment components due to bending stiffness and the rotational damping can act about different axes. While the bending moment due to the rotational spring depends on the instantaneous relative alignment of the links, the bending moment due to the rotational damper depends on the instantaneous relative angular velocity between the two links, the two of which are independent. In this research, rotational damping is ignored, and the internal bending moment is assumed to be solely due to the tether's bending stiffness.

The magnitude of the bending moment due to the rotational spring is found with the following expression.

$$M_j = k_b \beta_j \tag{3.26}$$

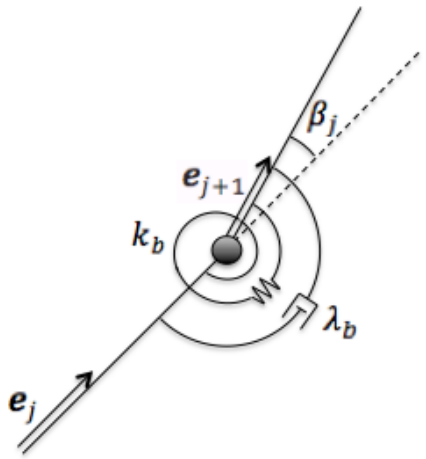

Fig. 3.6 Elemental internal bending moment components

Since β_j is the angle between the two unit vectors $\mathbf{e}_j$ and $\mathbf{e}_{j+1}$, this expression can be rewritten as:

$$M_j = k_b \arccos \frac{\mathbf{e}_j.\mathbf{e}_{j+1}}{|\mathbf{e}_j||\mathbf{e}_{j+1}|} = k_b \arccos \mathbf{e}_j.\mathbf{e}_{j+1} \tag{3.27}$$

The magnitudes of the discretized internal bending moments along the tether can therefore be calculated using only the elemental link direction vectors determined earlier and the tether's discretized bending stiffness k_b. The bending moments along the tether need to be found in vector form, so an expression for their respective unit direction vectors is required.

The direction of the bending moment of each rotational spring will be perpendicular to the unit direction vectors of the two links adjacent to it. For the case in Figure 3.6, if the links are assumed to be in the plane of the page, the bending moment axis will be perpendicular to the page. More specifically, by making a cut just beyond the jth mass, the internal bending moment derived above will act in the direction shown in the Figure 3.7.

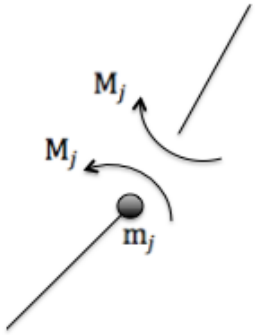

Fig. 3.7 Bending moment due to the jth rotational spring

Since the direction of the internal bending moment varies along the tether, the magnitude of the bending moment is insufficient and so a unit vector in the direction in which it acts is needed. To find the unit vector perpendicular to the two unit direction vectors of the adjacent links, their cross product can be taken. Since the two direction vectors are not perpendicular, the result must be altered such that its magnitude is 1.

$$\mathbf{e}_j \times \mathbf{e}_{j+1} = \sin\theta \mathbf{n}_j \tag{3.28}$$

Here, $\mathbf{n}_j$ is the unit vector perpendicular to the two adjacent links, and the direction of the bending moment (out of the page in this case). Diving by the magnitude of the vector produces an expression for the unit vector in the direction of the bending moment M_j.

$$\mathbf{n}_j = \frac{\mathbf{e}_j \times \mathbf{e}_{j+1}}{|\mathbf{e}_j \times \mathbf{e}_{j+1}|} \tag{3.29}$$

The internal bending moment vector for the jth element is therefore:

$$\mathbf{M}_j = M_j \mathbf{n}_j = k_b \arccos \mathbf{e}_j.\mathbf{e}_{j+1} \frac{\mathbf{e}_j \times \mathbf{e}_{j+1}}{|\mathbf{e}_j \times \mathbf{e}_{j+1}|} \tag{3.30}$$

For each time step, the internal bending moment vector can therefore be calculated using just the tether's current state vector and its bending stiffness. For the remainder of this section, $\mathbf{n}_j$ will refer to the unit vector in the direction perpendicular to the two adjacent links.

Calculating the Shear Force Along the Tether

Before forces can be resolved in the x, y and z directions, the shear forces at both ends of the element must be determined as they are unknown. In order to do this, bending moments about the point mass can be taken, and since all of the external forces act through the point mass in the lumped parameter model, expressions for the shear forces can be found in terms of the bending moments acting on the element, the expressions for which were deduced earlier. A new free body diagram is drawn below, showing only the components that produce a bending moment about the point mass for clarity; all forces that go through the point mass have been removed. No D'Alembert moment is included in the free body diagram because the link is massless. The centre of mass of the element is therefore at the point mass, and the moment of inertia of a point mass is equal to zero.

Since the model is 3-dimensional, the shear force N can act in any direction in the plane perpendicular to the elemental link, and therefore $\mathbf{e}_j$. To account for this, 2 orthogonal shear forces of unknown value are placed in the diagram in the shear plane, N_1 and N_2. It

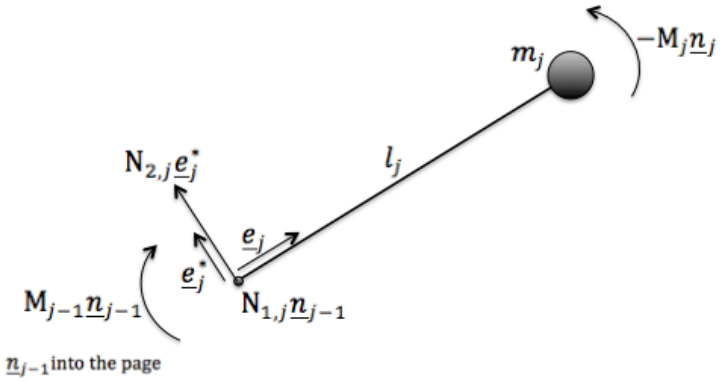

Fig. 3.8 A free body diagram of the jth element showing only the forces that contribute to a bending moment about the mass m_j

is important to remember that for a 3-dimensional tether model, the two bending moments on either side of the element do not necessarily act in the same direction; they each depend on the link's relative direction to the adjacent link on their respective side. The diagram is drawn such that the bending moment axis of M_{j-1}, $\mathbf{n}_{j-1}$ is perpendicular to and into the page. The element, and therefore the link direction vector $\mathbf{e}_j$, are in the plane of the page. The unit vector $\mathbf{e}_j^*$ is orthogonal to both $\mathbf{n}_{j-1}$ and $\mathbf{e}_j$, and is also in the plane of the page. The direction of the bending moment axis of M_j is $\mathbf{n}_j$ and is arbitrary. Taking moments about m_j:

$$\mathbf{M} = M_{j-1}\mathbf{n}_{j-1} - M_j\mathbf{n}_j + l_j(-\mathbf{e}_j) \times N_{2,j}\mathbf{e}_j^* + l_j(-\mathbf{e}_j) \times N_{1,j}\mathbf{n}_{j-1} = 0 \tag{3.31}$$

Upon determining the directions of the vector cross products, the equation simplifies to:

$$\mathbf{M} = M_{j-1}\mathbf{n}_{j-1} - M_j\mathbf{n}_j + l_jN_{2,j}\mathbf{n}_{j-1} - l_jN_{1,j}\mathbf{e}_j^* = 0 \tag{3.32}$$

The moments about a particular axis through the point mass can be found by taking the dot product of of each term with the direction vector of said axis. Expressions for the shear forces N_1 and N_2 can be found by taking the dot product of the sum of moments with the axes of the respective bending moments they produce.

The sum of bending moments about the point mass through an axis into the page is found by taking the dot product of the full expression with the unit vector $\mathbf{n}_{j-1}$.

$$\mathbf{M}.\mathbf{n}_{j-1} = M_{j-1}\mathbf{n}_{j-1}.\mathbf{n}_{j-1} - M_j\mathbf{n}_j.\mathbf{n}_{j-1} + l_jN_{2,j}\mathbf{n}_{j-1}.\mathbf{n}_{j-1} - l_jN_{1,j}\mathbf{e}_j^*.\mathbf{n}_{j-1} = 0 \tag{3.33}$$

Since $\mathbf{e}_j^*$ and $\mathbf{n}_{j-1}$ are orthogonal, the final term disappears. Rearranging gives a general expression for the shear force N_2.

$$\mathbf{N}_{2,j} = \frac{M_j \mathbf{n}_j . \mathbf{n}_{j-1} - M_{j-1}}{l_j} \mathbf{e}_j^* \tag{3.34}$$

The expressions for the bending moments and their unit direction vectors were derived in the previous section and are known. The direction vector $\mathbf{e}_j^*$ is found easily using the following cross product:

$$\mathbf{e}_j^* = \mathbf{e}_j \times \mathbf{n}_{j-1} \tag{3.35}$$

Similarly, to find N_1 the sum of the bending moments about the axis through the point mass in the direction $\mathbf{e}_j^*$ is found.

$$\mathbf{M}.\mathbf{e}_j^* = M_{j-1}\mathbf{n}_{j-1}.\mathbf{e}_j^* - M_j \mathbf{n}_j.\mathbf{e}_j^* + l_j N_{2,j}\mathbf{n}_{j-1}.\mathbf{e}_j^* - l_j N_{1,j}\mathbf{e}_j^*.\mathbf{e}_j^* = 0 \tag{3.36}$$

Since $\mathbf{e}_j^*$ and $\mathbf{n}_{j-1}$ are perpendicular, their dot product is zero. Simplifying and rearranging gives:

$$\mathbf{N}_{1,j} = -\frac{M_j \mathbf{n}_j . \mathbf{e}_j^*}{l_j} \mathbf{n}_{j-1} \tag{3.37}$$

The instantaneous shear forces acting on the elements have now been found, leaving no unknown internal forces.

Implementing the Tether's Aerodynamic Drag

The internal damping has now been accounted for through the dashpot component of the cable tension. External damping in the form of aerodynamic drag also acts on the tether. Two methods of implementing aerodynamic drag are considered and discussed in this section: the added mass approach and the drag equation.

For a solid body moving through a stationary fluid (i.e. no currents) the added mass approach can be used to account for the necessary acceleration of fluid as the body accelerates. This is done by increasing the body's inertia by a certain amount to model this increase in resistance to motion. For a small-scale thin cable moving through air, this extra mass can be considered negligible compared to the inertia of the tether itself, and so this step may not be crucial. For the full-scale high-altitude tethered balloon system where the tether is significantly thicker and longer, the drag force on the tether becomes significant and should be included.

Representing the cable element as a cylinder, the value of the added mass is:

$$m_{a,cyl} = \rho \pi R^2 L \tag{3.38}$$

The issue with using this method for a cylindrical tether element is that this expression was derived specifically for the motion in a direction perpendicular to the cylinder's axis. Using this added mass and increasing the element's inertia generally, implies that the resistance to motion of the cylinder due to the drag is equal in any direction, which is not the case in reality. The increased opposition to motion due to the surrounding fluid only applies for motion in a direction perpendicular to the axis of the cylinder, and not in a direction parallel to it. This implies that the body's increased resistance is only for motion in the plane perpendicular to the cylinder's axis, which generally increasing the mass doesn't account for. It is possible to resolve in said directions and apply the increased inertia as appropriate, but this defeats the purpose of what is supposed to be a simple approach to incorporating drag. For a taut tether however, in which the tether elements' motion is likely to be close to being transverse to the tether, this method can be a good approximation. For the case of the balloon's drag discussed later, this is not an issue as the drag force is the same for the motion of the balloon in any direction since it is spherical.

When incorporating this into the model however, care must be taken to account for the fact that the density of the surrounding air decreases with altitude, and so the inertia added to the lumped masses decreases as you travel up the tether for high altitude systems and also varies as the tether moves. This is expected, as where the air density is lower there will be less resistance to the acceleration of a body in the fluid. For the balloon, having such a large volume to mass ratio means that the added mass is comparable to the mass of the balloon, and its inclusion is necessary for both the full-scale and small-scale system models. The calculation of this is described later.

Applying this added mass approach to represent the drag due to the motion through the fluid is only applicable for situations where the fluid is initially stationary - i.e. if there is no wind in the tethered balloon case. This is clear by the fact that, in this case, the drag force doesn't necessarily act to reduce motion. With a wind present, the aerodynamic drag may result in an acceleration, and its direction is not necessarily parallel and opposite to motion. The direction of the drag force now depends on the relative velocity of the body and the fluid.

For cases where there is wind present, the drag equation is used to determine the drag force acting on each tether element. The drag force is time variant, and needs to be calculated for each tether element at each time step. It is dependent on the velocity of the element, the velocity of the wind and air density at its current altitude, and the angle of inclination of the element relative to these velocities. Tether elements are approximated as being cylindrical.

The general drag equation is written below:

$$F_D = \frac{1}{2}\rho u^2 C_D A_r \tag{3.39}$$

Here, u is the component of the relative velocity between the element and the wind in the direction perpendicular to the cylinder's axis. The drag force for a cylindrical tether element will therefore act in the plane perpendicular to the cylinder's axis. Its direction within the plane depends on the relative velocity between the cylinder and the wind. C_D is the drag coefficient and A_r is the reference area, which is equal to the projected area of the cylinder, and is therefore $l_j d$ for an element, where l_j is the element length and d is the tether's outer diameter.

The instantaneous wind velocity that the element experiences, $v_{w,j}$ is calculated using its instantaneous altitude, z_j and depends on the wind profile considered. The relative velocity is therefore equal to $\mathbf{v}_{w,j} - \dot{\mathbf{r}}_j$.

The relative velocity vector can be projected into the plane perpendicular to the element's axis by deducting the component that is parallel to the element's unit vector, $\mathbf{e}_j$:

$$\mathbf{u}_j = \left(\mathbf{v}_{w,j} - \dot{\mathbf{r}}_j\right) - \left(\left(\mathbf{v}_{w,i} - \dot{\mathbf{r}}_j\right).\mathbf{e}_j\right)\mathbf{e}_j \tag{3.40}$$

The vector equation for the drag on a tether element is therefore:

$$\mathbf{D}_j = \frac{1}{2}\rho_{a,j} C_D l_j d |\mathbf{u}_j| \mathbf{u}_j \tag{3.41}$$

Multiplying the modulus of $\mathbf{u}$ by the vector of u maintains its vector direction which is also the direction of the element drag force. Here $\rho_{a,j}$ refers to the air density at the element's instantaneous altitude.

It is important to add that in reality, the aerodynamic forces acting on the tether elements are expected to be much more complex due to the presence of vortex shedding. In this research, steady-state aerodynamic loading is used to model the system's response to wind flow for simplicity. The presence of vortex shedding in reality is expected to result in lateral vibrations of the tether in the direction perpendicular to the wind flow. While this research focuses on the larger-scale response of the system to disturbances, it would be interesting to incorporate dynamic wind loading in further work, especially as the cyclic tether stress caused by the vibrations poses an increased risk of fatigue.

Applying Newton's Second Law of Motion

Expressions for all of the forces, both internal and external have now been found, and Newton's second law of motion can now be applied to each element. Figure 3.9 shows a full free body diagram for an arbitrary jth element. The diagram is once again aligned such that element's link is in the plane of the page, although it is important to remember that the subsequent link is not necessarily to avoid losing generality. It is also drawn such that the direction vector of the (j-1)th bending moment, $\mathbf{n}_{j-1}$, is perpendicular and into the page. Here, $\mathbf{e}_{j+1}, \mathbf{e}^*_{j+1}, \mathbf{n}_j$ and $\mathbf{D}$ are not in the plane of the page, their direction is arbitrary. While the Cartesian direction vectors $\mathbf{i}, \mathbf{j}$ and $\mathbf{k}$ are orthogonal to each other, they are not necessarily aligned with the page in any way, as their relationship to the element direction vector $\mathbf{e}_j$ and the moment direction vector $\mathbf{n}_{j-1}$ is also arbitrary. The internal forces between two adjacent elements will act in opposite directions on each element, hence the negative values.

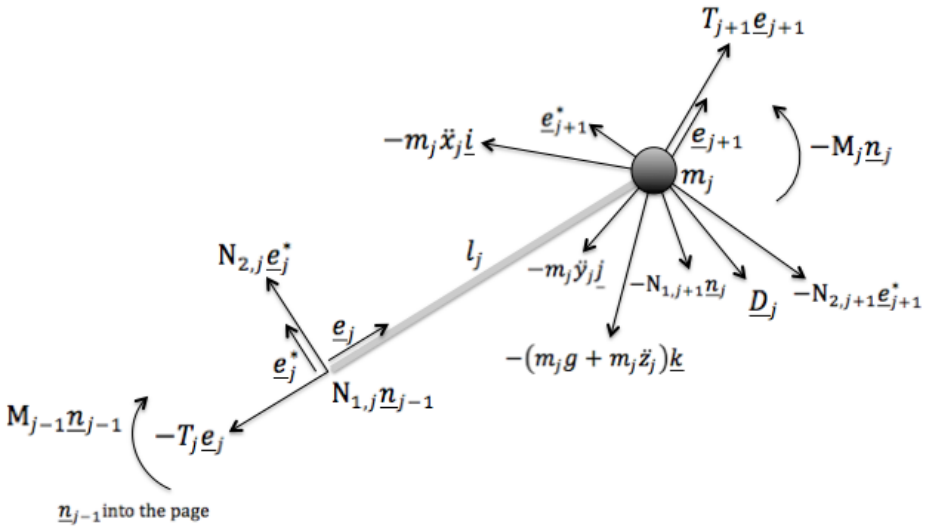

Fig. 3.9 A free body diagram of the jth element

Newton's second law of motion can be applied in the x, y and z directions for each element, and the equations of motion deduced. Since all the forces are already in Cartesian vector form, this is very easy to do.

Resolving forces in the $\mathbf{i}$ direction:

$$\begin{aligned} -m_j\ddot{x}_j - T_j\mathbf{e}_j.\mathbf{i} + T_{j+1}\mathbf{e}_{j+1}.\mathbf{i} + \mathbf{D}_j.\mathbf{i} + N_{1,j}\mathbf{n}_{j-1}.\mathbf{i} \\ + N_{2,j}\mathbf{e}^*_j.\mathbf{i} - N_{1,j+1}\mathbf{n}_j.\mathbf{i} - N_{2,j+1}\mathbf{e}^*_{j+1}.\mathbf{i} = 0 \end{aligned} \tag{3.42}$$

Similarly, resolving in the **j** direction:

$$\begin{aligned} -m_j\ddot{y}_j - T_j\mathbf{e}_j.\mathbf{j} + T_{j+1}\mathbf{e}_{j+1}.\mathbf{j} + \mathbf{D}_j.\mathbf{j} + N_{1,j}\mathbf{n}_{j-1}.\mathbf{j} \\ + N_{2,j}\mathbf{e}^*_j.\mathbf{j} - N_{1,j+1}\mathbf{n}_j.\mathbf{j} - N_{2,j+1}\mathbf{e}^*_{j+1}.\mathbf{j} = 0 \end{aligned} \tag{3.43}$$

Finally in the **k** direction:

$$\begin{aligned} -m_j\ddot{z}_j - m_j g - T_j\mathbf{e}_j.\mathbf{k} + T_{j+1}\mathbf{e}_{j+1}.\mathbf{k} + \mathbf{D}_j.\mathbf{k} + N_{1,j}\mathbf{n}_{j-1}.\mathbf{k} \\ + N_{2,j}\mathbf{e}^*_j.\mathbf{k} - N_{1,j+1}\mathbf{n}_j.\mathbf{k} - N_{2,j+1}\mathbf{e}^*_{j+1}.\mathbf{k} = 0 \end{aligned} \tag{3.44}$$

For the balloon element, the same process is followed, but the forces and therefore the free body diagram will differ slightly. This element length and mass, l_N and m_N will now represent the balloon diameter and mass respectively. An upward lift force acts upwards on the balloon and the balloon drag will act in an arbitrary direction depending on the wind velocity and the velocity of the balloon.

3.1.4 Lagrangian Derivation of Equations of Motion

Obtaining the same equations of motion using an entirely different method is a useful way to gain confidence in the work and verify that the equations are correct. However, another reason why the Lagrangian method is used in addition to the Newtonian one is that, while the Newtonian method is significantly more computationally efficient for the nonlinear system model, when it comes to linearizing the model with a large number of elements, using energy methods turns out to be the much more efficient method. It is therefore useful to verify that the energy method agrees with the force method before using it in further work.

In the Lagrangian method of obtaining a system's equations of motion, expressions are written out for the system's kinetic energy and potential energy in terms of the chosen generalised coordinates. For each generalised coordinate q_j in turn, Lagrange's equation is applied, producing a series of equations that can be simultaneously solved to produce the system's equations of motion. This is done using the Symbolic Toolbox in Matlab.

For the extensible system model, absolute 3D Euler angles θ_j and φ_j, and the link length l_j are used as the generalized coordinates. Since torsional motion is ignored in this research, the third Euler angle ψ_j is assumed to be 0 in analysis and ignored.

Deriving the Kinetic Energy Equation of the System

In order to derive an expression for the kinetic energy of the system, an expression for the absolute velocity of each element mass needs to be derived.

The absolute velocity of the *j*th mass is equal to the absolute velocity of the $(j-1)$th mass plus the relative velocity between them (i.e. the velocity due to the rotation and extension of the *j*th link). This can be written as:

$$\dot{\mathbf{r}}_j = \dot{\mathbf{r}}_{j-1} + \dot{l}_j \mathbf{e}_j + l_j \mathbf{e}_j \times \boldsymbol{\omega}_j \tag{3.45}$$

Since the velocity of the jth element is dependent on the velocities of all the previous elements, for which the direction vectors of the velocity components are different, the velocities need to be expressed in the Cartesian coordinate system so that they can be added together. Figure 3.10 shows the relative direction of the element direction vector to the Cartesian unit vectors.

Expressions for the unit vectors in the directions of the links $\mathbf{e}_j$ in the Cartesian coordinate system are written in terms of the absolute Euler angles of each element. For the *j*th element:

$$\mathbf{e}_j = \sin\theta_j \cos\varphi_j \mathbf{i} + \sin\theta_j \sin\varphi_j \mathbf{j} + \cos\theta_j \mathbf{k} \tag{3.46}$$

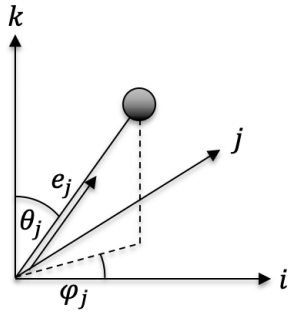

Fig. 3.10 Resolving $\mathbf{e}_j$ into Cartesian Coordinates

The absolute angular velocities of the elements ($\dot{\theta}_j$ and $\dot{\varphi}_j$ in the Euler coordinate system) also need to be expressed as vectors in the Cartesian coordinate system. For the *j*th element:

$$\boldsymbol{\omega}_j = -\dot{\theta}_j \sin\varphi_j \mathbf{i} + \dot{\theta}_j \cos\varphi_j \mathbf{j} + \dot{\varphi}_j \mathbf{k} \tag{3.47}$$

The position vector for the *j*th element is:

$$\mathbf{r}_j = l_1 \mathbf{e}_1 + l_2 \mathbf{e}_2 + \ldots + l_j \mathbf{e}_j \tag{3.48}$$

The absolute velocity of the *j*th element is therefore:

$$\begin{aligned}\dot{\mathbf{r}}_j &= \dot{l}_1\mathbf{e}_1 + l_1\dot{\mathbf{e}}_1 + \dot{l}_2\mathbf{e}_2 + l_2\dot{\mathbf{e}}_2 + \ldots + \dot{l}_j\mathbf{e}_j + l_j\dot{\mathbf{e}}_j \\ &= \dot{l}_1\mathbf{e}_1 + l_1\omega_1 \times \mathbf{e}_1 + \dot{l}_2\mathbf{e}_2 + l_2\omega_2 \times \mathbf{e}_{r_2} + \ldots + \dot{l}_j\mathbf{e}_j + l_j\omega_j \times \mathbf{e}_j \\ &= \sum_{i=1}^{j}(\dot{l}_i\mathbf{e}_i + l_i\omega_i \times \mathbf{e}_i)\end{aligned} \tag{3.49}$$

The kinetic energy of the *j*th element is:

$$T_j = \frac{1}{2}m_j|\dot{\mathbf{r}}_j|^2 \tag{3.50}$$

The expression for the total kinetic energy is the sum over all the elements.

$$T = \frac{1}{2}\sum_{j=1}^{N} m_j|\dot{\mathbf{r}}_j|^2 = \frac{1}{2}\sum_{j=1}^{N} m_j|\sum_{i=1}^{j}(\dot{l}_i\mathbf{e}_i + l_i\omega_i \times \mathbf{e}_i)|^2 \tag{3.51}$$

Deriving the Potential Energy Equation of the System

For the extensible model, the potential energy equation of the system includes components due to the gravitational potential energy of the elements and also the elastic potential energy due to the axial and rotational springs. The potential energy of an arbitrary jth element is therefore:

$$V_j = m_j g z_j + \frac{1}{2}k\big(|\mathbf{r}_j - \mathbf{r}_{j-1}| - L_j\big)^2 + \frac{1}{2}k_b\left(\arccos \mathbf{e}_j.\mathbf{e}_{j+1}\right)^2 \tag{3.52}$$

Here, z_j is the element height which is equal to $\mathbf{r}_j.\mathbf{k}$. Expressions for the position vectors $\mathbf{r}_j$ and element link direction vectors $\mathbf{e}_j$ were derived previously. The total potential energy of the system is the sum of the potential energies of all of the elements, and takes the following expression.

$$V = \sum_{j=1}^{N}\left(m_j g z_j + \frac{1}{2}k\big(|\mathbf{r}_j - \mathbf{r}_{j-1}| - L_j\big)^2 + \frac{1}{2}k_b\left(\arccos \mathbf{e}_j.\mathbf{e}_{j+1}\right)^2\right) \tag{3.53}$$

Deriving the System's Equations of Motion

Symbolic expressions for the kinetic and potential energies of the system in terms of the Euler angles and their derivatives have now been derived. By differentiating the symbolic expressions as appropriate, the model then uses the symbolic math toolbox to apply Lagrange's equation for each degree of freedom of the system, producing 3N equations. Lagrange's

equation takes the following form:

$$\frac{d}{dt}\left(\frac{\partial T}{\partial \dot{q}_j}\right) - \frac{\partial T}{\partial q_j} + \frac{\partial V}{\partial q_j} = P_j \tag{3.54}$$

Here, q_j are the generalised coordinates, in this case θ_j, φ_j and l_j. On the right hand side, P_j are the generalised forces. Since there are 3N generalised coordinates, 3N expressions are produced. These second order differential equations are the equations of motion of the system.

3.2 3-Dimensional Inextensible Tether Model

In this section, a chain-like inextensible cable model with no bending stiffness is considered. The cable is discretized into N finite segments, with the elements' masses lumped at nodes as before. The links connecting these nodes, however, are now massless rigid links. The axial stiffness of the cable is therefore assumed to be infinite in this case. For small or no bending stiffness, this is effectively a model of a chain. This model is also useful when representing cables of very large axial stiffness, as simply using a large stiffness value in the extensible model makes the software model computationally "stiff" resulting in very long running times, which, for a large scale model with many elements would become very tedious and inefficient.

Newtonian Derivation of Equations of Motion

For the extensible case where the point masses are connected by springs and dashpots, the internal forces in the links can be calculated easily as they are proportional to the extensions of the springs and dashpots which can easily be calculated from the element coordinates obtained from the state vectors. For the case of rigid links however, it is not as easy to calculate the internal forces between each pair of adjacent point masses. Here, simultaneous equations must be solved in order to find the tensions in the element links, which is more computationally demanding.

For the inextensible tether model, the lumped masses are connected by massless rigid links, as shown in Figure 3.11. While in the previous case, there were $3N$ degrees of freedom in 3 dimensions, and therefore $3N$ equations of motion, the current case introduces a new constraint and the number of degrees of freedom has been reduced to $2N$. $3N$ equations are written through resolving forces in the x, y and z directions on each element, and then these are reduced to $2N$ equations of motion through the elimination of the elemental tensions,

T_j. Since each element now has 2 degrees of freedom, θ_j and ϕ_j are now used instead of Cartesian coordinates.

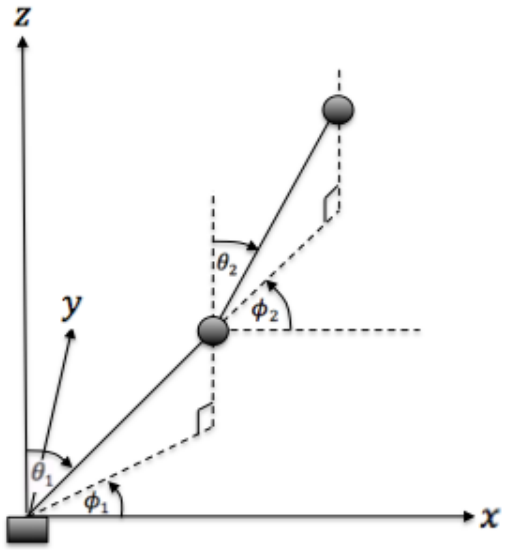

Fig. 3.11 Cable Elements for an Inextensible System

For a now constant element length L, the following expressions are found for the coordinates of an arbitrary element:

$$x_j = L\sum_{i=1}^{j}\sin\theta_i\cos\varphi_i \qquad y_j = L\sum_{i=1}^{j}\sin\theta_i\sin\varphi_i \qquad z_j = L\sum_{i=1}^{j}\cos\theta_i \tag{3.55}$$

By differentiating these twice, expressions for the Cartesian accelerations are found in terms of the Euler angles:

$$\begin{aligned}\ddot{x}_j = L\sum_{i=1}^{j}(&\ddot{\theta}_i\cos\theta_i\cos\phi_i - \dot{\theta}_i^2\sin\theta_i\cos\phi_i + \dot{\theta}\dot{\phi}_i\cos\theta_i\sin\phi_i \\ &- \ddot{\phi}_i\sin\theta_i\sin\phi_i - \dot{\phi}\dot{\theta}_i\cos\theta_i\sin\phi_i - \dot{\phi}_i^2\sin\theta_i\cos\phi_i)\end{aligned} \tag{3.56}$$

$$\begin{aligned}\ddot{y}_j = L\sum_{i=1}^{j}(&\ddot{\theta}_i\cos\theta_i\sin\phi_i - \dot{\theta}_i^2\sin\theta_i\sin\phi_i + \dot{\theta}\dot{\phi}_i\cos\theta_i\cos\phi_i \\ &+ \ddot{\phi}_i\sin\theta_i\cos\phi_i + \dot{\phi}\dot{\theta}_i\cos\theta_i\cos\phi_i - \dot{\phi}_i^2\sin\theta_i\sin\phi_i)\end{aligned} \tag{3.57}$$

$$\ddot{z}_j = -L\sum_{i=1}^{j}\ddot{\theta}_i\sin\theta_i + \dot{\theta}_i^2\cos\theta_i \tag{3.58}$$

Figure 3.12 shows a free body diagram of an arbitrary element in the inextensible chain model. Unlike the previous model, this model does not contain rotational springs between

elements (i.e. no bending stiffness) and so there is no internal bending moment acting within the tether. Taking bending moments about the point mass m_j proves that there are also no shear forces acting within the tether.

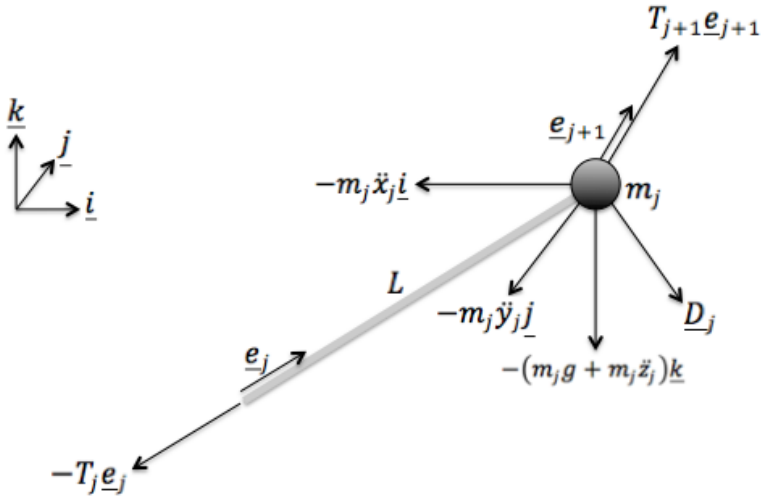

Fig. 3.12 Free body diagram of the jth element for an inextensible cable model

Resolving forces in the **i** direction:

$$-m_j\ddot{x}_j - T_j\mathbf{e}_j.\mathbf{i} + T_{j+1}\mathbf{e}_{j+1}.\mathbf{i} + \mathbf{D}_j.\mathbf{i} = 0 \tag{3.59}$$

Using the expression for $\mathbf{e}_j$ in equation 3.46 and defining the drag vector $\mathbf{D_j}$ as $[D_{j,x}\ D_{j,y}\ D_{j,z}]^T$, this equation becomes:

$$-m_j\ddot{x}_j - T_j\sin\theta_j\cos\phi_j + T_{j+1}\sin\theta_{j+1}\cos\phi_{j+1} + D_{j,x} = 0 \tag{3.60}$$

Similarly, for the **j** and **k** directions respectively, the following expressions are derived:

$$-m_j\ddot{y}_j - T_j\sin\theta_j\sin\phi_j + T_{j+1}\sin\theta_{j+1}\sin\phi_{j+1} + D_{j,y} = 0 \tag{3.61}$$

$$-m_j\ddot{z}_j - m_jg - T_j\cos\theta_j + T_{j+1}\cos\theta_{j+1} + D_{j,z} = 0 \tag{3.62}$$

The expressions for $\ddot{x}, \ddot{y}$ and $\ddot{z}$ derived in equations 3.56, 3.57 and 3.58 can be substituted into these expressions.

$$\begin{aligned}-m_jL\sum_{i=1}^{j}(&\ddot{\theta}_i\cos\theta_i\cos\phi_i - \dot{\theta}_i^2\sin\theta_i\cos\phi_i + \dot{\theta}\dot{\phi}_i\cos\theta_i\sin\phi_i - \ddot{\phi}_i\sin\theta_i\sin\phi_i - \dot{\phi}\dot{\theta}_i\cos\theta_i\sin\phi_i \\ &- \dot{\phi}_i^2\sin\theta_i\cos\phi_i) - T_j\sin\theta_j\cos\phi_j + T_{j+1}\sin\theta_{j+1}\cos\phi_{j+1} + D_x = 0\end{aligned} \tag{3.63}$$

$$-m_j L\sum_{i=1}^{j}(\ddot{\theta}_i\cos\theta_i\sin\phi_i-\dot{\theta}_i^2\sin\theta_i\sin\phi_i+\dot{\theta}\dot{\phi}_i\cos\theta_i\cos\phi_i+\ddot{\phi}_i\sin\theta_i\cos\phi_i+\dot{\phi}\dot{\theta}_i\cos\theta_i\cos\phi_i$$
$$-\dot{\phi}_i^2\sin\theta_i\sin\phi_i)-T_j\sin\theta_j\sin\phi_j+T_{j+1}\sin\theta_{j+1}\sin\phi_{j+1}+D_y=0 \tag{3.64}$$

$$m_j L\sum_{i=1}^{j}\ddot{\theta}_i\sin\theta_i+\dot{\theta}_i^2\cos\theta_i-m_j g-T_j\cos\theta_j+T_{j+1}\cos\theta_{j+1}+D_z=0 \tag{3.65}$$

For N elements, this leaves 3N equations which contain 3N unknowns; the tension in each element T_j, and the second derivatives of the Euler coordinates of each element, $\ddot{\theta}_j$ and $\ddot{\phi}_j$. As before, the equations for the last element, i.e. the balloon, will differ in that they will include the balloon's lift force and drag and will only contain one tension, T_N as there is no element on the other side of this one. An expression for T_N in terms of the other variables can be obtained from those, and substituted into the equations for the previous element, which contain the tensions T_N and T_{N-1}. This leaves an expression with only one tension, T_{N-1} which again can be substituted into the expression for the previous element, and so on. Once expressions for all of the tension values have been obtained, they can be substituted into the remainder of the 2N equations, eliminating the tensions from the equations, and leaving with 2N equations of motion for $\ddot{\theta}_j$ and $\ddot{\phi}_j$.

3.2.1 Lagrangian Derivation of Equations of Motion

Obtaining the equations of motion of this inextensible model using energy methods is very similar to the method used for the extensible model. The main difference is that the potential energy equation will not contain the terms due to elastic potential energy of the axial and rotational springs as in the previous case. The only contributions to the potential energy equation will be due to the gravitational potential energy of the elements.

The absolute velocity of the *j*th element will also no longer contain terms due to the link extensions and any relative motion between two elements will be purely due to rotation. Setting $\dot{l}_j$ to zero, the absolute velocity of the jth element collapses to:

$$\dot{\mathbf{r}}_j=L(\dot{\mathbf{e}}_1+\dot{\mathbf{e}}_2+\ldots+\dot{\mathbf{e}}_j)=L(\omega_1\times\mathbf{e}_1+\omega_2\times\mathbf{e}_2+\ldots+\omega_j\times\mathbf{e}_j)=L\sum_{i=1}^{j}\omega_i\times\mathbf{e}_i \tag{3.66}$$

As before, the expression for the total kinetic energy is the sum over all the elements.

$$T=\frac{1}{2}\sum_{j=1}^{N}m_j|\dot{\mathbf{r}}_j|^2=\frac{L}{2}\sum_{j=1}^{N}m_j|\sum_{i=1}^{j}\omega_i\times\mathbf{e}_i|^2 \tag{3.67}$$

Ignoring the terms due to the elastic potential energy of the axial and rotational springs, since in this model the tether has infinite axial and no bending stiffness, the potential energy collapses to the following expression:

$$V = \sum_{j=1}^{N} m_j g z_j \tag{3.68}$$

The remainder of the steps are exactly the same. The expressions for ω_j, $\mathbf{e}_j$ and z_j in terms of the Euler coordinates θ_j and ϕ_j from equations 3.47, 3.46 and 3.48 respectively, are substituted into the formulas for T and V, and Lagrange's equations are applied for each degree of freedom (θ_j and ϕ_j). This results in $2N$ equations that can be solved simultaneously to produce equations for the angular accelerations $\ddot{\theta}_j$ and $\ddot{\phi}_j$ in terms of the system's known state vector components $\theta_j, \phi_j, \dot{\theta}_j$ and $\dot{\phi}_j$. The equations of motion are thus derived. These are found to agree with those produced using the force method, as expected.

3.3 Modelling the Balloon

In this research, a spherical pressurised balloon is considered. Before its equation of motion can be derived, expressions for the balloon's instantaneous lift, drag and weight need to be established. It is important to account for the fact that, for a high altitude tethered balloon, the air density varies significantly with altitude, and so the balloon's lift and drag forces are also dependent on the balloon's altitude, and therefore vary with its motion. In addition to being dependent on the balloon's altitude, the instantaneous drag force vector is also dependent on the wind velocity at that particular altitude and the instantaneous velocity of the balloon.

The weight of the balloon depends on the density of the material it is made out of, and the volume of the material used. The expression for the balloon mass is written below.

$$m_b = A_{SA} t_b \rho_b = 4\pi r_b^2 t_b \rho_b \tag{3.69}$$

Here, A_{SA} is the surface area of the balloon, t_b is the balloon's skin thickness and ρ_b its density.

The lift force is equal to the weight of displaced air minus the weight of the helium inside the balloon. The lift force at any instant can be calculated with the following expression:

$$F_{lift} = \frac{4}{3}\pi r_b^3 \rho_{a,N} \left(1 - \frac{4}{29}\right) g \tag{3.70}$$

Here, 4/29 is the ratio of the density of Helium to the density of air.

For small scale tethered balloon system's in which the motion of the system is considered without the presence of any wind, one way to represent the balloon's drag is to use the added mass approach, as was explained in the previous section for the tether's drag. When the sphere accelerates through the air, some air must also accelerate around the sphere - an additional force is therefore required to move the air too. This additional resistance to motion can be incorporated into the model by increasing the sphere's inertia by a certain amount. The added mass can be calculated by considering the force exerted by the fluid to oppose its motion. The expression for the added mass for a sphere moving through a fluid is well known and is written below.

$$m_a = \frac{2}{3}\rho_{a,N}\pi R^3 \tag{3.71}$$

This additional mass is added to the mass of the body when considering the body's inertia, but not when considering the body's weight since drag has no effect on the gravitational force acting on the sphere.

Where winds are present, i.e. the surrounding fluid is not initially still, the drag equation is used as before. Once again, the relative velocity between the body and the fluid needs to be found first. Since this relative velocity is not necessarily parallel to the body's velocity, the added mass approach can no longer be used, and the drag equation needs to be applied instead.

The drag coefficient, C_D is a dimensionless coefficient that is dependant on the shape of the body as well as the Reynolds number, Re, which depends on the speed of the airflow. In this equation, u is the relative velocity between the object and the fluid flow, which would need to be calculated at every instant. In this case, the relative velocity does not need to be resolved, since the balloon is spherical. The drag is expected to be proportional in value to the square of u, because if the velocity of the fluid relative to the body is doubled, not only does the fluid hit the body at twice the velocity, but twice the amount of fluid will hit the body per unit time as well. The area A is known as the reference area, and is effectively the projected area of the body as viewed through the direction of its relative motion through the fluid. For the case of the sphere, this is independent of the direction of relative motion, and is always equal to the area of a circle with the same radius as the sphere in question.

The direction of the drag force is always parallel and opposite to the direction of the velocity of the body relative to the fluid, u. To account for this, equation 3.72 can be written in vector form. The magnitude of the force can be multiplied by the negative of a unit vector in the direction of the relative velocity u.

$$\mathbf{D}_b = -\frac{1}{2}\rho_{a,N}|\mathbf{u}|^2\frac{\mathbf{u}}{|\mathbf{u}|}C_D A = -\frac{1}{2}\rho_{a,N}|\mathbf{u}|\mathbf{u}C_D A = -\frac{1}{2}\rho_{a,N}|\dot{\mathbf{r}}_b - \mathbf{v}_{w,N}|\left(\dot{\mathbf{r}}_b - \mathbf{v}_{w,N}\right)C_D\pi r_b^2 \tag{3.72}$$

In both equations 3.71 and 3.72, the density $\rho_{a,N}$ refers to the density of the surrounding fluid, which in this case is the density of air at the balloon's altitude.

For both the extensible and inextensible tether models, the cable is modelled as a series of lumped masses connected by massless links. To combine the cable and balloon systems, the balloon is treated as an additional element on the cable model. The difference is that rather than having the physical parameters of the cable, this element has the physical parameters of the balloon, and also has the relevant balloon forces acting on it. The element mass will obviously be equal to the mass of the balloon. The length of this element is taken as being the radius of the balloon, to ensure that the 'lumped mass' of the balloon is correctly positioned at its centre of mass.

As for the tether elements, these external forces, along with the tension and bending moment acting on the balloon from the upmost tether element, can be resolved into x, y and z directions to obtain expressions for the balloon's accelerations. A free body diagram of the balloon is shown in the Figure 3.13.

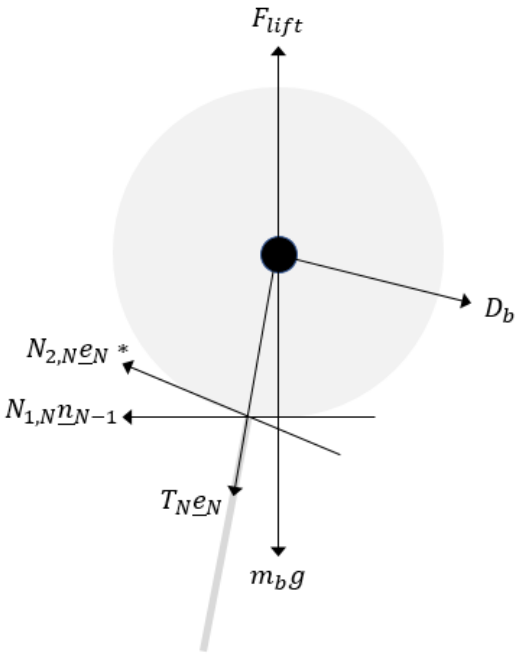

Fig. 3.13 A free body diagram of the balloon

The equations of motion for the balloon in the **i**,**j** and **k** directions are found:

$$-m_b\ddot{x}_b - T_N\mathbf{e}_N.\mathbf{i} + \mathbf{D}_b.\mathbf{i} + N_{1,N}\mathbf{n}_{N-1}.\mathbf{i} + N_{2,N}\mathbf{e}_N^*.\mathbf{i} = 0 \tag{3.73}$$

$$-m_b\ddot{y}_b - T_N\mathbf{e}_N.\mathbf{j} + \mathbf{D}_b.\mathbf{j} + N_{1,N}\mathbf{n}_{N-1}.\mathbf{j} + N_{2,N}\mathbf{e}_N^*.\mathbf{j} = 0 \tag{3.74}$$

$$-m_b\ddot{z}_b - m_b g - T_N\mathbf{e}_N.\mathbf{k} + \mathbf{D}_b.\mathbf{k} + N_{1,N}\mathbf{n}_{N-1}.\mathbf{k} + N_{2,N}\mathbf{e}_N^*.\mathbf{k} + F_{lift} = 0 \tag{3.75}$$

Chapter 4

Theory on Cables and Tethered Balloons

This section contains theory relevant to tethered balloon systems that will later used in the theoretical validations of the system and its components. There is generally little theory available on tethered balloons specifically, but a lot is widely available on cable systems individually. The cable component of the system can be validated against theory available on hanging chain dynamics by removing the balloon component and simply reversing the direction of the gravitational acceleration g, effectively turning the system upside-down. Theory on wave propagation can also be used to validate the transient motion of the cable in response to initial conditions. With the cable being the most complex component of the tethered balloon model, its validation is a big step in verifying the accuracy of the of the tethered balloon model. Theory on hanging chains and wave propagation is therefore included in this section.

In addition to this, inferences can also be made about the behavior of a tethered balloon system by considering the ways in which the subsystems are coupled and comparing it to similar systems. Although the natural frequencies and mode shapes of a tethered balloon system are not specifically known, they can be approximated as the superposition of the vibrations of more than one system. With the balloons resistance to motion being relatively large compared to that of the chain (due to its relatively large inertia and drag coefficient), we expect its vibration to be somewhat decoupled from that of the stretched cable. The cable is therefore expected to exhibit mode shapes and natural frequencies similar to those of a pinned-pinned stretched string. The balloon is able to oscillate however, and so we also expect to see a mode of lower frequency, in which the cable can be assumed to be straight, similar to the link of a pendulum. The expected frequency responses of the combined system are analytically derived in this section as a method of theoretical validation for the tethered balloon model.

4.1 Hanging Chain Dynamics

Theory on hanging chain dynamics is readily available in many text books but is included here for reference. The analysis in this section assumes small amplitude motion about the hanging chain's vertical equilibrium position and is linearized about this state.

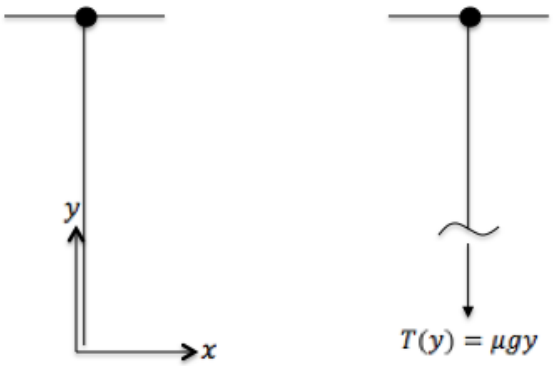

Fig. 4.1 Coordinate System of 2-Dimensional hanging chain and Diagram showing the internal tension along the chain

2-Dimensional motion is considered in this analysis, and so only 2 coordinates are needed; x and y. The vertical coordinate is taken in the upward direction, with the origin being taken as the free end of the hanging chain when it is at rest, as shown in the first diagram in Figure 4.1. The second diagram shows a cut at an arbitrary point along the chain and the corresponding internal tension at that point, which is equal to the weight of the chain section below that point which it is effectively supporting. The mass of the cut section will be equal to the mass per unit length of the chain μ, multiplied by the length of the cut section, y.

$$T(y) = \mu g y \tag{4.1}$$

The tension along the cable is therefore proportional to the height of the point from the origin. Since the amplitude of motion about this equilibrium state is assumed to be small, this tension function is assumed to be time invariant, and independent of the chain's motion.

Figure 4.2 below shows the hanging chain in an arbitrary position (amplitudes are exaggerated for clarity). An infinitesimal element of the tether is considered and Newton's second law of motion is applied to it.

Applying Newton's second law in the transverse i.e. horizontal direction produces the following expression:

$$\mu \Delta y \ddot{x} = \mathbf{T}(y).\mathbf{i} - \mathbf{T}(y+\Delta y).\mathbf{i} \tag{4.2}$$

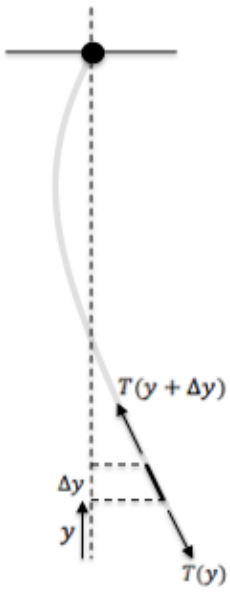

Fig. 4.2 Internal forces acting on an arbitrary infinitesimal chain element

Rearranging this expression:

$$\mu\ddot{x} = \frac{\mathbf{T}(y).\mathbf{i} - \mathbf{T}(y+\Delta y).\mathbf{i}}{\Delta y} = -\frac{\partial}{\partial y}(\mathbf{T}(y).\mathbf{i}) \tag{4.3}$$

Since deviations from the vertical are small, the tension resolved horizontally can be approximated as:

$$\mathbf{T}(y).\mathbf{i} = -\frac{\partial x}{\partial y}T(y) \tag{4.4}$$

The minus on the right hand side is due to the direction of rotation of the element in the diagram. If the element was rotated in the opposite direction to the vertical, this term would be positive, but the term on the right hand side of equation 4.3 would also be positive due to the changed directions of the tensions, leaving the overall equation unchanged. Substituting equations 4.4 and 4.1 into equation 4.3 produces the following equation:

$$\mu\ddot{x} = \frac{\partial}{\partial y}\left(\frac{\partial x}{\partial y}\mu g y\right) \tag{4.5}$$

Assuming the mass per unit length is uniform along the cable's length, this equation becomes:

$$\ddot{x} = g\frac{\partial}{\partial y}\left(\frac{\partial x}{\partial y}y\right) = g\left(\frac{\partial x}{\partial y} + y\frac{\partial^2 x}{\partial y^2}\right) \tag{4.6}$$

To solve this differential equation, the method of separation of variables can be applied, with a solution of the following form.

$$x(y,t) = Y(y)\,T(t) \tag{4.7}$$

Substituting this into the governing partial differential equation produces the following expression.

$$Y(y)\,\ddot{T}(t) = g\left(T(t)\frac{\partial Y(y)}{\partial y} + yT(t)\frac{\partial^2 Y(y)}{\partial y^2}\right) \tag{4.8}$$

By rearranging the equation, the variables can now be separated,

$$\frac{T''}{T} = \frac{g(Y' + yY'')}{Y} \tag{4.9}$$

The variables have been separated. Since the left hand side only depends on the time t and the right hand side only depends on the coordinate y, they must both be equal to some constant value, $-\omega^2$.

$$\frac{T''}{T} = \frac{g(Y' + yY'')}{Y} = -\omega^2 \tag{4.10}$$

The equations can then be considered separately.

$$T'' + T\omega^2 = 0 \tag{4.11}$$

$$gyY'' + gY' + \omega^2 Y = 0 \tag{4.12}$$

The solutions to the first of these are well known, and in order to deduce the solutions to the second, the substitution $y = gz^2/4\omega^2$ is applied. The equation then becomes:

$$z^2Y'' + zY' + z^2Y = 0 \tag{4.13}$$

This is a Bessel equation of order 0. Since this is a second order differential equation, its solution is a combination of two linearly independent general solutions, and takes the following form:

$$Y(z) = aJ_0(z) + bY_0(z) \tag{4.14}$$

Here, a and b are arbitrary constants, and J_0 and Y_0 are known as the Bessel functions of order zero. It is known that the Bessel function of the second kind $Y_0(z)$ goes to minus infinity at $z = 0$, and since the horizontal displacement of the free end of the chain is not infinite, its coefficient, b, must be equal to zero.

The natural frequencies of the hanging chain can be determined by imposing the boundary conditions at $y = L$, i.e. the fixed end of the hanging chain. The horizontal displacement at this point must be equal to zero at all times, $x(L,t) = 0$. Applying this yields the following:

$$Y(z_m) = aJ_0(z_m) = 0 \tag{4.15}$$

Here, z_m is the value of z corresponding to $y = L$. The natural frequencies are therefore found by equating z_m to the zeros of J_0, the values of which are well known, with each root corresponding to a vibration mode.

$$z_m = r_M \tag{4.16}$$

Here r_M is the Mth root of the Bessel function. Substituting the expression for z in terms of y and rearranging yields the following expression for the natural frequencies of a hanging chain:

$$\omega_M = \frac{r_M}{2}\sqrt{\frac{g}{L}} \tag{4.17}$$

As is clear from the equation, the natural frequencies of a hanging chain are solely dependent on the chain's length, and no other physical parameters of the chain. The corresponding mode shapes are therefore:

$$Y_M(y) = aJ_0\left(r_M\sqrt{\frac{y}{L}}\right) \tag{4.18}$$

4.2 Wave Propagation Theory

Theory on the transient effects on stretched strings is readily available and easily derived. For this case, a general stretched string system is considered rather than a hanging chain. For this reason the tension is assumed to be uniform through the length of the cable. As before, Newton's second law is applied to an infinitesimal element on the cable to produce a partial differential equation. Applying exactly the same method as before but with a constant tension T, the following equation is derived:

$$\mu\frac{\partial^2 x}{\partial t^2} = T\frac{\partial^2 x}{\partial y^2} \tag{4.19}$$

This linear second-order partial differential equation is known as the wave equation, and is the equation of motion of a general cable under tension, unlike the previous case which which was limited to a vertically hanging chain. While in the previous section this equation was used to determine the steady state behaviour of a hanging chain system, in this section it is used to analyze the system's transient response to a disturbance, such as an impulse along

the cable's length. The propagation of waves in such a system is determined and compared to the software model.

The partial differential equation above is rearranged and rewritten to incorporate the wave propagation velocity v, which is also defined below.

$$\frac{\partial^2 x}{\partial t^2} = v^2 \frac{\partial^2 x}{\partial y^2} \qquad v = \sqrt{\frac{T}{\mu}} \tag{4.20}$$

For small impulses, the system can be approximated as being a semi-infinite string. In this case, the coordinate system is taken such that the origin, $y = 0$ is at the fixed end of the string. The boundary condition of the system is therefore:

$$x(0,t) = 0 \tag{4.21}$$

To determine the system's transient response for a specific situation, the system's initial conditions are also required. Both an initial velocity profile as well as a deviation in the system's initial position are considered. To maintain generality, these are labelled as general functions as shown below:

$$x(y,0) = f(y) \qquad \frac{\partial x}{\partial t}(y,0) = g(y) \tag{4.22}$$

Since the wave equation in equation 4.19 takes the form of a difference between two squares equation, it can be re-written as follows:

$$\left[\frac{\partial}{\partial t} - v\frac{\partial}{\partial y}\right]\left[\frac{\partial}{\partial t} + v\frac{\partial}{\partial y}\right] x(y,t) = 0 \tag{4.23}$$

The solutions of this are therefore the solutions to either one of the following equations:

$$\left[\frac{\partial}{\partial t} + v\frac{\partial}{\partial y}\right] x(y,t) = 0 \qquad \left[\frac{\partial}{\partial t} - v\frac{\partial}{\partial y}\right] x(y,t) = 0 \tag{4.24}$$

The general solutions of these are:

$$x(y,t) = H(y+vt) \qquad x(y,t) = G(y-vt) \tag{4.25}$$

H and G are arbitrary functions that depend on the system's initial conditions. Since the partial differential equation is linear, its solution will be a sum of these.

$$x(y,t) = H(y+vt) + G(y-vt) \tag{4.26}$$

This general solution describes the superposition of two waves travelling in opposite directions with a speed v. The specific shapes of these waves can be found by applying the system's initial conditions to the general solution. For an initial displacement $f(y)$:

$$x(y,0) = H(y) + G(y) = f(y) \tag{4.27}$$

For an initial velocity $g(y)$:

$$\frac{\partial x}{\partial t}(y,0) = v\dot{H}(y) - v\dot{G}(y) = g(y) \tag{4.28}$$

By integrating the second of these equations and applying simultaneous equations, these can be solved for H and G, deducing expressions for the forwards and backwards travelling waves in terms of the initial conditions f and g.

$$H(y) = \frac{1}{2}\left[f(y) + \frac{1}{v}\int_0^y g(s)\,ds + C\right] \tag{4.29}$$

$$G(y) = \frac{1}{2}\left[f(y) - \frac{1}{v}\int_0^y g(s)\,ds - C\right] \tag{4.30}$$

These expressions are substituted into 4.26. The constant term C cancels. This leaves the solution for the transient response of the system for the general initial conditions f and g:

$$x(y,t) = \frac{1}{2}\left[f(y+vt) + \frac{1}{v}\int_0^{y+vt} g(s)\,ds\right] + \frac{1}{2}\left[f(y-vt) - \frac{1}{v}\int_0^{y-vt} g(s)\,ds\right] \tag{4.31}$$

One specific type of case which may be considered is the system's response to an impulse acting somewhere along the cable, or on the balloon for the tethered balloon case. In this situation, the displacement initial condition function will be zero, but the initial velocity profile will take the form of a delta function of magnitude A_0 located wherever the impulse is applied. For an impulse applied at an arbitrary coordinate y_{imp}, the initial condition functions are expressed below.

$$f(y) = 0 \qquad g(y) = A_0\delta(y - y_{imp}) \tag{4.32}$$

Substituting these expressions into equation 4.31 produces an equation for the impulse response of a stretched string:

$$\begin{aligned} x(y,t) &= H(y+vt) + G(y-vt) \\ &= \frac{1}{2v}\int_0^{y+vt} A_o\delta(s - y_{imp})\,ds - \frac{1}{2v}\int_0^{y-vt} A_o\delta(s - y_{imp})\,ds \end{aligned} \tag{4.33}$$

The forwards and backwards travelling waves in response to an impulse are therefore deduced:

$$H(y+vt) = \frac{A_0}{2v}, \quad y+vt > y_{imp} \tag{4.34}$$

$$G(y-vt) = -\frac{A_0}{2v}, \quad y-vt > y_{imp} \tag{4.35}$$

A schematic of these step travelling waves and the resultant cable response to the impulse are shown in Figure 4.3. It can be seen that for an impulse at y_{imp} a step wave of amplitude $A_0/2v$ travels from that point in both directions at a speed of v.

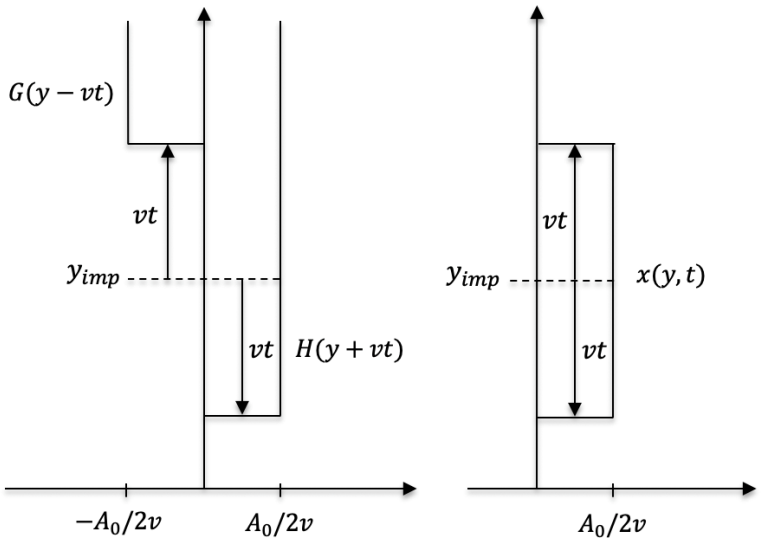

Fig. 4.3 Wave propagation transient response for an impulse applied at y_{imp}

The cable model can therefore be verified by applying an impulse somewhere along its length and comparing the response both qualitatively and quantitatively to the analysis derived in this section.

4.3 Tethered Balloon Dynamics

For small amplitude motion, theoretical estimations of the natural frequencies of a tethered balloon system can be made by approximating the dynamics of the system as being the superposition of the dynamics of two much simpler analytically solvable systems: the stretched string and the pendulum. This is possible because the inertia and drag forces that oppose the motion of the balloon are relatively large in value compared to those of the tether elements. Because of this, any mode shape involving the harmonic motion of the balloon is expected to have a natural frequency that is much lower than and therefore uncoupled

from the vibrations of the tether. This large difference in natural frequencies also arises due to the large value of the lift force compared to the gravitational forces acting on the system. This results in the tether being taut, and a large tether tension results in relatively high tether natural frequencies. The tether is therefore expected to behave similarly to a pinned-pinned stretched string, and the balloon's oscillatory motion is expected to behave similarly to a pendulum. While these are approximations, it is possible to alter the tethered balloon system model such that its behaviour approaches that of the systems mentioned, the natural frequencies of which can be derived analytically.

The weight of the tether elements results in a non-uniform tension along the tether, with the largest tension being located at the top, where the tether element has to support the weight of the entirety of the tether, and the lowest tension at the bottom. This uneven tension is expected to cause discrepancies between the system's natural frequencies and those of the analogous systems it is compared to, which assume a uniform cable tension. To minimise these discrepancies, a comparatively large lift value can be used, which would make the differences in tension due to the tether's weight small in comparison to the absolute tension values. Even better, the gravitational acceleration, g, can be set to zero, which would result in the system behaving as though it is in the horizontal plane, and make the resting tether tension uniform.

Another discrepancy that could arise in the stretched string modes is that the balloon is not actually a node, making the pinned-pinned approximation inaccurate. The system can be made to better mimic a simple stretched string system by increasing the inertia of the balloon. As the balloon's inertia increases to infinity, the behaviour is expected to approach that of a pinned-pinned stretched string system. Through minor alterations of the system's parameters, the behaviour of its components is expected to approach those of well understood systems and can therefore be validated analytically in the frequency domain.

The mode involving the harmonic motion of the balloon with no vibrations within the tether, behaves effectively like a pendulum (although upside down) and would intuitively be the lowest frequency vibration mode of the tethered balloon system. The tether in this mode behaves as a rigid link rather than a flexible cable and can therefore be modelled as such. The value of this first natural frequency can be found by modelling the tether as a rod and the balloon as a point mass (if the added mass approach is being used to model the balloon's drag, this should be included in its inertia) in the same way that the natural frequency of a pendulum is found for small amplitude motion. Since the combined system of the point mass attached to the rod behaves as a rigid body, the overall centre of mass can be located and the combined system can be approximated as a simple point mass at that location connected to the origin by a massless rigid link, as shown in Figure 4.4.

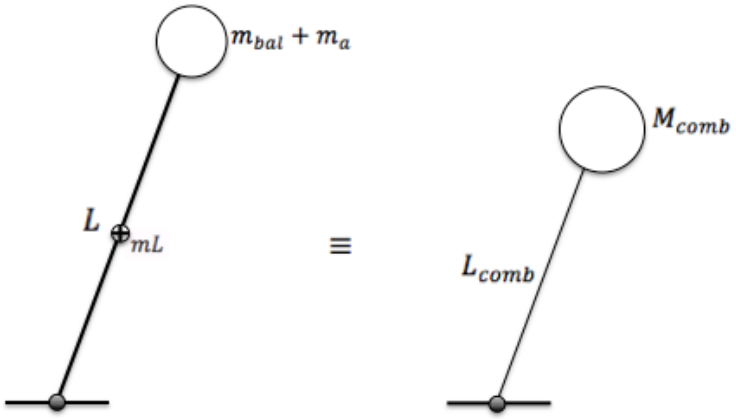

Fig. 4.4 Equivalent Upside-Down Pendulum System for a Tethered Balloon

Here, M_{comb} is the system's combined mass and L_{comb} is the distance of the combined system's centre of mass from the fixed end.

The combined mass of the system is equal to the sum of the mass of the tether, the mass of the balloon and the added mass due to the balloon's drag. The added mass value will be used in the inertial term of the combined system, but not in the external forces due to gravity which are left unchanged.

$$M_{comb} = mL + m_{bal} + m_a \tag{4.36}$$

The combined system pendulum length is found by determining the location of the centre of mass of the combined system.

$$L_{comb} = \frac{mL\left(\frac{L}{2}\right) + (m_{bal} + m_a)(L+R)}{M_{comb}} = \frac{mL\left(\frac{L}{2}\right) + (m_{bal} + m_a)(L+R)}{mL + m_{bal} + m_a} \tag{4.37}$$

By resolving the external forces acting on the system in a direction perpendicular to the rod, Newton's second law of motion can be applied to the combined mass in the direction of its instantaneous velocity. Figure 4.5 shoes a free body diagram of the combined pendulum system, including D'Alembert forces.

Resolving in a direction perpendicular to the pendulum's massless rod produces the following equation of motion:

$$M_{comb}L_{comb}\ddot{\theta} + \left(F_{lift} - m_{bal}g - mLg\right)\sin\theta = 0 \tag{4.38}$$

For small amplitude motion, small angle approximations can be applied and the equation can be linearized. Applying $\sin\theta \approx \theta$ and rearranging produces the following expression for

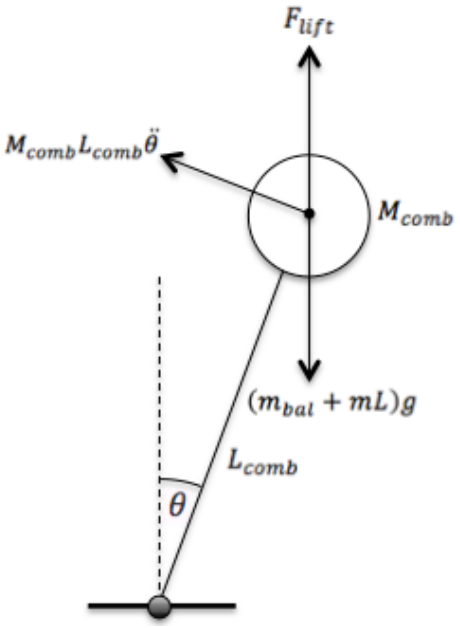

Fig. 4.5 Free Body Diagram of Equivalent Pendulum System

simple harmonic motion.

$$\ddot{\theta}+\frac{\left(F_{lift}-m_{bal}g-mLg\right)}{M_{comb}L_{comb}}\theta=0 \tag{4.39}$$

From this, an expression for the natural frequency of this mode can be obtained. The expression for the natural frequency of this mode is found to be:

$$f_{pen}=\frac{1}{2\pi}\sqrt{\frac{F_{lift}-mLg-m_{bal}g}{M_{comb}L_{comb}}} \tag{4.40}$$

In term's of the tethered balloon system's parameters only, this can be rewritten as:

$$f_{pen}=\frac{1}{2\pi}\sqrt{\frac{F_{lift}-mLg-m_{bal}g}{mL\left(\frac{L}{2}\right)+\left(m_{bal}+m_a\right)\left(L+R\right)}} \tag{4.41}$$

Having accounted for the the upside-down pendulum mode vibrations of the system in a rigid manner, the vibrations modes of the cable must now be considered. The balloon's motion has already been accounted for and it can therefore now be treated as being fixed in space. The taut tether can therefore be thought of as behaving like a stretched string that is pinned or attached at both ends. The remainder of the system's free vibration can therefore be thought of as a summation of the natural mode shapes of a stretched string. The fundamental

frequency of this 'stretched string', as well as its harmonics, can be calculated analytically and the expression for these is well known. The values of these are:

$$f_{string} = \frac{n}{2L}\sqrt{\frac{T}{m'}} \qquad n = 1, 2, 3 \ldots \tag{4.42}$$

In conclusion, it is expected that any steady state free motion of the tethered balloon system will be a superposition of the modes of two systems: any motion of the balloon can be accounted for by the pendulum mode, and all other motion of the tether is accounted for by the stretched string simplification. The FFT of a tethered balloon system is therefore expected to contain the natural frequencies of both of these systems, provided that the balloon's inertia is significantly larger than that of the tether elements.

Chapter 5

Validation of Nonlinear Cable and Tethered Balloon Models

Once the system model has been derived, it must be validated to ensure that it produces sufficiently accurate results before it can be used to make further predictions. There are two main ways of validating the system model: experimental validations and theoretical validations. In the former, small-scale practical experiments can be performed and used to experimentally validate the model by comparing its predicted response to actual measured data before it used to make predictions for the full-scale HATB system. In the latter, analytical methods may be available to predict outputs for a certain subset of what the model can produce, or for a simplified version of the model. The model may be altered to account for these simplifications, and outputs compared with those predicted analytically. If the theoretical and practical results are sufficiently similar to the model predictions, confidence is gained in the model and it can then be applied to predict the behavior of situations for which there is no theory available and experimentation cannot be done (the purpose of the software model is to predict the feasibility of the system before it can be practically implemented).

In this section, the nonlinear system model is validated primarily through practical experimentation conducted by Richard Andrews (2016) [7] on two hanging chains with varying axial stiffnesses and a tethered balloon. Theoretical estimates for the natural frequencies of the systems in the experimental setups are also calculated and compared to the FFTs of both the experimental results and the software model. Further and more accurate theoretical validations are made in Chapter 8. In addition to this, since one of the cable models is the limiting case of the other (as the spring stiffness approaches infinity, the extensible model approaches the inextensible model), a quick way of validating the two models to some extent

is to check that the response of the extensible model approaches that of the inextensible model as its stiffness increases.

5.1 Extensible and Inextensible Cable Model Comparison

For each model, the use of the force and energy methods to obtain each set of ODEs is a useful way of immediately gaining some confidence in the system's equations of motion if they agree. For the extensible tether model, the force and energy methods produced identical equations of motion, and therefore presented identical solutions for any specific initial state vector and external conditions the tether was subjected to. This increased the confidence in the equations of motion produced, and validated the system model to a certain extent. Similarly, the two methods produced the same results for the inextensible tether model.

While an elastic cable and an inextensible one will obviously behave differently, one way of further increasing confidence in both models was to compare them for a case in which the stiffness of the extensible tether model was set to a very large value. For this case, it is expected that the extensible and inextensible models will behave similarly. As the cable stiffness approaches infinity, the dynamic behaviour of the extensible model approaches that of the inextensible model.

While validating the models against each other by proving that they produce the same results for a given system is a step in the right direction, it doesn't necessarily mean that the models are both producing accurate results, as some simplifications and assumptions made feature in both models and may be sources of error. The models may agree with each other to a very large degree, but may differ when compared to results that are produced experimentally. This is therefore an insufficient validation method, but a useful one nonetheless. It is a convenient way to check that the models are consistent with each other without the requirement of any apparatus or experimental planning.

Theoretically the outputs of the two models should be very close to each other for any arbitrary system parameters and initial conditions provided that the spring stiffness in the inextensible model is set to a sufficiently large value. The use of a large spring stiffness in the nonlinear model however results in the model being computationally 'stiff'. This occurs when the solution being sought after varies slowly but solutions that vary quickly are superimposed onto this, resulting in the requirement of a very small time step and therefore a very long computational time. In this case this happens because a spring with a very large stiffness results in the introduction of very high frequency axial vibrations. As the stiffness of the springs is increased, the frequency of the axial vibrations increases, but their amplitude, and therefore effect on the overall motion of the cable, decreases. With the element positions

changing at such a high rate, a very small time step is required for convergence, resulting in the requirement of a very long computational time. A compromise was made when choosing the value of the spring stiffness, such that it was large enough for axial extension to have a minimal effect on the overall motion of the cable, but not so large that computational times are overly tedious.

A hanging chain with specific geometric and material properties and an initial state vector was modelled using both the extensible and inextensible cable models for comparison. Arbitrary system parameters were selected for the sole purpose of comparing the two cable models. These are summarised in Table 5.1.

Table 5.1 High Stiffness Chain Experimental Parameters

Parameter	Value
Chain Length (m)	5
Mass per Unit Length (kg/m)	0.02

A spring stiffness of the order of $10^7 N/m$ was used in the extensible cable model. As an initial state vector, an initial velocity was imposed to the element at the free end of the hanging cable. Applying an initial velocity to a mass is effectively the same as applying an impulse to the system at that location. The magnitude of the impulse used in this case was $I = 0.02Ns$. This impulse was chosen such that it was large enough to produce motion in which nonlinearities would be present. Figure 5.1 shows the output produced by both of the models in the form of the displacement of 5 equally spaced points along the cable over time.

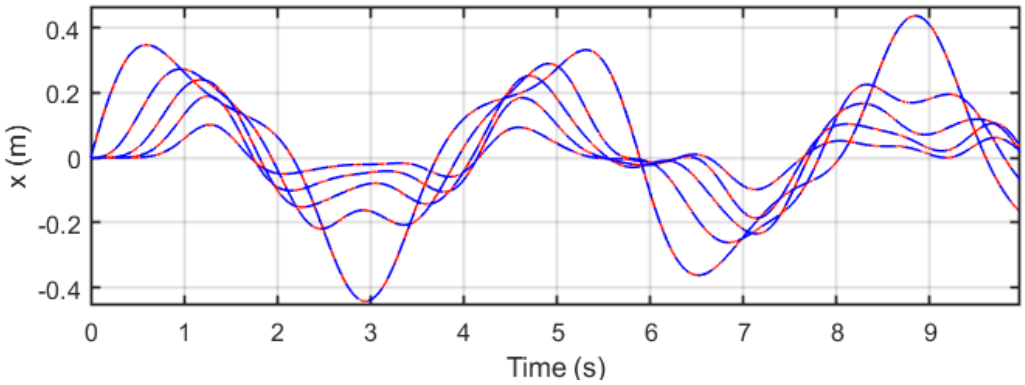

Fig. 5.1 Comparison of outputs of inextensible (blue) and high stiffness extensible (red) cable models for the impulse Response of a hanging chain

The red lines represent the output of the extensible model and the blue lines represent the output of the inextensible model. Qualitatively a very close agreement is seen between

the responses of the two models, with any differences not visible in the graph. Since the extensible cable model is not infinite however, some axial motion is expected to be present within the cable resulting in some low amplitude but high frequency motion of the elemental masses. Quantitatively, errors between the responses were of the order of 0.01%. Very close agreement is therefore observed between the high-stiffness extensible model and the inextensible model, as required.

5.2 Experimental Verification of Nonlinear Model

Although there is no experimental data available for high-altitude tethered balloons which could be used to validate the model, experimental data can be collected easily for a scaled down tethered balloon system and used to verify the accuracy of the model's output for any arbitrary motion. This is a big step in confirming that the model can be used to accurately predict the behaviour of the full scale high-altitude tethered balloon system, as it increases confidence that the model accurately captures the dynamics of tethered balloons. Comparing the hanging chain model to experimental data of hanging chains is also very useful, to make sure that the cable dynamics are accurately represented by the model, and help to identify the source of any inaccuracies by separating the combined system into its subsystems.

The software models were compared against real experimental data collected by Richard Andrews in 2016 [7], in which 2 video cameras and computer processing was used to obtain 3-dimensional coordinates for equally spaced points along a moving cable/tethered balloon at equally spaced time intervals over a period of time.

The parameters of the software model are set to the corresponding values of the experimental setup. The elemental mass, for example, was set as being the total mass of the cable divided by the number of elements chosen in the model. Other than the system parameters, the other input required for the software model is an initial state vector, which consists of the 3-dimensional coordinates as well as the 3-dimensional velocity components of each element.

Imposing a selected initial condition onto a physical cable system is difficult to do accurately, and so these initial states may not be exactly identical. Small variations will be amplified as the motion proceeds, making it difficult to distinguish between errors in the initial state and errors in the model itself, hence reducing the credibility and integrity of the validation. Rather than attempting to impose an initial state used by the model onto an experimental setup, which could result in unwanted and unaccounted for transient effects due to the human contact, an initial state is selected from the many time frames once the practical setup has already been set into motion. This method of obtaining a mid-motion initial state

vector from anywhere in a set of recorded readings is very useful as it eliminates the need to coordinate an actual initial state (e.g. release chain from a certain initial shape) between the model and the practical system in order to compare outcomes. In this case, transient effects due to the human contact with the cable have either been damped out or are accounted for within the selected initial state vector. This is also very repeatable, and for one sufficiently long run, the model can be tested for several initial state vectors.

The coordinates of the points along the tether can be taken at any instant in time from Andrews' data. From these, the model's elemental positions can be deduced using interpolation. The instantaneous velocities of the points along the cable at the chosen time are also required in the initial state vector of the software model. These can be deduced using the coordinates of the chosen time frame, those of the subsequent time frame and the length of time between them. By subtracting the position vectors of the jth element at 2 adjacent time frames, we obtain a vector describing the infinitesimal displacement of the element.

$$\mathbf{r}_{j,t+dt} - \mathbf{r}_{j,t} = \begin{bmatrix} dx_j \\ dy_j \\ dz_j \end{bmatrix} \tag{5.1}$$

Dividing each component of this vector by the length of time between the frames, dt produces an 'instantaneous' velocity vector. The term instantaneous is used loosely as this is actually the element's average velocity over the length of the time interval, but for a small enough time interval, this approaches the element's instantaneous velocity.

$$\dot{\mathbf{r}}_{j,t} = \frac{\mathbf{r}_{j,t+dt} - \mathbf{r}_{j,t}}{dt} = \begin{bmatrix} dx_j/dt \\ dy_j/dt \\ dz_j/dt \end{bmatrix} = \begin{bmatrix} \dot{x}_j \\ \dot{y}_j \\ \dot{z}_j \end{bmatrix} \tag{5.2}$$

With a complete set of element coordinates and velocities, an initial state vector can now be constructed and the software model can be run, producing a set of subsequent states which can be compared to the data recorded by Andrews in the time frames following the selected one.

This method also has its limitations however, and inaccuracies are likely to be present in the measurements of the instantaneous data. As mentioned earlier, the 'instantaneous' velocity is only an approximation, and its accuracy is limited by the selected duration of the discrete time frames. This is expected to be worst in cases where the selected initial time frame exhibits significant accelerations. Using large enough marker points to be viewed by the cameras also may reduce the accuracy of the instantaneous coordinates of the point. For

small amplitude motion, these could produce significant errors. The inaccuracies produced by these errors in measurements are likely to be significantly smaller than those produced by human error when attempting to impose an initial state physically.

The practical setups used for the experimental validation in the upcoming sections are two hanging chains (a chain with a large stiffness and an elastic cable with a low tensile stiffness) and a tethered balloon.

5.2.1 Hanging Chain Experiment

The method described was applied for both a high stiffness metal chain as well as an elastic chord with very low stiffness in order to validate both the inextensible and extensible cable models respectively. For the latter, Andrews obtained values for the stiffness and material damping experimentally and these were incorporated into the software model. The stiffness was obtained using a simple static load test from which the gradient of the force-extension graph was obtained. The magnitude of the damping was obtained by attaching a mass to the end of a section of the elastic chord to form a linear oscillator and observing the exponential rate at which the magnitude of the peaks decayed. In the practical setup, masses were attached to the elastic chord at 10 equally spaced points to increase the resting tension within the cable and better validate whether the model accurately captures behaviour influenced by significant axial deformation. The masses of these are added to the appropriate lumped masses in the system model that they respectively correspond to. Comparisons between the experimental data and the software model's predictions for the hanging chain systems are made for the two cable systems.

Validating the Inextensible Cable Model: High Stiffness Hanging Chain

The method described above was first applied to the high stiffness chain in order to validate the inextensible cable model. The parameters of the chain are displayed in Table 5.2. The axial stiffness is assumed to be infinite.

Table 5.2 High Stiffness Chain Experimental Parameters

Parameter	Value
Chain Length (m)	0.3430
Mass per Unit Length (kg/m)	0.0830

The system's trajectory for an arbitrary initial condition selected from the experimental run is plotted in Figure 5.2 in red alongside the subsequent experimentally recorded states in blue.

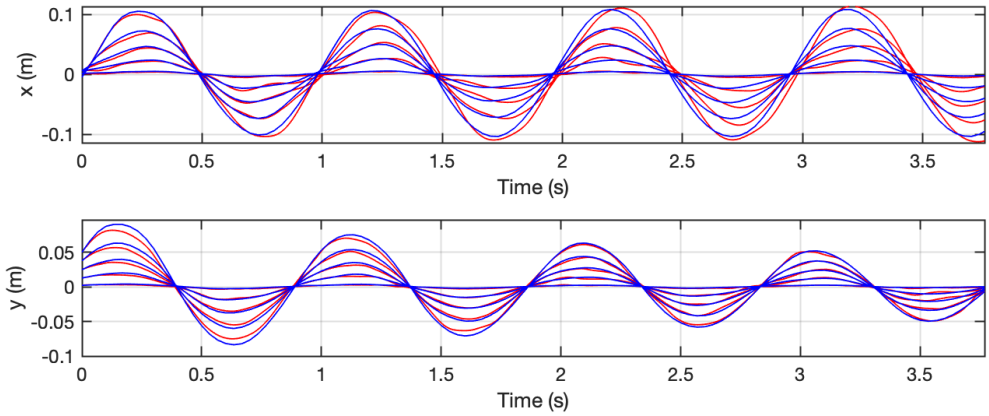

Fig. 5.2 Comparison of model output (red) and experimental data (blue) for a high stiffness hanging chain

For this case, the motion is dominated by the mode associated with the system's first natural frequency. Both the amplitude of motion and the frequency appear to closely agree on the whole, with the frequency of the first mode being visibly very slightly lower in the model for the x-direction motion. While this difference is small, the error is seen to build up as time goes on. The model prediction appears to have more visible higher frequency modes in its response which may be down to the inaccuracies present in the selected initial state exciting higher frequency modes. It was found that there was a calibration error in the experimental data which resulted in the origin not being exactly at the chains fixed end, which may have contributed to the discrepancies in the responses. This can be seen more clearly in the FFT of the response which has a non-zero magnitude at a frequency of 0Hz later in this section.

For this run, the observed motion appears to be steady and predictable. The model accurately predicted that the chain would follow an elliptical shape in the horizontal plain, the major axis of which displays a steady precession in the direction of its rotation. The calibration error makes it difficult to quantify the agreement of the two sets of results in the time domain since the starting coordinates of the points, as well as their initial velocities are actually incorrect due to this error. The results can be checked against the experimental data as well as theory more easily in the frequency domain. Fast Fourier Transforms for the software model (red) and the experimental data (blue) are plotted alongside each other in Figure 5.3. The accuracy of the peaks of the FFT of the experimental data is limited by the

short time duration of 5.9s over which it was run. For the software model, the FFT was taken for a system response of 100s in order to produce the more refined peaks.

Superimposed on to the graph are the theoretically derived natural frequencies of the chain in question in the black dashed lines. According to the theory derived in Section 4.1, the natural frequencies of a hanging chain are only dependent on the length of the chain, and can be calculated using the following relationship:

$$f_M = \frac{\omega_M}{2\pi} = \frac{r_M}{4\pi}\sqrt{\frac{g}{L}} \tag{5.3}$$

Here, f_M is the Mth natural frequency of the hanging chain, and r_M is the Mth root of the zero order Bessel function J_0, the first 3 of which have the values 2.4048, 5.5201 and 8.6537. Using the cable length in Table 5.2, the first three natural frequencies of the system according to theory are:

$$f = 1.0234Hz,\ 2.3492Hz,\ 3.6828Hz \tag{5.4}$$

Though only the first mode shows a large peak in this particular run, the location of the peaks in the FFT appear to strongly with each other and with the analytically derived first mode natural frequency. For the software model, small peaks can also be seen at the system's second and third natural frequencies that also agree closely with the theoretical natural frequencies of the system. The percentage error between the model's first natural frequency and the analytically derived one is less than 0.1%. The second and third peaks have a percentage error of 0.08% and 0.4% respectively. More accurate theoretical validations are made in Chapter 8, where the number of cable elements is greatly increased to better mimic a continuous cable system.

Extensible Model Validation: Low Stiffness Elastic Hanging Cable

In this section, the model of the extensible cable is validated by comparing its response to that of an elastic chord. As mentioned previously, 10 masses were added to equally spaced points along the chord to increase its resting tension and therefore produce larger axial deformations. The parameters of the cable are listed in Table 5.3.

For this system, the dynamics are more complex and less predictable, since the cable exhibits significant axial deformation as well as lateral motion, the two of which are highly coupled. The observed motion is therefore much less intuitive. For arbitrarily chosen initial states, plots of the motion as predicted by the model can be seen alongside the true

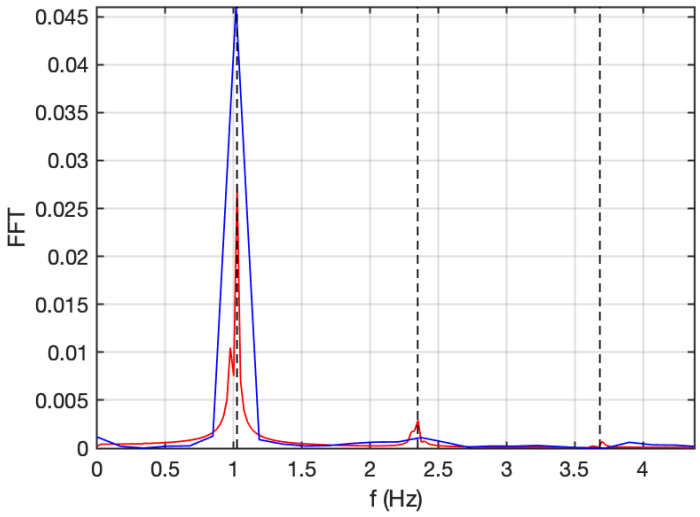

Fig. 5.3 FFT for high stiffness hanging chain response of system model (red) and experimental data (blue)

Table 5.3 Low Stiffness Cable Experimental Parameters

Parameter	Value
Unstretched Chain Length (m)	1.00
Mass per Unit Length (kg/m)	3.2e-4
Stiffness per Unit Length (N/m^2)	0.3049
Damping Coefficient per Unit Length (Ns/m^2)	0.0122
Point masses attached (kg)	0.0013
Number of masses	10
Spacing between masses (m)	0.1

experimental data in Figures 5.4 and 5.5 for two runs, the second of which exhibits a larger amount of axial deformation.

Despite the less intuitive appearance of the motion of the low stiffness chord, there is obviously only one correct solution for the system's motion in reality, and the model appears to predict it well. The model was also found to be very consistent and versatile, producing accurate results over long timescales for many different initial conditions and features of motion. This is clear from Figure 5.5, in which the model maintains its accuracy for a run containing large axial deformations as well as 3-dimensional transverse motion.

The model's response can be quantitatively validated by taking an FFT of its response in order to compare its natural frequencies to those that are theoretically derived. Due to the very short experimental run, the FFT is not plotted for the experimental data as the

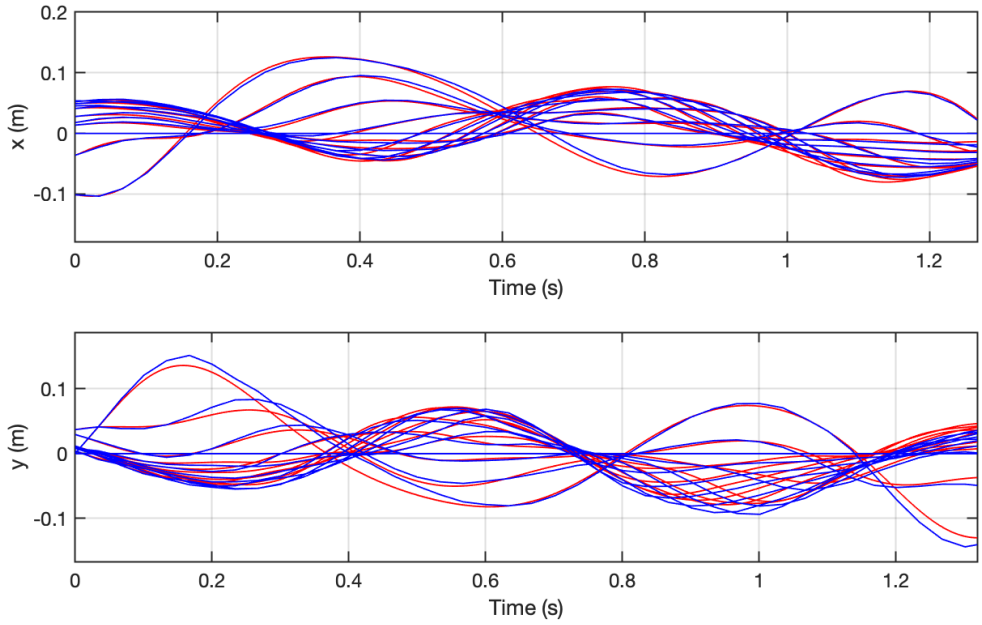

Fig. 5.4 Deviations with time of 10 equally spaced points along the cable in the x and y-directions measured experimentally (blue) and predicted by the software model (red)

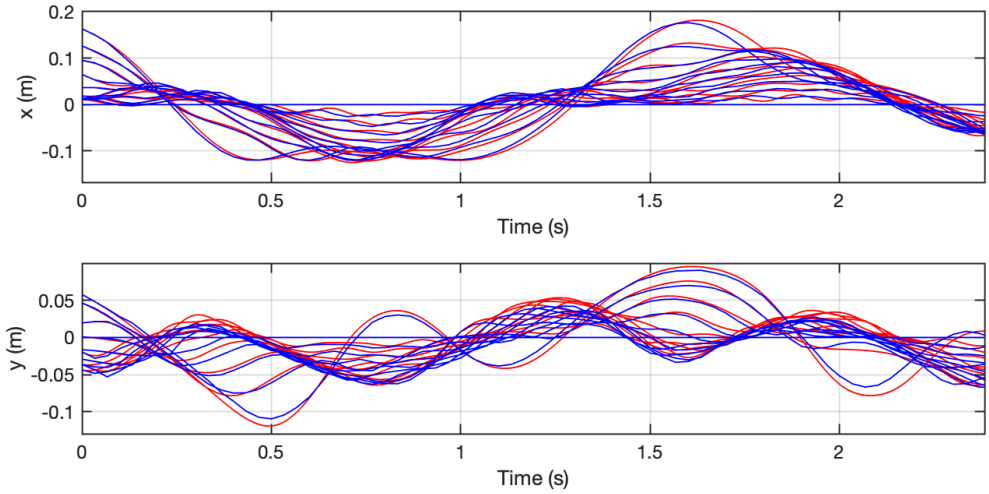

Fig. 5.5 Deviations with time of 10 equally spaced points along the cable in the x and y-directions measured experimentally (blue) and predicted by the software model (red)

frequency intervals are large and therefore inaccurate. The FFT of the motion midway along the cable in the x-direction of the response seen in Figure 5.5 is taken and plotted alongside the theoretical hanging chain natural frequencies for the system parameters. The theory for hanging chains assumes a constant length, so the analytically derived natural frequencies are

just approximate for this system. For this case, the resting hanging length of the cable is used rather than its unstretched length. This was found to be approximately 1.2m. Substituting into expression 5.3, the first five theoretical natural frequencies of the hanging cable are approximately:

$$f = 0.5472Hz,\ 1.256Hz,\ 1.969Hz,\ 2.683Hz,\ 3.400Hz \tag{5.5}$$

These are plotted in the vertical dashed lines alongside the FFT of the model's response.

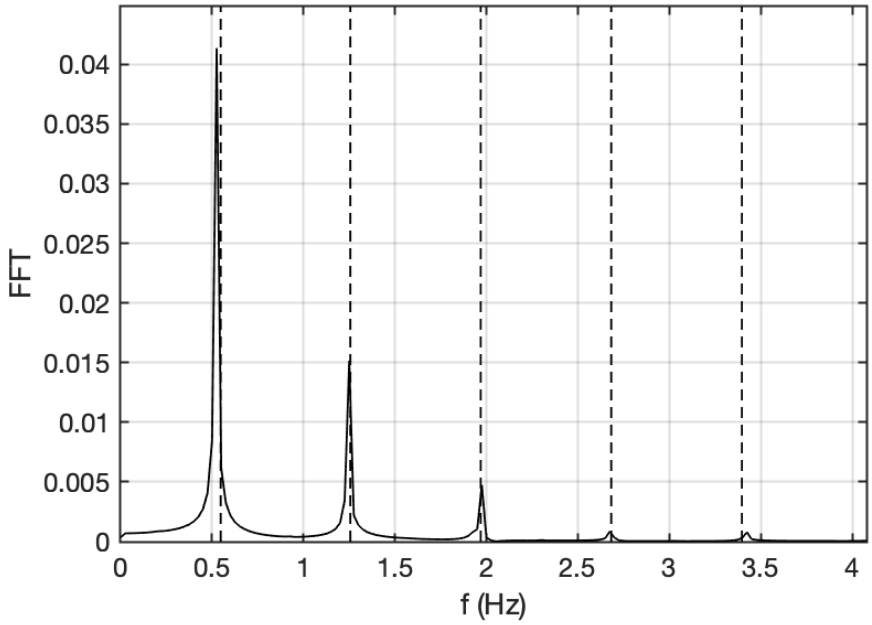

Fig. 5.6 FFT for low stiffness hanging chain response

As well as the qualitatively accurate time domain system response, the natural frequencies contained in the response are close to the approximate ones produced analytically for a hanging chain. There is a 4% difference in the first natural frequency, 0.5% in the second and 0.3% in the 3rd. These discrepancies are expected to be reduced for a cable model with a larger stiffness that is discretized into smaller elements, which is done in Chapter 8.

5.2.2 Tethered Balloon Experiment

In this section, a tethered balloon system [7] is used to experimentally validate the combined tethered balloon system model. The high stiffness metal chain used in the first experimental validation of the inextensible cable model is now used as the tether. The extensible tether model with the tension set to a large value was used in this case however, as this model is

more versatile and can be used for a wider range of applications. The high stiffness chain was selected as the tether over the elastic chord so that focus can be directed at the features of the motion that are due to the tethered balloon combined system rather than the phenomena caused by the axial deformation of the tether.

Similarly to the hanging chain validations, an arbitrary initial state vector is selected from Andrews' discrete time measurements of the balloon's motion following some arbitrary initial conditions used to initiate motion [7]. For the tethered balloon system, the initial state contains the 3D coordinates and velocities of equally spaced points along the tether as well as those of the centre of the balloon. The initial state vector is used as an input to the software model which then predicts the subsequent states for the desired time frame. The subsequent states predicted by the model can then be compared to the experimentally measured subsequent states to the chosen initial state vector.

Figure 5.7 shows the tethered balloon system's response to the initial state vector as predicted by the model, as an overview of the response before comparing separate aspects to the experimental data. The figures show the motion of 7 equally spaced points along the tether and the motion of the balloon, in the x and y-directions respectively.

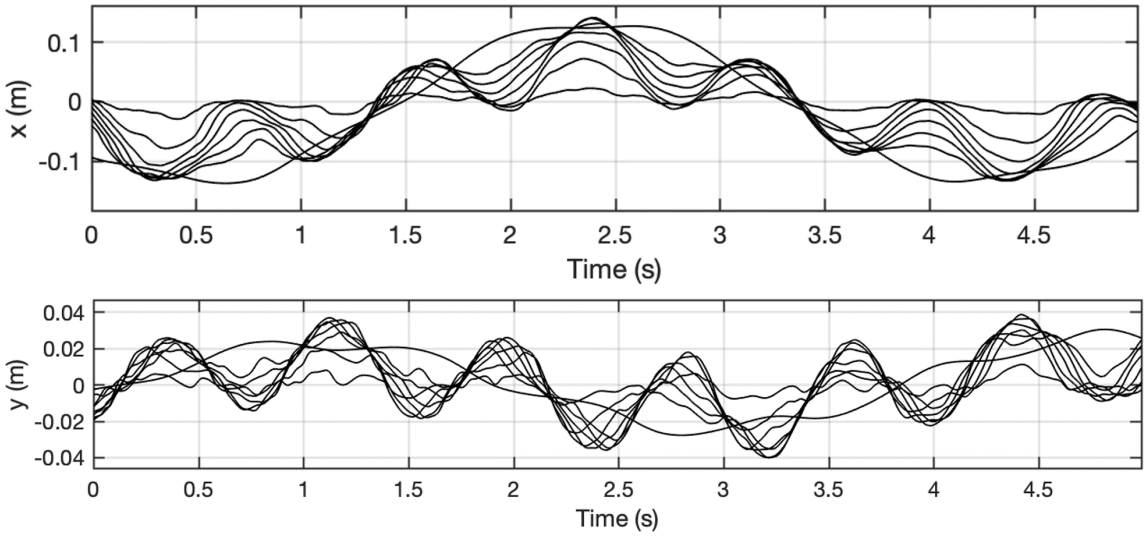

Fig. 5.7 Motion of equally spaced points along the tether and the centre of the balloon over time in the x and y directions as produced by the system model

Figure 5.8 shows plots of the balloon's motion as predicted by the model (red) alongside the measured subsequent motion of the balloon (blue), in the x and y directions. The model appears to predict the balloon's motion well, displaying visibly similar amplitudes and frequencies in the trajectory. It is important to note that a calibration error was once again present in the experimental data which may have contributed to the differences in the

responses. This is clearly visible from the fact that the oscillating motion of the balloon in the x-direction is not centred around zero for the blue line.

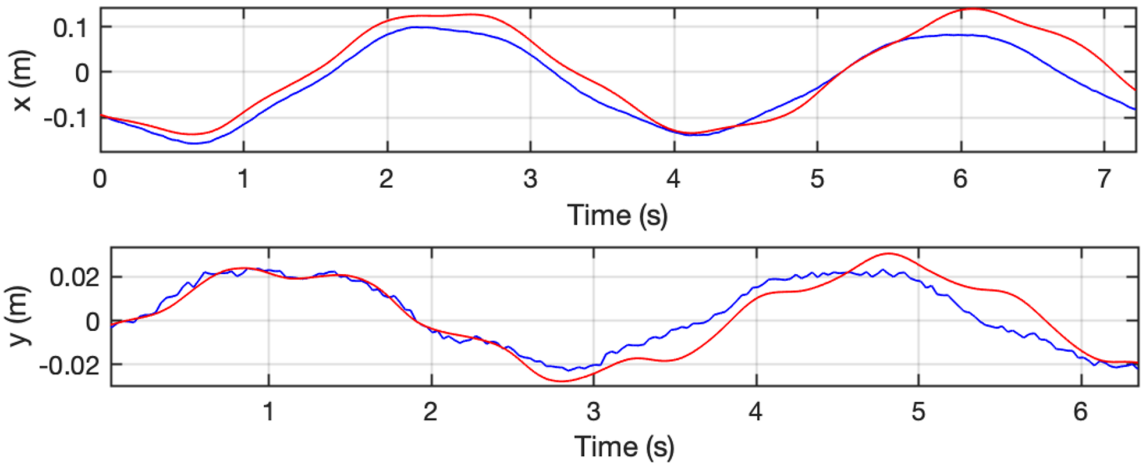

Fig. 5.8 Motion of the centre of the balloon over time in the x and y directions for the software model (red) and experimental data (blue)

The motion of the 7 equally spaced points along the tether are plotted once again (red), this time alongside the experimental measurements of the equivalent points (blue) in Figure 5.9.

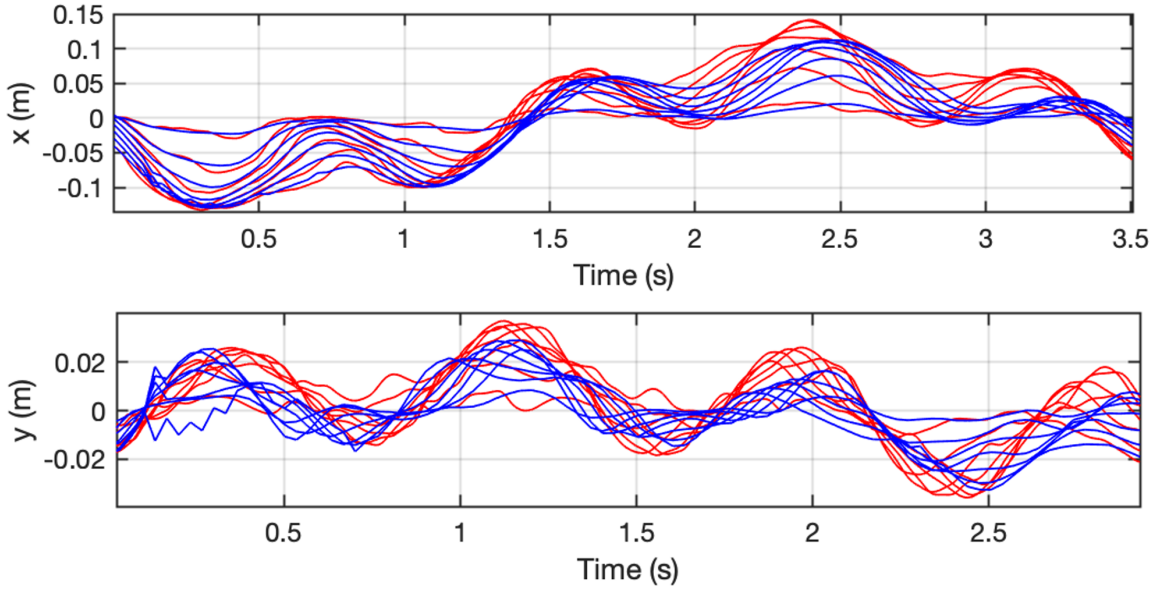

Fig. 5.9 Motion of equally spaced points along the tether over time in the x and y directions for the software model (red) and experimental data (blue)

Once again, similar shapes, trends and frequencies are visible in the displacement-time graphs above for the two data sets.

While visually many similarities can be seen between the two sets of data for both the balloon centre and the points along the tether, it is difficult to quantify the agreement of the two in the time domain. To further establish the agreement between the software model and the practical setup, the Fast Fourier Transform of the two responses was taken for a response comparison in the frequency domain. The Fast Fourier Transforms of the motion of the tether's middle node in the x-direction were computed for the model's predicted motion (red) as well as the data recorded in the experiments (blue) and the results are plotted in Figure 5.10. In addition to this, approximations are made for the natural frequencies of the system in question using the theory derived in Section 4.3. While the pendulum mode natural frequency is expected to be a reasonably close approximation, for the particular system in question, the tether is not expected to behave in a manner very similar to a stretched string. This is because the tension varies significantly along the tether, increasing by approximately 300% from the tether's fixed end to the balloon end. An approximate tension was selected by subtracting the system's weight from its lift, giving T=0.557N to obtain a very approximate estimate of the fundamental string frequency.

For the system used in the experimental setup, estimates of the system's expected natural frequencies were calculated. It was found that f_{pen}=0.271Hz and f_{string}=1.25Hz, 2.5Hz, 3.75Hz, etc. These are plotted alongside the FFTs in Figure 5.10 in black.

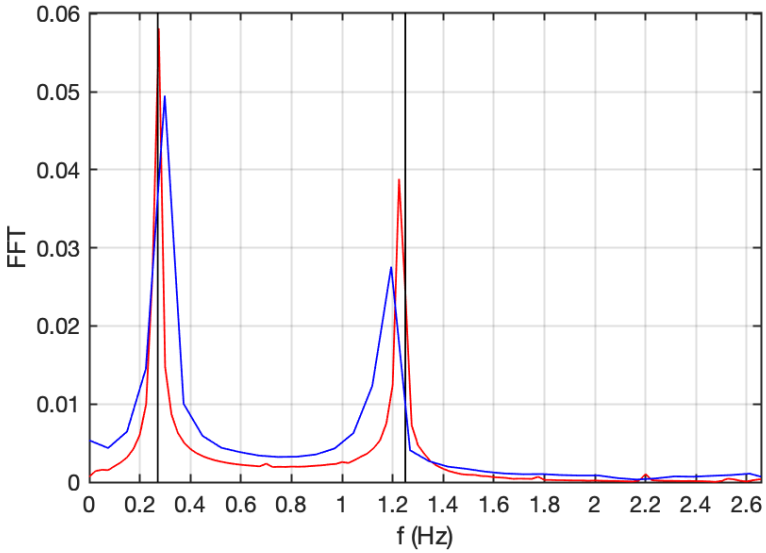

Fig. 5.10 FFT for the motion of a point close to the centre of the tether in the x-direction, for the model (red) and for the experimental data (blue) alongside analytically estimated natural frequencies (black)

It can be seen that the FFT graph of the experimental data has a non-zero value at 0Hz, which is due to the calibration error of the setup. The locations of the first two peaks for the software model and the experimental data appear to agree reasonably well with each other. The relatively short time duration for which experimental data is available resulted in very wide frequency intervals in its FFT, making its peak values inaccurate, and is a likely source of the discrepancies. The peaks also appear to coincide with the first two natural frequencies that were derived analytically. Since the response of the middle of the tether is considered in this case, the peak corresponding to the second stretched string natural frequency is expected to be small or close to 0 in the FFTs, as the midpoint of the tether is a node in the corresponding mode shape, as well as all subsequent string modes that are multiples of 2.

The tethered balloon system used in the experimental setup is not an ideal system for the estimations made in the derivation of the natural frequencies of a tethered balloon system. As well as having a tension that varies greatly along the tether's length, the balloon's inertia is not large enough compared to those of the tether elements for the balloon end to behave as though it is 'fixed'. For this reason, the second peak exhibited by both the experimental set up and the model's predicted output occurs at a frequency slightly lower that that of the fundamental frequency of an equivalent stretched string. A tethered balloon system better adjusted to minimise these sources of error is theoretically validated in Chapter 8.

Chapter 6

Optimal Control Theory

In this chapter, the methods of implementing feedback control that are to be used in attempt to reduce the risk of failure of the proposed HATB system are introduced. A brief discussion of potential control methods is provided, followed by a more detailed discussion of the selected type of feedback control, LQR. LQR control is applied to simplified system models, the dynamics of which are well known, as well as simplified versions of the tethered balloon model as an introduction to the methods that are to be applied to the full-scale system model. In the process of doing this, methods of system linearization and introduced and validated. In addition to its benefits to a system's dynamic response, the robustness of LQR as a feedback control method are investigated. The effects of the cost function selection on the system's dynamic response and robustness are also analysed. These are steps taken towards a deeper understanding of optimal control prior to its application to the full-scale 3-dimensional tethered balloon model.

6.1 Modern Vs. Classical Control

In this section, a brief comparison between modern and classical control is provided. The benefits of each of these are discussed.

Classical Control systems use Proportional-Integral-Derivative control to achieve desired performance criteria. In this type of control, analysis is predominately in the frequency domain, as Laplace transforms are used to simplify calculations otherwise involving complex differential equations. Modern or Optimal Control is memoryless, as at each time step the control input is proportional to the system's current state vector. Optimal control uses the state space form in the time domain.

Modern (Optimal) Control was chosen as the feedback control method for the tethered balloon system control over Classical (PID: Proportional-Integral-Derivative) Control for various reasons. Firstly, classical control is limited to Single-Input-Single-Output (SISO) systems, while modern control can cope with Multiple-Input-Multiple-Output (MIMO) systems. For the HATB control proposed in this research, the suggested control input is a driving force that would result in the motion of the tether's base. For a 3-dimensional tethered balloon system, the base motion is constrained to the horizontal plane and therefore has two degrees of freedom, and two control inputs are therefore required. Secondly, PID control is limited to linear cases only, while optimal control can handle the control of nonlinear systems. This is because, although the LQR controller is designed using a linear state space model (usually a linearized version of the system about an equilibrium state) non-linear system states are fed to the LQR, and since LQR has good robustness properties, the controller should be able to handle the systems' differences and preserve stability. For the majority of systems including the tethered balloon system in question, as a result of being highly nonlinear, it is important that the chosen control law is robust and therefore able to cope with the system's nonlinearities which were not present in its design. The extent of the LQR's robustness is studied in Section 6.5.2.

6.2 Linear Quadratic Control

LQR returns optimal controller gains for a linear plant with a quadratic cost function. By choosing the parameters Q and R, you are effectively choosing the relative importance of the control effort (u) and the error (deviation from 0) of the different states. LQR aims to minimize the "cost" of the control run, and so will work to reduce the deviations of states that are given relatively large coefficients. For a specific open loop system, the system's minimum 'cost' found by the minimisation of the cost function is unique and independent of the choices of Q and R. This implies that the absolute values inside the matrices are therefore irrelevant, and it is the relative costs of the states and the inputs that matter. For this reason, the input cost R is often taken as 1 for a single input system or an identity matrix for a multiple input system, and the state cost matrix Q is varied as desired. The state cost matrix Q is often taken as ρI, leaving only 1 degree of freedom (ρ) in the choice of the system's cost function, greatly simplifying the process.

Several methods can be used for choosing the weighting matrices Q and R. Most simply, trial and error with some degree of interpolation. Practical considerations must also be made, e.g. it is important that the control effort is given a realistic value by being assigned a high enough cost. Practically this translates to the model realistically simulating how readily the

base of the tethered balloon system should be made to move – it is not realistic to allow the base to move completely freely and so its relative cost should be reasonably high. in general, for a reel-in pay-out input on the other hand for example, the relative input cost R could be a lot lower, as a spinning motor used for this input is a much less 'costly' process than the acceleration of a ship. Choosing a small value of ρ (and therefore a relatively large input weighting) is referred to as an expensive controller, as you are attempting to stabilize the system with less energy, which is often the aim for a costly input. A large value choice of ρ, and therefore a relatively small input weighting, is referred to as a cheap controller. Here the input is penalized less, and greater importance is placed on having minimal state changes, which is often applied to system's in which the control input is 'cheap' to apply. There is a trade-off here, and a satisfactory compromise must be found.

By deciding on the specifications of the control system in question, Q and R can be estimated and then altered accordingly by trial and error to achieve the desired closed loop system response. Examples of criteria that need to be decided include the overshoot and the settling time. However it is important to also consider that in reality the control effort is also a limitation and to weight it accordingly.

Under a certain time invariant wind profile, the tethered balloon model will adopt an equilibrium position, which can be evaluated by resolving static forces. In order to design a feedback controller for the system under these external conditions, the model can be linearized for small amplitude motion about its equilibrium position. The linearized ODEs can be written in matrix form as follows:

$$[M]\,\ddot{\mathbf{x}} + [D]\,\dot{\mathbf{x}} + [K]\,\mathbf{x} = [F]\,\mathbf{u} \tag{6.1}$$

The linearized second order differential equations are then replaced with a single first order matrix differential equation and the model can be expressed in state space form:

$$\dot{\mathbf{x}} = A\mathbf{x} + B\mathbf{u} \tag{6.2}$$

$$\mathbf{y} = C\mathbf{x} + D\mathbf{u} \tag{6.3}$$

Here x is the state vector, u is the input vector and y is the measured output.

In equation 6.1, the vector x refers to a vector containing all of the generalised coordinates. In state space form however, the second order ODE is changed into a first order ODE. In order to do this, a state vector is required, which contains all of the generalised coordinates, as well as all of their derivatives. These can fully define the instantaneous state of a system. The second order ODE can be changed to a first order one, i.e. state space form as shown in the following equation. In equation 6.2, the vector x refers to the state vector, and contains

all of the generalised coordinates that define the system's position, and all of their derivatives. The linearized second order ODEs can therefore be transformed into state space form:

$$\dot{\mathbf{x}} = \begin{bmatrix} [0] & [I] \\ \left[-[M]^{-1}[K]\right] & \left[-[M]^{-1}[D]\right] \end{bmatrix} \mathbf{x} + \begin{bmatrix} [0] \\ [M]^{-1}[F] \end{bmatrix} \mathbf{u} \tag{6.4}$$

Comparing with equation 6.2, it's clear that the matrix in front of the state vector is the state space vector A, and the matrix in front of the input is the state space vector B. For a system with a single input, the matrix B collapses to a vector. The matrices C and D depend on what the measured variable of the system is. For full state feedback for example, in which all of states are known, the state space matrix C would be an identity matrix and D a matrix of zeros. The matrices A and B completely describe the system's dynamic behavior and C and D define what is measured. For any system linearized to the form expressed in equation 6.1, the state space matrices can be found directly:

$$A = \begin{bmatrix} [0] & [I] \\ \left[-[M]^{-1}[K]\right] & \left[-[M]^{-1}[D]\right] \end{bmatrix} \qquad B = \begin{bmatrix} [0] \\ [M]^{-1}[F] \end{bmatrix} \tag{6.5}$$

The stability of the open loop system can be determined by the eigenvalues of the state space matrix A. The system is stable if and only if all of the eigenvalues of A have negative real parts.

Incorporating a feedback cycle to the system involves making it such that the input u is linearly dependant on the state vector x. More specifically, a negative feedback cycle selects an input vector that is linearly dependant on x in such a way that it opposes any deviation from a reference vector r. Full-state feedback is assumed in this research.

Figure 6.1 shows a diagram of a typical LQR feedback loop. The precise way in which the instantaneous input is dependant on the instantaneous state vector is defined by the feedback gain matrix K, which is determined by the state space matrices of the system A and B, and the selected cost function matrices, Q and R.

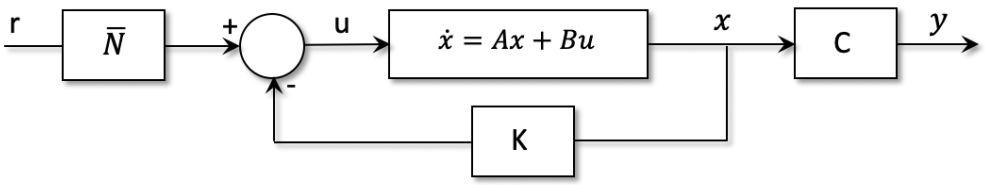

Fig. 6.1 LQR Feedback Control Loop

From the diagram, it is seen that the input vector **u** is related to the state vector **x** and the reference vector **r** by the following expression:

$$\mathbf{u} = \bar{N}\mathbf{r} - K\mathbf{x} \tag{6.6}$$

Substituting this expression into the first state space equation, yields the following altered first order ODE:

$$\dot{\mathbf{x}} = A\mathbf{x} + B(\bar{N}\mathbf{r} - K\mathbf{x}) = (A - BK)\mathbf{x} + B\bar{N}\mathbf{r} \tag{6.7}$$

Similarly, substituting equation 6.6 into the second state space equation results in the following expression for the measured output:

$$\mathbf{y} = C\mathbf{x} + D(\bar{N}\mathbf{r} - K\mathbf{x}) = (C - DK)\mathbf{x} + D\bar{N}\mathbf{r} \tag{6.8}$$

From equations 6.7 and 6.8, the altered closed loop state space matrices are found:

$$A_{CL} = [A - BK] \quad B_{CL} = [B\bar{N}] \quad C_{CL} = [C - DK] \quad D_{CL} = [D\bar{N}] \tag{6.9}$$

These closed loop state space matrices now completely define the dynamics of the linear closed loop system. By analogy with the open loop case, the stability of the closed loop system can be determined by calculating the eigenvalues of the matrix $[A - BK]$ and checking that they have negative real parts. If LQR methods are used to obtain the matrix, it must by definition be closed-loop stable. The quality of the dynamic response of the closed loop system is heavily dependant on the feedback gain matrix K which is dependant upon the selection of the cost function matrices. It is expected that upon increasing the value of the state cost matrix coefficient ρ, the closed-loop poles shift further left. If there is too much overshoot for example, the poles can be moved further to the left through the increase of the relative costs of the system's states. This requires more control effort however, so a compromise needs to be found.

Once the linearized model is used to derive a suitable feedback gain matrix K using the LQR method, the feedback matrix can then be extracted and applied to the original nonlinear system, thus eliminating any small amplitude approximations from the system model and providing a more accurate depiction of the system's behavior. However, the feedback system's stability in the linear model does not guarantee that stability will be maintained for larger amplitude motion in the nonlinear model, and so the robustness of the feedback control is just as important to consider as the stability.

6.3 Inverted Pendulum Control

Before applying optimal control methods to the complex tethered balloon system, it is useful to start with a simplified and well-known system that can then be built upon. A good example to consider is the inverted pendulum, as it is a widely understood system in the field of control [5][114], and is actually a subsystem of the cable model used in this research.

There are two main types of pendulums; the compound pendulum, in which the mass of the pendulum is evenly distributed along its length like a rod, and the simple pendulum, which consists of a light rod with a point mass at its end. While in the majority of the literature compound pendulums are considered, in this research a simple pendulum model will be used, to keep the model consistent with the lumped mass elements used in the tethered balloon system's cable model. The differences that arise when modelling these two systems are that for the compound pendulum, the centre of mass of the pendulum is located at the centre of the link's length, i.e. at $L/2$ and the moment of inertia of the pendulum about its centre of mass is that of a thin rod, i.e. the following expression:

$$I_{G,cp} = \frac{1}{2} m L^2 \tag{6.10}$$

The centre of mass of the simple pendulum, on the other hand, is located at the link's end, and its moment of inertia about its centre of mass is equal to zero, since all of the pendulum's mass is located at the centre of mass itself.

$$I_{G,sp} = 0 \tag{6.11}$$

A simple inverted pendulum is initially considered, before extending the model to a multibody system which can be extended into the lumped mass cable model.

6.3.1 Simple Inverted Pendulum

A diagram of a simple inverted pendulum is presented in Figure 6.2. This system is widely investigated and understood and a good starting point for applying LQR methods to tethered balloon systems, since an upside-down pendulum fixed to a movable trolley is effectively a simplified subsystem of the spatially discretized tethered balloon system considered in this research. For the feedback control of the tethered balloon system in which the control input involves the motion of the tether's base in the horizontal plane, the lowest tether element is modelled as being connected to a trolley. For no external forces, the trolley and first tether element are therefore structurally identical to an inverted simple pendulum system.

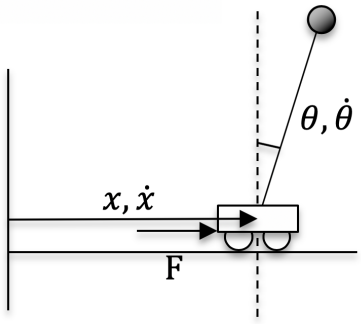

Fig. 6.2 Simple Inverted Pendulum System

The analysis of an inverted pendulum system is therefore useful in determining the dynamics of the base end of the tether and establish the relationship between the input and the motion of the base as well as the end of the tether attached to it. This inverted pendulum system analysis is also a useful and simple introduction to the linearization and LQR methods that will be applied to the more complex tethered balloon system model.

By using feedback control, the unstable inverted pendulum system can be made closed loop stable. Here, the control input is the horizontal force acting on the trolley, F. The system's states are the trolley's position and velocity, x and $\dot{x}$, and the pendulum's angle from the vertical and angular velocity, θ and $\dot{\theta}$.

In order to establish the system's state space matrices which are required for the application of LQR methods, the equations of motion of the system must be found and then linearized for small amplitude motion about the equilibrium position. In this case, the equilibrium position is such that the trolley's position, x, can take any value, and the pendulum's angle from the vertical, θ is equal to 0 radians. This equilibrium position is very unstable without closed loop feedback, and the aim of implementing feedback is to stabilize it and, building on that, improve its dynamic response to fit certain criteria.

For a base mass M, a pendulum mass m and a link length L, a free body diagram of the system is displayed in Figure 6.3. Since it is not a static system, d'Alambert forces are included in the diagram.

To find the equations of motion of the system, firstly moments about the trolley/base are taken.

$$mgL\sin\theta - m\ddot{x}L\cos\theta - mL^2\ddot{\theta} = 0 \tag{6.12}$$

Next, an equation for the horizontal equilibrium of the whole system is found:

$$F - (m+M)\ddot{x} + mL\dot{\theta}^2\sin\theta - mL\ddot{\theta}\cos\theta - b\dot{x} = 0 \tag{6.13}$$

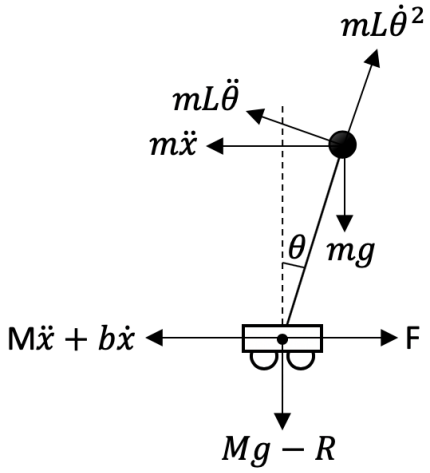

Fig. 6.3 Simple Inverted Pendulum Free Body Diagram

The two coupled nonlinear equations of motion can then be linearized by incorporating the fact that θ will be kept small, and making approximations accordingly. Upon making the appropriate small angle substitutions, the equations of motion collapse into the following expressions:

$$\ddot{x} + L\ddot{\theta} - g\theta = 0 \tag{6.14}$$

$$F - (m+M)\ddot{x} + mL\dot{\theta}^2\theta - mL\ddot{\theta} - b\dot{x} = 0 \tag{6.15}$$

In equation 6.15, the third term contains the product of 3 small terms in it and can therefore be assumed to be insignificant, leaving the following expression:

$$(m+M)\ddot{x} + mL\ddot{\theta} + b\dot{x} = F \tag{6.16}$$

This leaves us with 2 coupled second order linear differential equations. These can be combined into one matrix equation:

$$\begin{bmatrix} 1 & L \\ m+M & mL \end{bmatrix} \begin{bmatrix} \ddot{x} \\ \ddot{\theta} \end{bmatrix} + \begin{bmatrix} 0 & 0 \\ b & 0 \end{bmatrix} \begin{bmatrix} \dot{x} \\ \dot{\theta} \end{bmatrix} + \begin{bmatrix} 0 & g \\ 0 & 0 \end{bmatrix} \begin{bmatrix} x \\ \theta \end{bmatrix} = \begin{bmatrix} 0 \\ F \end{bmatrix} \tag{6.17}$$

From these second order equations of motion, a single first order differential matrix equation can be constructed using the expression in 6.4, leaving the system in state space

form as required:

$$\begin{bmatrix} \dot{v} \\ \dot{\theta} \\ \ddot{v} \\ \ddot{\theta} \end{bmatrix} = \begin{bmatrix} 0 & 0 & 1 & 0 \\ 0 & 0 & 0 & 1 \\ 0 & mg/M & -b/M & 0 \\ 0 & -g(M+m)/ML & b/ML & 0 \end{bmatrix} \begin{bmatrix} v \\ \theta \\ \dot{v} \\ \dot{\theta} \end{bmatrix} + \begin{bmatrix} 0 \\ 0 \\ 1/M \\ -1/mL \end{bmatrix} F \tag{6.18}$$

The state space matrices that define the system's small amplitude linear motion and are required to produce a feedback gain matrix K using LQR have therefore been obtained:

$$A = \begin{bmatrix} 0 & 0 & 1 & 0 \\ 0 & 0 & 0 & 1 \\ 0 & mg/M & -b/M & 0 \\ 0 & -g(m+M)/ML & b/ML & 0 \end{bmatrix} \quad B = \begin{bmatrix} 0 \\ 0 \\ 1/M \\ -1/mL \end{bmatrix} \tag{6.19}$$

The eigenvalues of A, which are equal to the poles of the system's open loop transfer function, can be found. The system is open loop stable if and only if the poles of the transfer function have negative real parts. For the case where $m = 0.5kg, M = 0.5kg, b = 0.1Ns/m$ and $a = 0.5m$, the eigenvalues of A are found to be as follows:

$$poles = 0,\ -6.3618,\ 6.1618,\ 0 \tag{6.20}$$

The 3rd pole has a positive real part and so the system is open loop unstable, as expected intuitively. Implementing a negative feedback controller can stabilize the system. To choose the gains of the feedback controller, a Linear-Quadratic Regulator (LQR) is used. The values of Q and R can be adjusted until the system's response fit the required criteria. This is done for the double inverted pendulum case studied in the next section.

6.3.2 Double Inverted Pendulum

To build upon the single inverted pendulum, additional pendulums can be added. Through the addition of multiple pendulums the system begins to resemble the discretized cable model used for the balloon's tether in this research. To represent a multiple element system, a double inverted pendulum is considered in the derivation of the system's state space form to avoid tedious maths. Obtaining the state space form expressions for systems containing additional elements follows the same process. This system is initially considered with no external forces, as a double inverted pendulum. Upon adding upward and horizontal forces to

the elements, the model effectively becomes a representation of a simplified 2-dimensional 2-element tethered balloon, the state space form of which is derived in the next section.

The double inverted pendulum is a system well known for its chaotic behaviour, which is not exhibited in a single pendulum system. The system being 'chaotic' implies that it has a very strong sensitivity to its initial conditions, and a very slight alteration in these would result in an arbitrarily large difference in its following trajectory. Despite being chaotic, the system is deterministic, meaning that all of the system's future states are fully dependent on the system's initial conditions and there is no random element to the motion. Each initial state has only one solution, but any infinitesimal differences in the initial state will result in a very different solution. Since it is extremely difficult to impose the exact same initial conditions twice in practise, it is near impossible to produce the exact same trajectory more than once. The reason for this is that its equations of motion consist of a set of ODEs that are highly coupled, and so the motion of each pendulum is highly dependent on the other, resulting in any discrepancies being amplified.

In this section, optimal control will be used to stabilize a double inverted pendulum. The system's equations of motion are derived and then linearized about the unstable equilibrium position of vertically upwards. The use of LQR to obtain a satisfactory dynamic response for what is normally a chaotic system is then investigated. The linearized equations of motion are derived using both force and energy methods in this section as a form of validation for the linearization process and the linearized ODEs derived, before applying it to the full scale tethered balloon system, which is effectively an extension of the model in this section.

The generalized coordinates used for this system are the position of the base, x_0, and the absolute angles from the vertical of the two pendulums, θ_1 and θ_2. A diagram of the system is presented in Figure 6.4.

The force method is used to obtain the system's linearized equations of motion in matrix form first. In a similar manner to the previous section, Newton's second law of motion is applied to the system. In this section however, each mass is considered separately, as an introduction to the methods that will be used for the multi-element tether systems in the next sections. A free body diagram of each mass is displayed in Figure 6.5, showing all the forces acting on it, including D'Alembert forces since the system is dynamic.

Forces are resolved in the Cartesian x and y directions for the pendulum masses, and in the x direction for the trolley since it is constrained to motion in the horizontal direction. Resolving forces on the trolley in a horizontal direction produces the following expression:

$$F + T_1 \sin\theta_1 - b\dot{x}_0 - M\ddot{x}_0 = 0 \tag{6.21}$$

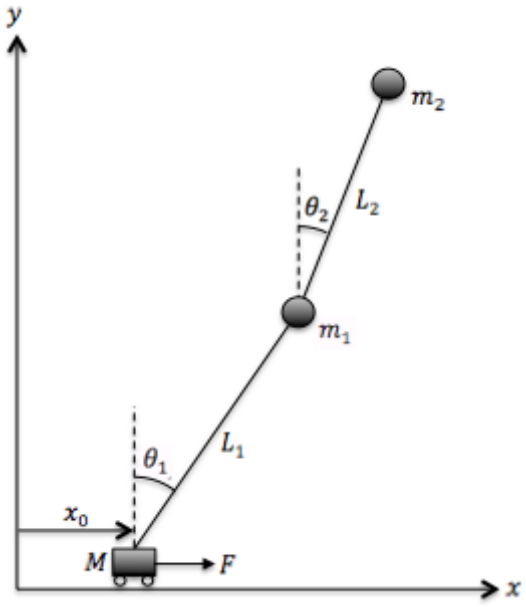

Fig. 6.4 Double Inverted Pendulum System

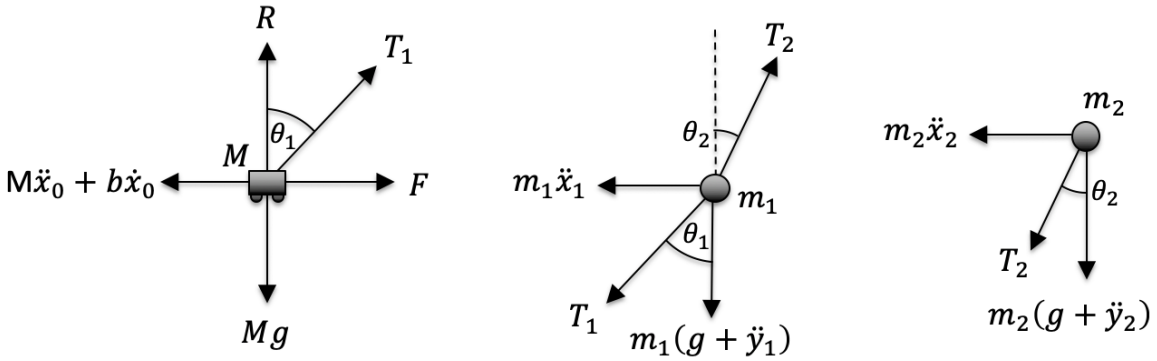

Fig. 6.5 FBDs of Double Inverted Pendulum Elements

Resolving forces on the first pendulum in the x and y directions respectively produces the following equations of motion of the mass m_1:

$$m_1\ddot{x}_1 + T_1 \sin\theta_1 - T_2 \sin\theta_2 = 0 \tag{6.22}$$

$$m_1\ddot{y}_1 + m_1 g + T_1 \cos\theta_1 - T_2 \cos\theta_2 = 0 \tag{6.23}$$

Similarly, resolving forces horizontally and vertically on the second pendulum produces 2 more equations:

$$m_2\ddot{x}_2 + T_2 \sin\theta_2 = 0 \tag{6.24}$$

$$m_2\ddot{y}_2 + m_2 g + T_2 \cos\theta_2 = 0 \tag{6.25}$$

This leaves 5 expressions for a 3 degree-of-freedom system. The tensions in the pendulums' links can be eliminated, leaving a set of three equations of motion, as required for a 3 degree-of-freedom system. Since equations 6.24 and 6.25 only contain the tension in the second pendulum, T_2 can be eliminated immediately. To do this, the equations are rearranged such that only the terms containing T_2 remain on the left hand side, and then equation 6.24 is divided by equation 6.25, leaving the following equation of motion:

$$\tan\theta_2 = \frac{\ddot{x}_2}{g+\ddot{y}_2} \tag{6.26}$$

T_2 can easily be eliminated from equations 6.22 and 6.23 by substituting the expressions for $T_2\sin\theta_2$ and $T_2\cos\theta_2$ which are directly available by rearranging equations 6.24 and 6.25. T_1 can then be eliminated by dividing equation 6.22 by equation 6.23 in the same way as before. This results in the following expression:

$$\tan\theta_1 = \frac{m_2\ddot{x}_2 + m_1\ddot{x}_1}{m_1(g+\ddot{y}_1) + m_2(g+\ddot{y}_2)} \tag{6.27}$$

Finally, T_1 can also be eliminated from equation 6.21, which, again, can be done easily by rearranging equation 6.22 to get an expression for $T_1\sin\theta_1$ that can be substituted directly.

$$m_1\ddot{x}_1 + m_2\ddot{x}_2 + b\dot{x}_0 + M\ddot{x}_0 - F = 0 \tag{6.28}$$

Equations 6.28, 6.26 and 6.27 are the three equations of motion of the system. The next thing that needs to be considered is that these equations are in terms of Cartesian coordinates rather than the selected generalised coordinates of the system. In order to change this, expressions for the cartesian coordinates and their derivatives are derived in terms of the generalised coordinates and then substituted into the equations of motion.

Using basic geometry, the expressions for the coordinates of the pendulum centre of masses are found and listed below:

$$x_1 = x_0 + L_1\sin\theta_1 \tag{6.29}$$

$$x_2 = x_0 + L_1\sin\theta_1 + L_2\sin\theta_2 \tag{6.30}$$

$$y_1 = L_1\cos\theta_1 \tag{6.31}$$

$$y_1 = L_1\cos\theta_1 + L_2\cos\theta_2 \tag{6.32}$$

Differentiating these equations twice produces expressions for the Cartesian accelerations of the two pendulums in terms of the generalised coordinates.

$$\ddot{x}_1 = \ddot{x}_0 + L_1\ddot{\theta}_1\cos\theta_1 - L_1\dot{\theta}_1^2\sin\theta_1 \tag{6.33}$$

$$\ddot{x}_2 = \ddot{x}_0 + L_1\ddot{\theta}_1\cos\theta_1 - L_1\dot{\theta}_1^2\sin\theta_1 + L_2\ddot{\theta}_2\cos\theta_2 - L_2\dot{\theta}_2^2\sin\theta_2 \tag{6.34}$$

$$\ddot{y}_1 = -L_1\ddot{\theta}_1\sin\theta_1 - L_1\dot{\theta}_1^2\cos\theta_1 \tag{6.35}$$

$$\ddot{y}_2 = -L_1\ddot{\theta}_1\sin\theta_1 - L_1\dot{\theta}_1^2\cos\theta_1 - L_2\ddot{\theta}_2\sin\theta_2 - L_2\dot{\theta}_2^2\cos\theta_2 \tag{6.36}$$

These substitutions can now be applied to convert the equations of motion such that they are in terms of the generalized coordinates, x_0, θ_1 and θ_2. Upon applying these substitutions, equation 6.28 becomes:

$$\begin{aligned} F - b\dot{x}_0 - M\ddot{x}_0 - m_1(\ddot{x}_0 + L_1\ddot{\theta}_1\cos\theta_1 - L_1\dot{\theta}_1^2\sin\theta_1) \\ - m_2(\ddot{x}_0 + L_1\ddot{\theta}_1\cos\theta_1 - L_1\dot{\theta}_1^2\sin\theta_1 + L_2\ddot{\theta}_2\cos\theta_2 - L_2\dot{\theta}_2^2\sin\theta_2) = 0 \end{aligned} \tag{6.37}$$

Equation 6.26 becomes:

$$\begin{aligned} \ddot{x}_0 + L_1\ddot{\theta}_1\cos\theta_1 - L_1\dot{\theta}_1^2\sin\theta_1 + L_2\ddot{\theta}_2\cos\theta_2 - L_2\dot{\theta}_2^2\sin\theta_2 \\ + (L_1\ddot{\theta}_1\sin\theta_1 + L_1\dot{\theta}_1^2\cos\theta_1 + L_2\ddot{\theta}_2\sin\theta_2 + L_2\dot{\theta}_2^2\cos\theta_2 - g)\tan\theta_2 = 0 \end{aligned} \tag{6.38}$$

Finally, equation 6.27 becomes:

$$\begin{aligned} m_2(\ddot{x}_0 + L_1\ddot{\theta}_1\cos\theta_1 - L_1\dot{\theta}_1^2\sin\theta_1 + L_2\ddot{\theta}_2\cos\theta_2 - L_2\dot{\theta}_2^2\sin\theta_2) \\ + m_1(\ddot{x}_0 + L_1\ddot{\theta}_1\cos\theta_1 - L_1\dot{\theta}_1^2\sin\theta_1) - \tan\theta_1(m_1(g - L_1\ddot{\theta}_1\sin\theta_1 - L_1\dot{\theta}_1^2\cos\theta_1) \\ + m_2(g - L_1\ddot{\theta}_1\sin\theta_1 - L_1\dot{\theta}_1^2\cos\theta_1 - L_2\ddot{\theta}_2\sin\theta_2 - L_2\dot{\theta}_2^2\cos\theta_2)) = 0 \end{aligned} \tag{6.39}$$

The system's nonlinear equations of motion have now been derived in terms of the chosen generalised coordinates. The next step is to linearize the model for small amplitude motion about the equilibrium position. Since the system is being linearized about the upright vertical equilibrium position that is $\theta_1 = \theta_2 = 0$, the deviations from this will be assumed to be small, and so small angle approximations are applied for the two angles. Any terms containing the products of more than one small terms are assumed to be negligible and are ignored.

Applying these to the nonlinear equations of motion produces the following set of linearized equations of motion in terms of the generalised coordinates, as required:

$$b\dot{x}_0 + M\ddot{x}_0 + m_1(\ddot{x}_0 + L_1\ddot{\theta}_1) + m_2(\ddot{x}_0 + L_1\ddot{\theta}_1 + L_2\ddot{\theta}_2) - F = 0 \tag{6.40}$$

$$\ddot{x}_0 + L_1\ddot{\theta}_1 + L_2\ddot{\theta}_2 - g\theta_2 = 0 \tag{6.41}$$

$$m_2(\ddot{x}_0 + L_1\ddot{\theta}_1 + L_2\ddot{\theta}_2) + m_1(\ddot{x}_0 + L_1\ddot{\theta}_1) - \theta_1 g(m_1 + m_2) = 0 \tag{6.42}$$

The system's full set of linearized equations of motion have now been found. One linearized, the system's equations can be written in matrix form, while effectively producing the system's mass, damping and stiffness matrices in the process.

$$\begin{bmatrix} m_1+m_2+M & (m_1+m_2)L_1 & m_2L_2 \\ m_1+m_2 & (m_1+m_2)L_1 & m_2L_2 \\ 1 & L_1 & L_2 \end{bmatrix} \begin{bmatrix} \ddot{x}_0 \\ \ddot{\theta}_1 \\ \ddot{\theta}_2 \end{bmatrix} + \begin{bmatrix} b & 0 & 0 \\ 0 & 0 & 0 \\ 0 & 0 & 0 \end{bmatrix} \begin{bmatrix} \dot{x}_0 \\ \dot{\theta}_1 \\ \dot{\theta}_2 \end{bmatrix} + \begin{bmatrix} 0 & 0 & 0 \\ 0 & -g(m_1+m_2) & 0 \\ 0 & 0 & -g \end{bmatrix} \begin{bmatrix} x_0 \\ \theta_1 \\ \theta_2 \end{bmatrix} = \begin{bmatrix} F \\ 0 \\ 0 \end{bmatrix} \tag{6.43}$$

The second method that uses the system's energies is now applied to the same system as a method of validating the linearised model. To start with, the total kinetic energy of the system is found. This will be equal to the sum of the individual kinetic energies of the masses in the system. In order to find the kinetic energy of each mass in the system, the velocities of each of the masses are required in terms of the generalised coordinates chosen in this section. These are found by differentiating expressions 6.29-6.32 once, producing the following expressions for the instantaneous velocities of the pendulums in Cartesian directions.

$$\dot{x}_1 = \dot{x}_0 + L_1\dot{\theta}_1\cos\theta_1 \tag{6.44}$$

$$\dot{x}_2 = \dot{x}_0 + L_1\dot{\theta}_1\cos\theta_1 + L_2\dot{\theta}_2\cos\theta_2 \tag{6.45}$$

$$\dot{y}_1 = -L_1\dot{\theta}_1\sin\theta_1 \tag{6.46}$$

$$\dot{y}_2 = -L_1\dot{\theta}_1\sin\theta_1 - L_2\dot{\theta}_2\sin\theta_2 \tag{6.47}$$

The expression for the total kinetic energy of the system is:

$$T = \frac{1}{2}M\dot{x}_0^2 + \frac{1}{2}m_1(\dot{x}_1^2 + \dot{y}_1^2) + \frac{1}{2}m_2(\dot{x}_2^2 + \dot{y}_2^2) \tag{6.48}$$

Applying the substitutions for the velocities derived above converts the equation so that it is in terms of the generalised coordinates as required.

$$\begin{aligned} T =& \frac{1}{2}M\dot{x}_0^2 + \frac{1}{2}m_1\left(\left(\dot{x}_0 + L_1\dot{\theta}_1\cos\theta_1\right)^2 + \left(-L_1\dot{\theta}_1\sin\theta_1\right)^2\right) \\ &+ \frac{1}{2}m_2\left(\left(\dot{x}_0 + L_1\dot{\theta}_1\cos\theta_1 + L_2\dot{\theta}_2\cos\theta_2\right)^2 + \left(-L_1\dot{\theta}_1\sin\theta_1 - L_2\dot{\theta}_2\sin\theta_2\right)^2\right) \end{aligned} \tag{6.49}$$

Multiplying out the brackets and applying $\cos^2 x + \sin^2 x = 1$ results in the following expression:

$$\begin{aligned} T =& \frac{1}{2}M\dot{x}_0^2 + \frac{1}{2}m_1\left(\dot{x}_0^2 + L_1^2\dot{\theta}_1^2 + 2\dot{x}_0L_1\dot{\theta}_1\cos\theta_1\right) \\ &+ \frac{1}{2}m_2\left(\dot{x}_0^2 + L_1^2\dot{\theta}_1^2 + L_2^2\dot{\theta}_2^2 + 2\dot{x}_0L_1\dot{\theta}_1\cos\theta_1 + 2\dot{x}_0L_2\dot{\theta}_2\cos\theta_2\right. \\ &\left. + 2L_1L_2\dot{\theta}_1\dot{\theta}_2\cos\theta_1\cos\theta_2 + 2L_1L_2\dot{\theta}_1\dot{\theta}_2\sin\theta_1\sin\theta_2\right) \end{aligned} \tag{6.50}$$

As before, to linearize for small amplitude motion about the equilibrium, the angles θ_1 and θ_2 can be assumed to be small, and small angle approximations can be applied to the expression. Terms containing products of more than 2 small terms are assumed to be negligible and are therefore ignored, leaving the following simplified expression for the kinetic energy of the system:

$$\begin{aligned} T \approx& \frac{1}{2}M\dot{x}_0^2 + \frac{1}{2}m_1\left(\dot{x}_0^2 + L_1^2\dot{\theta}_1^2 + 2\dot{x}_0L_1\dot{\theta}_1\right) \\ &+ \frac{1}{2}m_2\left(\dot{x}_0^2 + L_1^2\dot{\theta}_1^2 + L_2^2\dot{\theta}_2^2 + 2\dot{x}_0L_1\dot{\theta}_1 + 2\dot{x}_0L_2\dot{\theta}_2 + 2L_1L_2\dot{\theta}_1\dot{\theta}_2\right) \end{aligned} \tag{6.51}$$

From this, the entries of the linearized system's mass matrix can be obtained directly, using the following double derivative equation.

$$M_{i,j} = \frac{\partial^2 T}{\partial\dot{u}_i\partial\dot{u}_j} \tag{6.52}$$

In this expression, the terms u_i and u_j represent the generalised coordinates of the system that correspond to the row and column of the mass matrix entry respectively.

Applying the relevant partial double derivative for each entry to the kinetic energy equation produces the following mass matrix for the system:

$$M = \begin{bmatrix} m_1 + m_2 + M & (m_1 + m_2)L_1 & m_2L_2 \\ (m_1 + m_2)L_1 & (m_1 + m_2)L_1^2 & m_2L_1L_2 \\ m_2L_2 & m_2L_1L_2 & m_2L_2^2 \end{bmatrix} \tag{6.53}$$

While at this point the mass matrix is not identical to the one derived by the previous method, this may be down to the fact that common terms along the equations cancel out, and the equation in its entirety may be identical. The stiffness matrix must be found before this is determined.

The contents of the stiffness matrix can be found in a similar manner as the mass matrix, this time using the system's potential energy equation. An expression for the total potential energy is found. In this system, this consists of the sum of the gravitational potential energies of the masses in the system. Since the trolley is constrained to horizontal motion only, it does not show up in the potential energy equation.

$$V = m_1 g y_1 + m_2 g y_2 = m_1 g L_1 \cos\theta_1 + m_2 g \left(L_1 \cos\theta_1 + L_2 \cos\theta_2\right) \tag{6.54}$$

As before, small angle approximations are made to the expression for small amplitude motion about the equilibrium. This time, approximating $\cos x \approx 1$ is insufficient, and another term in the cosine expansion must be added to the approximation, i.e. $\cos x \approx 1 - x^2/2$.

$$V \approx m_1 g L_1 \left(1 - \frac{\theta_1^2}{2}\right) + m_2 g \left(L_1 \left(1 - \frac{\theta_1^2}{2}\right) + L_2 \left(1 - \frac{\theta_2^2}{2}\right)\right) \tag{6.55}$$

The following double derivatives can then be applied to this equation in order to find the entries of the stiffness matrix:

$$K_{1,j} = \frac{\partial^2 V}{\partial u_i \partial u_j} \tag{6.56}$$

Applying the double derivative corresponding to each entry produces the stiffness matrix of the linearized system expressed below:

$$K = \begin{bmatrix} 0 & 0 & 0 \\ 0 & -gL_1(m_1 + m_2) & 0 \\ 0 & 0 & -m_2 g L_2 \end{bmatrix} \tag{6.57}$$

The linearized matrix equation of motion as derived by this method is therefore written out in full:

$$\begin{bmatrix} m_1+m_2+M & (m_1+m_2)L_1 & m_2L_2 \\ (m_1+m_2)L_1 & (m_1+m_2)L_1^2 & m_2L_1L_2 \\ m_2L_2 & m_2L_1L_2 & m_2L_2^2 \end{bmatrix} \begin{bmatrix} \ddot{x}_0 \\ \ddot{\theta}_1 \\ \ddot{\theta}_2 \end{bmatrix} + \begin{bmatrix} b & 0 & 0 \\ 0 & 0 & 0 \\ 0 & 0 & 0 \end{bmatrix} \begin{bmatrix} \dot{x}_0 \\ \dot{\theta}_1 \\ \dot{\theta}_2 \end{bmatrix} + \begin{bmatrix} 0 & 0 & 0 \\ 0 & -gL_1(m_1+m_2) & 0 \\ 0 & 0 & -m_2gL_2 \end{bmatrix} \begin{bmatrix} x_0 \\ \theta_1 \\ \theta_2 \end{bmatrix} = \begin{bmatrix} F \\ 0 \\ 0 \end{bmatrix} \tag{6.58}$$

The equations in the second and third row can be simplified by cancelling out common factors, which would lead to the expressions being identical to those found using the force method. The linearized equations of motion that are produced are therefore identical for both methods, as they should be. Since the mass, stiffness and damping matrices of the system have now been derived and validated, the state space matrices are found using equation 6.4. These can be used to obtain a gain matrix and incorporate feedback control into the system using LQR methods.

Arbitrary parameter values are chosen for the system to be used as an example. The two pendulums are chosen to be identical in length and mass, just because this is often found in practise for double pendulums. The parameter values chosen for this example are displayed in the Table 6.1.

Table 6.1 Double Inverted Pendulum Parameter Values

Parameter	Value
M (kg)	0.5
m_1 (kg)	0.2
m_2 (kg)	0.2
L_1 (m)	0.15
L_2 (m)	0.15
b (Ns/m)	0.1

These are substituted into the mass, stiffness and damping matrices which are in turn used to determine the entry values in the state space matrices of the system.

The eigenvalues of the state space matrix A are found to be:

$$poles = 0,\ 15.9,\ -15.9,\ 7.8,\ -7.8,\ -0.1 \tag{6.59}$$

As expected, these include poles that have positive real values implying that the inverted double pendulum system is unstable without feedback control. Through the incorporation of feedback control, all the eigenvalues of the closed loop system's state space matrix A_{CL} are expected to have negative real parts and the system to therefore be stabilized.

Before the optimal gain matrix K can be obtained, the cost function for the system must be assigned. Since it is only the cost ratio that is significant rather than the cost values themselves, the input cost parameter R is set to $R = 1$ and the state cost parameter matrix Q is varied. A cost parameter is set for each of the system's states by entering the value into the corresponding diagonal of the Q matrix. The general format of the state cost matrix Q used in this section is:

$$Q = \begin{bmatrix} 1 & 0 & 0 & 0 & 0 & 0 \\ 0 & q & 0 & 0 & 0 & 0 \\ 0 & 0 & q & 0 & 0 & 0 \\ 0 & 0 & 0 & 1 & 0 & 0 \\ 0 & 0 & 0 & 0 & q & 0 \\ 0 & 0 & 0 & 0 & 0 & q \end{bmatrix} \tag{6.60}$$

The unit values correspond to the base displacement and velocity. These two states are closely linked to the input which has a unit cost value, so this is done to better separate the cost of the base motion, and the states that are deviations from the system's equilibrium. Assigning a high cost to these parameters would contradict the relatively low cost assigned to the input cost parameter R for a cheap system. The remainder of the states are given identical values, of magnitude q. While any choice of cost function parameters would result in a stabilized system using LQR, the selected values of these affect the system's dynamic response and determine whether or not the response meets any required criteria.

In the first case, q is set to 100. LQR methods are applied to determine the optimal gain matrix K for the selected cost function. For the remainder of this section, the controller designed based off of this cost function is referred to as Controller 1. The obtained gain matrix can then be implemented into the system. The effective state space 'A' matrix of the closed loop system is now equal to $A_{CL} = A - BK$. The eigenvalues of A_{CL} determine the stability of the closed loop system. These are calculated and it is found that the largest real part of the poles is -0.0057. As expected, all of the closed loop system's poles have negative real parts, implying that the system has been stabilized.

To observe the effects of the implementation of the feedback controller, the system is disturbed, and the response is observed. In order to simulate a disturbance to the equilibrium, the system is given a non-zero initial state. This was done in the form of a non-zero initial angular velocity applied to the second pendulum, $\dot{\theta}_2$. The controller is designed with the aim

of returning the two pendulums to their upright inverted equilibrium position. How efficiently it does this depends on the cost function parameters. The initial state vector is chosen as follows:

$$\mathbf{x}_0 = \begin{bmatrix} x_0 \\ \theta_1 \\ \theta_2 \\ \dot{x}_0 \\ \dot{\theta}_1 \\ \dot{\theta}_2 \end{bmatrix} = \begin{bmatrix} 0 \\ 0 \\ 0 \\ 0 \\ 0 \\ 0.5 \end{bmatrix} \tag{6.61}$$

This effectively mimics an impulse being applied to the top of the double inverted pendulum while it is in its equilibrium position. The size of the impulse can be calculated:

$$I = m_2(v_{2,t=0^+} - v_{2,t=0^-}) = m_2 L_2 \dot{\theta}_2 = 0.015Ns \tag{6.62}$$

For $q = 100$, the closed loop response to the impulse is plotted in Figure 6.6. This figure shows the motion of the base of the double pendulum, as well as the angles from the vertical of the two pendulums. The controller has successfully returned the system to its open-loop unstable equilibrium state and the double inverted pendulum has been stabilized.

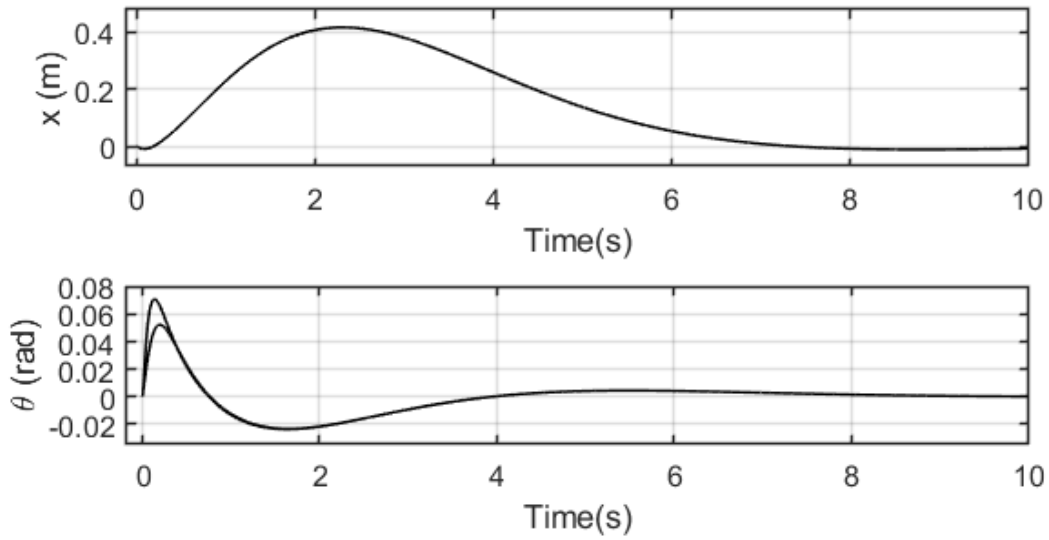

Fig. 6.6 Closed loop system response for double inverted pendulum for Controller 1 (q=100)

The effects of varying the cost function are investigated. A cheaper controller, Controller 2, and a more expensive controller, Controller 3, are designed based off of the cost functions summarised in Table 6.2.

Table 6.2 Cost Function Parameters q for the Double Inverted Pendulum Controllers

Controller	q
1	100
2	500
3	50

Controller 2 places more weight on reducing the deviations of the states from their equilibrium values and less on minimising the control effort, hence being 'cheap'. Controller 3 places relatively more weight on the control input, making it more 'expensive'. For an open-loop unstable system, the differences in the closed loop responses are not expected to be very large for varying cost functions, since deviations from the equilibrium state must be kept very small to avoid the loss of stability for whatever cost function that is selected. The effects of varying the cost function are investigated by comparing the closed loop system response for the same system and initial conditions. The first parts of the responses are plotted in Figure 6.7 for a clearer comparison.

As the controller becomes cheaper, and therefore allowed to exhibit larger control efforts for the same state vector, the base is seen to exhibit larger base motion. As a result of this, the maximum angular deviations of the pendulums in both the positive and negative directions are smallest as the controller gets cheaper. Equivalently, the most expensive controller, Controller 3, displays the least base motion and the largest range of angular motion exhibited by the pendulums. Cheaper controllers are also seen to exhibit a smaller overshoot. This is because, as well as having larger costs parameters assigned to the pendulum angles' absolute values, they also have larger cost values assigned to the rate of change of these, resulting in the slower return of these to their equilibrium values, and therefore a smaller overshoot.

It is therefore seen that LQR can be used to stabilize the double inverted pendulum, with a dynamic response that varies depending on the relative costs of the states and the input. The same method can be applied for more complex systems containing more elements, such as the more complex tethered balloon system models.

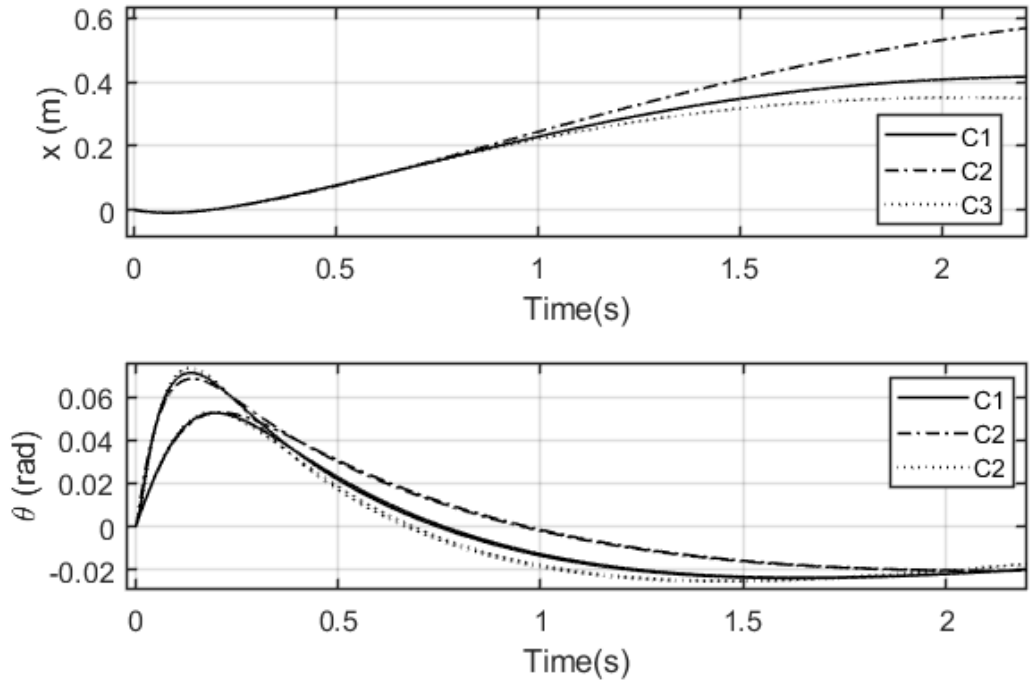

Fig. 6.7 Closed loop system response for double inverted pendulum for Controllers 1 (q=100), 2 (q=500) and 3 (q=50)

6.4 Tethered Balloon Feedback Control

In a similar fashion to the previous sections, the combined tethered balloon system can be linearized about its equilibrium position. The previous inverted pendulum examples assumed a vertical upward equilibrium position since no external forces act on these. For the case of the high altitude tethered balloons considered in this research, the balloon and cable are expected to be subjected to strong steady winds that vary with altitude, making the cable's equilibrium neither straight nor vertical. For this reason, the tethered balloon system is modelled as having unknown horizontal and vertical forces acting along the tether that can later be specified, to avoid the loss of generality. The equilibrium angles from the vertical of the tether elements are dependent on these external forces, and the system is linearized about this arbitrary equilibrium position. In order to do this, the angular generalized coordinates of the tether's elements, rather than being the absolute angles from the vertical, are chosen to be the angular deviations from the equilibrium. Since the system is linearized for small amplitude motion about the equilibrium, these angles are assumed to be small.

For a greatly simplified system of two elements, the linearized equations of motion are derived using both the force and energy methods in full. The system in question is presented

in Figure 6.8. It consists of two elements which have arbitrary but constant vertical and horizontal forces acting on them, and a trolley at the base to allow for base motion. The arbitrary forces are used to represent the lift force, and the drag forces acting on the tether and the balloon. Other than the additional external forces and therefore altered equilibrium, it can be seen that this model is identical to that used in the double inverted pendulum section.

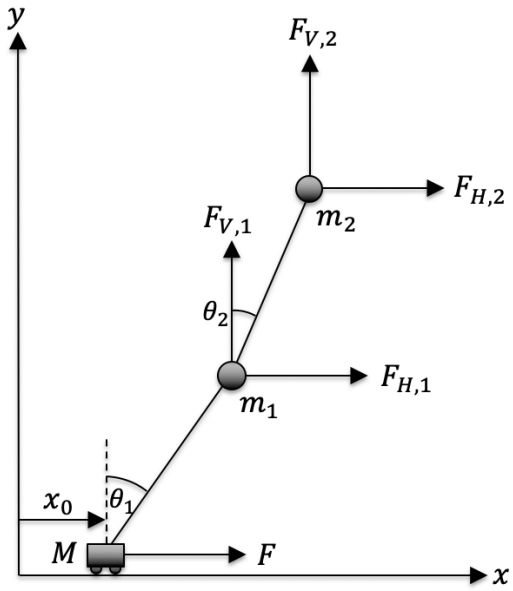

Fig. 6.8 Simplified 2-element tethered balloon model

The nonlinear equations of motion can be produced in the same way as before. The forces are resolved on each mass, and are almost identical to the previous case, but with the addition of the external forces that act on each mass.

Resolving forces on the trolley in a horizontal direction produces an identical equation to the double inverted pendulum case, since there are no additional forces on this mass:

$$F + T_1 \sin\theta_1 - b\dot{x}_0 - M\ddot{x}_0 = 0 \tag{6.63}$$

Forces are resolved horizontally and vertically for each of the two elements

$$m_1\ddot{x}_1 + T_1 \sin\theta_1 - T_2 \sin\theta_2 - F_{H,1} = 0 \tag{6.64}$$

$$m_1\ddot{y}_1 + m_1 g + T_1 \cos\theta_1 - T_2 \cos\theta_2 - F_{V,1} = 0 \tag{6.65}$$

$$m_2\ddot{x}_2 + T_2 \sin\theta_2 - F_{H,2} = 0 \tag{6.66}$$

$$m_2\ddot{y}_2 + m_2 g + T_2 \cos\theta_2 - F_{V,2} = 0 \tag{6.67}$$

As before, the link tensions are eliminated, leaving 3 nonlinear equations of motion in terms of the Cartesian coordinates. T_2 is eliminated by combining equations 6.66 and 6.67 to produce an equation of motion.

$$\tan\theta_2 = \frac{F_{H,2} - m_2\ddot{x}_2}{F_{V,2} - m_2 g - m_2\ddot{y}_2} \tag{6.68}$$

T_2 and T_1 are eliminated from equations 6.64 and 6.65 as before, producing another equation of motion:

$$\tan\theta_1 = \frac{F_{H,2} - m_2\ddot{x}_2 + F_{H,1} - m_1\ddot{x}_1}{F_{V,1} - m_1(g+\ddot{y}_1) + F_{V,2} - m_2(g+\ddot{y}_2)} \tag{6.69}$$

Expressions for the equilibrium angles from the vertical of the two links can be obtained from these expressions by setting velocities and accelerations to zero:

$$\tan\theta_{0,1} = \frac{F_{H,2} + F_{H,1}}{F_{V,1} - m_1 g + F_{V,2} - m_2 g} \qquad \tan\theta_{0,2} = \frac{F_{H,2}}{F_{V,2} - m_2 g} \tag{6.70}$$

Again, T_1 can also be eliminated from equation 6.63, which, as before, can be done easily by rearranging equation 6.64 to get an expression for $T_1\sin\theta_1$ that can be substituted directly.

$$F + F_{H,1} - m_1\ddot{x}_1 + F_{H,2} - m_2\ddot{x}_2 - b\dot{x}_0 - M\ddot{x}_0 = 0 \tag{6.71}$$

The coordinate substitutions are made in the same way as before. Upon applying these substitutions, equation 6.71 becomes:

$$\begin{aligned} F + F_{H,1} + F_{H,2} - b\dot{x}_0 - M\ddot{x}_0 - m_1(\ddot{x}_0 + L_1\ddot{\theta}_1\cos\theta_1 - L_1\dot{\theta}_1^2\sin\theta_1) \\ - m_2(\ddot{x}_0 + L_1\ddot{\theta}_1\cos\theta_1 - L_1\dot{\theta}_1^2\sin\theta_1 + L_2\ddot{\theta}_2\cos\theta_2 - L_2\dot{\theta}_2^2\sin\theta_2) = 0 \end{aligned} \tag{6.72}$$

Equation 6.68 becomes:

$$\begin{aligned} &F_{H,2}m_2(\ddot{x}_0 + L_1\ddot{\theta}_1\cos\theta_1 - L_1\dot{\theta}_1^2\sin\theta_1 + L_2\ddot{\theta}_2\cos\theta_2 - L_2\dot{\theta}_2^2\sin\theta_2) \\ &- \left(F_{V,2} - m_2(-L_1\ddot{\theta}_1\sin\theta_1 - L_1\dot{\theta}_1^2\cos\theta_1 - L_2\ddot{\theta}_2\sin\theta_2 - L_2\dot{\theta}_2^2\cos\theta_2 + g)\right)\tan\theta_2 = 0 \end{aligned} \tag{6.73}$$

Finally, equation 6.69 becomes:

$$\begin{aligned}
&F_{H,2} - m_2(\ddot{x}_0 + L_1\ddot{\theta}_1\cos\theta_1 - L_1\dot{\theta}_1^2\sin\theta_1 + L_2\ddot{\theta}_2\cos\theta_2 - L_2\dot{\theta}_2^2\sin\theta_2) \\
&\quad + F_{H,1} - m_1(\ddot{x}_0 + L_1\ddot{\theta}_1\cos\theta_1 - L_1\dot{\theta}_1^2\sin\theta_1) \\
&\quad - \tan\theta_1(F_{V,1} - m_1(g - L_1\ddot{\theta}_1\sin\theta_1 - L_1\dot{\theta}_1^2\cos\theta_1) \\
&\quad + F_{V,2} - m_2(g - L_1\ddot{\theta}_1\sin\theta_1 - L_1\dot{\theta}_1^2\cos\theta_1 - L_2\ddot{\theta}_2\sin\theta_2 - L_2\dot{\theta}_2^2\cos\theta_2)) = 0
\end{aligned} \tag{6.74}$$

In this case, θ_1 and θ_2 can no longer be assumed to be small. Their magnitudes are dependent on the horizontal and vertical forces acting on the elements, the magnitudes of which are arbitrary. The equations also need to be transformed such that they are in terms of the system's generalized coordinates, which θ_1 and θ_2 no longer are, and so a further substitution is needed. The following substitutions are made to ensure that the equations are in terms of the new angular generalized coordinates, u_1 and u_2:

$$\theta_j = \theta_{0,j} + u_j \tag{6.75}$$

The absolute angles from the vertical of the pendulums θ_j are therefore the sums of the corresponding equilibrium angles $\theta_{0,j}$ and the small deviations from from the equilibrium u_j, which are also the generalized angular coordinate of the system, as required.

Applying these substitutions produces the following set of equations, in which small angle approximations can now be applied for u_j. Terms containing the product of more than one small term are assumed to be negligible and can be ignored.

$$\begin{aligned}
F + F_{H,1} + F_{H,2} - b\dot{x}_0 - M\ddot{x}_0 - m_1(\ddot{x}_0 + L_1\ddot{u}_1\cos(\theta_{0,1}+u_1) - L_1\dot{u}_1^2\sin(\theta_{0,1}+u_1)) \\
- m_2(\ddot{x}_0 + L_1\ddot{u}_1\cos(\theta_{0,1}+u_1) - L_1\dot{u}_1^2\sin(\theta_{0,1}+u_1) + L_2\ddot{u}_2\cos(\theta_{0,2}+u_2) \\
- L_2\dot{u}_2^2\sin(\theta_{0,2}+u_2)) = 0
\end{aligned} \tag{6.76}$$

$$\begin{aligned}
&-m_2(\ddot{x}_0 + L_1\ddot{u}_1\cos(\theta_{0,1}+u_1) - L_1\dot{u}_1^2\sin(\theta_{0,1}+u_1) + L_2\ddot{u}_2\cos(\theta_{0,2}+u_2) \\
&\quad - L_2\dot{u}_2^2\sin(\theta_{0,2}+u_2)) + F_{H,2} - \big(F_{V,2} - m_2(-L_1\ddot{u}_1\sin(\theta_{0,1}+u_1) - L_1\dot{u}_1^2\cos(\theta_{0,1}+u_1) \\
&\quad - L_2\ddot{u}_2\sin(\theta_{0,2}+u_2) - L_2\dot{u}_2^2\cos(\theta_{0,2}+u_2) + g)\big)\tan(\theta_{0,2}+u_2) = 0
\end{aligned} \tag{6.77}$$

$$\begin{aligned}F_{H,2} - m_2(&\ddot{x}_0 + L_1\ddot{u}_1\cos(\theta_{0,1}+u_1) - L_1\dot{u}_1^2\sin(\theta_{0,1}+u_1) + L_2\ddot{u}_2\cos(\theta_{0,2}+u_2)\\ &- L_2\dot{u}_2^2\sin(\theta_{0,2}+u_2)) + F_{H,1} - m_1(\ddot{x}_0 + L_1\ddot{u}_1\cos(\theta_{0,1}+u_1) - L_1\dot{u}_1^2\sin(\theta_{0,1}+u_1))\\ &- \tan(\theta_{0,1}+u_1)(F_{V,1} - m_1(g - L_1\ddot{u}_1\sin(\theta_{0,1}+u_1) - L_1\dot{u}_1^2\cos(\theta_{0,1}+u_1))\\ &+ F_{V,2} - m_2(g - L_1\ddot{u}_1\sin(\theta_{0,1}+u_1) - L_1\dot{u}_1^2\cos(\theta_{0,1}+u_1) - L_2\ddot{u}_2\sin(\theta_{0,2}+u_2)\\ &- L_2\dot{u}_2^2\cos(\theta_{0,2}+u_2))) = 0\end{aligned} \tag{6.78}$$

The trigonometric identities for $\cos(a+b)$ and $\sin(a+b)$ can be used to expand out the sin and cos terms, and, applying small angle approximations to these leads to the following expressions that can be substituted into the equations of motion:

$$\sin(\theta_{0,j}+u_j) = \sin\theta_{0,j}\cos u_j + \sin u_j\cos\theta_{0,j} \approx \sin\theta_{0,j} + u_j\cos\theta_{0,j} \tag{6.79}$$

$$\cos(\theta_{0,j}+u_j) = \cos\theta_{0,j}\cos u_j - \sin\theta_{0,j}\sin u_j \approx \cos\theta_{0,j} - u_j\sin\theta_{0,j} \tag{6.80}$$

These substitutions are applied, and any terms containing the product of more than one small term are eliminated. The equations are simplified and like terms are collected, producing the following equations of motion:

$$(M+m_1+m_2)\ddot{x}_0 + (m_1+m_2)L_1\ddot{u}_1\cos\theta_{0,1} + m_2L_2\ddot{u}_2\cos\theta_{0,2} + b\dot{x}_0 = F + F_{H,1} + F_{H,2} \tag{6.81}$$

$$\begin{aligned}m_2\ddot{x}_0 + &m_2L_1\ddot{u}_1(\cos\theta_{0,1}\cos\theta_{0,2} + \sin\theta_{0,1}\sin\theta_{0,2}) + m_2L_2\ddot{u}_2(\cos^2\theta_{0,2} + \sin^2\theta_{0,2})\\ &+ u_2(F_{H,2}\sin\theta_{0,2} + F_{V,2}\cos\theta_{0,2} - m_2g\cos\theta_{0,2}) - F_{H,2}\cos\theta_{0,2} + F_{V,2}\sin\theta_{0,2}\\ &- m_2g\sin\theta_{0,2} = 0\end{aligned} \tag{6.82}$$

$$\begin{aligned}(m_1+m_2)\ddot{x}_0\cos\theta_{0,1} &+ L_1\ddot{u}_1(m_2\cos^2\theta_{0,1} + m_2\sin^2\theta_{0,1} + m_1\cos^2\theta_{0,1} + m_1\sin^2\theta_{0,1})\\ &+ m_2L_2\ddot{u}_2(\cos\theta_{0,1}\cos\theta_{0,2} + \sin\theta_{0,1}\sin\theta_{0,2})\\ &+ u_1(\sin\theta_{0,1}(F_{H,2}+F_{H,1}) + \cos\theta_{0,1}(F_{V,1}+F_{V,2} - m_1g - m_2g))\\ &- \cos\theta_{0,1}(F_{H,2}+F_{H,1}) + \sin\theta_{0,1}(F_{V,1}+F_{V,2} - m_1g - m_2g) = 0\end{aligned} \tag{6.83}$$

Using the static equilibrium equations (equation 6.70) derived previously, it can be seen that the constant terms in each of these equations equate to zero, and can be removed. In the first equation, the force applied to the base, F, will consist of a component required to balance out the external horizontal forces acting on the system, and the additional input force F_{IN} that will be used to control the system's motion. For this specific case, the following

substitution can be made for the base force F:

$$F = F_{IN} - F_{H,2} - F_{H,1} \tag{6.84}$$

Trigonometric identities can also be used to further simplify these equations. Applying all of the above yields the following simplified and finalized equations of motion:

$$(M+m_1+m_2)\ddot{x}_0 + (m_1+m_2)L_1\ddot{u}_1\cos\theta_{0,1} + m_2L_2\ddot{u}_2\cos\theta_{0,2} + b\dot{x}_0 = F_{IN} \tag{6.85}$$

$$\begin{aligned} m_2\ddot{x}_0 + m_2L_1\ddot{u}_1\cos(\theta_{0,1}-\theta_{0,2}) + m_2L_2\ddot{u}_2 \\ + u_2(F_{H,2}\sin\theta_{0,2} + F_{V,2}\cos\theta_{0,2} - m_2g\cos\theta_{0,2}) = 0 \end{aligned} \tag{6.86}$$

$$\begin{aligned} (m_1+m_2)\ddot{x}_0\cos\theta_{0,1} + L_1\ddot{u}_1(m_2+m_1) + m_2L_2\ddot{u}_2\cos(\theta_{0,1}-\theta_{0,2}) \\ + u_1(\sin\theta_{0,1}(F_{H,2}+F_{H,1}) + \cos\theta_{0,1}(F_{V,1}+F_{V,2}-m_1g-m_2g)) = 0 \end{aligned} \tag{6.87}$$

The equations of motion have now been linearized about the arbitrary non-zero equilibrium position of the system. These equations can now be assembled into matrix form:

$$\begin{aligned} &\begin{bmatrix} m_1+m_2+M & (m_1+m_2)L_1\cos\theta_{0,1} & m_2L_2\cos\theta_{0,2} \\ (m_1+m_2)\cos\theta_{0,1} & (m_1+m_2)L_1 & m_2L_2\cos(\theta_{0,1}-\theta_{0,2}) \\ m_2 & m_2L_1\cos(\theta_{0,1}-\theta_{0,2}) & m_2L_2 \end{bmatrix} \begin{bmatrix} \ddot{v} \\ \ddot{\theta}_1 \\ \ddot{\theta}_2 \end{bmatrix} \\ &+ \begin{bmatrix} b & 0 & 0 \\ 0 & 0 & 0 \\ 0 & 0 & 0 \end{bmatrix} \begin{bmatrix} \dot{v} \\ \dot{\theta}_1 \\ \dot{\theta}_2 \end{bmatrix} + \begin{bmatrix} 0 & 0 & 0 \\ 0 & K(2,2) & 0 \\ 0 & 0 & K(3,3) \end{bmatrix} \begin{bmatrix} v \\ \theta_1 \\ \theta_2 \end{bmatrix} = \begin{bmatrix} F_{IN} \\ 0 \\ 0 \end{bmatrix} \end{aligned} \tag{6.88}$$

The entries of the stiffness matrix take the following expressions:

$$K(2,2) = \sin\theta_{0,1}(F_{H,2}+F_{H,1}) + \cos\theta_{0,1}(F_{V,1}+F_{V,2}-m_1g-m_2g) \tag{6.89}$$

$$K(3,3) = F_{H,2}\sin\theta_{0,2} + F_{V,2}\cos\theta_{0,2} - m_2g\cos\theta_{0,2} \tag{6.90}$$

The energy method is also adapted to account for the external forces acting on the elements, and the resulting non-zero equilibrium state. As before, the system's kinetic energy equation is required in terms of the generalized coordinates. The expression for the kinetic energy of the system is unchanged by the introduction of the external forces acting on the elements (Equation 6.50). This time, the angular substitutions from equation 6.75 are applied

to this equation in order to introduce the generalized coordinates u_j into the expression.

$$\begin{aligned} T =& \frac{1}{2}M\dot{x}_0^2 + \frac{1}{2}m_1\left(\dot{x}_0^2 + L_1^2\dot{u}_1^2 + 2\dot{x}_0 L_1\dot{u}_1\cos(\theta_{0,1}+u_1)\right) \\ &+ \frac{1}{2}m_2\big(\dot{x}_0^2 + L_1^2\dot{u}_1^2 + L_2^2\dot{u}_2^2 + 2\dot{x}_0 L_1\dot{u}_1\cos(\theta_{0,1}+u_1) + 2\dot{x}_0 L_2\dot{u}_2\cos(\theta_{0,2}+u_2) \\ &+ 2L_1L_2\dot{u}_1\dot{u}_2\cos(\theta_{0,1}+u_1)\cos(\theta_{0,2}+u_2) + 2L_1L_2\dot{u}_1\dot{u}_2\sin(\theta_{0,1}+u_1)\sin(\theta_{0,2}+u_2)\big) \end{aligned} \tag{6.91}$$

Again, since small amplitude motion about the equilibrium is assumed, small angle approximations can be made for u_j. The substitutions in equations 6.79 and 6.80 are applied. Terms containing products of more than two small terms are considered negligible and can be ignored.

$$\begin{aligned} T \approx& \frac{1}{2}M\dot{x}_0^2 + \frac{1}{2}m_1\left(\dot{x}_0^2 + L_1^2\dot{u}_1^2 + 2\dot{x}_0 L_1\dot{u}_1\cos\theta_{0,1}\right) + \frac{1}{2}m_2\big(\dot{x}_0^2 + L_1^2\dot{u}_1^2 + L_2^2\dot{u}_2^2 \\ &+ 2\dot{x}_0 L_1\dot{u}_1\cos\theta_{0,1} + 2\dot{x}_0 L_2\dot{u}_2\cos\theta_{0,2} + 2L_1L_2\dot{u}_1\dot{u}_2\cos\theta_{0,1}\cos\theta_{0,2} \\ &+ 2L_1L_2\dot{u}_1\dot{u}_2\sin\theta_{0,1}\sin\theta_{0,2}\big) \end{aligned} \tag{6.92}$$

As in the previous section, the entries of the matrix are found using the double partial differential equation described in 6.52. The mass matrix of the simplified tethered balloon system is therefore:

$$M = \begin{bmatrix} m_1+m_2+M & (m_1+m_2)L_1\cos\theta_{0,1} & m_2L_2\cos\theta_{0,2} \\ (m_1+m_2)L_1\cos\theta_{0,1} & (m_1+m_2)L_1^2 & m_2L_1L_2\cos(\theta_{0,1}-\theta_{0,2}) \\ m_2L_2\cos\theta_{0,2} & m_2L_1L_2\cos(\theta_{0,1}-\theta_{0,2}) & m_2L_2^2 \end{bmatrix} \tag{6.93}$$

To derive the stiffness matrix of the system, the potential energy equation is required. One possible way of incorporating the external forces into the Lagrangean model is to treat them in the same way as the gravitational potential energy terms. The potential energy equation will therefore contain some additional terms due to the constant external forces.

$$\begin{aligned} V =& (m_1g - F_{V,1})y_1 + (m_2g - F_{V,2})y_2 - F_{H,1}x_1 - F_{H,2}x_2 \\ =& (m_1g - F_{V,1})L_1\cos\theta_1 + (m_2g - F_{V,2})\left(L_1\cos\theta_1 + L_2\cos\theta_2\right) - F_{H,1}(x_0 + L_1\sin\theta_1) \\ &- F_{H,2}(x_0 + L_1\sin\theta_1 + L_2\sin\theta_2) \end{aligned} \tag{6.94}$$

Applying the angular substitutions in equation 6.75, the expression becomes:

$$\begin{aligned} V =&(m_1 g - F_{V,1}) L_1 \cos(\theta_{0,1} + u_1) + (m_2 g - F_{V,2}) \left(L_1 \cos(\theta_{0,1} + u_1) + L_2 \cos(\theta_{0,2} + u_2)\right) \\ &- F_{H,1}(x_0 + L_1 \sin(\theta_{0,1} + u_1)) - F_{H,2}(x_0 + L_1 \sin(\theta_{0,1} + u_1) + L_2 \sin(\theta_{0,2} + u_2)) \end{aligned} \tag{6.95}$$

Applying the substitutions in equations 6.79 and 6.80 would result in a stiffness matrix containing only zeros, so additional terms are needed when approximating sin and cos of the small angles u_j.

$$\sin(\theta_{0,j} + u_j) = \sin\theta_{0,j} \cos u_j + \sin u_j \cos\theta_{0,j} \approx (1 - \frac{u_j^2}{2}) \sin\theta_{0,j} + u_j \cos\theta_{0,j} \tag{6.96}$$

$$\cos(\theta_{0,j} + u_j) = \cos\theta_{0,j} \cos u_j - \sin\theta_{0,j} \sin u_j \approx (1 - \frac{u_j^2}{2}) \cos\theta_{0,j} - u_j \sin\theta_{0,j} \tag{6.97}$$

These approximations are substituted into the potential energy equation, limiting it to cases involving small deviations from the equilibrium:

$$\begin{aligned} V \approx&(m_1 g - F_{V,1}) L_1 ((1 - \frac{u_1^2}{2}) \cos\theta_{0,1} - u_1 \sin\theta_{0,1}) \\ &+ (m_2 g - F_{V,2}) \left(L_1 ((1 - \frac{u_1^2}{2}) \cos\theta_{0,1} - u_1 \sin\theta_{0,1}) + L_2 ((1 - \frac{u_2^2}{2}) \cos\theta_{0,2} - u_2 \sin\theta_{0,2})\right) \\ &- F_{H,1}(x_0 + L_1 ((1 - \frac{u_1^2}{2}) \sin\theta_{0,1} + u_1 \cos\theta_{0,1})) \\ &- F_{H,2}(x_0 + L_1 ((1 - \frac{u_1^2}{2}) \sin\theta_{0,1} + u_1 \cos\theta_{0,1}) + L_2 ((1 - \frac{u_2^2}{2}) \sin\theta_{0,2} + u_2 \cos\theta_{0,2})) \end{aligned} \tag{6.98}$$

Applying the double partial differential equation to this expression for each combination of generalized coordinates produces the following diagonal stiffness matrix:

$$K = \begin{bmatrix} 0 & 0 & 0 \\ 0 & K(2,2) & 0 \\ 0 & 0 & K(3,3) \end{bmatrix} \tag{6.99}$$

The non-zero entries of the matrix contain the following expressions:

$$K(2,2) = (F_{V,1} + F_{V,2} - m_1 g - m_2 g) L_1 \cos\theta_{0,1} + (F_{H,1} + F_{H,2}) L_1 \sin\theta_{0,1} \tag{6.100}$$

$$K(3,3) = (F_{V,2} - m_2 g) L_2 \cos\theta_{0,2} + F_{H,2} L_2 \sin\theta_{0,2} \tag{6.101}$$

It can be seen that the matrix differential equation produced is identical to the one produced using the force method, with the exception of constant factors that can be cancelled out. This method has therefore been validated to some extent, and can be extended and applied to systems with many elements.

It can also be seen that, upon setting the magnitudes of the external forces and the equilibrium angles to zero, the matrix equation reverts to that of the double inverted pendulum case derived in the previous section, as expected.

For the same system parameters used in the double inverted pendulum case displayed in Table 6.1, the following external forces are selected arbitrarily:

Table 6.3 External Force Values Acting on Simple Tethered Balloon Model

Force	Value (N)
$F_{V,1}$	0
$F_{V,2}$	15
$F_{H,1}$	1
$F_{H,2}$	4

Using the system's parameter values along with the external forces acting on its elements, the open-loop state space matrices are derived for small amplitude motion about the system's non-vertical equilibrium. The eigenvalues of the matrix A are found, with the largest real part of a pole being 0. This implies the system is marginally stable, which is expected since no damping was included in the model.

For a state cost parameter of magnitude $q = 100$, LQR methods were applied to produce a feedback gain matrix for the system, K. While the system is not unstable in this case, feedback control can be used to make the system closed-loop asymptotically stable and generally improve its dynamic response.

An identical disturbance is applied to the system as was done in the double inverted pendulum case - an impulse of magnitude $I = 0.015Ns$ on the second element's end. Figure 6.9 displays the system's closed-loop response alongside its open-loop response for reference.

The benefits of implementing feedback control are clear in this diagram. The open loop response is marginally stable as expected, continuing to oscillate indefinitely. The closed loop response however dampens out quite quickly, with the pendulum angles completely returning to their equilibrium values within 2.5 seconds, despite the lack of damping within the open loop model.

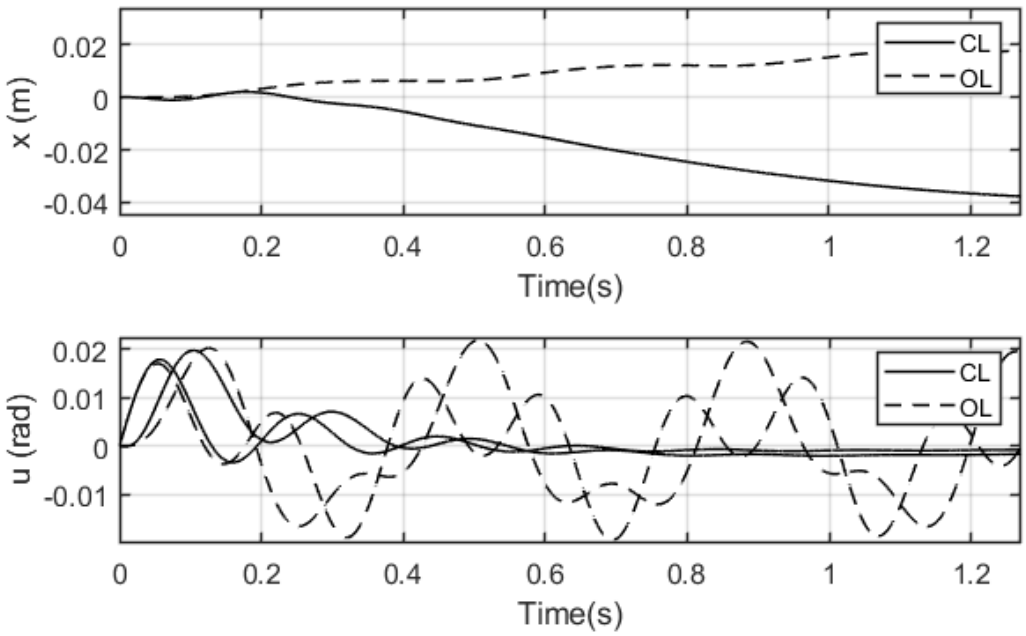

Fig. 6.9 Closed Loop (CL) and Open Loop (OL) impulse responses for simple balloon model, showing base displacement x and angular deviations from the equilibrium, u_1 and u_2.

6.4.1 3D Tethered Balloon Control

The same process of linearizing the system model, converting it to state space form and using LQR to design a suitable controller can be applied for a 3-dimensional cable or tethered balloon system. Expanding to 3-dimensions allows for the use of feedback control to improve the system's dynamic response to out-of-plane disturbances, which is equally important and necessary when considering a HATB. This results in additional coordinates being required to specify the system's state. For an extensible cable model, each element has 3 degrees of freedom in 3 dimensions, and for an inextensible model, each element has 2 degrees of freedom. The tether's base is now allowed to move in the horizontal plane rather than unidirectionally, and therefore has 2 degrees of freedom for a 3D system model. The base is now defined by the coordinates x_0 and y_0, and absolute Euler angles θ_i and ϕ_i of each elemental link are used to specify the positions of each of the lumped masses, as well as the balloon. For an extensible cable model, the element length l_i is also required to define the element's position.

While for the 2D case the input used was an in-plane horizontal scalar force value, for the 3D case, the input is now chosen to be a force vector in the horizontal plane acting on the

base of the tether. This takes the following form:

$$u = \begin{bmatrix} F_x \\ F_y \end{bmatrix} \tag{6.102}$$

The derivation of the linearized ODE matrix equation for a 3-dimensional cable/tethered balloon system is described in detail in Chapter 7, where general expressions for the mass, stiffness and damping matrices of a cable system are derived.

6.5 Robustness of LQR Control

While the dynamic response of the system is important to consider when implementing feedback control, it is also very important to consider the robustness of the controller, as in reality there are likely to be errors and inaccuracies in the controller's design. In order to safely implement feedback control, the controller must not be sensitive to these potential errors, and must have a large error margin before losing stability to minimise the risks of failure. Fortunately LQR is generally a robust method of control. This section investigates the robustness of LQR control through the derivation stability margins of LQR in general, and methods of quantifying the robustness of specific closed loop systems. The theory derived in this section is based on Anderson and Moore, 2014 [6]. The effects of weight selection on the controller's robustness is also investigated. The first section looks at the derivation of Nyquist plots for optimal control by adapting the control loop such that it is analogous with classical control. Nyquist plots are useful in obtaining theoretical gain and phase margins of the closed loop linear systems.

6.5.1 Nyquist Diagrams for Optimal Control

In Classical control, Nyquist plots in the frequency domain can be used to quantify the system's robustness using the gain and phase margins. It is known that by altering the optimal control closed loop system diagram, it can be made analogous to that of classical control, and a Nyquist plot can be plotted and gain and phase margins deduced. This is very useful as it can allow for comparisons to be made between controllers with varying Q and R values and insight can be gained into the robustness of LQR. This theory is widely available in books and is included here for completeness. In this section a single input system is used for simplification, although the theory can be expanded to multiple input systems.

Figure 6.10 shows a typical classical feedback loop and Figure 6.11 shows a typical optimal control feedback loop. While classical control involves the dynamic feedback of the

system's output, optimal control involves memory-less state feedback. It is however possible to rearrange the optimal feedback loop such that it becomes analogous to a classical control loop with a unity feedback gain.

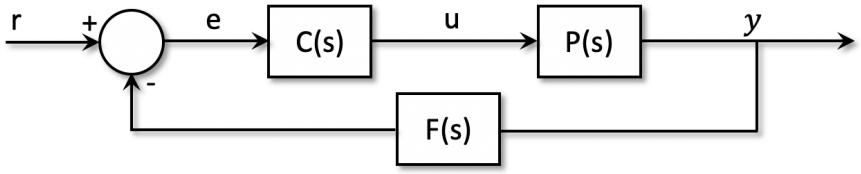

Fig. 6.10 Classical Control Feedback Loop

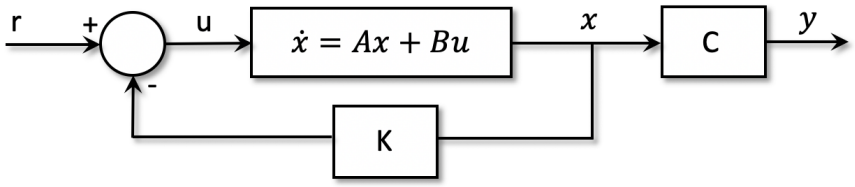

Fig. 6.11 Optimal Control Feedback Loop

The optimal feedback loop in Figure 6.11 can be redrawn into the form shown in Figure 6.12 which is completely equivalent. The closed loop can therefore be seen as a classical control loop with unity negative feedback around the section of the loop in the dashed box which is effectively a single-input-single-output system, the transfer function of which can be derived.

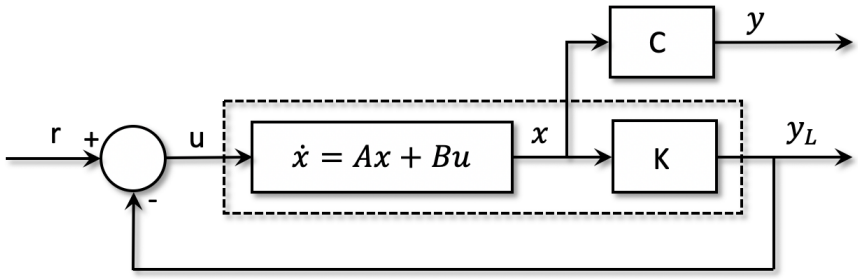

Fig. 6.12 Optimal Control Loop rearranged into a SISO with unity negative feedback

Using this form, classical control methods can be applied by treating the section of the loop in the dashed rectangle as a 'system' having unity negative feedback. This can be done because this system is a single-input single-output system, as required for classical control. The Nyquist diagram of the system can be plotted and the optimal controller's gain and phase margins can be deduced. In order to do this, the transfer function of this system, equal to the product of the frequency domain transfer functions of the 2 individual blocks, is required.

The Laplace Transform of the state space differential equation is taken, producing the following expression:

$$sX(s) = AX(s) + BU(s) \tag{6.103}$$

The expression is rearranged, producing the transfer function between X and U:

$$\frac{X(s)}{U(s)} = (sI - A)^{-1} B \tag{6.104}$$

This is a vector of transfer functions between each state and the input, with the vector length equal to the number of states in the system. In order to find the transfer function of the SISO system in the dashed box, the transfer function between the output of the loop Y_L and X is also needed:

$$\frac{Y_L(s)}{X(s)} = K \tag{6.105}$$

The transfer function of the system in the dashed rectangle is therefore:

$$\frac{Y(s)}{U(s)} = K(sI - A)^{-1} B \tag{6.106}$$

Since K has dimensions (1, N) and $(sI - A)^{-1} B$ has dimensions (N, 1), the transfer function of the whole 'system' $K(sI - A)^{-1} B$ has dimensions (1, 1). The optimal controller therefore behaves as a SISO, with a single transfer function, as required.

The Nyquist diagram of the system can be plotted by substituting $s = j\omega$:

$$W(j\omega) = K(j\omega I - A)^{-1} B \tag{6.107}$$

6.5.2 Robustness of LQR – Stability Margins

For a specific closed loop linearized system, the Nyquist plot can therefore be drawn, and from it, gain and phase margins can be obtained to quantify the system's robustness. Using known theory on LQR, lower bounds for the gain and phase margins of optimal feedback control system's in general can be derived.

In general, for any single input LQR system, the following inequality, which is known as the Return Difference Inequality and is derived from the Ricatti equation, holds:

$$|1 + K(j\omega I - A)^{-1} B| \geq 1 \tag{6.108}$$

This means that for any LQR closed loop system the plot of $K(j\omega I - A)^{-1}B$, and therefore the system's Nyquist plot, avoids a circle centered at $-1+0j$ that has a unit radius. This has a very important significance on the gain and phase margins of any LQR system.

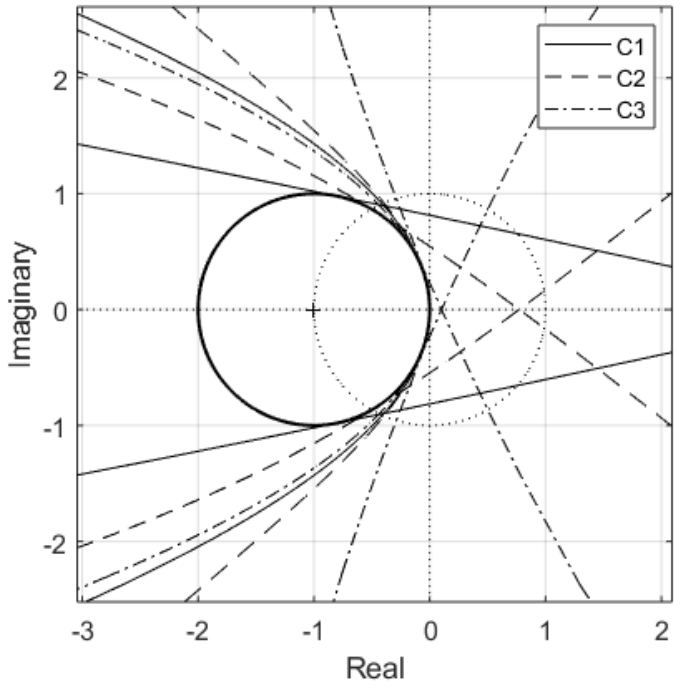

Fig. 6.13 Nyquist plots for a simplified model of a HATB with 3 feedback controllers of varying cost functions, C1-C3

Figure 6.13 shows the Nyquist plot of a simplified model of a HATB with different feedback gains, resulting from varying choices of the state and input weighting matrices, Q and R respectively. As expected for LQR control, whatever the selected values for the Q and R matrices are, the Nyquist plot never enters the critical circle.

Gain Margin Lower Bound for LQR systems

Since applying LQR control to a linearized system is known to result in the system's closed loop asymptotic stability, the number of counterclockwise encirclements of the $-1+0j$ point by the system's Nyquist plot must also necessarily be equal to the number of poles of the system's derived open loop transfer function $(K(j\omega I - A)^{-1}B)$ that are in the right half plane. Since the return difference inequality constrains the Nyquist plot from entering the unit circle of centre $-1+0j$, any point inside the circle has to have the same number of counterclockwise encirclements as the $-1+0j$ point itself.

The gain margin of a closed loop system is the amount by which the system's feedback gain can be changed before the system becomes unstable. If the gain is multiplied by some constant factor β, the system will maintain its asymptotic stability if the Nyquist plot of the altered transfer function $\beta K(j\omega I - A)^{-1}B$ has the same number of counterclockwise encirclements of $-1+0j$ as it has poles in the right hand plane. This is equivalent to number of times the original Nyquist plot encircles the point $-(1/\beta)+0j$ point in a counterclockwise direction. Since it has already been established that any point inside the unit circle of centre $-1+0j$ must have the same number of counterclockwise encirclements as the $-1+0j$ point, a range of stable values of β can be obtained that hold for any LQR system. The Return Difference inequality therefore guarantees stability for a the range of values of β that satisfy the following inequality:

$$-2 < -(1/\beta) < 0 \tag{6.109}$$

All LQR systems are therefore stable for $\beta > 1/2$.

Phase Margin Lower Bound for LQR systems

The phase margin of closed loop system is the amount of phase shift that would result in the system's loss of stability. In a Nyquist plot, this can be found from the amount of negative phase shift that would result in the $\omega > 0$ part of the Nyquist plot crossing the $-1+0j$ point. The points on the Nyquist plot of unity distance from the origin can be found by plotting a unit circle centred around the origin, and the minimum clockwise rotation required until the first of these reaches the $-1+0j$ would be the system's phase margin. Once again, the return difference inequality constrains the Nyquist plots of LQR systems in a way that places a lower bound on the phase margins of LQR systems. The minimum possible phase shift would be if a point on the $\omega > 0$ part of the plot of magnitude one were to lie on the critical circle in the 3$^{\text{rd}}$ quadrant of the graph since the Nyquist plot cannot go inside the circle. This point is marked in Figure 6.14 with a star. The minimum phase margin for an LQR system is therefore 60°.

Robustness of LQR – Tolerance to Time Delays

It is important to consider the system's sensitivity to time delays, as these are very likely to be present in real life situations. The Nyquist plot is also very useful as it allows us to calculate the maximum time delay tolerated by the linear closed loop system before losing stability. Time delays result in frequency-dependent negative phase shifts, altering the system's open loop transfer function to $K(j\omega I - A)^{-1}Be^{j\omega T}$ where T is the length of the time delay. Each point along the plot will preserve its magnitude, but shift clockwise by ωT radians. To

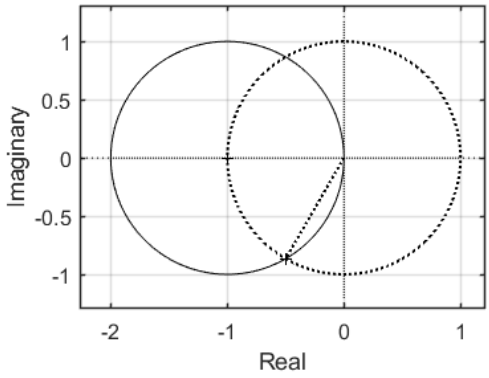

Fig. 6.14 Nyquist plot limits for LQR for the derivation of the phase margin lower bound

establish whether the system will remain stable for a certain time delay T, firstly all the points along the plot that have a magnitude of unity are located. Their respective phase shifts are calculated, $\omega_i T$. As long as the time delay induced phase shift of each point on the unit circle is smaller than the negative phase shift required to reach the $-1+0j$ point, ϕ_i, the closed loop system remains stable. The smallest time delay that would cause the system to lose stability can also be calculated as an upper limit to tolerable time delays for the feedback system. To do this, the values of ϕ_i/ω_i are calculated for all of the points on the plot that have unity magnitude, and the smallest value is selected.

Since no point can lie within the critical circle, the minimum value of ϕ_i is 60°. So, as long as the largest value of $\omega_i T$ is smaller than 60°, the system will remain stable. Therefore the time delay tolerance bound for LQR is $T < \pi/3\omega_{max}$ for points on the unit circle centered on the origin.

To summarize the above, using the return difference inequality, certain general bounds can be applied to the gain and phase margins and therefore the robustness of LQR controllers. These are tabulated below.

Table 6.4 Lower bounds for the maximum tolerable time delays for the different controllers deduced from the Nyquist plots

Parameter	Guaranteed Stability Range for LQR
Gain Factor	$1/2 < b < \infty$
Phase Shift	$\phi < \pi/3$
Time Delay	$T_d < \pi/3\omega_{max}$

Effects of Cost Parameter Selection on System Robustness

The lower bounds for the stability margins derived prove that LQR has good robustness properties in general. For specific systems, the actual values will depend on the choice of the quadratic weight matrices, Q and R as well as the system's parameters. The cost parameters should be selected based on the desired response of the system, i.e. stability and dynamic performance, as well as the robustness properties, i.e. the closed loop system's sensitivity to uncertainties and time delays. The effects of varying the cost function parameters on an LQR system's robustness are investigated in this section. The effects of the cost function selection on the system's stability margins is explored using the double inverted pendulum system as an example. This is because an open-loop unstable system would allow us to gain more insight into the effect of controller selection on robustness, while open-loop stable systems may have some infinite stability margins.

For the double inverted pendulum considered in Section 6.3.2, Nyquist diagrams are plotted and compared for 3 different controllers in Figure 6.15, designed based off of 3 different cost functions. The input costs as well as the state costs corresponding to the base displacement and velocity are kept at 1, and the remainder of the state costs are are changed for each controller. The state cost parameters of Controller 1 were given a uniform value of 100. Controller 2 was selected as a relatively cheap control system with state cost values of 500, and Controller 3 was selected as a relatively expensive control system with state cost values of 50. Figure 6.15 shows both the general shapes of the Nyquist plots as well as a closeup of the where the plots cross the unit circle centred about the origin as these are significant in determining the system's phase margin.

For all 3 controllers, beyond some factor β, the closed loop system can be seen to become unstable, as the Nyquist plot crosses the real axis counterclockwise twice. The location of the intersection, and therefore the minimum value of β varies between the controllers, and is therefore dependent on the selected cost function. These are determined and displayed in Table 6.5. It can be seen that, as the relative costs of the states increase (and the input cost decreases), there is a larger tolerance for reducing the magnitudes of the gain matrix. This makes sense, as, for a relatively low input cost and high state costs, the gain matrix produced using LQR will have larger entry magnitudes, since a larger control effort is allowed. Because of this, there is more room for error upon reducing these values.

The close-up of the Nyquist plots shows that the choice of cost parameters also has an impact on the phase margin. The phase margin appears to increase as the state costs increase (i.e. for cheaper control). The phase margins of the 3 controllers are displayed in Table 6.6.

The effect of the choice of cost parameters on the closed loop system's sensitivity to time delays is considered. From the close up of the Nyquist plots, it can be seen that the

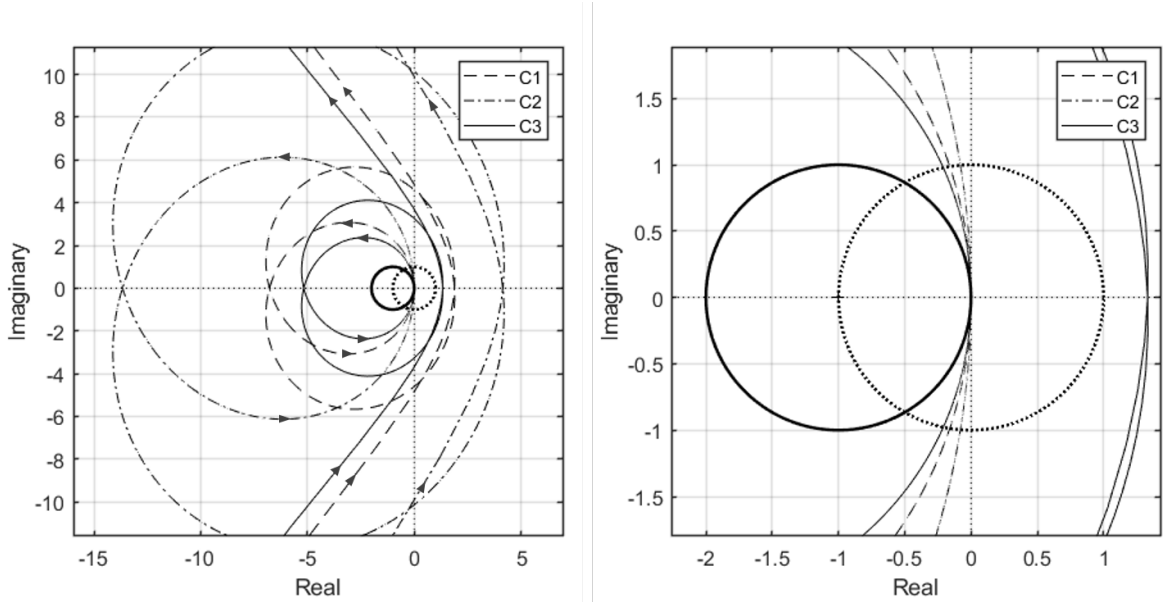

Fig. 6.15 Nyquist plots for closed loop double inverted pendulum systems using three controllers with different cost functions, C1-C3

Table 6.5 Lower bounds for the maximum tolerable time delays for the different controllers deduced from the Nyquist plots

Controller	Q_i/Q_1	x-intercept	β_{min}
1	1	-6.80	0.15
2	5	-13.65	0.07
3	0.5	-5.19	0.19

$\omega > 0$ section of each plot only crosses the unit circle centred around the origin once. The frequencies corresponding to these intersections are found for each of the closed loop systems. Using these, along with the negative phase shifts that would lead these points to the $-1+0j$ point (same as the phase margins in this case), an upper margin can be found for tolerable time delays for each of the closed loop systems. These are displayed in Table 6.6.

Table 6.6 Lower bounds for the maximum tolerable time delays for the different controllers deduced from the Nyquist plots

Controller	Q_i/Q_1	ω (rad/s)	ϕ (rad)	T_{max} (s)
1	1	160.7	1.41	0.009
2	5	324.5	1.49	0.005
3	0.5	122.2	1.36	0.010

As expected, longer time delays are tolerable for expensive control. In cheap control, the control effort is assigned a lower cost (and state errors a higher cost), which results in more energy being used in the system's stabilisation, both because its cheap to and because state errors now have a larger relative cost. This manifests as larger and faster inputs, which are therefore susceptible to bigger errors if a time delay is present. The more gradual inputs of an expensive control system are less affected by time delays due to their slower varying nature.

For the 2-element simple balloon model analysed in Section 6.4 with a cost function parameter of $q = 100$, the Nyquist plot is displayed in Figure 6.16. The sub-figure on the left shows a more general visual of the Nyquist plot, and the sub-figure on the right displays a close-up of the Nyquist plot close to the unit circle centred around $-1+0j$ for the deduction of the system's phase and time delay margins.

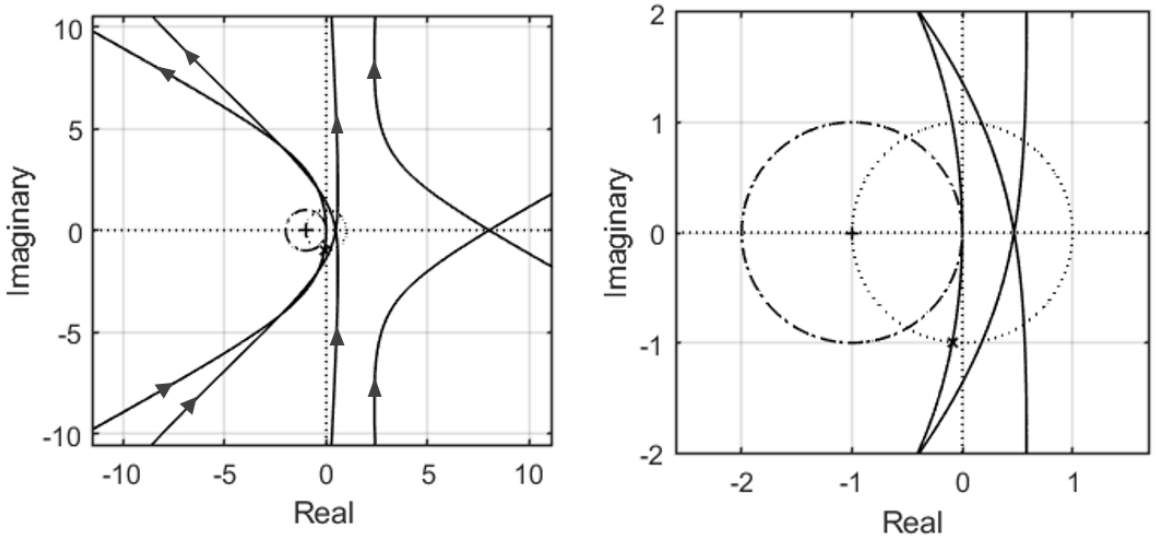

Fig. 6.16 Nyquist plots for closed loop simple balloon model using a controller with q=100

The Nyquist plot of this closed loop system is seen to never cross the negative real axis, which means that it has an infinite gain margin. This is expected, as the system is open loop stable and is therefore expected to remain stable as its feedback gain matrix decreases to zero.

For the phase margin, the point on the Nyquist plot that falls on the unit circle about the origin that would require the smallest negative phase shift to reach the $-1+0j$ point is marked on the right hand side diagram with a cross. The negative phase shift in question is found to have a value of 1.48 radians, which is therefore the system's phase margin.

This point turns out to also be relevant in the calculation of the system's maximum tolerable time delay, as, between the points that lay on the unit circle, it has the smallest

value of ϕ_i/ω_i. The frequency corresponding to the point is found to be $\omega = 116.3 rad/s$, making the maximum allowable time delay for the closed loop system equal to:

$$T_{max} = \left(\frac{\phi_i}{\omega_i}\right)_{min} = \frac{1.480}{116.3} = 0.0127s \tag{6.110}$$

Once again, the phase and time delay margins of the system are dependent on the choice of cost function used to design the controller in the same way as was shown for the double inverted pendulum system. The gain margin is independent of the selected cost function, and is infinite regardless for an open-loop stable system.

The benefits of LQR control have been studied for simplified system models and the effects of the cost function selection on the system's response and robustness have been determined. The same methods of producing a suitable feedback controller for the system can be applied to the HATB which is effectively an extension of the models studied. The methods of deducing the system's state space form that were used are tedious however, and for 3-dimensional systems with many tether elements, deriving these is very computationally demanding. To avoid applying these tedious methods for much more complex cable systems, general expressions for the entries of the mass, stiffness and damping matrices are derived in the next section, allowing the linearized second order matrix ODE to be computed directly for any cable or tethered balloon system.

Chapter 7

Full-Scale Tethered Balloon System Model Linearization

With both the force and energy methods of deriving the mass and stiffness matrices being so computationally complex and therefore requiring a running time that is not feasible for large scale systems with thousands of elements, a method of linearizing the system directly by substituting its parameters into matrix entry expressions is developed. This is done through the observation of patterns in the system's energy equations. This was found to produce identical mass and stiffness matrices to the methods described previously in a hugely reduced computational time.

This section includes a detailed analysis of the derivation of the entries of the mass and stiffness matrices for both a 2-dimensional and 3-dimensional tethered balloon system model. The method for the 2-dimensional model is included for its relative clarity, but can be skipped as it is a simplified version of the 3-dimensional model derivation.

7.1 Derivation of Mass Matrix for 2D Extensible Model

Since the system is linearized for small motion about its equilibrium position, the angular deviations of the elements as well as their extensions are assumed to be small and are used as generalized coordinates. For a 2-dimensional system, this includes the angular deviation from the equilibrium of each element, u_j and the deviation from the element's equilibrium length, v_j.

In order to derive the mass matrix of the system using energy methods, an expression for the system's total kinetic energy must be derived. In order to do this, the absolute velocities of every element in the system that has mass need to be found.

Figure 7.1 shows the respective velocities relative to the system's base of each of the lumped masses as sums of vector components. The velocity of the j*th* element will be equal to the sum of the velocity of the (j-1)*th* element and the relative velocity between the two elements. For an inextensible tether model the relative velocity is solely due to the rotation of the link connecting the two masses, whereas for an extensible model there is an added axial velocity due to the extension of the link. In the extensible cable case, each element has 2 degrees of freedom rather than one, and the mass matrix has dimensions $2N+1 \times 2N+1$ including the coordinate that defines the position of the base.

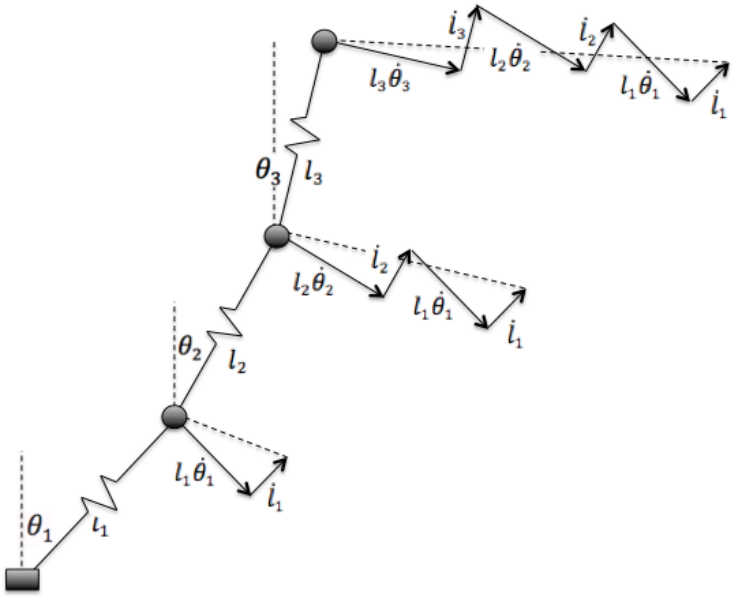

Fig. 7.1 Diagram showing the velocity components of the extensible cable elements for 2-dimensional motion

Figure 7.2 shows a close-up of the velocity components of the second element in the system as well as the horizontal components of each of these, to illustrate the way in which the elements' absolute velocity is resolved into Cartesian components.

For a stationary base, the component of the element's velocity in the x-direction is therefore:

$$\dot{x}_2 = l_2\dot{\theta}_2\cos\theta_2 + l_1\dot{\theta}_1\cos\theta_1 + \dot{l}_2\sin\theta_2 + \dot{l}_1\sin\theta_1 \tag{7.1}$$

In the remainder of this section it is assumed that the base can move horizontally to avoid the loss of generality and to allow for the introduction of feedback control using base motion as an input. Incorporating base motion results in an additional horizontal velocity component for each element, equal to the velocity of the base. For an arbitrary jth element, the velocities

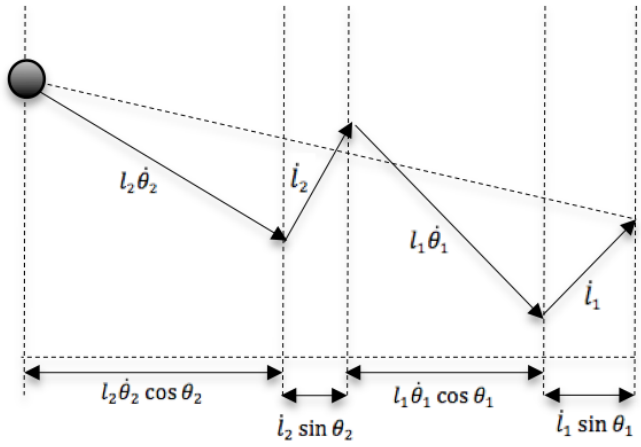

Fig. 7.2 Velocity diagram of the 2nd element

in the horizontal and vertical directions take the following form:

$$\dot{x}_j = \dot{x}_0 + l_1\dot{\theta}_1\cos\theta_1 + l_2\dot{\theta}_2\cos\theta_2 \ldots + l_j\dot{\theta}_j\cos\theta_j + \dot{l}_1\sin\theta_1 + \dot{l}_2\sin\theta_2 \ldots + \dot{l}_j\sin\theta_j \quad (7.2)$$

$$\dot{y}_j = -\left(l_1\dot{\theta}_1\sin\theta_1 + l_2\dot{\theta}_2\sin\theta_2 \ldots + l_j\dot{\theta}_j\sin\theta_j\right) + \dot{l}_1\cos\theta_1 + \dot{l}_2\cos\theta_2 \ldots + \dot{l}_j\cos\theta_j \quad (7.3)$$

Here, $\dot{x}_0$ is the velocity of the base of the tethered balloon system. The vertical velocity of the base $\dot{y}_0$ is zero as the base is constrained to moving in the horizontal plane, and will therefore not be included in calculations. For a system with a stationary base, $\dot{x}_0$ can be set to zero.

The kinetic energy of the jth element is therefore equal to:

$$\begin{aligned} T_j &= \frac{1}{2}m\left(\dot{x}_j^2 + \dot{y}_j^2\right) \\ &= \frac{1}{2}m\Big[\left(\dot{x}_0 + l_1\dot{\theta}_1\cos\theta_1 + l_2\dot{\theta}_2\cos\theta_2 \ldots + l_j\dot{\theta}_j\cos\theta_j + \dot{l}_1\sin\theta_1 + \dot{l}_2\sin\theta_2 \ldots + \dot{l}_j\sin\theta_j\right)^2 \\ &\quad + \left(-\left(l_1\dot{\theta}_1\sin\theta_1 + l_2\dot{\theta}_2\sin\theta_2 \ldots + l_j\dot{\theta}_j\sin\theta_j\right) + \dot{l}_1\cos\theta_1 + \dot{l}_2\cos\theta_2 \ldots + \dot{l}_j\cos\theta_j\right)^2\Big] \end{aligned} \quad (7.4)$$

Multiplying this out and collecting like terms gives:

$$\begin{aligned}T_i = \frac{1}{2}m_i\Big(& l_1^2\dot{\theta}_1^2\left(\cos^2\theta_1+\sin^2\theta_1\right)+l_2^2\dot{\theta}_2^2\left(\cos^2\theta_2+\sin^2\theta_2\right)\ldots+l_i^2\dot{\theta}_i^2\left(\cos^2\theta_i+\sin^2\theta_i\right)\\ & +\dot{l}_1^2\left(\cos^2\theta_1+\sin^2\theta_1\right)+\dot{l}_2^2\left(\cos^2\theta_2+\sin^2\theta_2\right)\ldots+\dot{l}_i^2\left(\cos^2\theta_i+\sin^2\theta_i\right)\\ & +2l_1l_2\dot{\theta}_1\dot{\theta}_2\left(\cos\theta_1\cos\theta_2+\sin\theta_1\sin\theta_2\right)\ldots\\ & +2l_{i-1}l_i\dot{\theta}_{i-1}\dot{\theta}_i\left(\cos\theta_{i-1}\cos\theta_i+\sin\theta_{i-1}\sin\theta_i\right)+2\dot{l}_1\dot{l}_2\left(\cos\theta_1\cos\theta_2+\sin\theta_1\sin\theta_2\right)\\ & \ldots+2\dot{l}_{i-1}\dot{l}_i\left(\cos\theta_{i-1}\cos\theta_i+\sin\theta_{i-1}\sin\theta_i\right)+2\dot{l}_1l_2\dot{\theta}_2\left(\sin\theta_1\cos\theta_2-\cos\theta_1\sin\theta_2\right)\\ & +2\dot{l}_2l_1\dot{\theta}_1\left(\sin\theta_2\cos\theta_1-\cos\theta_2\sin\theta_1\right)\ldots+2\dot{l}_{i-1}l_i\dot{\theta}_i\left(\sin\theta_{i-1}\cos\theta_i-\cos\theta_{i-1}\sin\theta_i\right)\\ & +\dot{x}_0^2+2\dot{x}_0l_1\dot{\theta}_1\cos\theta_1+2\dot{x}_0l_2\dot{\theta}_2\cos\theta_2\ldots+2\dot{x}_0l_i\dot{\theta}_i\cos\theta_i\\ & +2\dot{x}_0\dot{l}_1\sin\theta_1+2\dot{x}_0\dot{l}_2\sin\theta_2\ldots+2\dot{x}_0\dot{l}_i\sin\theta_i\Big)\end{aligned} \tag{7.5}$$

Trigonometric identities can be applied to simplify the expression. In order to linearize the system, the kinetic energy expression needs to be altered such that it is expressed in terms of the system's generalised coordinates, which are the small deviations from the system's equilibrium state. Substituting $l_j = l_{0,j} + v_j$ and $\theta_j = \theta_{0,j} + u_j$ and eliminating small terms as appropriate results in the following expression:

$$\begin{aligned}T_i = & \frac{1}{2}m_i\Big(l_{0,1}^2\dot{u}_1^2+l_{0,2}^2\dot{u}_2^2\ldots+l_{0,i}^2\dot{u}_i^2+\dot{v}_1^2+\dot{v}_2^2\ldots+\dot{v}_i^2+\dot{x}_0^2+2l_{0,1}l_{0,2}\dot{u}_1\dot{u}_2\cos\left(\theta_{0,1}-\theta_{0,2}\right)\ldots\\ & +2l_{0,i-1}l_{0,i}\dot{u}_{i-1}\dot{u}_i\cos\left(\theta_{0,i-1}-\theta_{0,i}\right)+2\dot{v}_1\dot{v}_2\cos\left(\theta_{0,1}-\theta_{0,2}\right)\ldots\\ & +2\dot{v}_{i-1}\dot{v}_i\cos\left(\theta_{0,i-1}-\theta_{0,i}\right)+2\dot{v}_1l_{0,2}\dot{u}_2\sin\left(\theta_{0,1}-\theta_{0,2}\right)+2\dot{v}_2l_{0,1}\dot{u}_1\sin\left(\theta_{0,2}-\theta_{0,1}\right)\ldots\\ & +2\dot{v}_{i-1}l_{0,i}\dot{u}_i\sin\left(\theta_{0,i-1}-\theta_{0,i}\right)+2\dot{x}_0l_{0,1}\dot{u}_1\cos\theta_{0,1}+2\dot{x}_0l_{0,2}\dot{u}_2\cos\theta_{0,2}\ldots\\ & +2\dot{x}_0l_{0,i}\dot{u}_i\cos\theta_{0,i}+2\dot{x}_0\dot{v}_1\sin\theta_{0,1}+2\dot{x}_0\dot{v}_2\sin\theta_{0,2}\ldots+2\dot{x}_0\dot{v}_i\sin\theta_{0,i}\Big)\end{aligned} \tag{7.6}$$

An expression for the system's total kinetic energy can be derived in summation form and simplified by identifying terms that are common to the kinetic energies of multiple elements. The total kinetic energy of the system is therefore:

$$
\begin{aligned}
T_{tot} &= \frac{1}{2} m_{base} \dot{x}_0^2 + \frac{1}{2} \left((N-i)\, m + m_b \right) \dot{x}_0^2 \\
&+ \frac{1}{2} \sum_{i=1}^{N} \Bigg(\left((N-i)\, m + m_b \right) \left(l_{0,i}^2 \dot{u}_i^2 + \dot{v}_i^2 + 2\dot{x}_0 l_{0,i} \dot{u}_i \cos\theta_{0,i} + 2\dot{x}_0 \dot{v}_i \sin\theta_{0,i} \right) \\
&+ \sum_{j=1, j\neq i}^{N} \left[\left((N-i)\, m + m_b \right) \left(\left(l_{0,i} l_{0,j} \dot{u}_i \dot{u}_j + \dot{v}_i \dot{v}_j \right) \cos(\theta_{0,i} - \theta_{0,j}) + \dot{v}_i l_{0,j} \dot{u}_j \sin(\theta_{0,i} - \theta_{0,j}) \right) \right] \Bigg)
\end{aligned}
\tag{7.7}
$$

Here, m_{base} is the mass of the system's base, m is the mass of each discretized element, and m_b is the mass of the balloon. From this linearized expression, the system's mass matrix can be deduced by applying th appropriate double partial derivatives for the matrix entries. For the case where the base is fixed, $\dot{x}_0$ can be set to zero and the mass matrix M of the system $(2N \times 2N)$ can be thought of as containing four different sub-matrices, each of which has dimensions $N \times N$ and can be calculated separately using double partial differentiations.

$$
M = \begin{bmatrix} M_1 & M_2 \\ M_3 & M_4 \end{bmatrix} \tag{7.8}
$$

The first matrix M_1 involves the partial differentiation of the potential energy equation with respect to two of the angular deviations only, M_4 with respect to two extensions only, and the other two matrices are differentiated with respect to one of each.

$$
M_1(i,j) = \frac{\partial^2 T_{TOT}}{\partial \dot{u}_i \partial \dot{u}_j} \qquad M_2(i,j) = M_3^T(i,j) = \frac{\partial^2 T_{TOT}}{\partial \dot{u}_i \partial \dot{v}_j} \qquad M_4(i,j) = \frac{\partial^2 T_{TOT}}{\partial \dot{v}_i \partial \dot{v}_j} \tag{7.9}
$$

Through careful inspection of the kinetic energy equation, the following set of equations are deduced, from which the entries of the four sub-matrices of the mass matrix can be found directly. The mass matrix of a 2-dimensional tethered balloon system under any steady-state

external conditions can therefore be obtained directly using the following expressions:

$$M_1(i,j)_{i=j} = l_{0,i}^2((N-i)m+m_b) \tag{7.10}$$

$$M_1(i,j)_{i\neq j} = l_{0,i}l_{0,j}((N-i)m+m_b)\cos\left(\theta_{0i}-\theta_{0j}\right) \tag{7.11}$$

$$M_4(i,j)_{i=j} = ((N-i)m+m_b) \tag{7.12}$$

$$M_4(i,j)_{i\neq j} = ((N-i)m+m_b)\cos\left(\theta_{0i}-\theta_{0j}\right) \tag{7.13}$$

$$M_2(i,j)_{i=j} = M_3(i,j)_{i=j} = 0 \tag{7.14}$$

$$M_2(i,j)_{i\neq j} = M_3(j,i)_{i\neq j} = l_{0,i}((N-j)m+m_b)\sin\left(\theta_{0,j}-\theta_{0,i}\right) \tag{7.15}$$

For the case where the base is able to move in the horizontal direction, there is an additional degree of freedom, x_0, and so the mass matrix will have an additional row and column and its dimensions will now be $2N+1\times 2N+1$. Taking the base displacement as the first degree of freedom in the vector, the additional first row can be thought of as having 3 1-Dimensional matrix components:

$$M' = \begin{bmatrix} M_1' & M_2' & M_3' \end{bmatrix} \tag{7.16}$$

The first matrix has dimensions 1×1, and the second and third matrices have dimensions $1\times N$, making the row length $2N+1$ as required. Applying the relevant double derivatives, the new first row of the mass matrix will contain the following components:

$$M_1'(1,1) = \frac{\partial^2 T_{TOT}}{\partial \dot{x}_0^2} = (N-1)m+m_b+m_{base} \tag{7.17}$$

$$M_2'(1,j) = \frac{\partial^2 T_{TOT}}{\partial \dot{x}_0 \partial \dot{u}_j} = ((N-j)m+m_b)\,l_{0,j}\cos\theta_{0,j} \tag{7.18}$$

$$M_3'(1,j) = \frac{\partial^2 T_{TOT}}{\partial \dot{x}_0 \partial \dot{v}_j} = ((N-j)m+m_b)\sin\theta_{0,j} \tag{7.19}$$

Since the mass matrix is symmetric, the additional column at the front of the matrix will be the transverse of this row. The remainder of the matrix will remain unchanged.

For vibrations in the θ direction only, i.e. axial vibrations can be neglected, the kinetic energy equation collapses to the following expression and the same procedure can be

followed.

$$\begin{aligned} T_{tot} = \frac{1}{2} m_{base} \dot{x}_0^2 + \frac{1}{2} \left((N-i)\, m + m_b \right) \dot{x}_0^2 \\ + \frac{1}{2} \sum_{i=1}^{N} \Bigg(\left((N-i)\, m + m_b \right) \left(l_{0,i}^2 \dot{u}_i^2 + 2 \dot{x}_0 l_{0,i} \dot{u}_i \cos\theta_{0,i} \right) \\ + \sum_{j=1, j\neq i}^{N} \left[\left((N-i)\, m + m_b \right) \left(\left(l_{0,i} l_{0,j} \dot{u}_i \dot{u}_j \right) \cos(\theta_{0,i} - \theta_{0,j}) \right) \right] \Bigg) \end{aligned} \tag{7.20}$$

7.2 Derivation of Stiffness Matrix for 2D Extensible Model

While calculating the stiffness matrix is relatively computationally fast compared to the mass matrix (the sub-matrices are diagonal matrices, meaning only 4N matrix values are non-zero and need to be found, as opposed to $4N^2$ in the mass matrix), for a system where the number of elements is of the order of 1000, it is still largely time consuming to evaluate the potential energy equation of the system and execute two partial differentiations for each matrix entry. As before, this method uses energy analysis methods to decipher a pattern in the individual elements' potential energies and therefore derive simplified expressions for the entries of the stiffness matrix, to hugely improve the computational complexity of producing a linearized version of the model.

In order to obtain expressions for the entries of the system's stiffness matrix, an expression for the system's total potential energy must be derived. Figure 7.3 displays the first few elements of the tether, assuming a stationary base at the origin.

General expressions for the heights and horizontal distances relative to the tether's base are derived in terms of the elements' angles from the vertical, θ_j and their instantaneous lengths, l_j.

$$y_j = l_1 \cos\theta_1 + l_2 \cos\theta_2 \ldots + l_j \cos\theta_j \tag{7.21}$$

$$x_j = l_1 \sin\theta_1 + l_2 \sin\theta_2 \ldots + l_j \sin\theta_j \tag{7.22}$$

For the case of a moving base, these are added to the nonzero coordinates of the base to obtain the elements' absolute coordinates. The vertical coordinate of the jth element remains unchanged, while the horizontal coordinate becomes:

$$x_j = x_0 + l_1 \sin\theta_1 + l_2 \sin\theta_2 \ldots + l_j \sin\theta_j \tag{7.23}$$

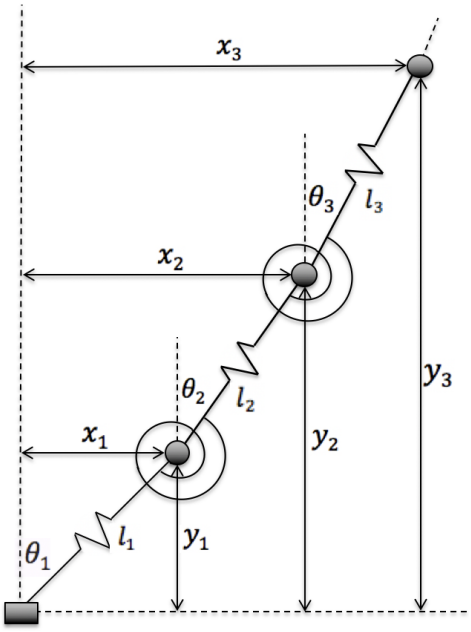

Fig. 7.3 Diagram of extensible tether model

A moving base is assumed in the derivation of the total potential energy equation of the system to avoid the loss of generality.

In this section, the external forces acting on the system's elements are assumed to be approximately constant for small amplitude motion (these vary with altitude and altitude variations are assumed to be small) and are accounted for in the potential energy equation. The potential energy equation of an arbitrary *j*th element therefore includes components due to the gravitational potential energy, the remainder of the constant external forces, and the elastic potential energy due to the axial and rotational springs. The potential energy of an arbitrary jth element is therefore:

$$\begin{aligned} V_j =& (mg - F_{y,j}) y_j - F_{x,j} x_j + \frac{1}{2} k \left(l_j - L_j\right)^2 + \frac{1}{2} k_b \left(\theta_{j+1} - \theta_j\right)^2 \\ =& (mg - F_{y,j}) \left(l_1 \cos\theta_1 + l_2 \cos\theta_2 \ldots + l_j \cos\theta_j\right) \\ & - F_{x,j} \left(x_0 + l_1 \sin\theta_1 + l_2 \sin\theta_2 \ldots + l_j \sin\theta_j\right) + \frac{1}{2} k \left(l_j - L_j\right)^2 + \frac{1}{2} k_b \left(\theta_{j+1} - \theta_j\right)^2 \end{aligned} \tag{7.24}$$

Here, L_j is the unstretched length of the jth element; this is different to the equilibrium length of the element, $l_{0,j}$, as the element may be stretched under equilibrium conditions. As in the previous case, a simplified expression of the total potential energy of the system can found by observing the patterns in the individual potential energies of the elements.

The potential energy of the final element, i.e. the balloon, will take a slightly different form since the forces acting on it as well as its 'element' length (which in this case is the radius of the balloon) will be different.

The total potential energy of the system is the sum of the potential energies of all of the system's elements. By observing patterns in the individual potential energies of the elements (e.g. the $mgl_1 \cos\theta_1$ term can be seen to appear in all but one, i.e. $N-1$ expressions), a simplified expression for the potential energy can be written as:

$$\begin{aligned} V_{TOT} =& \frac{1}{2}k_b\left(\theta_2-\theta_1\right)^2+\frac{1}{2}k_b\left(\theta_3-\theta_2\right)^2\ldots+\frac{1}{2}k_{b,bal}\left(\theta_N-\theta_{N-1}\right)^2 \\ &+\frac{1}{2}k\left(l_1-L\right)^2+\frac{1}{2}k\left(l_2-L\right)^2\ldots+\frac{1}{2}k_N\left(l_N-L_N\right)^2 \\ &+l_1\cos\theta_1\left(mg(N-1)+m_bg-F_{y,1}-F_{y,2}\ldots-F_{y,N}-F_{lift}\right) \\ &+l_2\cos\theta_2\left(mg(N-2)+m_bg-F_{y,2}\ldots-F_{y,N}-F_{lift}\right)\ldots \\ &+l_N\cos\theta_N\left(m_bg-F_{y,N}-F_{lift}\right)-l_1\sin\theta_1\left(F_{x,1}+F_{x,2}\ldots+F_{x,N}\right) \\ &-l_2\sin\theta_2\left(F_{x,2}\ldots+F_{x,N}\right)\ldots-l_N\sin\theta_NF_{x,N}-x_0\left(F_{x,1}+F_{x,2}\ldots+F_{x,N}\right) \end{aligned} \tag{7.25}$$

Since the absolute angle from the vertical of each element is equal to its equilibrium angle (a constant) summed to a small angular deviation from the equilibrium, i.e. $\theta_j=\theta_{0,j}+u_j$, the following substitutions can be made using trigonometric identities:

$$\cos\theta_j=\cos\left(\theta_{0,j}+u_j\right)=\cos\theta_{0,j}\cos u_j-\sin\theta_{0,j}\sin u_j \tag{7.26}$$

$$\sin\theta_j=\sin\left(\theta_{0,j}+u_j\right)=\sin\theta_{0,j}\cos u_j+\sin u_j\cos\theta_{0,j} \tag{7.27}$$

Applying small angle approximations to these results in the following expressions:

$$\cos\theta_j=\left(1-\frac{1}{2}u_j^2\right)\cos\theta_{0,j}-u_j\sin\theta_{0,j} \tag{7.28}$$

$$\sin\theta_j=\left(1-\frac{1}{2}u_j^2\right)\sin\theta_{0,j}+u_j\cos\theta_{0,j} \tag{7.29}$$

Making these substitutions along with $l_j=l_{0,j}+v_j$ and putting the expression into summation form produces the following expression for the linearized total potential energy

of the system for small amplitude motion about its equilibrium state:

$$V_{TOT} = \sum_{j=1}^{N} \Bigg(((1 - \frac{1}{2}u_j^2)\cos\theta_{0,j} - u_j \sin\theta_{0,j}) \left(l_{0,j} + v_j\right) \left((mg - F_{V,j})(N-j) + m_b g - F_{lift}\right) \\ - ((1 - \frac{1}{2}u_j^2)\sin\theta_{0,j} + u_j \cos\theta_{0,j}) \left(l_{0,j} + v_j\right) \left(F_j + F_{j+1} \ldots + F_N\right) \\ + \frac{1}{2}k\left(v_j + l_{0,j} - L_j\right)^2 + \frac{1}{2}k_b\left(\theta_{0,j+1} + u_{j+1} - \theta_{0,j} - u_j\right)^2 \Bigg) - x_0\left(F_1 + F_2 \ldots + F_N\right) \tag{7.30}$$

The entries of the stiffness matrix can be found by partially differentiating the potential energy equation twice, with respect to the two generalized coordinates corresponding to the row and column of the matrix. In multiplying out the above equation, any terms containing the product of more than two small terms (us and vs) are eliminated, as they are relatively small compared to the other terms. For the case where the base is stationary, the stiffness matrix of the system can be thought of as containing four different matrices, each of which has dimensions $N \times N$ and can be calculated separately using double partial differentiations.

$$K = \begin{bmatrix} K_1 & K_2 \\ K_3 & K_4 \end{bmatrix} \tag{7.31}$$

The first matrix K_1 involves the partial differentiation of the potential energy equation with respect to two of the angular deviations only, K_4 with respect to two extensions only, and the other two matrices are differentiated with respect to one of each.

$$K_1(i,j) = \frac{\partial^2 V_{TOT}}{\partial u_i \partial u_j} \qquad K_2(i,j) = K_3^T(i,j) = \frac{\partial^2 V_{TOT}}{\partial u_i \partial v_j} \qquad K_4(i,j) = \frac{\partial^2 V_{TOT}}{\partial v_i \partial v_j} \tag{7.32}$$

While the matrix K is not a diagonal matrix, it is found that each sub-matrix is actually a diagonal matrix. The non-zero entries along the diagonals of each sub-matrix can be found by the following general equations, again found by spotting clear patterns in the results of the double partial differentiations:

$$K_1(i,j)_{i=j,i=1,N} = -l_{0,i}\left((mg - F_{V,i})(N-i) + m_b g - F_{lift}\right)\cos\theta_{0,i} \\ + l_{0,i}\left(F_i + F_{i+1} \ldots + F_N\right)\sin\theta_{0,i} + k_b \tag{7.33}$$

$$K_1(i,j)_{i=j,i=2:N-1} = -l_{0,i}\left((mg - F_{V,i})(N-i) + m_b g - F_{lift}\right)\cos\theta_{0,i} \\ + l_{0,i}\left(F_i + F_{i+1} \ldots + F_N\right)\sin\theta_{0,i} + 2k_b \tag{7.34}$$

$$K_1(i,j)_{i=j+1,j-1} = -k_b \tag{7.35}$$

$$\begin{aligned} K_2(i,j)_{i=j} = K_3(i,j)_{i=j} = &-\left((mg - F_{V,i})(N-i) + m_b g - F_{lift}\right)\sin\theta_{0,i} \\ &-(F_i + F_{i+1} \ldots + F_N)\cos\theta_{0,i} \end{aligned} \tag{7.36}$$

$$K_4(i,j)_{i=j,\ i<N} = k \quad K_4(i,j)_{i=j,i=N} = k_{bal} \tag{7.37}$$

$$K_1(i,j)_{i\neq j} = K_2(i,j)_{i\neq j} = K_3(i,j)_{i\neq j} = K_4(i,j)_{i\neq j} = 0 \tag{7.38}$$

For the case where the base is allowed to move in the horizontal direction, i.e. x_0 is not equal to zero, the system has an additional degree of freedom, so the stiffness matrix dimensions will increase from $2N \times 2N$ to $2N+1 \times 2N+1$. The additional row can be thought of as containing 3 matrices, as in the mass matrix.

$$K' = \begin{bmatrix} K'_1 & K'_2 & K'_3 \end{bmatrix} \tag{7.39}$$

Similarly to the mass matrix, the first matrix has dimensions 1×1, and the second and third matrices have dimensions $1 \times N$, making the row length $2N+1$ as required.

However, it can be seen from the potential energy equation that the terms containing the x_0 coordinate only contain this coordinate, and none of them contain its square. This means that these terms will disappear for any and all of the double derivatives relevant to this coordinate. The additional row and column of the stiffness matrix will therefore only contain zeros.

$$K'_1(1,1) = \frac{\partial^2 V_{TOT}}{\partial x_0^2} = 0 \quad K'_2(1,j) = \frac{\partial^2 V_{TOT}}{\partial x_0 \partial u_j} = 0 \quad K'_3(1,j) = \frac{\partial^2 V_{TOT}}{\partial x_0 \partial v_j} = 0 \tag{7.40}$$

7.3 Derivation of Mass Matrix for 3D Extensible Model

This method was expanded to 3 dimensions to allow for the out-of-plane motion of the tether and balloon. Although in reality the equilibrium position of the tethered balloon system is likely to be planar, to avoid the loss of generality, the equilibrium Euler angle ϕ of each element is taken as being arbitrary. Practically this may occur because of the possible variation of wind direction along the tether, or because of some other external forces acting on the system. Upon the addition of the Euler angle ϕ to define the 3-dimensional position of each element, the number of degrees of freedom of the system now increases to 2N for the inextensible tether model (θ, ϕ) and 3N for the extensible model (θ, ϕ, l).

Figure 7.4 shows a diagram of the two tether elements in arbitrary 3-dimensional space.

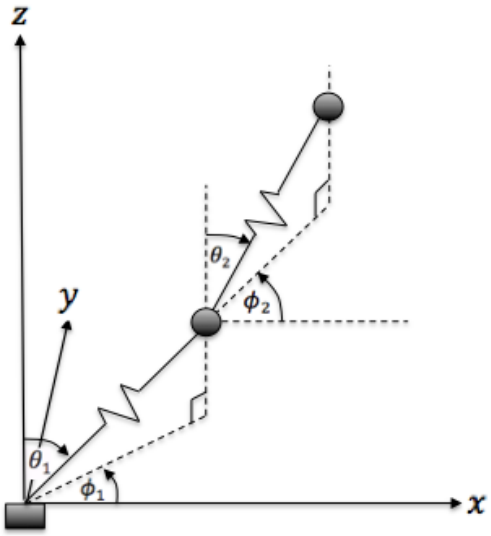

Fig. 7.4 Diagram of 3D Extensible Tether Model

The coordinates of the tether's elements can be found by resolving the links into the 3 Cartesian directions. General expressions for the coordinates of an arbitrary jth element are derived:

$$x_j = x_0 + l_1 \sin\theta_1 \cos\phi_1 + l_2 \sin\theta_2 \cos\phi_2 \ldots + l_j \sin\theta_j \cos\phi_j \tag{7.41}$$

$$y_j = y_0 + l_1 \sin\theta_1 \sin\phi_1 + l_2 \sin\theta_2 \sin\phi_2 \ldots + l_j \sin\theta_j \sin\phi_j \tag{7.42}$$

$$z_j = l_1 \cos\theta_1 + l_2 \cos\theta_2 \ldots + l_j \cos\theta_j \tag{7.43}$$

In order to compute the kinetic energy of an arbitrary element along the tether, its absolute velocity vector is required. To avoid the more complex vector diagrams of the 3-dimensional velocity components, equations 7.41-7.43 can be differentiated to produce expressions for the velocity components in the x, y and z directions of an arbitrary element j.

$$\begin{aligned}\dot{x}_j =& \dot{x}_0 + \dot{l}_1 \sin\theta_1 \cos\phi_1 + l_1\dot{\theta}_1 \cos\theta_1 \cos\phi_1 - l_1\dot{\phi}_1 \sin\theta_1 \sin\phi_1 + \dot{l}_2 \sin\theta_2 \cos\phi_2 \\ &+ l_2\dot{\theta}_2 \cos\theta_2 \cos\phi_2 - l_2\dot{\phi}_2 \sin\theta_2 \sin\phi_2 \ldots + \dot{l}_j \sin\theta_j \cos\phi_j + l_j\dot{\theta}_j \cos\theta_j \cos\phi_j \\ &- l_j\dot{\phi}_j \sin\theta_j \sin\phi_j\end{aligned} \tag{7.44}$$

$$\begin{aligned}\dot{y}_j =& \dot{y}_0 + \dot{l}_1 \sin\theta_1 \sin\phi_1 + l_1\dot{\theta}_1 \cos\theta_1 \sin\phi_1 + l_1\dot{\phi}_1 \sin\theta_1 \cos\phi_1 + \dot{l}_2 \sin\theta_2 \sin\phi_2 \\ &+ l_2\dot{\theta}_2 \cos\theta_2 \sin\phi_2 + l_2\dot{\phi}_2 \sin\theta_2 \cos\phi_2 \ldots + \dot{l}_j \sin\theta_j \sin\phi_j + l_j\dot{\theta}_j \cos\theta_j \sin\phi_j \\ &+ l_j\dot{\phi}_j \sin\theta_j \cos\phi_j\end{aligned} \tag{7.45}$$

$$\dot{z}_j = \dot{l}_1 \cos\theta_1 - l_1\dot{\theta}_1 \sin\theta_1 + \dot{l}_2 \cos\theta_2 - l_2\dot{\theta}_2 \sin\theta_2 \ldots + \dot{l}_j \cos\theta_j - l_j\dot{\theta}_j \sin\theta_j \tag{7.46}$$

The system's kinetic energy consists of the sum of the kinetic energies of all of the individual elements in the system. This includes the tether elements, the balloon, and the base. The kinetic energy of an arbitrary tether element can be found using the its absolute velocity components that were derived above.

$$\begin{aligned}
T_j &= \frac{1}{2}m\left(\dot{x}_j^2+\dot{y}_j^2+\dot{z}_j^2\right)\\
&= \frac{1}{2}m\big[\big(\dot{x}_0+\dot{l}_1\sin\theta_1\cos\phi_1+l_1\dot{\theta}_1\cos\theta_1\cos\phi_1-l_1\dot{\phi}_1\sin\theta_1\sin\phi_1+\dot{l}_2\sin\theta_2\cos\phi_2\\
&\quad+l_2\dot{\theta}_2\cos\theta_2\cos\phi_2-l_2\dot{\phi}_2\sin\theta_2\sin\phi_2\ldots+\dot{l}_j\sin\theta_j\cos\phi_j+l_j\dot{\theta}_j\cos\theta_j\cos\phi_j\\
&\quad-l_j\dot{\phi}_j\sin\theta_j\sin\phi_j\big)^2+\big(\dot{y}_0+\dot{l}_1\sin\theta_1\sin\phi_1+l_1\dot{\theta}_1\cos\theta_1\sin\phi_1+l_1\dot{\phi}_1\sin\theta_1\cos\phi_1\\
&\quad+\dot{l}_2\sin\theta_2\sin\phi_2+l_2\dot{\theta}_2\cos\theta_2\sin\phi_2+l_2\dot{\phi}_2\sin\theta_2\cos\phi_2\ldots+\dot{l}_j\sin\theta_j\sin\phi_j\\
&\quad+l_j\dot{\theta}_j\cos\theta_j\sin\phi_j+l_j\dot{\phi}_j\sin\theta_j\cos\phi_j\big)^2+\big(\dot{l}_1\cos\theta_1-l_1\dot{\theta}_1\sin\theta_1+\dot{l}_2\cos\theta_2\\
&\quad-l_2\dot{\theta}_2\sin\theta_2\ldots+\dot{l}_j\cos\theta_j-l_j\dot{\theta}_j\sin\theta_j\big)^2\big]
\end{aligned} \tag{7.47}$$

Upon multiplying out the brackets, collecting like terms and applying trigonometric identities to simplify, the expression for the kinetic energy of the jth element becomes:

$$
\begin{aligned}
T_j = &\frac{1}{2} m_i \left(\dot{x}_0^2 + \dot{y}_0^2 + \dot{l}_1^2 + \dot{l}_2^2 \ldots + \dot{l}_j^2 + l_1^2\dot{\theta}_1^2 + l_2^2\dot{\theta}_2^2 \ldots + l_j^2\dot{\theta}_j^2 + l_1^2\dot{\phi}_1^2 \sin^2\theta_1 + l_2^2\dot{\phi}_2^2 \sin^2\theta_2 \ldots \right. \\
&+ l_j^2\dot{\phi}_j^2 \sin^2\theta_j + 2l_1 l_2 \dot{\theta}_1\dot{\theta}_2 \left(\cos\theta_1 \cos\theta_2 \cos\left(\phi_1 - \phi_2\right) + \sin\theta_1 \sin\theta_2\right) \ldots \\
&+ 2l_{j-1} l_j \dot{\theta}_{j-1}\dot{\theta}_j \left(\cos\theta_{j-1} \cos\theta_j \cos\left(\phi_{j-1} - \phi_j\right) + \sin\theta_{j-1} \sin\theta_j\right) \\
&+ 2l_1 l_2 \dot{\phi}_1\dot{\phi}_2 \sin\theta_1 \sin\theta_2 \cos\left(\phi_1 - \phi_2\right) \ldots + 2l_{j-1} l_j \dot{\phi}_{j-1}\dot{\phi}_j \sin\theta_{j-1} \sin\theta_j \cos\left(\phi_{j-1} - \phi_j\right) \\
&+ 2\dot{l}_1\dot{l}_2 \left(\sin\theta_1 \sin\theta_2 \cos\left(\phi_1 - \phi_2\right) + \cos\theta_1 \cos\theta_2\right) \ldots \\
&+ 2\dot{l}_{j-1}\dot{l}_j \left(\sin\theta_{j-1} \sin\theta_j \cos\left(\phi_{j-1} - \phi_j\right) + \cos\theta_{j-1} \cos\theta_j\right) \\
&+ \dot{x}_0\dot{l}_1 \sin\theta_1 \cos\phi_1 + \dot{x}_0\dot{l}_2 \sin\theta_2 \cos\phi_2 \ldots + \dot{x}_0\dot{l}_j \sin\theta_j \cos\phi_j \\
&+ l_1\dot{x}_0\dot{\theta}_1 \cos\theta_1 \cos\phi_1 + l_2\dot{x}_0\dot{\theta}_2 \cos\theta_2 \cos\phi_2 \ldots + l_j\dot{x}_0\dot{\theta}_j \cos\theta_j \cos\phi_j \\
&- l_1\dot{x}_0\dot{\phi}_1 \sin\theta_1 \sin\phi_1 - l_2\dot{x}_0\dot{\phi}_2 \sin\theta_2 \sin\phi_2 \ldots - l_j\dot{x}_0\dot{\phi}_j \sin\theta_j \sin\phi_j \\
&+ \dot{y}_0\dot{l}_1 \sin\theta_1 \sin\phi_1 + \dot{y}_0\dot{l}_2 \sin\theta_2 \sin\phi_2 \ldots + \dot{y}_0\dot{l}_j \sin\theta_j \sin\phi_j \\
&+ l_1\dot{y}_0\dot{\theta}_1 \cos\theta_1 \sin\phi_1 + l_2\dot{y}_0\dot{\theta}_2 \cos\theta_2 \sin\phi_2 \ldots + l_j\dot{y}_0\dot{\theta}_j \cos\theta_j \sin\phi_j \\
&+ l_1\dot{y}_0\dot{\phi}_1 \sin\theta_1 \cos\phi_1 + l_2\dot{y}_0\dot{\phi}_2 \sin\theta_2 \cos\phi_2 \ldots + l_j\dot{y}_0\dot{\phi}_j \sin\theta_j \cos\phi_j \\
&+ 2\dot{l}_1 l_2 \dot{\theta}_2 \left(\sin\theta_1 \cos\theta_2 \cos\left(\phi_1 - \phi_2\right) - \cos\theta_1 \sin\theta_2\right) \\
&+ 2\dot{l}_2 l_1 \dot{\theta}_1 \left(\sin\theta_2 \cos\theta_1 \cos\left(\phi_2 - \phi_1\right) - \cos\theta_2 \sin\theta_1\right) \ldots \\
&+ 2\dot{l}_j l_{j-1} \dot{\theta}_{j-1} \left(\sin\theta_j \cos\theta_{j-1} \cos\left(\phi_j - \phi_{j-1}\right) - \cos\theta_j sin\theta_{j-1}\right) \\
&+ 2\dot{l}_1 l_2 \dot{\phi}_2 \sin\theta_1 \sin\theta_2 \sin\left(\phi_1 - \phi_2\right) + 2\dot{l}_2 l_1 \dot{\phi}_1 \sin\theta_2 \sin\theta_1 \sin\left(\phi_2 - \phi_1\right) \ldots \\
&+ 2\dot{l}_j l_{j-1} \dot{\phi}_{j-1} \sin\theta_j \sin\theta_{j-1} \sin\left(\phi_j - \phi_{j-1}\right) + 2l_1 l_2 \dot{\theta}_1\dot{\phi}_2 \cos\theta_1 \sin\theta_2 \sin\left(\phi_1 - \phi_2\right) \\
&\left. + 2l_2 l_1 \dot{\theta}_2\dot{\phi}_1 \cos\theta_2 \sin\theta_1 \sin\left(\phi_2 - \phi_1\right) \ldots + 2l_j l_{j-1} \dot{\theta}_1\dot{\phi}_{j-1} \cos\theta_j \sin\theta_{j-1} \sin\left(\phi_j - \phi_{j-1}\right)\right)
\end{aligned}
\tag{7.48}
$$

Next, the expression is linearized for small amplitude motion about the system's equilibrium, by making the following substitutions:

$$\theta_j = \theta_{0,j} + u_j \tag{7.49}$$

$$l_j = l_{0,j} + v_j \tag{7.50}$$

$$\phi_j = \phi_{0,j} + w_j \tag{7.51}$$

Here, $\theta_{0,j}$, $l_{0,j}$ and $\phi_{0,j}$ are the equilibrium values of the coordinates, and u_j, v_j and w_j are the small deviations from these equilibrium values. Upon making these substitutions, small angle approximations can be made for u_j and w_j, and any terms containing the products

of more than two small terms are considered negligible and ignored. For cos and sin terms, the following expansion expressions are substituted into the equation:

$$\cos\theta_j = \cos(\theta_{0,j} + u_j) = \cos\theta_{0,j}\cos u_j - \sin\theta_{0,j}\sin u_j \approx \cos\theta_{0,j} - u_j\sin\theta_{0,j} \tag{7.52}$$

$$\sin\theta_j = \sin(\theta_{0,j} + u_j) = \sin\theta_{0,j}\cos u_j + \cos\theta_{0,j}\sin u_j \approx \sin\theta_{0,j} + u_j\cos\theta_{0,j} \tag{7.53}$$

$$\cos\phi_j = \cos(\phi_{0,j} + w_j) = \cos\phi_{0,j}\cos w_j - \sin\phi_{0,j}\sin w_j \approx \cos\phi_{0,j} - w_j\sin\phi_{0,j} \tag{7.54}$$

$$\sin\phi_j = \sin(\phi_{0,j} + w_j) = \sin\phi_{0,j}\cos w_j + \cos\phi_{0,j}\sin w_j \approx \sin\phi_{0,j} + w_j\cos\phi_{0,j} \tag{7.55}$$

Expressions 7.49-7.55 are substituted into the kinetic energy equation, and terms containing the products of more than two small terms are ignored, producing the following linearized expression for the kinetic energy of an arbitrary element in the system for small amplitude

vibration:

$$
\begin{aligned}
T_j = &\frac{1}{2}m_i\Big(\dot{x}_0^2+\dot{y}_0^2+\dot{v}_1^2+\dot{v}_2^2\ldots+\dot{v}_j^2+l_{0,1}^2\dot{u}_1^2+l_{0,2}^2\dot{u}_2^2\ldots\\
&+l_{0,j}^2\dot{u}_j^2+l_{0,1}^2\dot{w}_1^2\sin^2\theta_{0,1}+l_{0,2}^2\dot{w}_2^2\sin^2\theta_{0,2}\ldots\\
&+l_{0,j}^2\dot{w}_j^2\sin^2\theta_{0,j}+2l_{0,1}l_{0,2}\dot{u}_1\dot{u}_2\left(\cos\theta_{0,1}\cos\theta_{0,2}\cos\left(\phi_{0,1}-\phi_{0,2}\right)+\sin\theta_{0,1}\sin\theta_{0,2}\right)\ldots\\
&+2l_{0,j-1}l_{0,j}\dot{u}_{j-1}\dot{u}_j\left(\cos\theta_{0,j-1}\cos\theta_{0,j}\cos\left(\phi_{0,j-1}-\phi_{0,j}\right)+\sin\theta_{0,j-1}\sin\theta_{0,j}\right)\\
&+2l_{0,1}l_{0,2}\dot{w}_1\dot{w}_2\sin\theta_{0,1}\sin\theta_{0,2}\cos\left(\phi_{0,1}-\phi_{0,2}\right)\ldots\\
&+2l_{0,j-1}l_{0,j}\dot{w}_{j-1}\dot{w}_j\sin\theta_{0,j-1}\sin\theta_{0,j}\cos\left(\phi_{0,j-1}-\phi_{0,j}\right)\\
&+2\dot{v}_1\dot{v}_2\left(\sin\theta_{0,1}\sin\theta_{0,2}\cos\left(\phi_{0,1}-\phi_{0,2}\right)+\cos\theta_{0,1}\cos\theta_{0,2}\right)\ldots\\
&+2\dot{v}_{j-1}\dot{v}_j\left(\sin\theta_{0,j-1}\sin\theta_{0,j}\cos\left(\phi_{0,j-1}-\phi_{0,j}\right)+\cos\theta_{0,j-1}\cos\theta_{0,j}\right)\\
&+2\dot{x}_0\dot{v}_1\sin\theta_{0,1}\cos\phi_{0,1}+2\dot{x}_0\dot{v}_2\sin\theta_{0,2}\cos\phi_{0,2}\ldots+2\dot{x}_0\dot{v}_j\sin\theta_{0,j}\cos\phi_{0,j}\\
&+2l_{0,1}\dot{x}_0\dot{u}_1\cos\theta_{0,1}\cos\phi_{0,1}+2l_{0,2}\dot{x}_0\dot{u}_2\cos\theta_{0,2}\cos\phi_{0,2}\ldots+2l_{0,j}\dot{x}_0\dot{u}_j\cos\theta_{0,j}\cos\phi_{0,j}\\
&-2l_1\dot{x}_0\dot{w}_1\sin\theta_{0,1}\sin\phi_{0,1}-2l_{0,2}\dot{x}_0\dot{w}_2\sin\theta_{0,2}\sin\phi_{0,2}\ldots-2l_{0,j}\dot{x}_0\dot{w}_j\sin\theta_{0,j}\sin\phi_{0,j}\\
&+2\dot{y}_0\dot{v}_1\sin\theta_{0,1}\sin\phi_{0,1}+2\dot{y}_0\dot{v}_2\sin\theta_{0,2}\sin\phi_{0,2}\ldots+2\dot{y}_0\dot{v}_j\sin\theta_{0,j}\sin\phi_{0,j}\\
&+2l_{0,1}\dot{y}_0\dot{u}_1\cos\theta_{0,1}\sin\phi_{0,1}+2l_{0,2}\dot{y}_0\dot{u}_2\cos\theta_{0,2}\sin\phi_{0,2}\ldots+2l_{0,j}\dot{y}_0\dot{u}_j\cos\theta_{0,j}\sin\phi_{0,j}\\
&+2l_{0,1}\dot{y}_0\dot{w}_1\sin\theta_{0,1}\cos\phi_{0,1}+2l_{0,2}\dot{y}_0\dot{w}_2\sin\theta_{0,2}\cos\phi_{0,2}\ldots+2l_{0,j}\dot{y}_0\dot{w}_j\sin\theta_{0,j}\cos\phi_{0,j}\\
&+2\dot{v}_1l_{0,2}\dot{u}_2\left(\sin\theta_{0,1}\cos\theta_{0,2}\cos\left(\phi_{0,1}-\phi_{0,2}\right)-\cos\theta_{0,1}\sin\theta_{0,2}\right)\\
&+2\dot{v}_2l_{0,1}\dot{u}_1\left(\sin\theta_{0,2}\cos\theta_{0,1}\cos\left(\phi_{0,2}-\phi_{0,1}\right)-\cos\theta_{0,2}\sin\theta_{0,1}\right)\ldots\\
&+2\dot{v}_jl_{0,j-1}\dot{u}_{j-1}\left(\sin\theta_{0,j}\cos\theta_{0,j-1}\cos\left(\phi_{0,j}-\phi_{0,j-1}\right)-\cos\theta_{0,j}\sin\theta_{0,j-1}\right)\\
&+2\dot{v}_1l_{0,2}\dot{w}_2\sin\theta_{0,1}\sin\theta_{0,2}\sin\left(\phi_{0,1}-\phi_{0,2}\right)+2\dot{v}_2l_{0,1}\dot{w}_1\sin\theta_{0,2}\sin\theta_{0,1}\sin\left(\phi_{0,2}-\phi_{0,1}\right)\ldots\\
&+2\dot{v}_jl_{0,j-1}\dot{w}_{j-1}\sin\theta_{0,j}\sin\theta_{0,j-1}\sin\left(\phi_{0,j}-\phi_{0,j-1}\right)\\
&+2l_{0,1}l_{0,2}\dot{u}_1\dot{w}_2\cos\theta_{0,1}\sin\theta_{0,2}\sin\left(\phi_{0,1}-\phi_{0,2}\right)\\
&+2l_{0,2}l_{0,1}\dot{u}_2\dot{w}_1\cos\theta_{0,2}\sin\theta_{0,1}\sin\left(\phi_{0,2}-\phi_{0,1}\right)\ldots\\
&+2l_{0,j}l_{0,j-1}\dot{u}_j\dot{w}_{j-1}\cos\theta_{0,j}\sin\theta_{0,j-1}\sin\left(\phi_{0,j}-\phi_{0,j-1}\right)\Big)
\end{aligned}
\tag{7.56}
$$

The total kinetic energy of the system is therefore the sum of the kinetic energies of all of the tether elements, as well as those of the balloon and the base. Expressing these in

summation form:

$$
\begin{aligned}
T_{tot} = {} & \frac{1}{2} m_{base}\left(\dot{x}_0^2+\dot{y}_0^2\right)+\frac{1}{2}\left((N-1)\,m+m_b\right)\left(\dot{x}_0^2+\dot{y}_0^2\right) \\
& +\frac{1}{2}\sum_{i=1}^{N}\Bigg(\left((N-i)\,m+m_b\right)\left(\dot{v}_i^2+l_{0,i}^2\dot{u}_i^2+l_{0,i}^2\dot{w}_i^2\sin^2\theta_{0,i}+2l_{0,i}\dot{x}_0\dot{u}_i\cos\theta_{0,i}\cos\phi_{0,i}\right. \\
& \quad +2\dot{x}_0\dot{v}_i\sin\theta_{0,i}\cos\phi_{0,i}-2l_{0,i}\dot{x}_0\dot{w}_i\sin\theta_{0,i}\sin\phi_{0,i}+2l_{0,i}\dot{y}_0\dot{u}_i\cos\theta_{0,i}\sin\phi_{0,i} \\
& \quad \left.+2\dot{y}_0\dot{v}_i\sin\theta_{0,i}\sin\phi_{0,i}+2l_{0,i}\dot{y}_0\dot{w}_i\sin\theta_{0,i}\cos\phi_{0,i}\right)+ \\
& \quad \sum_{j=1}^{i-1}\Bigg[\left((N-i)\,m+m_b\right)\left(l_{0,i}l_{0,j}\dot{u}_i\dot{u}_j\left(\cos\theta_{0,i}\cos\theta_{0,j}\cos\left(\phi_{0,i}-\phi_{0,j}\right)+\sin\theta_{0,i}\sin\theta_{0,j}\right)\right. \\
& \qquad +\dot{v}_i\dot{v}_j\left(sin\theta_{0,i}\sin\theta_{0,j}\cos\left(\phi_{0,i}-\phi_{0,j}\right)+\cos\theta_{0,i}\cos\theta_{0,j}\right) \\
& \qquad +l_{0,i}l_{0,j}\dot{w}_i\dot{w}_j\sin\theta_{0,i}\sin\theta_{0,j}\cos\left(\phi_{0,i}-\phi_{0,j}\right) \\
& \qquad +\dot{v}_i l_{0,j}\dot{u}_j\left(\sin\theta_{0,i}\cos\theta_{0,j}\cos\left(\phi_{0,i}-\phi_{0,j}\right)-cos\theta_{0,i}\sin\theta_{0,j}\right) \\
& \qquad +\dot{v}_i l_{0,j}\dot{w}_j\sin\theta_{0,i}\sin\theta_{0,j}\sin\left(\phi_{0,i}-\phi_{0,j}\right) \\
& \qquad \left.+l_{0,i}l_{0,j}\dot{u}_i\dot{w}_j\cos\theta_{0,i}\sin\theta_{0,j}\sin\left(\phi_{0,i}-\phi_{0,j}\right)\right)\Bigg]+ \\
& \quad \sum_{j=i+1}^{N}\Bigg[\left((N-j)\,m+m_b\right)\left(l_{0,i}l_{0,j}\dot{u}_i\dot{u}_j\left(\cos\theta_{0,i}\cos\theta_{0,j}\cos\left(\phi_{0,i}-\phi_{0,j}\right)+\sin\theta_{0,i}\sin\theta_{0,j}\right)\right. \\
& \qquad +\dot{v}_i\dot{v}_j\left(sin\theta_{0,i}\sin\theta_{0,j}\cos\left(\phi_{0,i}-\phi_{0,j}\right)+\cos\theta_{0,i}\cos\theta_{0,j}\right) \\
& \qquad +l_{0,i}l_{0,j}\dot{w}_i\dot{w}_j\sin\theta_{0,i}\sin\theta_{0,j}\cos\left(\phi_{0,i}-\phi_{0,j}\right) \\
& \qquad +\dot{v}_i l_{0,j}\dot{u}_j\left(\sin\theta_{0,i}\cos\theta_{0,j}\cos\left(\phi_{0,i}-\phi_{0,j}\right)-\cos\theta_{0,i}\sin\theta_{0,j}\right) \\
& \qquad +\dot{v}_i l_{0,j}\dot{w}_j\sin\theta_{0,i}\sin\theta_{0,j}\sin\left(\phi_{0,i}-\phi_{0,j}\right) \\
& \qquad \left.\left.+l_{0,i}l_{0,j}\dot{u}_i\dot{w}_j\cos\theta_{0,i}\sin\theta_{0,j}\sin\left(\phi_{0,i}-\phi_{0,j}\right)\right)\Bigg]\Bigg)
\end{aligned}
\tag{7.57}
$$

For the case of a stationary base ($\dot{x}_0=\dot{y}_0=0$), the mass matrix of the 3D extensible tethered balloon model can be thought to comprise of 9 sub-matrices:

$$
M=\begin{bmatrix} M_1 & M_2 & M_3 \\ M_4 & M_5 & M_6 \\ M_7 & M_8 & M_9 \end{bmatrix} \tag{7.58}
$$

For a coordinate state vector of the form $[u_1\ u_2\ldots u_N\ v_1\ v_2\ldots v_N\ w_1\ w_2\ldots w_N]^T$, the entries of the sub-matrices of the system's mass matrix comprise of the following double

partial differentials:

$$M_1(i,j) = \frac{\partial^2 T_{TOT}}{\partial \dot{u}_i \partial \dot{u}_j} \quad M_2(i,j) = M_4^T(i,j) = \frac{\partial^2 T_{TOT}}{\partial \dot{u}_i \partial \dot{v}_j} \quad M_3(i,j) = M_7^T(i,j) = \frac{\partial^2 T_{TOT}}{\partial \dot{u}_i \partial \dot{w}_j}$$
$$M_5(i,j) = \frac{\partial^2 T_{TOT}}{\partial \dot{v}_i \partial \dot{v}_j} \quad M_6(i,j) = M_8^T(i,j) = \frac{\partial^2 T_{TOT}}{\partial \dot{v}_i \partial \dot{w}_j} \quad M_9(i,j) = \frac{\partial^2 T_{TOT}}{\partial \dot{w}_i \partial \dot{w}_j} \tag{7.59}$$

While the mass matrix as a whole is symmetric, the sub-matrices are not necessarily symmetric so care must be taken when calculating their entries. Matrices 1, 5 and 9 are symmetric since they appear at the diagonal of the mass matrix. Sub-matrices 2-4 and 6-8 are not symmetric, although each will be equal to the transverse of the sub-matrix to which it reflects along the matrix M's diagonal. Through careful inspection of the kinetic energy equation, the following set of equations are deduced, from which the entries of the nine sub-matrices of the mass matrix can be found directly.

$$M_1(i,j)_{i=j} = l_{0,i}^2((N-i)m + m_b) \tag{7.60}$$
$$M_1(i,j)_{i\neq j} = l_{0,i}l_{0,j}((N-i)m + m_b)\left(\cos\theta_{0,i}\cos\theta_{0,j}\cos\left(\phi_{0,i} - \phi_{0,j}\right) + \sin\theta_{0,i}\sin\theta_{0,j}\right) \tag{7.61}$$
$$M_5(i,j)_{i=j} = ((N-i)m + m_b) \tag{7.62}$$
$$M_5(i,j)_{i\neq j} = ((N-i)m + m_b)\left(\sin\theta_{0,i}\sin\theta_{0,j}\cos\left(\phi_{0,i} - \phi_{0,j}\right) + \cos\theta_{0,i}\cos\theta_{0,j}\right) \tag{7.63}$$
$$M_9(i,j)_{i=j} = l_{0,i}^2((N-i)m + m_b)\sin^2\theta_{0,i} \tag{7.64}$$
$$M_9(i,j)_{i\neq j} = l_{0,i}l_{0,j}((N-i)m + m_b)\sin\theta_{0,i}\sin\theta_{0,j}\cos\left(\phi_{0,i} - \phi_{0,j}\right) \tag{7.65}$$
$$M_2(i,j)_{i=j} = M_3(i,j)_{i=j} = M_4(i,j)_{i=j} = M_6(i,j)_{i=j} = M_7(i,j)_{i=j} = M_8(i,j)_{i=j} = 0 \tag{7.66}$$
$$M_2(i,j)_{i>j} = l_{0,i}((N-i)m + m_b)\left(\sin\theta_{0,j}\cos\theta_{0,i}\cos\left(\phi_{0,j} - \phi_{0,i}\right) - \cos\theta_{0,j}\sin\theta_{0,i}\right) \tag{7.67}$$
$$M_2(i,j)_{j>i} = l_{0,i}((N-j)m + m_b)\left(\sin\theta_{0,j}\cos\theta_{0,i}\cos\left(\phi_{0,j} - \phi_{0,i}\right) - \cos\theta_{0,j}\sin\theta_{0,i}\right) \tag{7.68}$$
$$M_3(i,j)_{i>j} = l_{0,i}l_{0,j}((N-i)m + m_b)\cos\theta_{0,i}\sin\theta_{0,j}\sin\left(\phi_{0,i} - \phi_{0,j}\right) \tag{7.69}$$
$$M_3(i,j)_{j>i} = l_{0,i}l_{0,j}((N-j)m + m_b)\cos\theta_{0,i}\sin\theta_{0,j}\sin\left(\phi_{0,i} - \phi_{0,j}\right) \tag{7.70}$$
$$M_6(i,j)_{i>j} = l_{0,j}((N-i)m + m_b)\sin\theta_{0,i}\sin\theta_{0,j}\sin\left(\phi_{0,i} - \phi_{0,j}\right) \tag{7.71}$$
$$M_6(i,j)_{i<j} = l_{0,j}((N-j)m + m_b)\sin\theta_{0,i}\sin\theta_{0,j}\sin\left(\phi_{0,i} - \phi_{0,j}\right) \tag{7.72}$$
$$M_4(i,j) = M_2(i,j)^T \quad M_7(i,j) = M_3(i,j)^T \quad M_8(i,j) = M_6(i,j)^T \tag{7.73}$$

For the tethered balloon system with a non-stationary base, the linearization of which is required for the design of a feedback controller with a base force input, the coordinate vector will contain 2 additional coordinates that define the position of the tether's base, x_0 and y_0. As a result of this, the mass and stiffness matrices will have 2 additional rows and columns for a 3-dimensional system that correspond to these additional coordinates. Assuming the coordinate state vector is in the form $[x_0\ y_0\ u_1\ u_2 \ldots u_N\ v_1\ v_2 \ldots v_N\ w_1\ w_2 \ldots w_N]^T$, these additional rows and columns would appear before the ones derived previously and the new mass matrix will appear as follows:

$$M_{mb} = \begin{bmatrix} M_{0,1} & M_{0,2} & M_{0,3} & M_{0,4} & M_{0,5} \\ M'_{0,2} & M_{0,6} & M_{0,7} & M_{0,8} & M_{0,9} \\ M'_{0,3} & M'_{0,7} & M_1 & M_2 & M_3 \\ M'_{0,4} & M'_{0,8} & M_4 & M_5 & M_6 \\ M'_{0,5} & M'_{0,9} & M_7 & M_8 & M_9 \end{bmatrix} \tag{7.74}$$

The additional sub-matrices, which are actually 1-dimensional, can be calculated using the following double partial differential equations:

$$\begin{gathered} M_{0,1} = \frac{\partial^2 T_{TOT}}{\partial \dot{x}_0^2} \quad M_{0,2} = \frac{\partial^2 T_{TOT}}{\partial \dot{x}_0 \partial \dot{y}_0} \quad M_{0,3}(1,j) = \frac{\partial^2 T_{TOT}}{\partial \dot{x}_0 \partial \dot{u}_j} \\ M_{0,4}(1,j) = \frac{\partial^2 T_{TOT}}{\partial \dot{x}_0 \partial \dot{v}_j} \quad M_{0,5}(1,j) = \frac{\partial^2 T_{TOT}}{\partial \dot{x}_0 \partial \dot{w}_j} \quad M_{0,6} = \frac{\partial^2 T_{TOT}}{\partial \dot{y}_0^2} \\ M_{0,7}(1,j) = \frac{\partial^2 T_{TOT}}{\partial \dot{y}_0 \partial \dot{u}_j} \quad M_{0,8}(1,j) = \frac{\partial^2 T_{TOT}}{\partial \dot{y}_0 \partial \dot{v}_j} \quad M_{0,9}(1,j) = \frac{\partial^2 T_{TOT}}{\partial \dot{y}_0 \partial \dot{w}_j} \end{gathered} \tag{7.75}$$

Once again, through the careful inspection of the expression for the system's total kinetic energy, expressions for the entries of the additional sub-matrices are derived:

$$M_{0,1} = m_{base} + (N-1)m + m_b \tag{7.76}$$

$$M_{0,2} = 0 \tag{7.77}$$

$$M_{0,6} = m_{base} + (N-1)m + m_b \tag{7.78}$$

$$M_{0,3}(1,j) = ((N-j)m + m_b) l_{0,j} \cos\theta_{0,j} \cos\phi_{0,j} \tag{7.79}$$

$$M_{0,4}(1,j) = ((N-j)m + m_b) \sin\theta_{0,j} \cos\phi_{0,j} \tag{7.80}$$

$$M_{0,5}(1,j) = -((N-j)m + m_b) l_{0,j} \sin\theta_{0,j} \sin\phi_{0,j} \tag{7.81}$$

$$M_{0,7}(1,j) = ((N-j)m + m_b) l_{0,j} \cos\theta_{0,j} \sin\phi_{0,j} \tag{7.82}$$

$$M_{0,8}(1,j) = ((N-j)m + m_b) \sin\theta_{0,j} \sin\phi_{0,j} \tag{7.83}$$

$$M_{0,9}(1,j) = ((N-j)m + m_b) l_{0,j} \sin\theta_{0,j} \cos\phi_{0,j} \tag{7.84}$$

7.4 Derivation of Stiffness Matrix for 3D Extensible Model

As in the 2-dimensional case, the effects of the wind drag forces are accounted for in the potential energy equation. This is possible because, for small amplitude motion about its equilibrium position, the altitude of each element varies very slightly and so the wind forces exerted on the elements can be taken as constant. The direction of the wind drag acting on each element is also taken as being constant since the elements' orientations are assumed to remain fairly constant. The potential energy of each element therefore consists of components due to the wind forces, its gravitational potential energy, and the elastic potential energies due to the axial and rotational springs once again.

The potential energy due to a rotational spring between two arbitrary elements is equal to:

$$V_{b,j} = \frac{1}{2} k_b \beta_j^2 = \frac{1}{2} k_b (\beta_{0,j} + \beta'_j)^2 = \frac{1}{2} k_b (\beta_{0,j}^2 + 2\beta_{0,j}\beta'_j + \beta'^2_j) \tag{7.85}$$

Here, β_j is the angle between the unit vectors of two consecutive element links, as shown in Figure 3.6. The direction of this angle is arbitrary in 3-dimensional space. For small amplitude motion about the equilibrium, β_j can be thought of as being the sum of the equilibrium angle $\beta_{0,j}$ and the small angular deviation from this, β'_j. The small angle β'_j can be approximated using the small relative angular deviations of the consecutive links in the Euler directions. The relative distance moved by the links end can be related to the components of the relative distance moved due to u and w using Pythagoras:

$$(\beta'_j l_{j+1})^2 = (l_{j+1}(u_{j+1} - u_j))^2 + (l_{j+1} \sin\theta_{j+1}(w_{j+1} - w_j))^2 \tag{7.86}$$

Cancelling the common l_j^2 factors and substituting into the expression for the potential energy due to the rotational spring produces the following expression in terms of the generalised coordinates of the system:

$$V_{b,j} = \frac{1}{2} k_b (\beta_{0,j}^2 + 2\beta_{0,j}\beta'_j + (u_{j+1} - u_j)^2 + \sin^2\theta_{j+1}(w_{j+1} - w_j)^2) \tag{7.87}$$

While expressions for the first two terms in this equation can be derived and substituted, this is unnecessary because these terms will disappear upon applying the double partial differentials to this expression.

Using equations 7.41, 7.42 and 7.43 for the position coordinates of the jth element, an expression for the total potential energy of an arbitrary element is found:

$$\begin{aligned}V_j =& \frac{1}{2}k_b\beta_j^2 + \frac{1}{2}k\left(l_j - L\right)^2 + (mg - F_{z,j})z_j - F_{x,j}x_j - F_{y,j}y_j \\ =& \frac{1}{2}k_b\beta_j^2 + \frac{1}{2}k\left(l_j - L\right)^2 + (mg - F_{z,j})\left(l_1\cos\theta_1 + l_2\cos\theta_2 \ldots + l_j\cos\theta_j\right) \\ & - F_{x,j}\left(x_0 + l_1\sin\theta_1\cos\phi_1 + l_2\sin\theta_2\cos\phi_2 \ldots + l_j\sin\theta_j\cos\phi_j\right) \\ & - F_{y,j}\left(y_0 + l_1\sin\theta_1\sin\phi_1 + l_2\sin\theta_2\sin\phi_2 \ldots + l_j\sin\theta_j\sin\phi_j\right)\end{aligned} \tag{7.88}$$

Here, $F_{x,j}$, $F_{y,j}$ and $F_{z,j}$ are the components of the wind drag forces acting on the jth element in the x, y and z directions respectively. As in the previous case, a simplified expression of the total potential energy of the system is found by observing the patterns in the individual potential energies of the elements.

$$\begin{aligned}V_{TOT} =& \frac{1}{2}k_b\beta_1^2 + \frac{1}{2}k_b\beta_2^2 \ldots + \frac{1}{2}k_b\beta_N^2 + \frac{1}{2}k\left(l_1 - L\right)^2 + \frac{1}{2}k\left(l_2 - L\right)^2 \ldots + \frac{1}{2}k_N\left(l_N - L_N\right)^2 \\ & + l_1\cos\theta_1\left(mg(N-1) + m_bg - F_{z,1} - F_{z,2} \ldots - F_{z,N} - F_{lift}\right) \\ & + l_2\cos\theta_2\left(mg(N-2) + m_bg - F_{z,2} \ldots - F_{z,N} - F_{lift}\right) \ldots \\ & + l_N\cos\theta_N\left(m_bg - F_{z,N} - F_{lift}\right) - l_1\sin\theta_1\cos\phi_1\left(F_{x,1} + F_{x,2} \ldots + F_{x,N}\right) \\ & - l_2\sin\theta_2\cos\phi_2\left(F_{x,2} \ldots + F_{x,N}\right) \ldots - l_N\sin\theta_N\cos\phi_N F_{x,N} \\ & - l_1\sin\theta_1\sin\phi_1\left(F_{y,1} + F_{y,2} \ldots + F_{y,N}\right) - l_2\sin\theta_2\sin\phi_2\left(F_{y,2} \ldots + F_{y,N}\right) \ldots \\ & - l_N\sin\theta_N\sin\phi_N F_{y,N} - x_0\left(F_{x,1} + F_{x,2} \ldots + F_{x,N}\right) - y_0\left(F_{y,1} + F_{y,2} \ldots + F_{y,N}\right)\end{aligned} \tag{7.89}$$

Once again, expressions 7.49-7.51 are substituted into the energy equation in order to linearize it. In this case however, an additional small (second order) term is included in the expansion of $\cos u_j$ and $\cos w_j$, and so the following expressions are substituted:

$$\cos\theta_j = \cos\theta_{0,j}\cos u_j - \sin\theta_{0,j}\sin u_j \approx (1 - \frac{1}{2}u_j^2)\cos\theta_{0,j} - u_j\sin\theta_{0,j} \tag{7.90}$$

$$\sin\theta_j = \sin\theta_{0,j}\cos u_j + \cos\theta_{0,j}\sin u_j \approx (1 - \frac{1}{2}u_j^2)\sin\theta_{0,j} + u_j\cos\theta_{0,j} \tag{7.91}$$

$$\cos\phi_j = \cos\phi_{0,j}\cos w_j - \sin\phi_{0,j}\sin w_j \approx (1 - \frac{1}{2}w_j^2)\cos\phi_{0,j} - w_j\sin\phi_{0,j} \tag{7.92}$$

$$\sin\phi_j = \sin\phi_{0,j}\cos w_j + \cos\phi_{0,j}\sin w_j \approx (1 - \frac{1}{2}w_j^2)\sin\phi_{0,j} + w_j\cos\phi_{0,j} \tag{7.93}$$

Upon applying these substitutions as well as the expression for β_j' derived earlier (equation 7.86), the expression for the total potential energy for the system for small amplitude vibration

is derived and simplified:

$$
\begin{aligned}
V_{TOT} &= -x_0\left(F_{x,1}+F_{x,2}\ldots+F_{x,N}\right)-y_0\left(F_{y,1}+F_{y,2}\ldots+F_{y,N}\right)\\
&+\sum_{i=1}^{N}\Bigg[\frac{1}{2}k_i(v_i+l_{0,i}-L)^2+\frac{1}{2}k_b(\beta_{0,j}^2+2\beta_{0,j}\beta_j'+(u_{j+1}-u_j)^2+\sin^2\theta_{0,j+1}(w_{j+1}-w_j)^2)\\
&+\left((1-\frac{1}{2}u_i^2)\cos\theta_{0,i}-u_i\sin\theta_{0,i}\right)\left(l_{0,i}+v_i\right)\left(mg\left(N-i\right)+m_bg-F_{z,i}\ldots-F_{z,n}-F_{lift}\right)\\
&-\left((1-\frac{1}{2}u_i^2)\sin\theta_{0,i}+u_i\cos\theta_{0,i}\right)\left((1-\frac{1}{2}w_i^2)\cos\phi_{0,i}-w_i\sin\phi_{0,i}\right)\left(l_{0,i}+v_i\right)\left(F_{x,i}\ldots+F_{x,N}\right)\\
&-\left((1-\frac{1}{2}u_i^2)\sin\theta_{0,i}+u_i\cos\theta_{0,i}\right)\left((1-\frac{1}{2}w_i^2)\sin\phi_{0,i}+w_i\cos\phi_{0,i}\right)\left(l_{0,i}+v_i\right)\left(F_{y,i}\ldots+F_{y,N}\right)\Bigg]
\end{aligned}
\tag{7.94}
$$

Similar to the mass matrix, for the case of a stationary base, the stiffness matrix can be thought of as containing 9 sub-matrices:

$$
K=\begin{bmatrix}K_1 & K_2 & K_3\\ K_4 & K_5 & K_6\\ K_7 & K_8 & K_9\end{bmatrix}
\tag{7.95}
$$

The partial differential equations required to determine each of these sub-matrices (for the same state vector order as was used in the previous section) are shown below:

$$
\begin{aligned}
K_1(i,j)&=\frac{\partial^2V_{TOT}}{\partial u_i\partial u_j} \quad K_2(i,j)=K_4^T(i,j)=\frac{\partial^2V_{TOT}}{\partial u_i\partial v_j} \quad K_3(i,j)=K_7^T(i,j)=\frac{\partial^2V_{TOT}}{\partial u_i\partial w_j}\\
K_5(i,j)&=\frac{\partial^2V_{TOT}}{\partial v_i\partial v_j} \quad K_6(i,j)=K_8^T(i,j)=\frac{\partial^2V_{TOT}}{\partial v_i\partial w_j} \quad K_9(i,j)=\frac{\partial^2V_{TOT}}{\partial w_i\partial w_j}
\end{aligned}
\tag{7.96}
$$

Multiplying out the equation for the potential energy, followed by eliminating small terms and the application of the partial differential equations results in the following equations, which can be used to determine the entries of the stiffness matrix of a 3-dimensional extensible tethered balloon system directly and therefore computationally efficiently.

$$
\begin{aligned}
K_1(i,j)_{i=j,i=2:N-1} =& -l_{0,i}\left(mg\left(N-i\right)+m_bg-F_{z,i}-F_{z,i+1}-F_{z,N}-F_{lift}\right)\cos\theta_{0,i}\\
&+l_{0,i}\left(F_{x,i}+F_{x,i+1}\ldots+F_{x,N}\right)\sin\theta_{0,i}\cos\phi_{0,i}\\
&+l_{0,i}\left(F_{y,i}+F_{y,i+1}\ldots+F_{y,N}\right)\sin\theta_{0,i}\sin\phi_{0,i}+2k_b
\end{aligned}
\tag{7.97}
$$

$$\begin{aligned} K_1(i,j)_{i=j,i=1,N} = &- l_{0,i}\left(mg(N-i)+m_bg-F_{z,i}-F_{z,i+1}-F_{z,N}-F_{lift}\right)\cos\theta_{0,i} \\ &+ l_{0,i}\left(F_{x,i}+F_{x,i+1}\ldots+F_{x,N}\right)\sin\theta_{0,i}\cos\phi_{0,i} \\ &+ l_{0,i}\left(F_{y,i}+F_{y,i+1}\ldots+F_{y,N}\right)\sin\theta_{0,i}\sin\phi_{0,i}+k_b \end{aligned} \tag{7.98}$$

$$K_1(i,j)_{j=i-1,i+1} = -k_b \tag{7.99}$$

$$\begin{aligned} K_2(i,j)_{i=j} = K_4(i,j)_{i=j} = &-\left(mg(N-i)+m_bg-F_{lift}\right)\sin\theta_{0,i} \\ &-\left(F_{x,i}+F_{x,i+1}\ldots+F_{x,N}\right)\cos\theta_{0,i}\cos\phi_{0,i}-\left(F_{y,i}+F_{y,i+1}\ldots+F_{y,N}\right)\cos\theta_{0,i}\sin\phi_{0,i} \end{aligned} \tag{7.100}$$

$$K_5(i,j)_{i=j,\ i<N} = k \qquad K_5(i,j)_{i=j,i=N} = k_N \tag{7.101}$$

$$\begin{aligned} K_3(i,j)_{i=j} = K_7(i,j)_{i=j} = &l_{0,i}\left(F_{x,i}+F_{x,i+1}\ldots+F_{x,N}\right)\cos\theta_{0,i}\sin\phi_{0,i} \\ &- l_{0,i}\left(F_{y,i}+F_{y,i+1}\ldots+F_{y,N}\right)\cos\theta_{0,i}\cos\phi_{0,i} \end{aligned} \tag{7.102}$$

$$\begin{aligned} K_6(i,j)_{i=j} = K_8(i,j)_{i=j} = &\left(F_{x,i}+F_{x,i+1}\ldots+F_{x,N}\right)\sin\theta_{0,i}\sin\phi_{0,i} \\ &-\left(F_{y,i}+F_{y,i+1}\ldots+F_{y,N}\right)\sin\theta_{0,i}\cos\phi_{0,i} \end{aligned} \tag{7.103}$$

$$\begin{aligned} K_9(i,j)_{i=j,i=2:N-1} = &l_{0,i}\left(F_{x,i}+F_{x,i+1}\ldots+F_{x,N}\right)\sin\theta_{0,i}\cos\phi_{0,i} \\ &+ l_{0,i}\left(F_{y,i}+F_{y,i+1}\ldots+F_{y,N}\right)\sin\theta_{0,i}\sin\phi_{0,i}+k_b(sin^2\theta_{0,j}+sin^2\theta_{0,j-1}) \end{aligned} \tag{7.104}$$

$$\begin{aligned} K_9(1,1) = &l_{0,1}\left(F_{x,1}+F_{x,2}\ldots+F_{x,N}\right)\sin\theta_{0,1}\cos\phi_{0,1} \\ &+ l_{0,1}\left(F_{y,1}+F_{y,2}\ldots+F_{y,N}\right)\sin\theta_{0,1}\sin\phi_{0,1}+k_bsin^2\theta_{0,2} \end{aligned} \tag{7.105}$$

$$K_9(N,N) = l_{0,N}F_{x,N}\sin\theta_{0,N}\cos\phi_{0,N}+l_{0,N}F_{y,N}\sin\theta_{0,N}\sin\phi_{0,N}+k_bsin^2\theta_{0,N} \tag{7.106}$$

$$K_9(i,j)_{j=i+1} = -k_b\sin^2\theta_{0,j} \qquad K_9(i,j)_{j=i-1} = -k_b\sin^2\theta_{0,i} \tag{7.107}$$

All the sub-matrices aside from K_1 and K_9 are diagonal matrices. K_1 and K_9 have non-zero entries immediately adjacent to their diagonals, and the remainder of the entries are zero. The following is therefore true:

$$\begin{aligned} K_2(i,j)_{i\neq j} = K_3(i,j)_{i\neq j} = K_4(i,j)_{i\neq j} = K_5(i,j)_{i\neq j} \\ = K_6(i,j)_{i\neq j} = K_7(i,j)_{i\neq j} = K_8(i,j)_{i\neq j} = 0 \end{aligned} \tag{7.108}$$

For the case where the tether's base is not stationary as is required to design the controller with base motion as an input, the stiffness matrix has two additional rows and columns preceding the sub-matrices described, just as in the mass matrix designed for a moving base,

M_{mb}. The corresponding stiffness matrix therefore looks like:

$$K_{mb} = \begin{bmatrix} K_{0,1} & K_{0,2} & K_{0,3} & K_{0,4} & K_{0,5} \\ K'_{0,2} & K_{0,6} & K_{0,7} & K_{0,8} & K_{0,9} \\ K'_{0,3} & K'_{0,7} & K_1 & K_2 & K_3 \\ K'_{0,4} & K'_{0,8} & K_4 & K_5 & K_6 \\ K'_{0,5} & K'_{0,9} & K_7 & K_8 & K_9 \end{bmatrix} \tag{7.109}$$

As for the 2-dimensional case however, applying the double partial differentials that correspond to these additional rows and columns gives 0 for all of the entries. This is expected, since the horizontal displacement of the system's base does not contribute in any way to its potential energy.

$$K_{0,1} = K_{0,2} = K_{0,6} = 0 \tag{7.110}$$

$$K_{0,3}(1,j) = K_{0,4}(1,j) = K_{0,5}(1,j) = K_{0,7}(1,j) = K_{0,8}(1,j) = K_{0,9}(1,j) = 0 \tag{7.111}$$

7.5 Damping Matrices for 2D and 3D Extensible Models

Unlike the mass and stiffness matrices, the damping matrix of an extensible cable system with axial damping can be deduced directly by inspection. As seen in Figure 7.5, the only source of cable damping found in the system model is parallel and therefore directly analogous to the elemental axial stiffness, k. The only difference is that, instead of being associated with the element extension, v, it is associated with the rate of extension $\dot{v}$.

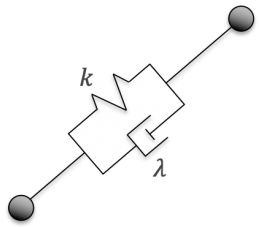

Fig. 7.5 Elemental Link Components for Extensible Cable Model

Similarly to the mass and stiffness matrices, for the 3D model, the damping matrix D will have dimensions $3N \times 3N$ assuming a stationary base, and can be thought of as containing 9 sub-matrices.

$$D = \begin{bmatrix} D_1 & D_2 & D_3 \\ D_4 & D_5 & D_6 \\ D_7 & D_8 & D_9 \end{bmatrix} \tag{7.112}$$

Since the only sub-matrix associated with the axial damping is D_5 which corresponds to the $\dot{v}_j$ states, the remainder of the sub-matrices will contain only zeros. Analogous to the axial stiffness, the entries of sub-matrix D_5 can be calculated directly using the following expressions:

$$D_5(i,j)_{i=j,i<N} = \lambda \quad D_5(i,j)_{i=j,i=N} = \lambda_N \quad D_5(i,j)_{i\neq j} = 0 \tag{7.113}$$

Once again, for a non-stationary base, the damping matrix D_{mb} gains an additional row and column, making its dimensions $3N+2 \times 3N+2$. These will only be non-zero at the entries that coincide with the matrix's diagonal, where they will contain the damping value associated with the base motion in both the x and y directions, b. Labelling the additional sub-matrices in a manner analogous with those of the stiffness matrix in equation 7.109, the nonzero entries of the additional matrix components are therefore:

$$D_{0,1} = D_{0,6} = b \tag{7.114}$$

For the 2-dimensional model, the damping matrix is the same, but without the rows and columns which correspond to the Euler angle ϕ.

7.6 Mass and Stiffness Matrices for 3D Inextensible Model

The equations of the system's total kinetic and potential energies can be easily altered to account for the system's inextensibility by setting $v_j = \dot{v}_j = 0$ and therefore making the element lengths constant, i.e. $l_j = L$. The mass, stiffness and damping matrix entry expressions can also be adjusted by setting the equilibrium element lengths to $l_{0,j} = L$ and removing all of the rows and columns that correspond to the v_j coordinates and their derivatives, yielding matrices of order $2N+2$. The mass matrix collapses to:

$$M_{mb,inext} = \begin{bmatrix} M_{0,1} & M_{0,2} & M_{0,3} & M_{0,5} \\ M'_{0,2} & M_{0,6} & M_{0,7} & M_{0,9} \\ M'_{0,3} & M'_{0,7} & M_1 & M_3 \\ M'_{0,5} & M'_{0,9} & M_7 & M_9 \end{bmatrix} \tag{7.115}$$

For an tethered balloon model with an inextensible cable the mass matrix can therefore be found directly using the following expressions:

$$M_1(i,j)_{i=j} = L_i^2\left((N-i)m+m_b\right) \tag{7.116}$$

$$M_1(i,j)_{i\neq j} = L_iL_j\left((N-i)m+m_b\right)\left(\cos\theta_{0,i}\cos\theta_{0,j}\cos\left(\phi_{0,i}-\phi_{0,j}\right)+\sin\theta_{0,i}\sin\theta_{0,j}\right) \tag{7.117}$$

$$M_9(i,j)_{i=j} = L_i^2\left((N-i)m+m_b\right)\sin^2\theta_{0,i} \tag{7.118}$$

$$M_9(i,j)_{i\neq j} = L_iL_j\left((N-i)m+m_b\right)\sin\theta_{0,i}\sin\theta_{0,j}\cos\left(\phi_{0,i}-\phi_{0,j}\right) \tag{7.119}$$

$$M_3(i,j)_{i=j} = M_7(i,j)_{i=j} = 0 \tag{7.120}$$

$$M_3(i,j)_{i>j} = L_iL_j\left((N-i)m+m_b\right)\cos\theta_{0,i}\sin\theta_{0,j}\sin\left(\phi_{0,i}-\phi_{0,j}\right) \tag{7.121}$$

$$M_3(i,j)_{j>i} = L_iL_j\left((N-j)m+m_b\right)\cos\theta_{0,i}\sin\theta_{0,j}\sin\left(\phi_{0,i}-\phi_{0,j}\right) \tag{7.122}$$

$$M_7(i,j) = M_3(i,j)^T \tag{7.123}$$

$$M_{0,1} = m_{base}+(N-1)m+m_b \tag{7.124}$$

$$M_{0,2} = 0 \tag{7.125}$$

$$M_{0,6} = m_{base}+(N-1)m+m_b \tag{7.126}$$

$$M_{0,3}(1,j) = ((N-j)m+m_b)l_{0,j}\cos\theta_{0,j}\cos\phi_{0,j} \tag{7.127}$$

$$M_{0,5}(1,j) = -((N-j)m+m_b)l_{0,j}\sin\theta_{0,j}\sin\phi_{0,j} \tag{7.128}$$

$$M_{0,7}(1,j) = ((N-j)m+m_b)l_{0,j}\cos\theta_{0,j}\sin\phi_{0,j} \tag{7.129}$$

$$M_{0,9}(1,j) = ((N-j)m+m_b)l_{0,j}\sin\theta_{0,j}\cos\phi_{0,j} \tag{7.130}$$

The stiffness matrix collapses in an analogous way, and the entries can be calculated using the following expressions:

$$\begin{aligned} K_1(i,j)_{i=j} = &-L_i\left(mg(N-i)+m_bg-F_{lift}\right)\cos\theta_{0,i} \\ &+L_i\left(F_{x,i}+F_{x,i+1}\ldots+F_{x,N}\right)\sin\theta_{0,i}\cos\phi_{0,i} \\ &+L_i\left(F_{y,i}+F_{y,i+1}\ldots+F_{y,N}\right)\sin\theta_{0,i}\sin\phi_{0,i} \end{aligned} \tag{7.131}$$

$$\begin{aligned} K_2(i,j)_{i=j} = K_3(i,j)_{i=j} = &L_i\left(F_{x,i}+F_{x,i+1}\ldots+F_{x,N}\right)\cos\theta_{0,i}\sin\phi_{0,i} \\ &-L_i\left(F_{y,i}+F_{y,i+1}\ldots+F_{y,N}\right)\cos\theta_{0,i}\cos\phi_{0,i} \end{aligned} \tag{7.132}$$

$$\begin{aligned} K_4(i,j)_{i=j} = &L_i\left(F_{x,i}+F_{x,i+1}\ldots+F_{x,N}\right)\sin\theta_{0,i}\cos\phi_{0,i} \\ &+L_i\left(F_{y,i}+F_{y,i+1}\ldots+F_{y,N}\right)\sin\theta_{0,i}\sin\phi_{0,i} \end{aligned} \tag{7.133}$$

$$K_1(i,j)_{i\neq j} = K_2(i,j)_{i\neq j} = K_3(i,j)_{i\neq j} = K_4(i,j)_{i\neq j} = 0 \tag{7.134}$$

$$K_{0,1} = K_{0,2} = K_{0,6} = K_{0,3}(1,j) = K_{0,5}(1,j) = K_{0,7}(1,j) = K_{0,9}(1,j) = 0 \tag{7.135}$$

Chapter 8

Theoretical Validations of Nonlinear and Linear Models

In this section, the nonlinear and linearized system models are validated by comparing them to each other and to the analytically derived expected responses for various aspects of the system's behaviour. The transient responses of the two models are initially compared for arbitrary small amplitude 3-dimensional motion for both an open loop and closed loop system. The systems are then compared for various vibration modes, including hanging chain dynamics, tethered balloon dynamics and bending beam dynamics to ensure that all aspects of the nonlinear system model have been linearized correctly. To then validate the responses of both the models, the number of cable elements is increased to $N = 300$, and the responses of the systems are compared to those derived theoretically for continuous systems.

8.1 Comparing the Linear and Nonlinear Responses for Small Amplitude Motion

A quick way of validating the linearized system is to check it against the nonlinear model for small amplitude vibration. In order to do this, the parameters of the two models are set as being the same to represent the same physical model, the same external conditions are applied, and the same initial state vector is selected for the two models. This was initially done for both systems being open loop systems, i.e. without the implementation of feedback, and then feedback control was introduced to both models.

As long as the initial state deviation is small enough such that the subsequent motion about the equilibrium is of small amplitude and linearization approximations are therefore

valid, the two systems are expected to produce close responses. The system parameters and initial conditions chosen in this section are completely arbitrary, with the sole aim of demonstrating that the dynamic behaviour of the two models varies by a very small percentage for small amplitude motion.

In this section, the wind drag is taken as being independent of the velocity of the tether elements and balloon, as this component is neglected in the linearization of the system due to the fact that it contains the square of a small value (the component of the drag force that opposes motion is proportional to the square of the velocity). For the sake of the validation of the remainder of the linearization, the wind damping is therefore also removed in the nonlinear model. The wind drag due to the wind's velocity is kept as normal.

The arbitrary selected parameters for this validation are summarised in Table 8.1.

Table 8.1 Tethered Balloon System Parameter Values for Validation

Parameter	Value
Tether Length, L (m)	20
Tether Diameter, r_t (m)	0.001
Tether Density, ρ (kgm^{-3})	1600
Tether Young's Modulus, E (GPa)	0.5
Damping Coeff times Length, λL (Ns)	10
Balloon Diameter, d_b (m)	1
Balloon Thickness, t_b (μm)	50
Balloon Wall Density, ρ_b (kgm^{-3})	1000

In this case, the tether has a low stiffness. This was selected so that the equilibrium element extensions are non-zero and the system exhibits significant axial motion, in order to validate that aspect of the linearization as well. The combination of parameters result in a taut and stretched tether.

A steady-state uniform wind velocity profile of magnitude 2m/s in the positive x-direction is selected, again, arbitrarily. The system's equilibrium state under these external conditions is calculated, and these values, along with the system's parameter values, are inserted into the expressions for the mass, stiffness and damping matrix entries derived in Section 7, producing a linearized version of the system.

8.1.1 Open Loop System Validation

The open loop tethered balloon linear system is initially validated for a stationary base. An in-plane initial angular velocity is applied to the balloon in the positive θ-direction such that the initial speed of the balloon is 0.3m/s. This is translated into Cartesian velocity values for

the nonlinear system's initial state vector. Figure 8.1 displays the motion of 3 arbitrary points along the tether's length in the x-direction for both systems as a result of the initial condition applied. The nonlinear system response is plotted in red and linear system response in black.

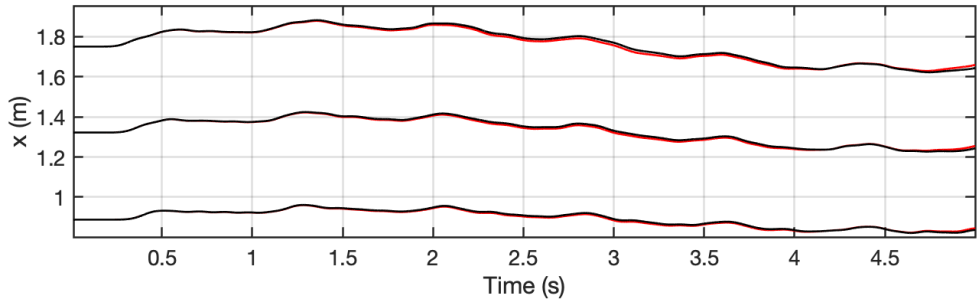

Fig. 8.1 Horizontal motion in the x-direction of equally spaced points along the tether for the nonlinear (red) and linear (black) system models for identical initial conditions (impulse on balloon in $\dot{\theta}$ direction)

To highlight the precision of the higher frequency motion in the response, Figure 8.2 shows a close-up of how the Euler angle θ varies with time for the tether elements for a shorter time frame. A very good agreement is seen between the nonlinear and linear models, validating the linearization process.

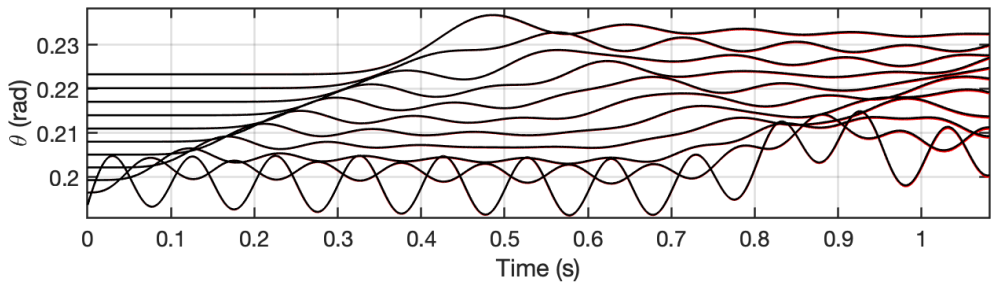

Fig. 8.2 Variations in θ coordinates of equally spaced points along the tether for the nonlinear (red) and linear (black) system models for identical initial conditions (impulse on balloon in $\dot{\theta}$ direction)

The tethered balloon system model is 3-dimensional however, and so a 2-dimensional validation of the linearized model is insufficient. To validate all aspects of the linear model, an out-of-plane initial velocity is applied to the balloon in the positive y-direction of magnitude 0.3m/s. The resultant out of plane motion of equally spaced points along the tether is plotted in Figure 8.3 for the two models.

Once again, the agreement of the higher frequency modes that are present in the response is shown using a short duration plot comparing the variation of the Euler angles ϕ of the tether elements for the two models in Figure 8.4.

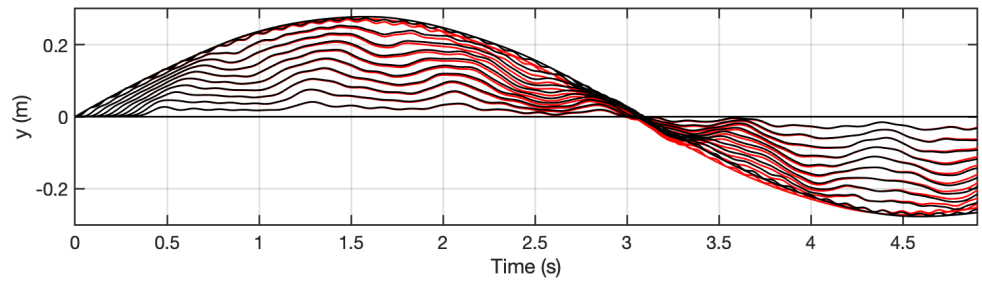

Fig. 8.3 Horizontal motion in the y-direction of equally spaced points along the tether for the nonlinear (red) and linear (black) system models for identical initial conditions (impulse on balloon in $\dot{\phi}$ direction)

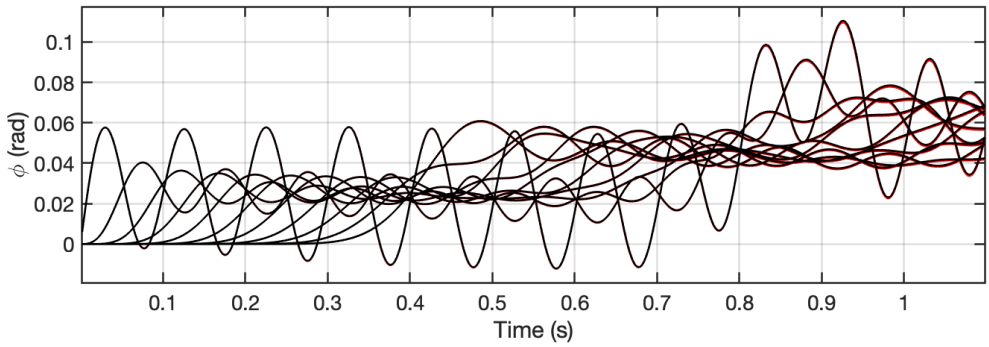

Fig. 8.4 Variations in ϕ coordinates of equally spaced points along the tether for the nonlinear (red) and linear (black) system models for identical initial conditions (impulse on balloon in $\dot{\phi}$ direction)

In order to validate the linearization of the dynamics of the system's movable base, an arbitrary input vector can be applied to the open loop linear and nonlinear systems for comparison. In the open loop system case, the input is the force vector and can be set to anything. A random signal is generated for both the x and y directions independently and these are applied to the base as input force signals. The resultant base speed in the x and y directions are plotted in 8.5 for the two models.

While the displacement of the base does not need to be small and so no approximations are made for its magnitude, slight discrepancies in the responses may arise due to the tensions exerted on the base by the fixed end of the tether which may vary in magnitude and direction. The base motion is seen to agree closely for an open loop input signal for the two models. Once again, the motion of the tethered balloon system was also seen to agree closely for the two models.

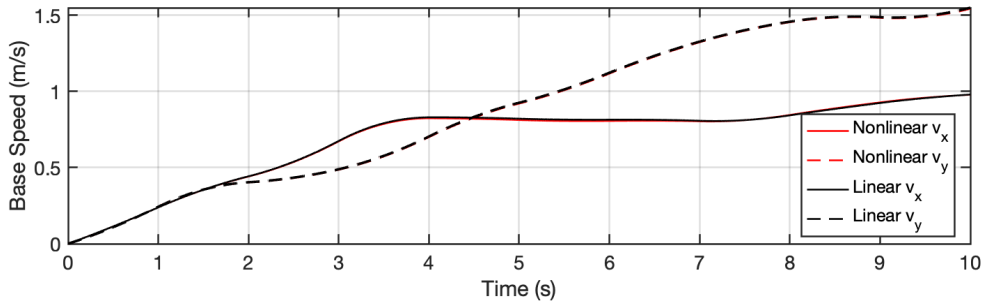

Fig. 8.5 Base motion in response to a randomly generated signal for the nonlinear (red) and linear (black) models in the x and y directions

8.1.2 Closed Loop System Validation

The linearized system model can be used to produce a suitable feedback gain matrix K using LQR. Although the controller is designed based on the linear system, it is more beneficial to model the closed loop system using the nonlinear tethered balloon system model as this is a more accurate representation of the system. For the HATB case studies, it is expected that larger amplitude motion will be observed and nonlinearities will become significant and affect the system's response. In this section, the closed loop nonlinear model is validated against the closed loop linear model for small amplitude vibration.

For the same system used in the previous section, the linear model along with an arbitrarily selected cost function, is used to produce a matrix K for the system. The feedback gain designed based on the linearized system is then implemented into the nonlinear system. Within the ode45 function, at each time step the input force values are calculated based on the system's current state vector using the gain matrix K as follows:

$$\mathbf{u} = \mathbf{F} = \bar{N}\mathbf{r} - K\mathbf{x} \tag{8.1}$$

The instantaneous x and y components of the input force are calculated and applied to the base at each time step, resulting in a nonlinear closed loop system model.

For the case of an in-plane initial velocity applied to the balloon identical to that considered in Section 8.1.1, the closed loop nonlinear system response was compared to the closed loop linear system response. Adjusting the feedback controller to improve the system's dynamic response is not the focus of this section, and it is assumed that any base motion is feasible.

Figure 8.6 shows the closed loop system responses of the nonlinear system (red) and the linear system (black). The open loop system response is plotted in grey alongside these, for reference.

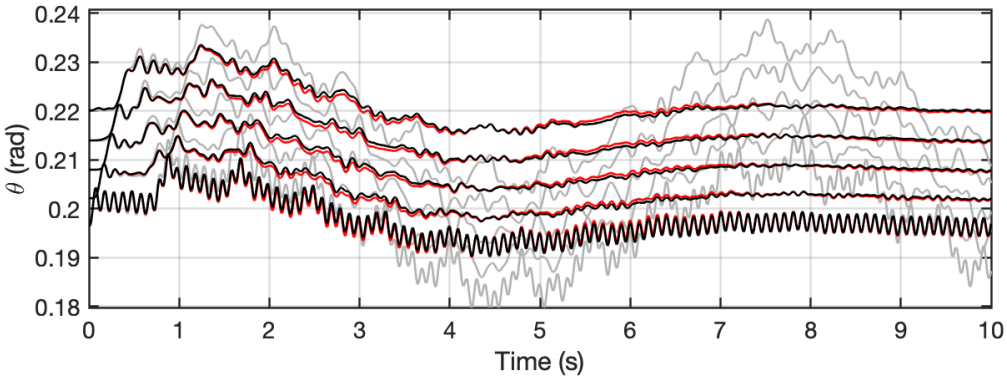

Fig. 8.6 Comparison of the closed loop responses of the nonlinear (red) and linear (black) system models. The open loop response is plotted in grey for reference.

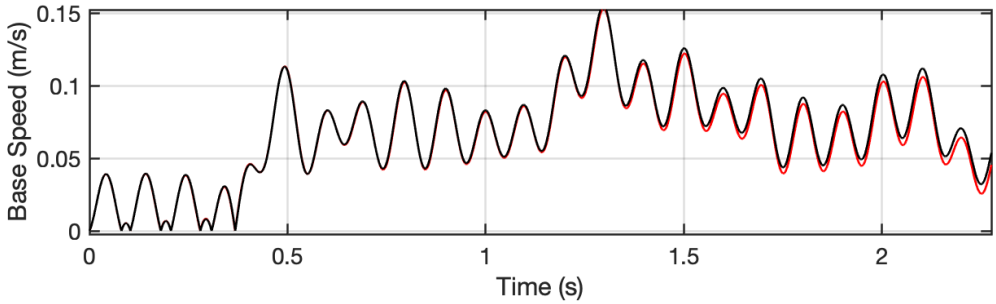

Fig. 8.7 Base speed for the closed loop responses of the nonlinear (red) and linear (black) system models

Figure 8.7 displays a comparison of the closed loop base motion for each of these.

8.2 Hanging Chain Validation

In this section, the cable model is validated using the hanging chain dynamics theory in Section 4.1 for many cable elements. Equation 5.3 can be used to validate the discretized model of the tether by determining the natural frequencies of its free vibrations as a hanging cable. Free vibrations can be induced by applying an initial displacement or velocity to the hanging chain's equilibrium state. In order to quantitatively validate the system's natural frequencies, applying an initial velocity to one of the system's elements is a good way of initiating motion. This is because imposing an initial velocity to one of the masses in the system is practically equivalent to applying an impulse to the system at that point, and impulses often result in the excitation of multiple of the system's natural frequencies at once. A fast Fourier transform can then be applied to the system's motion, and the natural

frequencies can be deduced all at once (although some may be missing depending on the specific driving and observation points used).

The expression for the natural frequencies of a hanging chain is rewritten for the the calculation of the frequency f in Hz:

$$f_M = \frac{\omega_M}{2\pi} = \frac{r_M}{4\pi}\sqrt{\frac{g}{L}} \tag{8.2}$$

Here, r_M is the Mth root of the zero order Bessel function. The first few values of these are:

$$r_M = 2.4048,\ 5.5201,\ 8.6537,\ 11.7915\ldots \tag{8.3}$$

The natural frequencies of a hanging chain are therefore only dependent on the chain's length L. A chain of length $L = 3m$ is considered in this section. Before theoretical validations are made, the equivalent linear and nonlinear hanging chain models are compared to ensure that they produce sufficiently similar responses for small amplitude motion. This is done firstly as a method of validating the system's linearization, and secondly, so that if the systems behave very closely, the linear and more computationally efficient model can then be used in the theoretical validation. This is useful because the number of discretized cable elements is set to N=300 in the validation, to better mimic a continuous system.

For $N = 15$, the transient responses of the two systems are compared for an impulse in Figure 8.8. The magnitude of the impulse was kept small enough such that the amplitude of motion was of the order of 10^{-5} as seen in the Figure. The nonlinear response is plotted in red, and the linear response is plotted in black.

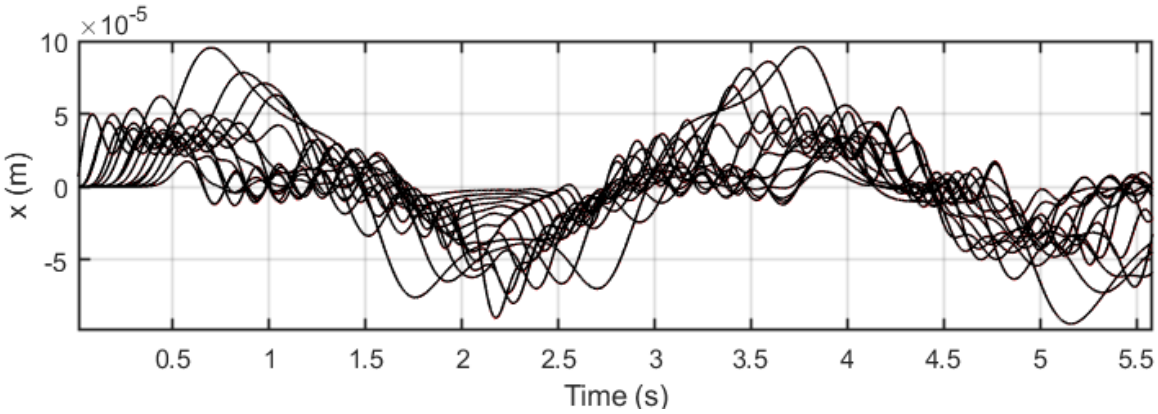

Fig. 8.8 Impulse response of a hanging chain model of length L=3m for the nonlinear model (red) and the linearized model (black)

It is clear that the responses are almost perfectly identical in the time domain. FFTs are taken for long duration impulse responses and compared in Figure 8.9. Once again, very close agreement is seen between the linear and nonlinear hanging chain models.

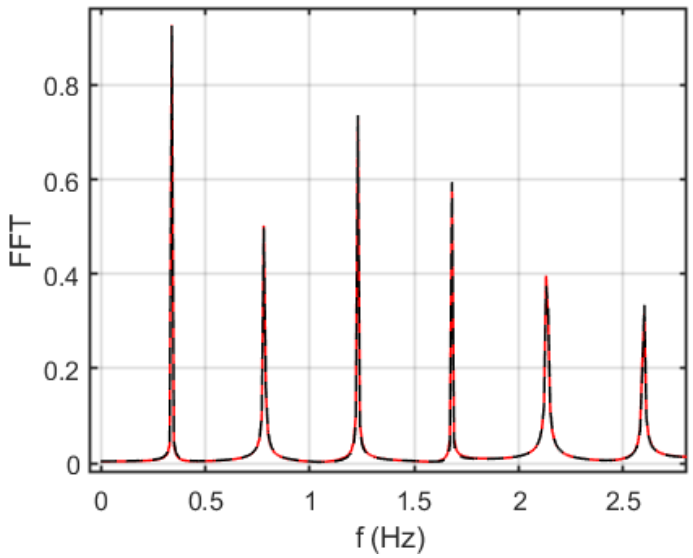

Fig. 8.9 FFT for the impulse response of a hanging chain model of length L=3m for the nonlinear model (red) and the linearized model (black)

Now that the linear hanging chain model has been validated, the number of cable elements is increased to $N = 300$ for the theoretical validation. The first few theoretical natural frequencies for a hanging chain of length $L = 3m$ are calculated:

$$f_M = \frac{r_M}{4\pi}\sqrt{\frac{g}{L}} = 0.3461Hz,\ 0.7943Hz,\ 1.2453Hz,\ 1.6968Hz\ldots \tag{8.4}$$

For $N = 300$, the FFT of the system's impulse response is taken and plotted in Figure 8.10. The peak values are displayed, and the theoretical natural frequencies are plotted alongside these in dashed lines for reference.

A very close agreement is seen between the discretized software model's response, and the natural frequency values predicted analytically. The accuracy of the FFT plots is also limited by the time duration of the signal onto which it is applied, which may be a significant contributing factor to the discrepancies between the values. The largest percentage error between the model's natural frequencies and the predicted ones is 0.07%.

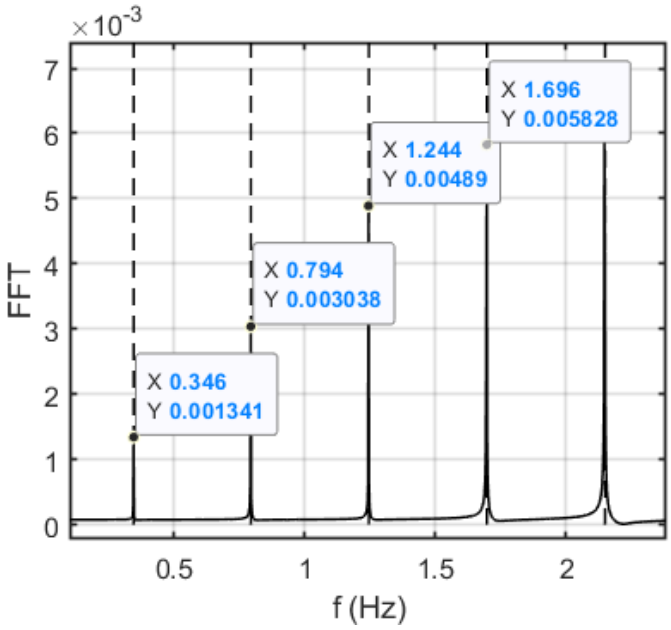

Fig. 8.10 FFT for the impulse response of a hanging chain model of length L=3m for N=300

8.3 Theoretical validations of Linearized Balloon Model

Several different aspects of the tethered balloon model can be validated against theory by making adjustments to system's parameters such that they begin to approach simpler system's for which analytical theory is readily available. These include a stretched string, a pendulum, bending beams with a variety of boundary conditions, and beams under tensile loading. The bending properties are validated in Section 8.4. In this section, theoretical validations are made on the tethered balloon model using the theory derived on wave propagation in stretched cables and the approximate frequency response of a tethered balloon system. The bending stiffness is set to zero in this section.

8.3.1 Wave Propagation Validation

In this section, the cable model is validated by comparing its transient impulse response to the expected behaviour derived in Section 4.2. Qualitatively, a step wave travelling from the impulse point in both directions is expected to be seen. The wave velocity and amplitude of the step wave can be checked against the theory for a quantitative validation of the response. While the theory is derived for a semi-infinite stretched string, for impulse magnitudes such that the horizontal deviation is small compared to the length of the cable, the theory is expected to apply for the tethered balloon system.

The wave propagation theory also assumes a uniform tension in the cable, which is not the case for a vertical tether. To minimise the effects of the varying tension along the tether due to its own weight, a relatively large lift force is used, reducing the percentage difference in the tension at the top and bottom of the tether.

As derived in Section 4.2, qualitatively, the response of the system to an impulse is a travelling step function wave. Quantitatively the wave speed should be c (equation 4.20), and the transverse amplitude of the wave should be equal to $A_0/2c$. A_0 is the magnitude of the delta function that describes the initial velocity function along the length of the cable (equation 4.32). For a discretized cable model, the initial velocity profile will not be delta function. For an impulse applied to an arbitrary jth element in the discretized cable model, a diagram of the initial velocity profile along the cable's length is displayed in Figure 8.11.

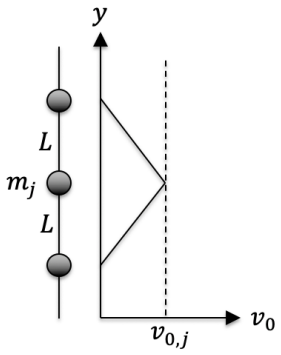

Fig. 8.11 Initial velocity function for the impulse equivalent of a discretized system

As the element length L decreases, the initial velocity profile more closely resembles that of a delta function. A_0 is effectively the area under the delta function that defines the initial velocity for the continuous system in the theory, and its equivalent value for the discrete system can be found by calculating the area under the velocity profile:

$$A_{0,d} = Lv_{0,j} \tag{8.5}$$

The value of A_0 is also known to be equal to the following expression in a continuous system:

$$A_0 = I/\mu \tag{8.6}$$

Here, I is the magnitude of the impulse and μ is the mass per unit length of the cable. A quick calculation shows that this is also satisfied for the analogous discrete system:

$$A_{0,d} = \frac{I}{\mu} = \frac{m_j v_{0,j}}{\mu} = \frac{\mu L v_{0,j}}{\mu} = Lv_{0,j} \tag{8.7}$$

A_0 is therefore equal to the magnitude of the impulse divided by the mass per unit length of the cable. The amplitude of the resulting step wave is therefore equal to:

$$x_0 = \frac{A_0}{2c} = \frac{I/\mu}{2\sqrt{T/\mu}} \tag{8.8}$$

A balloon impulse is considered. The theory assumes that the impulse takes place somewhere along a semi-infinite string fixed at one end. To adapt this to the tethered balloon case (not semi-infinite) in which the impulse is applied to the balloon, the value of the impulse applied to the balloon is doubled in the equations above so that it is equivalent to a continuous string rather than a free end. This is due to the equivalency displayed in Figure 8.12.

Fig. 8.12 Equivalent impulse magnitude for a semi-infinite string and for an impulse applied to the free end of a non-semi-infinite string

For a balloon impulse, $I_{bal} = I_{inf}/2$ and the amplitude of the step wave therefore becomes:

$$x_{0,b} = \frac{I_{inf}/\mu}{2\sqrt{T/\mu}} = \frac{I_{bal}/\mu}{\sqrt{T/\mu}} \tag{8.9}$$

A balloon impulse is considered in the validation. The mass of the base was increased to a very large value to better mimic the behavior of a fixed end. While a model with a fixed end could have been used, this was done to more accurately pinpoint the time taken for the wave to reach the tether's fixed end. A large value was used for the lift to increase the tension in the tether and make the variations in tension due to the tether's weight less significant.

Arbitrary system values were selected. This was done for a balloon tethered at 20m high, for 15 elements. The mass of the balloon was set to 0.05kg, the mass per unit length of the tether set to 0.02kg/m and the lift force was set to 100N. The tension was found to vary between 99.6N at the tether's top and 96.0N at the tether's bottom. An average value of 98N was used in calculations.

The theoretical wave speed was calculated:

$$c = \sqrt{\frac{T}{\mu}} = \sqrt{\frac{98}{0.02}} = 70m/s \tag{8.10}$$

The time taken for the square wave to reach the bottom should therefore be:

$$t = \frac{L}{c} = \frac{20}{70} = 0.286s \tag{8.11}$$

This can be compared to the delay in the motion of the tethered balloon's base in Figure 8.13 that displays the motion of the heavy base with time.

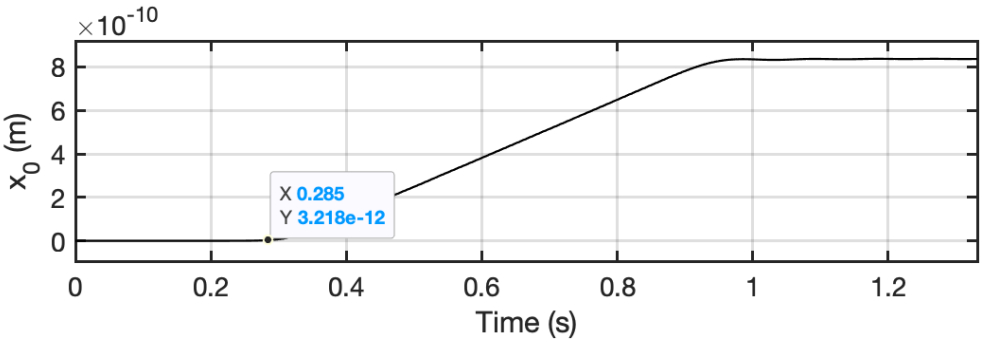

Fig. 8.13 Base motion for an impulse applied to the balloon

It can be seen that there is a close agreement between the analytically predicted time taken for the wave to reach the base and that seen in the model's response, with a percentage error of about 0.35%. This error can be accounted for by the fact that the tension is not constant throughout the cable and the fact that the system is discretized rather than continuous.

The perpendicular deviations from the equilibrium of the points along the tether are plotted in Figure 8.14 and a travelling step wave can clearly be observed. When the wave reached the heavy base of the tether it is seen to be reflected, as expected. The corner of the step function is blunt and not perfectly horizontal however, which is expected for a discretized cable system that cannot exhibit high frequency modes. A sharper step wave is expected for a system discretized into smaller elements.

In order to calculate the theoretical amplitude of the step wave, the value of A_0 must first be calculated:

$$\begin{aligned} A_0 = &\frac{I_{inf}}{\mu} = \frac{2I_{bal}}{\mu} = \frac{2m_{bal}\dot{x}_{0,bal}}{\mu} = \frac{2m_{bal}\dot{\theta}_{0,bal}L_{bal}}{\mu} \\ = &\frac{2 \times 0.05 \times 0.001 \times 1.333}{0.02} = 0.0067m^2/s \end{aligned} \tag{8.12}$$

The theoretical amplitude of the step wave can then be calculated:

$$x_0 = \frac{A_0}{2c} = \frac{0.0067}{140} = 4.786 \times 10^{-5}m \tag{8.13}$$

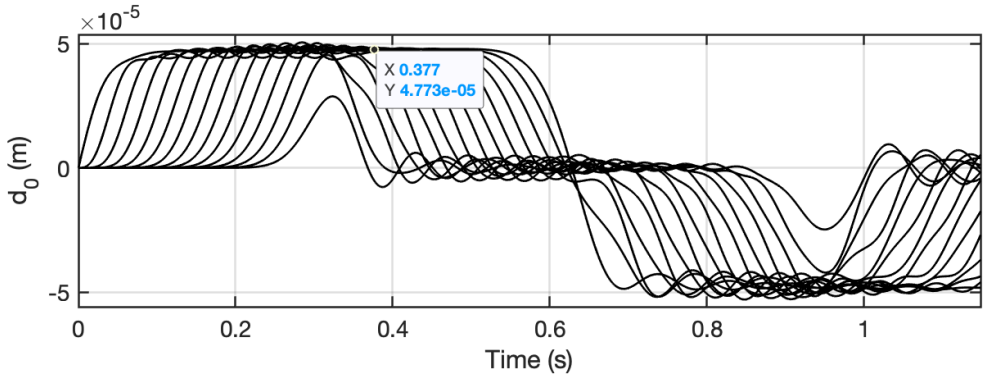

Fig. 8.14 Lateral displacements from the equilibrium of equally spaced points along the cable in response to a balloon impulse

The amplitude of the step wave in the model's impulse response is marked in Figure 8.14. This was found to agree very closely with the predicted amplitude, with a percentage error of only 0.27%. The cable model's impulse response is seen to behave as expected. Increasing the number of elements in the cable is expected to reduce these errors further.

8.3.2 Frequency Response Validation

In this section, the frequency response of the tethered balloon model is validated against the approximate expected natural frequencies of the system derived in Section 4.3. In order to validate the natural frequencies found by taking the FFT of the system's response more accurately, the system is made to better resemble those for which the natural frequencies are known. By increasing the balloon's mass so that it is significantly larger than the mass of the tether and therefore has a significantly larger inertia, the tether's natural frequencies should resemble those of a pinned-pinned stretched string. For the system used in the previous section, the balloon mass was increased to 5kg for this purpose. While this results in a reduction in the overall tension in the tether, for a 100N lift force the tension variation along the tether's length remains small compared to its absolute value making it approximately uniform (the tension difference between the tether's ends is approximately 8%).

Before increasing the number of elements of the cable in the linear model to values large enough to mimic a continuous system, the linear system is first checked against the nonlinear system to ensure that it is a good substitute for validating the nonlinear system model. For a tether impulse, the small amplitude transient motion is compared for the two models in the time domain in Figure 8.15. The linear system response is plotted in black and the nonlinear system response is plotted in red. The response is almost identical for a long duration of time.

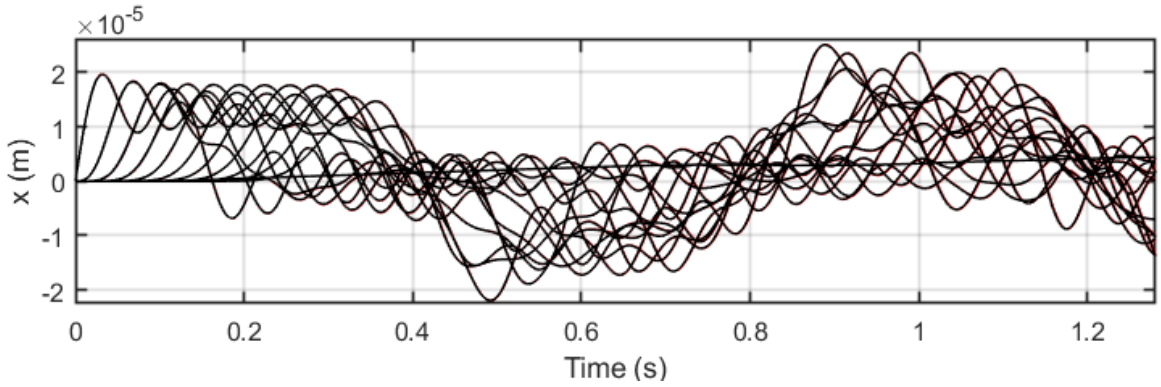

Fig. 8.15 Comparison of time domain transient response of tethered balloon system for the nonlinear (red) and linear (black) models.

The FFTs of the responses are also compared in Figure 8.16. The natural frequencies of the linear and nonlinear systems are seen to agree very closely, with errors smaller than 0.5%.

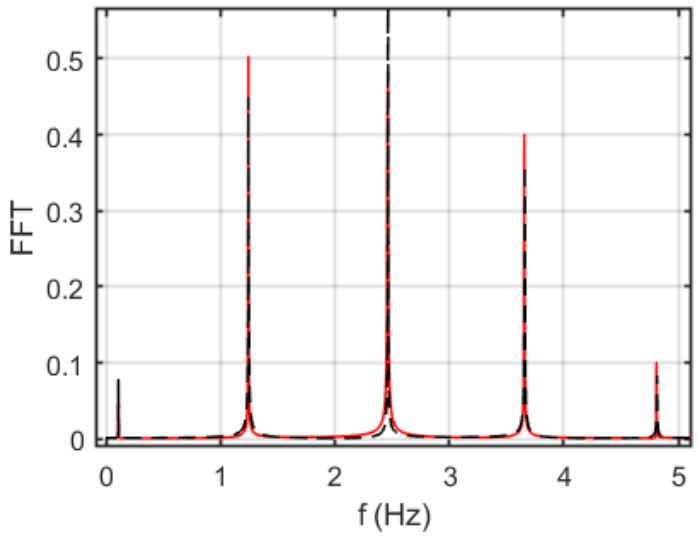

Fig. 8.16 Comparison of the FFT of the tethered balloon system response for the nonlinear (red) and linear (black) models

Since the linear model has been proven to behave very closely to the nonlinear model, it is then used in the theoretical validation, for which the number of cable elements is increased to N=300, for a better comparison to the theoretical values derived for a continuous system.

For this system, the tension at the bottom of the tether is 47N and the tension at the top is approximately 51N. An average value of $T = 49N$ was used in calculations. For the specific

case in question the equivalent stretched string natural frequencies are calculated:

$$f_{string} = \frac{n}{2L}\sqrt{\frac{T}{m'}} = \frac{n}{2\,(20)}\sqrt{\frac{49}{0.02}} = 1.2374,\ 2.4749,\ 3.7123,\ 4.9497\ldots \tag{8.14}$$

The FFT of the impulse response of the system for N=300 is plotted in Figure 8.17. The frequencies of the peak values are displayed, and the analytically calculated natural frequencies are plotted alongside these in dashed lines. It can be seen that the second natural frequency onwards closely resemble those of an equivalent stretched string, as expected.

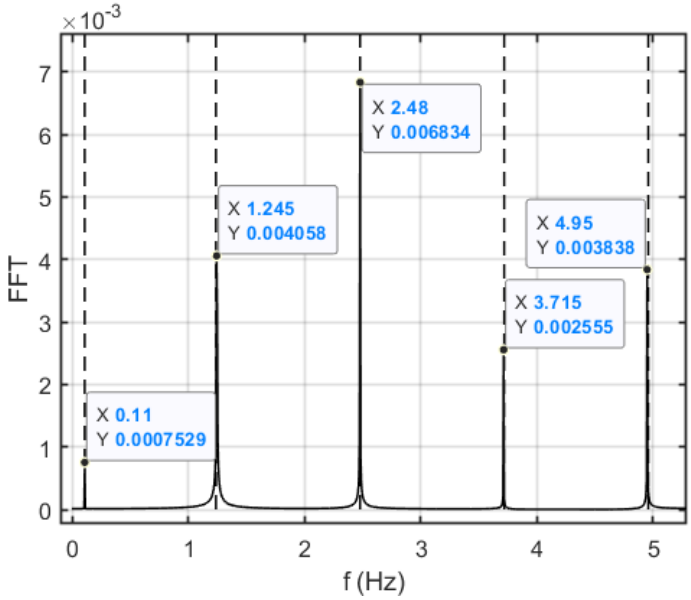

Fig. 8.17 FFT of the tethered balloon system response for N=300

The largest percentage error in the model's natural frequencies compared to those derived analytically is 0.6%. The likely source of error in these values is the non-uniform tension along the tether which is likely to have an impact on the system's frequency response.

The lowest frequency mode is unaccounted for by the stretched string approximation. For this mode, the balloon is no longer approximated as a node, but as an antinode. This motion resembles that of an upside-down pendulum, with the cable approximated as being rigid. Inserting the system's parameter values into the expression derived for the equivalent pendulum system produces a predicted value for the system's lowest natural frequency:

$$f_{pendulum} = \frac{1}{2\pi}\sqrt{\frac{F_L - M_{comb}g}{M_{comb}L_{comb}}} = \frac{1}{2\pi}\sqrt{\frac{100-(5+0.02\times 20)\times 9.81}{(5+0.02\times 20)\times 19}} = 0.108Hz \tag{8.15}$$

The lowest natural frequency of the system therefore agrees with that of an equivalent up-side-down pendulum closely, with a percentage error of a bit below 2%. The close agreement of the system's natural frequencies with those of systems it is expected to behave similarly to increases confidence in the tethered balloon system model.

8.4 Validating the System's Bending Properties - Beam Approximation

Now that the axial/string-like properties of the tether have now been validated by modeling it as a stretched string with no bending stiffness, the rotational springs used in the model should also be validated using beam theory. To do this, the bending stiffness was increased so that the tether behaves like a beam. The gravitational acceleration, g, was set to zero to eliminate the influence of gravity on the system. For the bending beam case, boundary conditions need to be considered. Through the application of simple adjustments to the model's parameters, the system can be made to behave as if beam end constraints are present without much change to the system model.

In comparing the discretized system's beam-like response to continuous beam theory, the relationship between the rotational spring stiffness k_b and the flexural rigidity of an equivalent continuous structure EI derived in Section 3.1.2 can be validated. If the natural frequencies of the discretized model agree with those derived theoretically for an equivalent continuous system, that is a good indication that the established relationship between the two parameters is valid.

Euler-Bernoulli Beam Theory

Initially the tension was set to zero in the tether so that simple Euler-Bernoulli Beam Theory can be applied to the system. Under no external force, the ordinary differential equation of the system is:

$$EI\frac{\partial^4 y}{\partial x^4} + \mu\frac{\partial^2 y}{\partial t^2} = 0 \tag{8.16}$$

Setting $y = Ye^{j\omega t}$, the equation becomes:

$$EI\frac{\partial^4 Y}{\partial x^4} - \omega^2 \mu Y = 0 \tag{8.17}$$

The general solution for this is:

$$Y_n = A_1 cosh(\beta_n x) + A_2 sinh(\beta_n x) + A_3 cos(\beta_n x) + A_4 sin(\beta_n x) \tag{8.18}$$

Here, β_n is equal to:

$$\beta_n = \left(\frac{\mu\omega_n^2}{EI}\right)^{1/4} \tag{8.19}$$

A_1, A_2, A_3 and A_4 are constants that depend on the boundary conditions of the system. Two different sets of boundary conditions are considered in the validation: a clamped-free (cantilever) beam and a clamped-pinned beam.

Clamped-Free Beam Validation

A cantilever beam is initially considered. The discretized software model can be altered to resemble and therefore behave like this system. This can either be done by setting the rotational spring at the fixed end of the beam to a very large stiffness or by constraining the acceleration of the first element to zero. This limits the rotation of the fixed end to a very small value or zero respectively, as required. With the other end remaining free as it was, the system is expected to behave like a cantilever.

In the theoretical derivation, boundary conditions are also imposed at the fixed end that represent a clamped constraint: the displacement and gradient are equal to 0.

$$Y(0) = 0,\ \frac{dY}{dx}(0) = 0 \tag{8.20}$$

At the free end, the bending moment and the shear force must be equal to zero. Since no external forces are applied to the free end, internal forces must also be zero for the equilibrium of an infinitesimal segment cut from that end of the beam. Mathematically this translates into the second and third derivatives of the displacement at $x = L$ being equal to 0.

$$\frac{d^2Y}{dx^2}(L) = 0,\ \frac{d^3Y}{dx^3}(L) = 0 \tag{8.21}$$

Applying these boundary conditions, it is found that the natural frequencies are governed by the following expression:

$$cosh(\beta_n L)\, cos(\beta_n L) + 1 = 0 \tag{8.22}$$

The solutions of this can be found numerically, whether on Matlab using *vpasolve* or using the Newton-Raphson method. The first few solutions are:

$$\beta_1 L = 1.875,\ \beta_2 L = 4.6941,\ \beta_3 L = 7.8548,\ \beta_4 L = 10.9955 \tag{8.23}$$

The natural frequencies can then be calculated using the following relationship:

$$\omega_n = (\beta_n L)^2 \sqrt{\frac{EI}{\mu L^4}} \tag{8.24}$$

For $L = 20m$, a flexural rigidity of $EI = 2627Nm^2$ and a mass per unit length $m = 0.02$, the lateral displacement can be equated for the continuous and discrete systems, and the equivalent discrete elemental bending stiffness is calculated and applied to the model. The rotational spring stiffness is found to be $k_b = 12.9kNm/rad$.

Before the linear bending beam model is validated against the theory for N=300 to better mimic a continuous system, it is important to ensure that, for small amplitude motion, the response is very close to that of the equivalent nonlinear model. Once it is confirmed that the linear model behaves sufficiently closely to the nonlinear model, it can be used for the theoretical validation instead, since it is more computationally efficient. For N=15, an impulse is applied to the beam in both the linear and nonlinear models for a comparison. The time domain responses of both models are plotted in Figure 8.18. The nonlinear model response is plotted in red and the linear response in black.

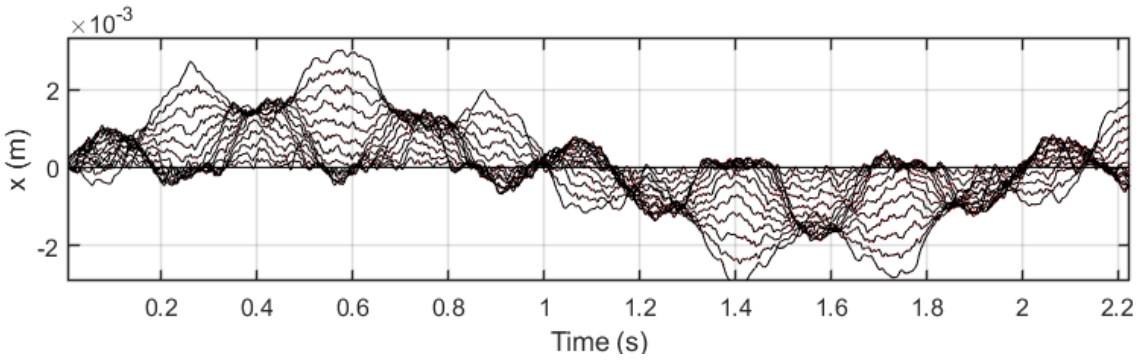

Fig. 8.18 Comparison of the impulse response of the system constrained to behave like a cantilever beam for the nonlinear system model (red) and the linearized system model (black)

It is clear that the responses are almost identical. To further validate the agreement between the two models, the FFT of the response is taken for both models, and these are plotted in Figure 8.19. Once again, an almost identical agreement is observed.

Since it has been confirmed that the nonlinear and linear models behave almost identically for small amplitude motion, the number of elements is increased to $N = 300$ for the theoretical validation.

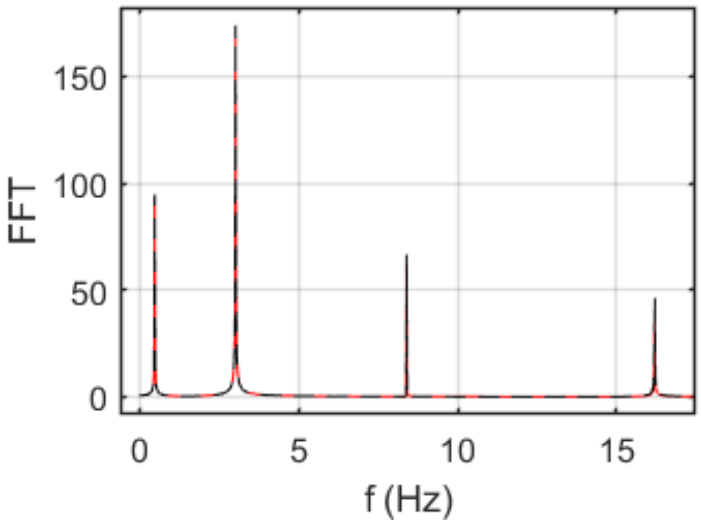

Fig. 8.19 FFT of the impulse response of the system constrained to behave like a cantilever beam for the nonlinear system model (red) and the linearized system model (black)

The system's parameter values are substituted into the following expression to obtain the theoretical natural frequencies of the bending beam system.

$$f_n = \frac{\omega_n}{2\pi} = \frac{(\beta_n L)^2}{2\pi}\sqrt{\frac{EI}{mL^4}} \tag{8.25}$$

The predicted first four natural frequencies of the system are obtained:

$$f_1 = 0.5070Hz \quad f_2 = 3.1748Hz \quad f_3 = 8.8970Hz \quad f_4 = 17.4343Hz \tag{8.26}$$

By applying a Fast Fourier Transform to the system's impulse response, the theoretical natural frequencies are compared to those of the discretized model. Figure 8.20 shows the FFT of the beam's impulse response with the system's first four natural frequencies displayed, alongside the theoretical natural frequencies shown by the dashed lines.

There is a very good agreement between the sets of natural frequencies. The largest percentage error between the theoretical natural frequencies and those produced by the model is 1.4%, for the first mode, with the remainder of the modes having percentage errors smaller than 0.5%. The close agreement in the natural frequencies validates the method of conversion between the continuous and discretized bending parameters.

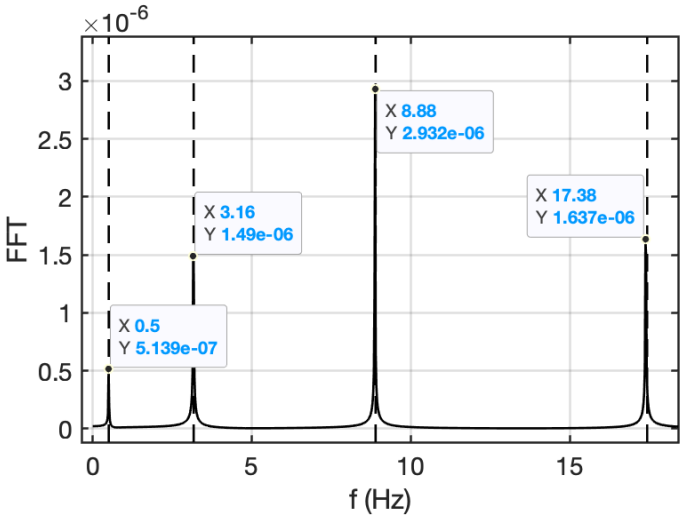

Fig. 8.20 FFT for an impulse response of the system constrained to behave like a cantilever beam for N=300 plotted alongside the theoretical natural frequencies (dashed)

Clamped-Pinned Beam Validation

To further validate the bending properties of the system, the natural frequencies can be checked for those of bending beams with different boundary conditions. In the theoretical analysis, the boundary conditions for a clamped-pinned case are applied. The model can be altered to more closely resemble this, and it is expected that the natural frequencies of the model will shift towards these.

In order to mimic a pinned end, the mass of the element at the free end was increased to a very large value, greatly increasing its inertia. An infinite inertia would be equivalent to a pinned end, so by increasing the inertia to a large value it is expected that the natural frequencies will approach those of a clamped-pinned system. Since the gravitational acceleration g was set to zero, this has no effect on the system's weight or tension.

The same method was followed, initially assuming T=0. Applying the relevant boundary conditions, it is found that the natural frequencies are governed by the following equation:

$$\tan x = \tanh x \tag{8.27}$$

The solutions of this can be found numerically and are widely known. The first four solutions are:

$$\beta_1 L = 3.927, \quad \beta_2 L = 7.069 \quad \beta_2 L = 10.210 \quad \beta_2 L = 13.352 \tag{8.28}$$

The natural frequencies can then be found by substituting these solutions, as well as the system's parameter values, into expression 8.25 once again. For the clamped-pinned approximation, the values of these according to the theory are therefore:

$$f_1 = 2.224Hz \quad f_2 = 7.206Hz \quad f_3 = 15.03Hz \quad f_4 = 25.71Hz \tag{8.29}$$

The FFT of the model's response is plotted in Figure 8.21 for comparison. The values have clearly shifted away from those of a clamped-free system, and approached those of a clamped-pinned system, showing close agreement with the theoretical values calculated for an equivalent clamped-pinned system.

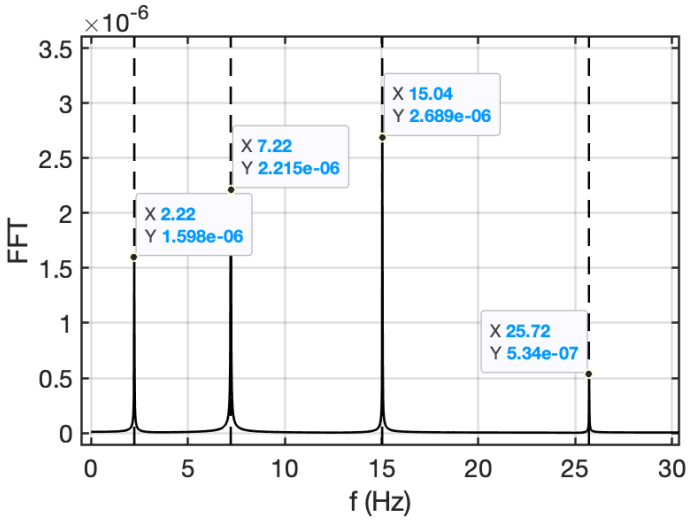

Fig. 8.21 FFT for an impulse response of the system constrained to behave like a clamped-pinned beam for N=300 plotted alongside the theoretical natural frequencies (dashed)

The percentage errors of the natural frequencies are all less than 0.2% for this case.

8.4.1 Beam Under Tensile Loading

Having checked that the tether behaves correctly in bending by increasing its bending stiffness until it behaves in a beam-like manner, tension was re-introduced to the system to compare its behavior to that of a beam under axial tension. This ensures that axial and bending properties combined are behaving correctly.

The ordinary differential equation of a bean under tensile loading takes the form:

$$EI\frac{\partial^4 y}{\partial x^4} - T\frac{\partial^2 y}{\partial x^2} + \mu\frac{\partial^2 y}{\partial t^2} = 0 \tag{8.30}$$

Setting $y = Ye^{j\omega t}$, the expression becomes:

$$EI\frac{\partial^4 Y}{\partial x^4} - T\frac{\partial^2 Y}{\partial x^2} - \omega^2 \mu Y = 0 \tag{8.31}$$

This was initially considered for the cantilever beam system analysed in the previous section, only now with a 'lift' force applied to introduce axial tension. It is expected that the addition of the tensile loading will result in a positive shift in the natural frequencies of the system. Applying the relevant boundary conditions, it can be found that for a clamped-free system, the natural frequencies of the beam under tension can be approximated using the following equation [65]:

$$\frac{f_n|_{P>0}}{f_n|_{P=0}} \approx \sqrt{1 + \frac{P}{|P_{CR}|}\frac{(\beta_1 L)^2}{(\beta_n L)^2}}\ , n = 1,2,3\ldots \tag{8.32}$$

P_{CR} is the beam's buckling load, and depends on the system's boundary conditions. For the clamped-free case in question, it can be calculated using the following expression:

$$P_{CR} = \frac{\pi^2 EI}{4L^2} \tag{8.33}$$

For the case considered in this section, with $EI = 2627Nm^2$ and $L = 20m$:

$$P_{CR} = \frac{\pi^2 (2627)}{4(20)^2} = 16.20N \tag{8.34}$$

For a tension of magnitude 100N, the frequency ratios can therefore be calculated, and from these, the altered natural frequencies are found:

$$\frac{f_1|_{P=100}}{f_1|_{P=0}} = 2.678, \quad \frac{f_2|_{P=100}}{f_2|_{P=0}} = 1.409, \quad \frac{f_3|_{P=100}}{f_3|_{P=0}} = 1.163, \quad \frac{f_4|_{P=100}}{f_4|_{P=0}} = 1.086 \tag{8.35}$$

$$f_1|_{P=100} = 1.358Hz \quad f_2|_{P=100} = 4.473Hz \quad f_3|_{P=100} = 10.34Hz \quad f_3|_{P=100} = 18.90Hz \tag{8.36}$$

The FFT of the system's impulse response is plotted once again in Figure 8.22, and the natural frequencies are compared to those derived theoretically. The FFT of the same system under no tension is plotted alongside these in grey to highlight the frequency shift that has taken place due to the introduction of the tensile force.

The largest percentage error in the natural frequencies is 11.6% and is for the first natural frequency of the system. The remainder of the natural frequencies all have a percentage error smaller than 2%. It is expected that the larger discrepancies in this case are due to the

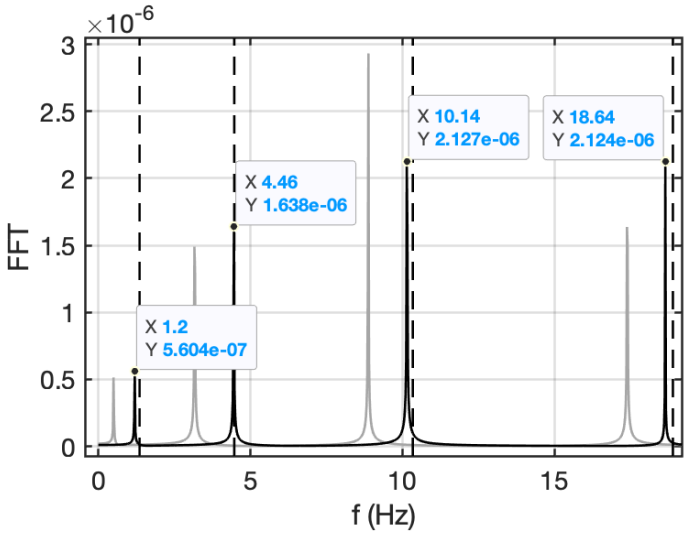

Fig. 8.22 FFT for an impulse response of the system constrained to behave like a cantilever beam under a 100N tensile force (black) plotted alongside the theoretical natural frequencies (dashed) and the FFT of the zero tension system (grey)

fact that the expressions for the natural frequencies of beams under tensile loading are just approximations.

A similar method was followed for the clamped-pinned case. The approximate natural frequencies of the bean under these constraints under tension can be found using the following equation:

$$\frac{f_n|_{P>0}}{f_n|_{P=0}} \approx \sqrt{1+\frac{P}{|P_{CR}|}\frac{(\beta_1 L)^2}{(\beta_n L)^2}}, n = 1,2,3\ldots \tag{8.37}$$

For the clamped-pinned case, the beam's buckling load can be calculated using:

$$P_{CR} = \frac{2.046\pi^2 EI}{L^2} \tag{8.38}$$

The ratios of the natural frequencies for a beam tension of 100N to those for a beam under no tension were calculated, and from these, the predicted values of the natural frequencies of the clamped-pinned beam under tension:

$$\frac{f_1|_{P=100}}{f_1|_{P=0}} = 1.324, \quad \frac{f_2|_{P=100}}{f_2|_{P=0}} = 1.110, \quad \frac{f_3|_{P=100}}{f_3|_{P=0}} = 1.054, \quad \frac{f_4|_{P=100}}{f_4|_{P=0}} = 1.032 \tag{8.39}$$

$$f_1|_{P=100} = 2.945Hz \quad f_2|_{P=100} = 8.002Hz \quad f_3|_{P=100} = 15.85Hz \quad f_3|_{P=100} = 26.54Hz \tag{8.40}$$

These are plotted alongside the FFT of the model's response under a 100N tensile force in Figure 8.23.

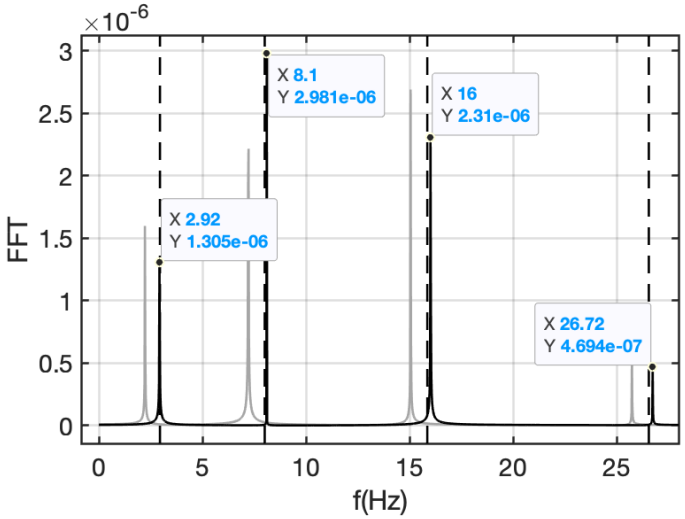

Fig. 8.23 FFT for an impulse response of the system constrained to behave like a clamped-pinned beam under a 100N tensile force plotted alongside the theoretical natural frequencies (dashed) and the FFT of the zero tension system (grey)

Once again, a very good agreement is seen between the peaks of the FFT and the analytically derived natural frequencies of the system. In this case, the largest percentage error is 1.2% for the first mode, with the rest of the errors being less than 1%.

8.5 Effects of Nonlinearities on System Models

While the theoretical analysis aids in validating the linear behaviour of the system, in practise, the tethered balloon system is expected to exhibit larger amplitude motion, in which nonlinearities have an impact on the system's response.

While a very strong agreement was observed between both the nonlinear and linear models and the theoretically derived frequency response for all of the systems analysed in this chapter, as the amplitude of motion is increased, discrepancies between the FFTs of the nonlinear model and the theoretical natural frequencies are expected to arise. While analytically quantifying the change in response due to the introduction of nonlinearities is difficult, a quick and simple way to validate that the nonlinearities are behaving as expected is to observe the direction of the frequency shift as these become more prominent, and compare this to the known behaviour of different systems undergoing nonlinear motion.

A quick way to investigate the effect of the nonlinearities on the system's dynamic behavior is to vary the amplitude of motion and observe the changes in the system's FFT.

Contrary to the nonlinear model, the increase in amplitude of the linear model's time domain response is expected to have no effect on the system's natural frequencies. By comparing the frequency responses of the linear and nonlinear models for larger amplitude vibration, the direction of the shift in natural frequencies due to the nonlinearities can be established and analysed. In order to initiate larger amplitude non-linear dynamic behaviour, an impulse of larger magnitude is used. This was done for both the hanging chain and tethered balloon models.

8.5.1 Effects of Nonlinearities on Tethered Balloon System

In this section, the tethered balloon system used in Section 8.3 is slightly altered to further decouple the stretched string and upside-down pendulum vibration modes, so that the effects of the nonlinearities on each of these can be investigated separately. This was done by further increasing the mass of the balloon to 10kg, which acts to increase the balloon's inertia, leading the system to more closely resemble a pinned stretched string. An increased balloon weight results in a reduced overall tension in the tether, which reduces the tension uniformity along the tether due to the increased impact of the tension variation due to the tether's weight. In addition to this, a reduced tether tension results in a negative shift in the natural frequencies of the stretched string modes, shifting these closer to the pendulum mode which defeats the purpose of increasing the balloon's mass to further decouple these modes. To avoid a reduction in tension due to the balloon's increased weight, the lift force is also increased to 150N, with the aim of maintaining a fairly constant tension throughout the tether's length.

Initially, a small magnitude impulse is applied to the system to obtain a linear FFT for reference. The impulse was applied to the tether rather than the balloon, as a balloon impulse is expected to only excite the lowest frequency pendulum mode. For an tether impulse applied at $s/L = 0.25$, the small-amplitude linear frequency response of the system is plotted in Figure 8.24. Here, the FFTs of the responses of 3 points in the system are plotted.

It can be seen that the 4th string mode, or the 5th mode overall, is missing. This is due to the fact that the impulse was applied a quarter of the way along the 'stretched string', which is known to be a node in the fourth mode and its multiples. The black line representing the balloon's response shows a significant peak at the lowest frequency pendulum mode, and very small if any peaks at the rest, as expected. The blue line is the response of the centre of the tether. This FFT shows very small peaks at the even numbers of the stretched string modes, which is expected since the centre of a string is a node in these modes. This is not quite zero however, likely because, with the system not actually being exactly symmetric (because the balloon is not actually a fixed end) the node may not be exactly in the centre, therefore slightly exciting the second stretched string mode and its multiples. The green

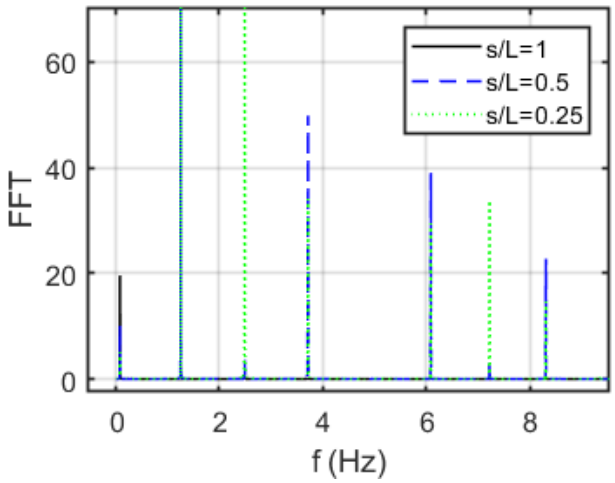

Fig. 8.24 Small amplitude FFT for the impulse response of several points along the tethered balloon, for an impulse at s/L=0.25

line displays the response at a quarter of the way along the tether, and is therefore a driving point resonance. This has a visible peak at all the modes except the 4th string mode and its multiples, as expected.

These have now been established as the system's natural frequencies before any nonlinearities come into play, and are a useful reference point when it comes to understanding the effects of nonlinearities. The FFT was repeated for an impulse much larger in magnitude. The focus was first placed on the stretched string modes of the tethered balloon system. In order to excite as many of these as possible, the impulse was applied close to the fixed end of the tether. The FFT of the linear system response is plotted in black as a reference and the nonlinear system's FFT is plotted in red in Figure 8.25.

The nonlinearities have clearly resulted in an upward shift in the stretched string mode natural frequencies of the system. This is due to the spring stiffening phenomenon exhibited by many similar systems, including a stretched string. In these cases, the stiffness constant increases with increasing amplitude of deflection. An increase in a string's stiffness results in a rise in its natural frequencies, as exhibited in this case. Intuitively, as the amplitude of motion increases, the instantaneous tension opposing the deflection also increases, causing an increased natural frequency. It is also noticeable that the peaks are not as thin as those seen by the linear model's frequency response. This is because, for a long duration time domain response, the amplitude of motion decreases over time, due to the axial damping in the model. As the amplitude decreases with time, nonlinearities become less prominent and the frequency shifts downwards towards those observed by the linear model. When the

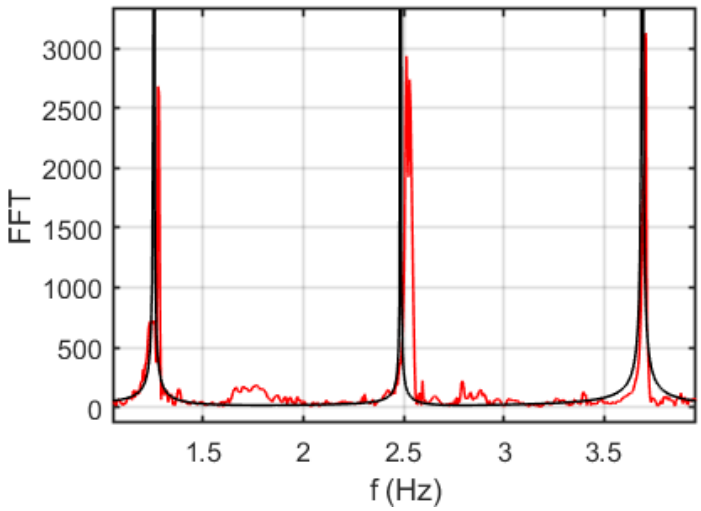

Fig. 8.25 FFT of a large amplitude impulse response of the tethered balloon model (L=20m) for nonlinear System (red) and linear system (black) showing the 2nd-4th vibration modes of the system

FFT is taken for the entire duration, the presence of the varied frequencies in the response manifests as thicker and shorter peaks.

In this particular response, the first natural frequency (pendulum mode) appeared unaffected by increase in amplitude of motion. With the impulse being applied near to the fixed end of the tether, the amplitude of motion of the balloon, and therefore the excitation of the pendulum mode, was relatively small. Because of this, the motion remained fairly linear and the natural frequency appeared unchanged.

Unlike the stretched string case, pendulums exhibit a spring softening effect that takes place when nonlinearities come into play, so it is expected that the first natural frequency of the system will shift downwards for higher amplitude balloon motion. In order to excite large amplitude motion of the system's first mode of vibration, an impulse of large magnitude is applied to the balloon. The FFT of the balloon's response is then plotted in Figure 8.26 for the nonlinear system in red, alongside the response of the linear system in black for reference.

There is a clear negative shift in the natural frequency of the pendulum mode in the presence of nonlinearities, as expected. A quick analysis of a pendulum proves that its nonlinear effects display a softening spring phenomenon, in which an increased amplitude results in a reduced natural frequency. Figure 8.27 shows a diagram of a simple pendulum.

Resolving forces in the direction perpendicular to the pendulum's link, the equation of motion of the pendulum is found:

$$mL\ddot{\theta} + mg\sin\theta = 0 \tag{8.41}$$

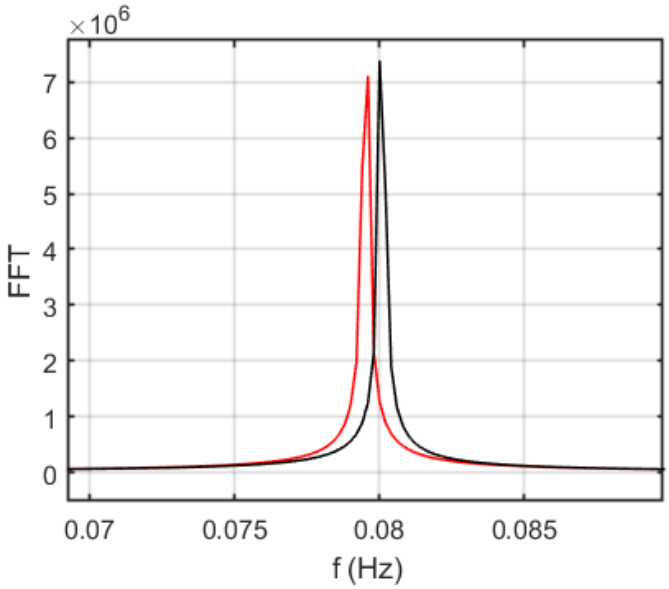

Fig. 8.26 FFT of a large amplitude impulse response of the tethered balloon model (L=20m) for nonlinear System (red) and linear system (black) showing the first vibration mode of the system

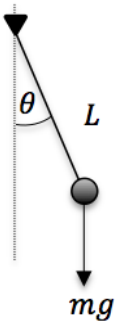

Fig. 8.27 Diagram of a Simple Pendulum

The expression is simplified and rearranged:

$$\ddot{\theta} + \frac{g}{L}\sin\theta = 0 \tag{8.42}$$

For small amplitude motion, the substitution $\sin\theta \approx \theta$ is applied, leaving an equation in the form of simple harmonic motion from which the natural frequency can be easily obtained, $\omega = \sqrt{g/L}$. Since we are no longer considering very small amplitude motion, an extra term can be introduced from the series expansion of $\sin\theta$, written below:

$$\sin\theta = \theta - \frac{1}{6}\theta^3 + O\left(\theta^5\right) \tag{8.43}$$

The substitution therefore becomes:

$$\sin\theta \approx \theta - \frac{1}{6}\theta^3 \tag{8.44}$$

Upon making the substitution and rearranging, the equation of motion can therefore be approximated as:

$$\ddot{\theta} = -\frac{g}{L}\left(\theta - \frac{1}{6}\theta^3\right) \tag{8.45}$$

This equation of motion consists of both a linear term and an additional nonlinear term. While the linear term results in a component of the acceleration that opposes the displacement, the nonlinear term results in a component, although small, in the opposite direction that reduces the magnitude of the acceleration towards the equilibrium. This results in a larger time period and therefore a lower frequency. As θ becomes large enough that θ^3 becomes significant, this becomes apparent in the frequency analysis. It is clear from analysis however, that quite a large amplitude of motion is required before nonlinearities have an effect on this mode, which is explained by the fact that the nonlinear term is a third order term. For an angle θ as large as 20°, the value of the nonlinear component is still only 2% of the value of the linear one at that instant of maximum amplitude (and the difference is even smaller throughout the rest of the motion).

8.5.2 Effects of Nonlinearities on Hanging Chain System

The same method is applied to the hanging chain model for further validation of the system's nonlinearities. The hanging chain is expected to behave in a softening spring manner, for reasons analogous to the pendulum case described above.

For a hanging chain system identical to the one used in Section 8.2, an impulse is applied just over 2/3s of the way along the chain from the fixed end. The magnitude of this impulse is such that the amplitude of motion of towards the free end of the hanging chain is around 0.4m for a hanging chain length of 3m. The FFT of the response is plotted for the nonlinear model in red, and the linear model in black once again, in Figure 8.28. It can be seen that the natural frequencies of the nonlinear hanging chain system model have shifted downwards, as predicted.

The system's nonlinearities have therefore been qualitatively validated to some extent through their effects on the frequency responses of multiple systems. This, in addition to the experimental validation in which nonlinearities are present due to amplitude of motion being of significant magnitude, allow the nonlinear model to be used for simulations with confidence.

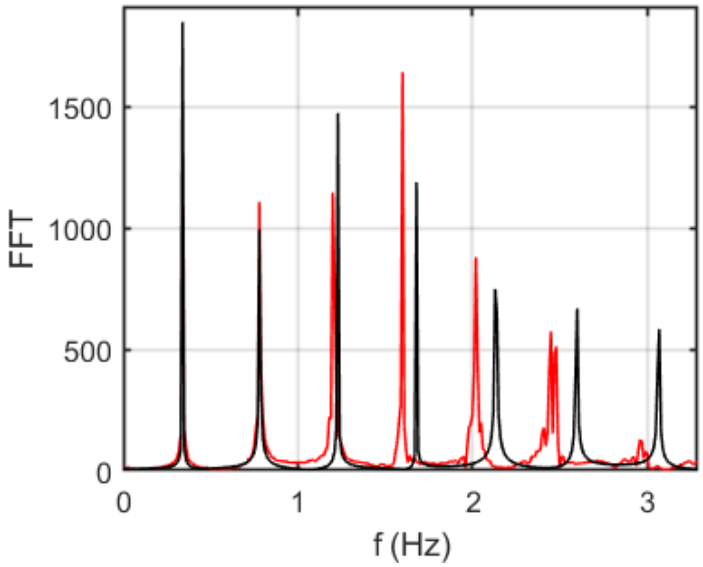

Fig. 8.28 FFT of a large amplitude impulse response of the hanging chain model of Length L=3m for nonlinear System (red) and linear system (black)

Chapter 9

SPICE Case Studies

With both the nonlinear and linearized tethered balloon models having been validated to a satisfactory extent using theory and experimentation, they can now be used to determine the responses of cases that cannot be done easily in practise, such as the full-scale HATB system. While the tethered balloon models can be used for a wide range of applications, the application that initiated this research is stratospheric partial injection for climate engineering, and these models were developed to determine the feasibility of using high altitude tethered balloons as the transport method. In this section, the tethered balloon model is used to assess the safety of the HATB system for this application under the expected external conditions and study its open and closed loop response to potential disturbances.

In order to do this, appropriate system parameters for the application in question must be selected and entered into the model. A discussion of the parameter selection is provided in this Chapter. The expected steady-state external conditions of the system must also be accounted for, i.e. expressions for the wind velocity profile and air density which are both functions of altitude must be obtained and incorporated into the model. Once this is done, the system's response to a range of disturbances can be investigated, with and without feedback control. Several case studies are considered, and the dynamic responses are displayed and discussed. The use of feedback control to reduce the risk of the system's failure is investigated. This research is only focused on performance feasibility, and does not consider the the initial setting up or rising of the balloon. For some of the case studies, only 2-dimensional motion in the plane of the system is considered and in other cases full 3-dimensional motion is considered. The effects of parameter uncertainties and time lags are considered for cases in which feedback control is used to investigate the robustness of the controllers.

9.1 Modelling the External Conditions

In this section, the external conditions that are typically expected to be experienced by a high altitude tethered balloon are mentioned and incorporated into the software model. In doing this, the balloon's steady state can be reached and used as a starting point to investigate the effects of any disturbances. The steady state external conditions discussed in this section are the wind velocities and the surrounding air density, both of which vary with altitude.

9.1.1 Steady State Wind Velocity Profile

Incorporating a steady state wind velocity profile with a realistic shape and magnitude is important, as it has a big impact on the tethered balloon's expected equilibrium. With the balloon and tether's projected area being so large, the wind drag forces on the system are also expected to be very large and shift the equilibrium away from the vertical. Wind speeds are known to peak at an altitude of around 10km before reducing to a minimum at around 20km and then increasing again. Data points of wind speeds at varying altitudes up to 20km were estimated somewhat conservatively from available plots of experimental data [38] and are plotted in Figure 9.1 in red.

With the balloon tethered at a height of 20km and the peak wind velocity occurring at around 10km, it is important to consider the balloon's stability in these conditions. This is because, a dip in the balloon's altitude subjects it to both faster wind speeds and a larger air density, both of which contribute to the increase in the wind drag forces acting to push the balloon even further down, which may result in instability.

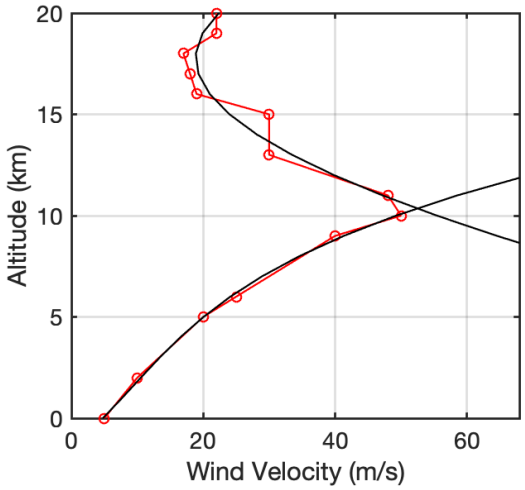

Fig. 9.1 Experimentally obtained wind velocity data [38] and regression of wind profile.

Two ways of modelling the wind velocity profile using the experimental values obtained were considered:

1. Piecewise linear velocity profile – this is done by simply connecting the experimental data points with piecewise linear segments, as seen in Figure 9.1 by the lines connecting the point markers.

2. Fit polynomials to the data – to do this, the the data is split into two sections, above and below the peak wind speed at an altitude of 10km. Regression analysis is then applied to the two sets of data individually to produce polynomials that fit each section.

Either of these could have been used, but the decision was made to model the wind velocity profile using the polynomials to avoid unrealistic discontinuous wind gradients with altitude. This option was also selected because it is more of an average of the kind of wind profile that is expected, rather than a specific case. Upon performing the regression analysis, the following two 3rd degree polynomials were produced:

For an altitude of 10.4km or less, the wind velocity can be found using:

$$v_{x,SS} = 0.0274z^3 - 0.1324z^2 + 3.0308z + 4.7786 \qquad z \leq 10.4km \tag{9.1}$$

For an altitude of more than 10.4km, the wind velocity can be found using:

$$v_{x,SS} = 0.0115z^3 + 0.0789z^2 - 13.7333z + 173.3561 \qquad z > 10.4km \tag{9.2}$$

These functions are plotted alongside the experimental data points in Figure 9.1 and are seen to closely fit the data points.

These expressions are used to describe the steady state wind velocity profile for all of the HATB case studies in this chapter. In the nonlinear model, at each time step, the z coordinate (i.e. altitude) of each element is used to determine the instantaneous wind velocity the element is subjected to using expressions 9.1 and 9.2. From these values, the drag forces acting on the elements can be determined.

9.1.2 Wind Gust Loads

Besides being able to withstand the expected steady state loading during its operation, the HATB must be able to endure changes in the external conditions to be suitable for long duration use. This includes the general variation of the wind velocity profile over time as well as more short-term wind disturbances, i.e. wind gusts.

The most commonly used velocity profile [42] used to represent a wind gust has the shape defined by the following expression:

$$v_g = \frac{v_{g,max}}{2}\left(1 - \cos\frac{\pi h}{H}\right) \qquad 0 < h < 2H \tag{9.3}$$

where $v_{g,max}$ is the peak velocity of the gust, x is the penetration distance and H is the gust gradient length. According to the FAA, the maximum gust gradient length that should be considered is 800ft which is equivalent to around 250m. The suggested range of values for the peak velocity $v_{g,max}$ is between 7.5m/s and 10.5m/s.

For the case of the largest suggested wind gust, with a gust gradient length of $H = 250m$ and peak velocity of $v_{g,max} = 10.5m/s$, the gust profile is plotted in Figure 9.2.

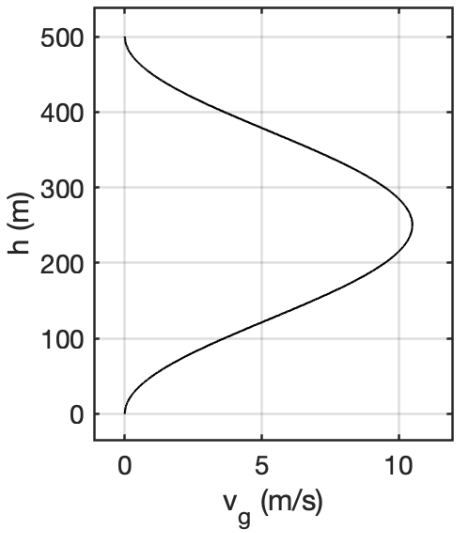

Fig. 9.2 Wind Gust Velocity Profile Shape

In order to model the presence of a gust, the wind gust velocity profile is superimposed onto the steady state wind the HATB is subjected to at the appropriate altitude and direction. The system's response to wind gusts is a hugely important step in determining its feasibility as a delivery method as these are bound to occur regularly during its long-term operation.

9.1.3 Air Density

The density of air also varies with altitude. It can be calculated using the following relationship:

$$\rho(z) = \frac{p(z)M}{RT(z)} \tag{9.4}$$

Here, p is the air pressure, M is the molar mass of air, R is the ideal gas constant and T is the temperature. The values of p and T are also dependent on the altitude and must be calculated. The expression for the temperature as a function of the altitude z is:

$$T(z) = T_0 - L_T z \tag{9.5}$$

Here, L_T is the temperature lapse rate. The air pressure as a function of the altitude is:

$$p(z) = p_0 \left(1 - \frac{L_T z}{T_0}\right)^{gM/RL_T} \tag{9.6}$$

Here, p_0 is atmospheric pressure at sea level. Using these expressions, the air density can be calculated at any altitude. Figure 9.3 shows a plot of the air density variation with altitude.

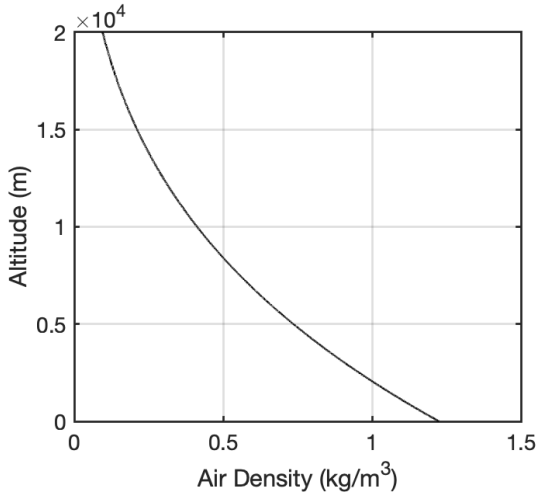

Fig. 9.3 Air Density Variation with Altitude

Similarly to the wind velocity vector, an instantaneous air density vector is calculated using the instantaneous z-direction coordinates of the elements. At each time step, this vector contains the N values of air density experienced by the N elements of the system that can then be used in the calculation of the wind drag forces and the balloon's lift force.

The air density variation influences the motion of the tethered balloon in two opposing ways, for which a balance is found for the system's equilibrium. As the balloon descends and the air density exponentially increases, the drag force due to the wind increases favoring further descent of the balloon. Simultaneously however, the increased surrounding air density also results in an increase in the lift force of the balloon which favors the balloon rising, since the relative density of the helium inside the balloon to the surroundings decreases.

9.2 High-Altitude Tethered Balloon Parameter Values

In this section, the choices for the system's parameter values are listed and discussed. These are chosen specifically to suit the application in question; stratospheric particle injection. The choices of these values are mostly based on the research done by Davidson et al, 2012 [30].

The optimal balloon altitude decided upon is around 20km, placing the balloon within and at the lower end of the stratosphere. This altitude was selected as a compromise, as it is high enough above the tropopause such that the injected particles remain and spread through the stratosphere without being lost to the troposphere, but increasing the design altitude further would require a much larger balloon to generate a sufficient lift force. Wind velocities are also at their lowest at this altitude as seen in Figure 9.1. This is important as it means that relatively low winds act on the balloon during its operation, which is beneficial since the balloon's effective area is very large and therefore sensitive to wind drag.

Since the wind forces along the tether and on the balloon deflect the system's shape from the vertical by a significant amount, the chosen tether length is longer than 20km, to prevent its operational altitude from sinking below 20km under the expected steady winds. The total length of the tether is therefore selected as being 21.5km.

The balloon diameter is chosen to be $315m$, and its wall thickness $375\mu m$. The balloon is assumed to be made of polyethylene film or similar which has a density of around $1000kgm^{-3}$. This combination of balloon volume and mass is expected to generate sufficient lift to keep the balloon's altitude at around 20km under steady state conditions. The balloon's mass can be calculated by multiplying the volume of the balloon's wall with its density.

$$m_b = 4\pi r_b^2 t_b \rho_b \tag{9.7}$$

The function of the tethered balloon system is to transport particles to the stratosphere. For this reason, the tether, rather than being taken as being circular in cross section, is taken as being a pipe to allow for the transportation of the chemical through it. During operation, the fluid will be pumped through it at a high pressure, meaning that the tether will be under both very high longitudinal stresses and very high hoop stresses. A variety of possible materials are discussed in Davidson et al 2012 [30], with the most suitable to date being identified as an aramid fibre composite. Aramid fibres have very good strength-to-weight properties, and generally have a very high tensile strength (around 750MPa) and Young's modulus (around 100GPa). While Aramid fibres have a density of $1440kgm^{-3}$, the fibre-reinforced composite material that is proposed to be used for the tether has a density of $1600kgm^{-3}$. Since the tether will be carrying the high pressure fluid during operation, the mass of the

fluid is included in the model. 250 tonnes of fluid are assumed to be equally spread along the tether during operation.

In order to withstand the large longitudinal and hoop stresses the tether will be under, it must have sufficiently thick walls. Increasing the pipe thickness results in a heavier tether and also a larger effective area for drag forces so a compromise must be made when choosing these parameters. The outer diameter of the tether's cross-section is chosen to be $0.2m$ and the inner diameter $0.1m$. Figure 9.4 shows the proposed cross section of the tether.

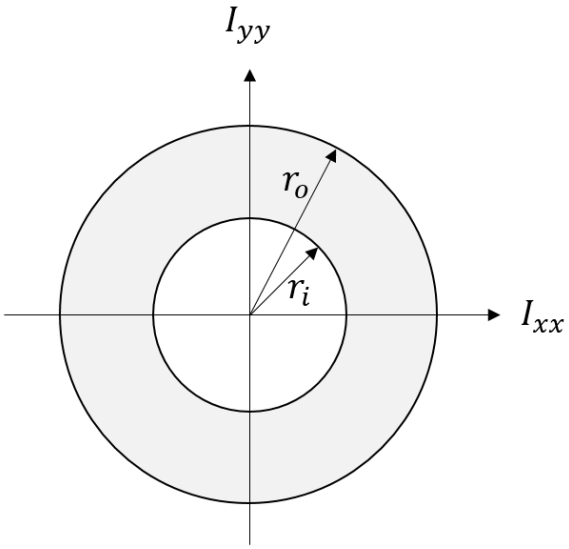

Fig. 9.4 Tether Cross Section

The cross sectional area is calculated:

$$A_{CS} = \pi \left(r_0^2 - r_i^2 \right) \tag{9.8}$$

The tether's mass per unit length, μ, will be equal to the density of the fibre-reinforced composite multiplied by its cross sectional area, plus the mass of the fluid divided by the tether's length.

$$\mu = \rho A_{CS} + \frac{m_{fl}}{L} \tag{9.9}$$

The mass of an element, m_e is equal to the mass per unit length multiplied by the length of an element, L_e:

$$m_e = \left(\rho A_{CS} + \frac{m_{fl}}{L} \right) L_e = \frac{\rho A_{CS} L + m_{fl}}{N} \tag{9.10}$$

The tether's cross sectional shape will have an influence on the tether's cross sectional area moment of inertia and therefore its flexural rigidity and rotational spring bending stiffness k_b.

Since the cross section is axially symmetric, $I_{xx} = I_{yy}$, the area moment of inertia is identical for any axis in the plane of the cross section going through the centre of the pipe. The area moment of inertia for any axis can be calculated using the following equation:

$$I_{xx} = I_{yy} = \frac{\pi}{4}\left(r_0^4 - r_i^4\right) \tag{9.11}$$

Using this, the flexural rigidity of the tether, EI, can be calculated. The tether's bending stiffness can then be discretized using the equation relating the flexural rigidity to the elemental rotational spring stiffness k_b, derived in Section 3.1.2:

$$k_b = \frac{3EI}{2N^3 L_e} \sum_{j=1}^{N} (j-1)(2N-j) \tag{9.12}$$

The tether's longitudinal stiffness is also discretized using this expression for the elemental axial spring stiffness:

$$k = \frac{EA_{CS}}{L_e} \tag{9.13}$$

A rough calculation of the Reynolds number at the balloon's operational altitude yields a value of the order of 10^7. Using values for the density ρ_b and dynamic viscosity of air μ_b [40] at an altitude of 20km, this is shown:

$$Re_b = \frac{\rho_b v_{w,b} d_b}{\mu_b} = \frac{0.089 \times 20 \times 315}{1.42 \times 10^{-5}} = 3.9 \times 10^7 \tag{9.14}$$

This falls well into the supercritical region. As discussed in the literature review, this equates to a drag coefficient of around 0.15 for a fixed sphere. For a tethered buoyant sphere, this number is expected to increase significantly, and a variation of selected values can be seen in different studies. Since this is a preliminary assessment in which the vibrations due to turbulence are ignored, 0.4 is selected and considered an appropriate estimation in the majority of this section. The effects of varying the drag coefficient are investigated however, and a conservative value of 0.7 is also tested to ensure the system remains safe.

A similar calculation was performed for the point approximately midway along the tether, and a Reynolds number of the order of 10^5 was found. From this, a drag coefficient of 1.2 was estimated for the tether by treating it as a cylinder in crossflow.

Table 9.1 shows a summary of the selected parameters of the HATB system.

Table 9.1 Tethered Balloon System Parameter Values

Parameter	Value
Tether Length, L	21.5km
Tether Outer Diameter, d_o	0.2m
Tether Inner Diameter, d_i	0.1m
Tether Density, ρ	$1600 kgm^{-3}$
Tether Young's Modulus, E	100GPa
Tether Drag Coefficient, $C_{d,t}$	1.2
Mass of Fluid in Pipe, m_{fl}	250,000kg
Balloon Diameter, d_b	315m
Balloon Thickness, t_b	$375 \mu m$
Balloon Wall Density, ρ_b	$1000 kgm^{-3}$
Balloon Drag Coefficient, $C_{d,b}$	0.4

9.3 High-Altitude Tethered Balloon Steady State

Before analyzing the high-altitude tethered balloon's response to disturbances, the system's steady state response to expected wind conditions is observed to ensure its expected operational state is satisfactory. The selected parameters along with the external conditions derived in the previous section are applied to the model and the system's open loop response under no disturbances and steady conditions can be observed to start with. From a purely vertical stationary state, the tethered balloon system will move in the direction of the wind until it settles into its equilibrium position.

For the wind velocity profiles found using the regressions in the previous section and the tethered balloon parameters in the table above, the equilibrium shape of the tethered balloon system once it has settled is displayed in Figure 9.5 below for $N = 600$. The static equilibrium is displayed for drag coefficients of magnitude 0.2, 0.4 and a conservative 0.7.

Table 9.2 Key Equilibrium State Parameters for Different Drag Coefficient Values.

Parameter	$C_d = 0.2$	$C_d = 0.4$	$C_d = 0.7$
Balloon Altitude	20.40km	20.27km	20.04km
Maximum Tether Tension	11.1MN	11.4MN	11.7MN
Maximum Tether Stress	470MPa	483MPa	498MPa
Minimum Tether Tension	1.36MN	1.70MN	2.16MN

In order to be proved satisfactory, the steady state of the system must meet certain criteria that ensure its safety and performance. If any of these criteria are not satisfied, adjustments

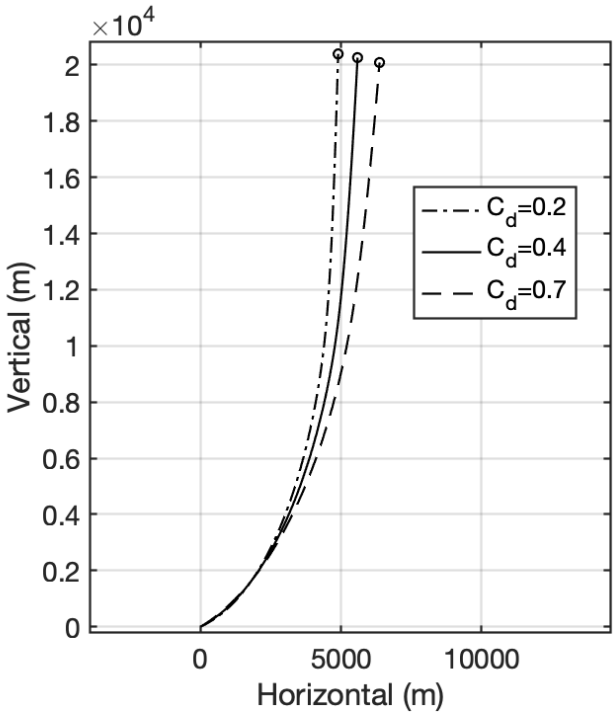

Fig. 9.5 High-Altitude Tethered Balloon Equilibrium Position for drag coefficients of magnitude 0.2, 0.4 and 0.7 under the steady-state wind velocity profile displayed in Fig. 9.1.

would need to be made to the materials or geometry selected for the system until they are. These are listed below:

1. Balloon steady state position at a height of around 20km.

   The chosen desired system altitude is 20km, for the reasons discussed previously. The altitude of the centre of the balloon at steady state is found to be 20.27km for the selected parameters (for $C_d = 0.4$) and expected external conditions. This is an acceptable value for the balloon's operational altitude and no parameter alterations are made to tweak this.

2. The tether tension must be positive everywhere along the tether's length to avoid the formation of kinks.

   One of the possible issues that may arise upon using a tethered balloon for the application in question is the formation of kinks in the cable, which may result in the cable breaking. In order to avoid this, it is important that the system is designed such that the tensile force throughout the tether's length is positive during operation, and large enough that it is unlikely to drop to below zero during minor disturbances. The minimum tension along the tether is calculated by the program, and its value is found

to be $T_{min} = 1.70MN$. As expected, this tensile force is situated at the tether's base, where the element in question has to support the weight of the least length of tether. This value is positive and appears to be sufficiently large to avoid easily reaching zero under the effects of disturbances. No parameter alterations are needed.

3. The maximum longitudinal stress along the tether must not exceed the decided upper limit.

   The longitudinal stress is calculated for each element along the tether to ensure that it is well below the tensile strength of the material from which it is made, including a safety factor. The maximum tension along the tether is found to be $T_{max} = 11.4MN$ and is located at the top end of the tether, just below the balloon, which is expected since this point must support the weight of the entirety of the tether. Dividing the maximum tension by the cross-sectional area of the tether calculates the maximum longitudinal stress in the tether. The magnitude of this is found to be $\sigma_{L,max} = 483MPa$. The short-term tensile strength of aramid fibres is around 2700MPa. To account for the fact that the stress is sustained, a reduction factor of 50% is applied to this value, producing a recommended sustained stress limit of 1350MPa [46]. Accounting for a safety factor as well as the expected deterioration of the material over time, Davidson et al. [30] suggested a design stress of 750MPa. The maximum tensile stress exhibited by the model is safely below this, so no adjustments are made.

4. The maximum hoop stress experienced by the tether does not exceed the maximum allowable value.

   In order to transport the fluid to the stratosphere at a rate sufficient to fulfil the requirements of the system's application, a high pressure pump has to be used at the tether's base. The high pressure required to counteract both the weight of the fluid and the frictional pressure drop is expected to subject the tether to large hoop stresses and so it is important to ensure that these fall within the acceptable range of values. The maximum internal pressure (and therefore hoop stress) would occur at the tether's base in order to force the fluid upwards to the stratosphere.

   It is estimated that around 10 million tonnes of SO_2 is required per year, which, split over the suggested number of HATBs, 4, requires a flow rate of 2.5 million tonnes per year or $96kgs^{-1}$ for each tethered balloon [30]. For a fluid density of $\rho_{fluid} = 1400kgm^{-3}$ the volumetric flow rate is found to be $0.069m^3s^{-1}$. Dividing by the internal area of the pipe gives the average fluid velocity, $8.7ms^{-1}$.

The required pumping pressure is determined by the sum of the static head and the frictional pressure drop. The approximate static head due to the weight of the fluid above the pump at ground level is found using:

$$p_s = \rho_{fluid} g h \approx 270MPa \tag{9.15}$$

For a fluid velocity which doesn't exceed $9ms^{-1}$, the frictional pressure drop for the system is found to be approximately 200MPa [30]. While the sum of these is below 500MPa or 5000bar, this is selected as a conservative value for the required internal pressure of the pipe at ground level.

A relationship between the internal pressure of the pipe p_i and the resulting hoop stress σ_h can be found by considering the cross-section of a short length of tether dy, displayed in Figure 9.6.

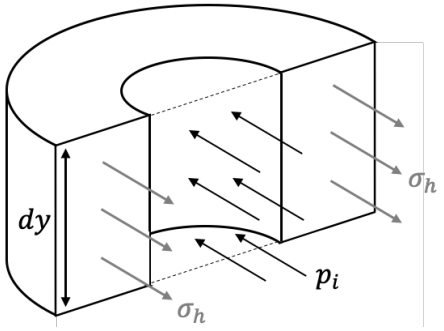

Fig. 9.6 Stresses acting on a cross-section of a small length of tether.

Forces can be resolved by considering the areas over which p_i and σ_h act, giving:

$$p_i d_i dy = \sigma_h (d_o - d_i) dy \tag{9.16}$$

where d_i and d_o are the cable's inner and outer diameters respectively. Since for the selected system parameters $d_o = 2d_i$, this expression collapses to:

$$p_i = \sigma_h \tag{9.17}$$

For a conservative maximum internal pressure of 5000bar at the tether's base, the maximum hoop stress experienced by the tether is 500MPa, which falls below the selected maximum acceptable tether stress of 750MPa which includes a safety factor.

5. The hoop stress experienced by the balloon is low enough below the yield stress of polyethylene.

It is important to ensure that the stress in the skin of the balloon does not exceed the strength of polyethylene to ensure that the balloon would not burst. The hoop stress of the balloon is dependent on the pressure difference between the inside and outside of the balloon, and is therefore dependant on the balloons altitude. At some altitude, the external air pressure may be low enough that the relative internal pressure of the balloon would cause it to burst. The diagram below shows a cross-section through the middle of the balloon, and the stresses acting on it.

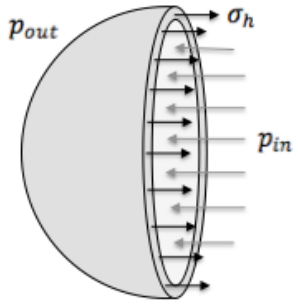

Fig. 9.7 Stresses acting on a cross-section through the centre of the balloon

Forces can be resolved for the half balloon to produce the equation relating the balloon's skin's hoop stress to the pressures inside and outside the balloon. This is done by multiplying the stresses by the areas on which they are acting to produce force values.

$$2\pi r_b t_b \sigma_h = \pi r_b^2 (p_{in} - p_{out}) \tag{9.18}$$

The hoop stress can therefore be found using the following simplified expression:

$$\sigma_h = \frac{r_b (p_{in} - p_{out})}{2t_b} \tag{9.19}$$

Davidson et al. [30] suggest that the balloon is pressurized, with a differential pressure such that operating hoop stress in the balloon's skin is at the low value of around $170 Nm^{-2}$ for the chosen parameters of the system. This value being very much below the tensile strength of polyethylene is important to ensure that the balloon's differential pressure does not cause it to burst if its altitude increases due to a disturbance. The use of a low wall stress at operation also means that the balloon will be able to expand as it rises, reducing the growth rate of the differential pressure as the balloon rises. Minimising the balloon's altitude deviation is therefore a crucial aspect of improving the safety of the HATB system.

9.4 Uniform and Steady Design Wind Speed of 55m/s

In Davidson et al. [30], there was discussion of having used a wind speed of $55ms^{-1}$ as a design wind speed to prevent blow-over. Blow-over occurs when the balloon's altitude drops to a point where the increased wind velocity it is subjected to overpowers its lift force and the balloon continues to descend, losing stability. This is another important reason why minimising the balloon's altitude deviation is the primary aim of the implementation of feedback control later in this chapter.

A uniform and steady wind of $55ms^{-1}$ was therefore applied along the length of the tethered balloon model starting from its equilibrium state to observe its response and ensure that such winds do not lead to the system's failure. Figure 9.8 shows the response for the case of $C_d = 0.4$. Such a wind profile is not expected to occur in reality and is simply applied as an extreme case to assess whether blow-over occurs.

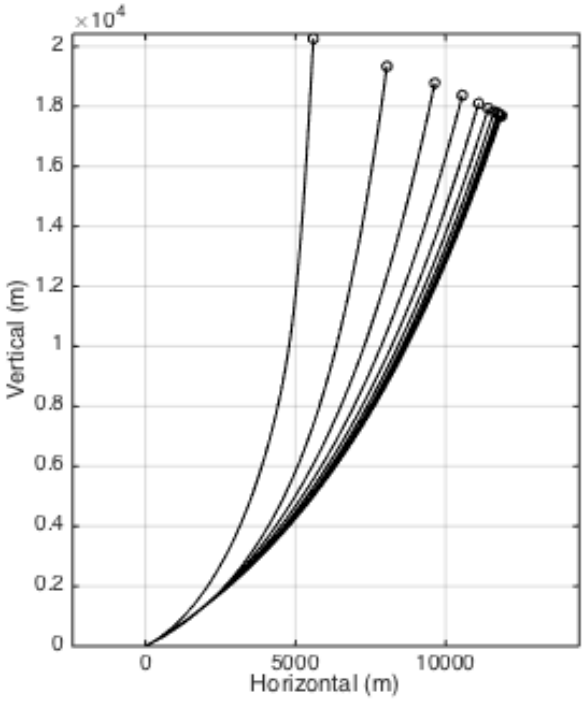

Fig. 9.8 HATB response to a uniform and steady wind speed of 55m/s on balloon and tether

The balloon is seen to move horizontally in the direction of the wind and downwards, and the system adopts a new equilibrium state at with a larger angle from the vertical. Despite the significant drop in altitude (the balloon has dropped to an altitude of 17.7km), the system remains stable. The system took a little bit over 15 minutes to reach its new equilibrium

state from its original one. Upon returning the wind profile to the steady-state, the system safely returns to its expected steady state equilibrium. The system can therefore survive a continuous uniform wind speed of $55ms^{-1}$ without exhibiting blow-over. At this new equilibrium, the maximum tension in the tether is 17.3MN, which corresponds to a maximum longitudinal stress of 732MPa. Davidson et al. [30] used a design stress of 750MPa for a design wind speed of 55m/s so agreement can be seen here.

For the system's selected design, no blow-over was observed for this wind profile even for the conservative drag coefficient value of 0.7.

9.5 Wind Gusts with $v_{g,max} = 10.5m/s$

In this section the effects of the suggested wing gust profiles [42] on the VHATB are investigated. Gusts have the largest impact on the system's critical parameters when they act on the balloon, so the gust is set up such that its peak velocity acts at the balloon's altitude. The gust wind profile is superimposed onto the existing steady-state wind conditions.

In-plane and out-of-plane wind gusts with the velocity profiles indicated in Figure 9.2 are applied on the balloon individually. The resulting deflected shape of the tether in the x-z plane of the in-plane wind gust is plotted in Figure 9.9 on the left hand side, and the deflected shape of the tether in the y-z plane due to the out-of-plane (in the positive y-direction) wind gust is plotted on the right hand side. The balloon's altitude variation with time is plotted for

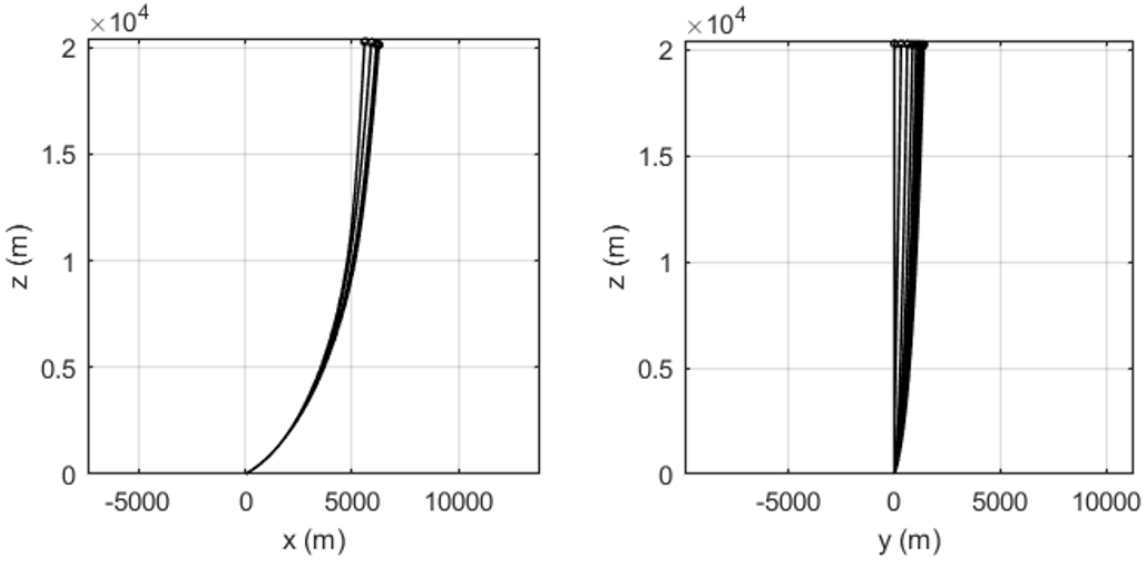

Fig. 9.9 HATB shape variation with time in response to in-plane (left) and out-of-plane (right) wind gusts on the balloon of peak velocity 10.5m/s.

both of these cases in Figure 9.10 to assess the risk that balloon gusts of this magnitude pose on the VHATB system.

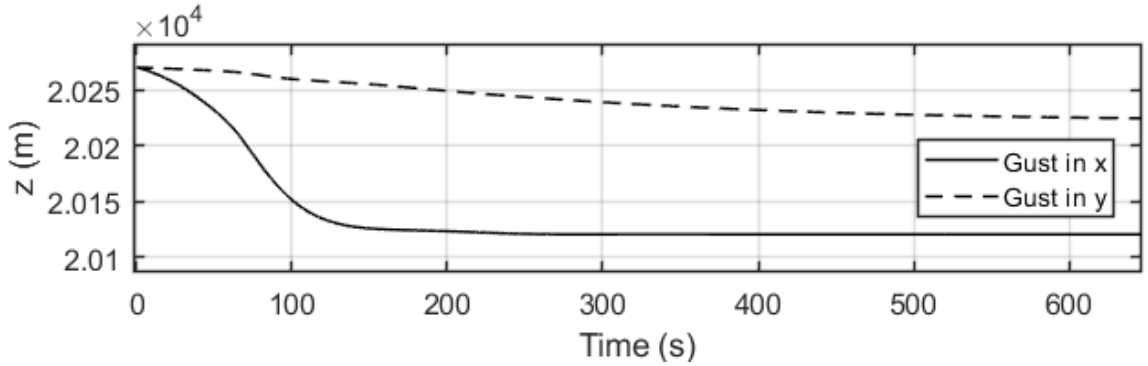

Fig. 9.10 Balloon altitude response to in-plane (left) and out-of-plane (right) wind gusts on the balloon of peak velocity 10.5m/s.

The in-plane wind gust can be seen to have more of an impact on the balloon's altitude which is expected due to the tether's initial shape in this plane not being vertical (at the vertical the rate of change of altitude with rotation is at a minimum). Table 9.3 summarises the key parameters of the system's response to the gusts on the balloon in the x-direction and y-direction respectively. The changes in the critical parameters are approximately 3.5 times larger for the in plane balloon gust.

Table 9.3 Comparison of Key Parameters of Response to 45m/s Balloon Gust for Open and Closed Loop Systems

Parameter	In-Plane Gust	Out-of-Plane Gust
Minimum Altitude Reached by Balloon	20.12km	20.23km
Altitude Drop from Eqm (%)	0.7%	0.2%
Maximum Tension Experienced by Tether	11.7MN	11.5MN
Maximum Tether Stress	497MPa	487MPa
Increase in Maximum Tether Stress from Eqm (%)	2.9%	0.8%

For the in-plane gust, the altitude is seen to drop by 0.7% to an altitude of 20.12km. While the responses don't seem to affect the system very drastically, the system's responses to more severe wind changes are investigated later in this section, and the effects of introducing feedback control for improved stability are analysed.

9.6 Linearizing the HATB System

Having selected parameter values that produce a satisfactory equilibrium state, the feasibility of the system can be determined by its maintained safe operation under a variety of possible disturbances. This research proposes the possibility of improving the system's behaviour under such disturbances through the implementation of feedback control. In order to design a controller using LQR the system first needs to be linearized about its equilibrium state. This section gives a brief description of the linearization process, and a validation of the full-scale linearized system model.

The high-altitude tethered balloon system is linearized using the mass, stiffness and damping matrix entry equations derived for 3-dimensional balloon systems in Chapter 7. These require values for the system's parameters listed in table 9.1, the resultant equilibrium states for the external conditions in question (these can be calculated using statics or extracted from the nonlinear system model), as well as the steady-state wind drag forces under equilibrium which depend on the elements' steady state altitudes. These are all substituted into the equations to produce fully numerical mass, stiffness and damping matrices that define the system's dynamic behaviour for small amplitude motion, both laterally and axially, about the equilibrium state in question. The system's linear dynamics can be fully described by an equation of the form:

$$[M]\ddot{x} + [D]\dot{x} + [K]x = 0 \tag{9.20}$$

Since these equations were derived for a non-planar 3D equilibrium state to avoid the loss of generality, such a state is chosen for the validation of the system's linearization, to avoid the simplification of these matrices. In order to achieve a non-planar equilibrium state, wind directions that vary with altitude are required. The following arbitrary wind conditions are applied to the system:

$$\begin{aligned} \mathbf{v}_{w,ss} &= (30\mathbf{i} + 0\mathbf{j} + 0\mathbf{k})ms^{-1} \qquad h < 10km \\ \mathbf{v}_{w,ss} &= (0\mathbf{i} + 30\mathbf{j} + 0\mathbf{k})ms^{-1} \qquad h > 10km \end{aligned} \tag{9.21}$$

The wind speed therefore has a uniform magnitude of $30ms^{-1}$ with a direction that changes at approximately the middle of the system's altitude. This is not a realistic wind profile, and is solely used as an example for the 3D linearization validation. The 3-dimensional nonlinear model is allowed to settle into its equilibrium state under these external conditions. Figure 9.11 shows plots of the system's equilibrium shapes in the x and y directions respectively.

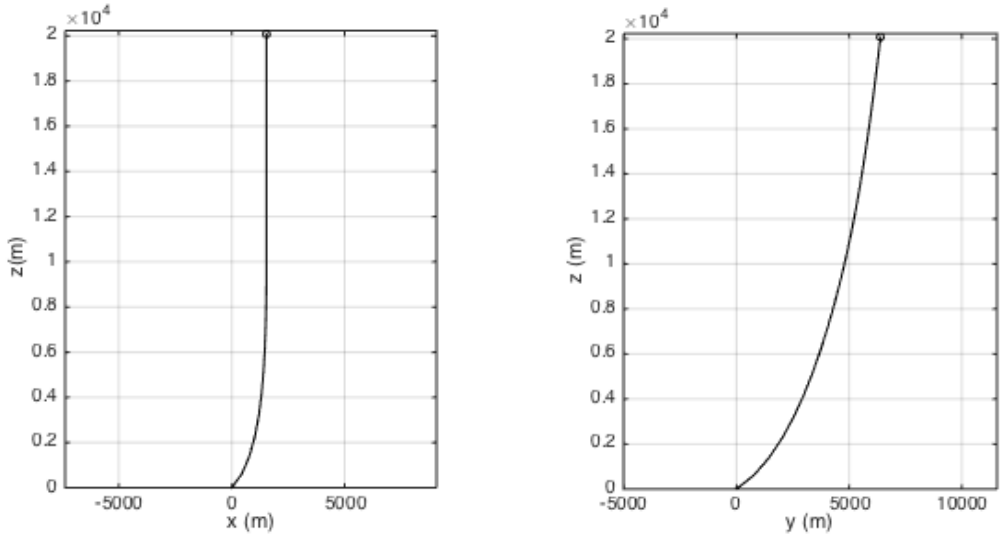

Fig. 9.11 HATB Equilibrium State for a wind profile of 30m/s that changes direction at 10km

The system's equilibrium exhibits a much larger deflection in the y-direction than in the x-direction. This is expected, for two reasons. Firstly, the balloon is subjected to a wind velocity that is in the y-direction, and its relatively large projected area means a larger wind force. Secondly, the wind forces create a bigger moment about the fixed end as they get further away and the wind forces in the y-direction are further away in this case. Above an altitude of 10km, the elements show no more changes in the x-direction, as expected.

The linear system response is then compared to the nonlinear system response for relatively small amplitude motion, to validate the linear model before using it to design a controller. An impulse is applied to the balloon in both models, through the application of an initial velocity of magnitude 30m/s in the direction that corresponds to an initial angular velocity in the $\dot{\theta}$ direction. The initial angular velocity applied to the balloon is therefore:

$$\dot{\theta}_{0,N} = \frac{30}{l_{0,N}} = \frac{30}{r_b} = 0.19 rad/s \tag{9.22}$$

The angular velocity $\dot{\theta_N}$ is one of the states of the linearized model, and so this value can be put straight into the initial state vector. Since the nonlinear model uses Cartesian coordinates, the following expressions are used to determine the equivalent Cartesian initial

velocities:

$$\dot{x}_{0,N} = l_N \dot{\theta}_{0,N} \cos\theta_{0,N} \cos\phi_{0,N} \tag{9.23}$$

$$\dot{y}_{0,N} = l_N \dot{\theta}_{0,N} \cos\theta_{0,N} \sin\phi_{0,N} \tag{9.24}$$

$$\dot{z}_{0,N} = -l_N \dot{\theta}_{0,N} \sin\theta_{0,N} \tag{9.25}$$

The equilibrium Euler angles in these expressions can be determined from the equilibrium Cartesian coordinates of the system using the following expressions:

$$\theta_{0,j} = \tan^{-1}\left(\frac{\sqrt{\left(y_{0,j} - y_{0,j-1}\right)^2 + \left(x_{0,j} - x_{0,j-1}\right)^2}}{z_{0,j} - z_{0,j-1}}\right) \tag{9.26}$$

$$\phi_{0,j} = \tan^{-1}\left(\frac{y_{0,j} - y_{0,j-1}}{x_{0,j} - x_{0,j-1}}\right) \tag{9.27}$$

Since the Nth element is close to being vertical and its ϕ angle is approximately $\pi/2$ due to the wind velocity acting in the y-direction at that end, the majority of the motion observed due to the initial angular velocity $\dot{\theta}_{0,N}$ will be in the y-direction. The equivalent initial conditions are applied to their respective model, and Figure 9.12 shows a comparison of the response in the y-direction of the two models for 20 equally spaced points along the tether (the graph is zoomed in for clarity). The nonlinear model response is plotted in red, and the linearized model response is plotted in black.

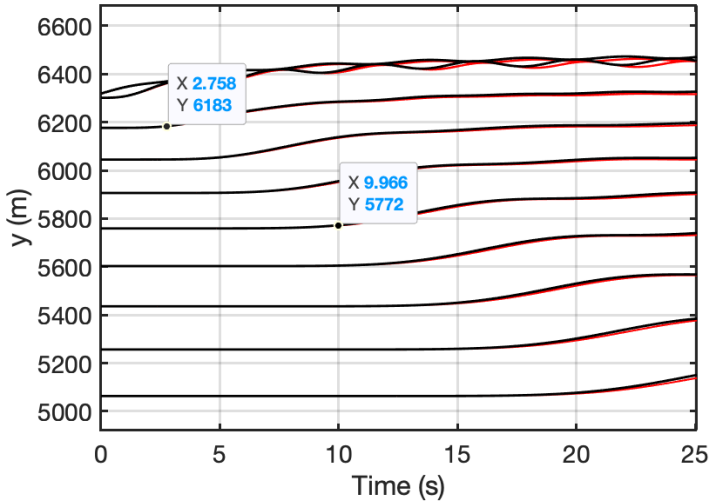

Fig. 9.12 Impulse response of VHATB for nonlinear (red) and linear (black) models

A close agreement is seen between the models, as required. Some quick calculations can be done to check the validity of both of the models quantitatively in addition to this. The wave velocity and amplitude of the step wave are checked against the expressions derived in Section 4.2.

Figure 9.12 shows the graph data for when two points nearer to the top end of the tether begin to deviate from their equilibrium position. Since the tension varies quite dramatically along the tether, these two points are selected such that they are relatively close to each other as the wave velocity is expected to be fairly constant between them.

The average tension between the two points is calculated, and is found to be $9.86MN$. The expected wave speed is therefore calculated using the mean tension between the points in question:

$$c = \sqrt{\frac{T}{m'}} = \sqrt{\frac{T}{\rho A_{CS} + m_{fl}/L}} = 447.1m/s \tag{9.28}$$

The wave speed as determined by the model can be calculated from the data in Figure 9.12 for comparison. The graph shows data for 20 equally spaced points along the tether, making the distance between each pair of adjacent points equal to $L/20$, which is equal to 1075m. The distance between the two points shown on the graph is therefore equal to $3 \times 1075 = 3225m$. Using the time values taken from the graph, the wave velocity as according to the two models' response is therefore:

$$c_{model} = \frac{d}{t} = \frac{3225}{9.97 - 2.76} = 447.4m/s \tag{9.29}$$

The model's wave speed and the one calculated theoretically have a percentage error of less than 0.07% showing very good agreement with the theory. Errors may be accounted for by the non-uniform tension and the fact that the model is spatially discretized.

In addition to the wave speed, the amplitude of the square wave can also be checked analytically. A_0 is first calculated using the system's parameter values:

$$A_0 = \frac{2m_b\dot{x}_{0,N}}{\mu} = \frac{2 \times 1.17 \times 10^5 \times 30}{49.3} = 142340m^2/s \tag{9.30}$$

The amplitude of the square wave produced in response to an impulse on the balloon is therefore:

$$y_0 = \frac{A_0}{2c} = \frac{142340}{2 \times 447} = 159.2m \tag{9.31}$$

This can be compared to the data taken from Figure 9.13 which shoes the y-coordinate of a point before and after it exhibits the step wave displacement.

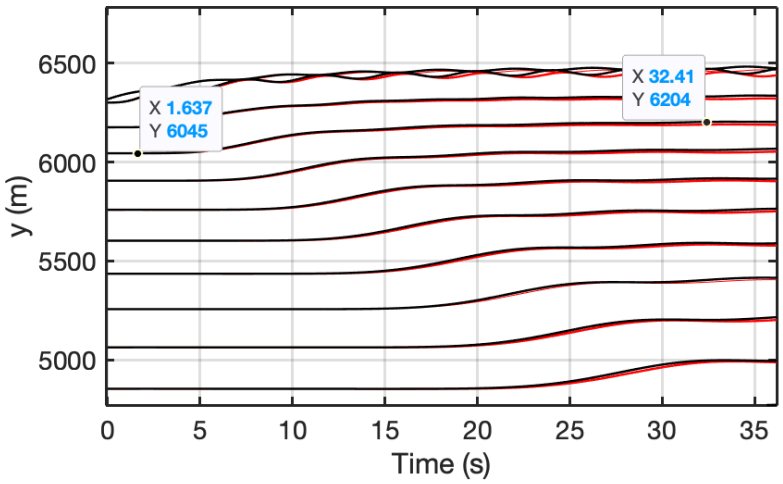

Fig. 9.13 Impulse response of VHATB for nonlinear (red) and linear (black) models

The amplitude of the step wave in the response of the models is equal to the difference between these values:

$$y_{0,model} = 6204 - 6045 = 159m \tag{9.32}$$

The percentage difference in these two values is just over 0.1%.

The linearized model therefore not only shows close agreement with the nonlinear model for relatively small amplitude motion, but they both display behaviour that agrees closely with what theory would suggest, increasing confidence in both models and the linearization process. The linear model can now be used to produce a feedback controller for the nonlinear system model.

9.7 Implementing Feedback Control

Upon the introduction of disturbances, some of the parameters are expected to deviate from their suggested operational values. Limits must be applied to the extent to which they can deviate from their desired values without compromising the safety of the system. Feedback control is then introduced to investigate the extent to which it can help to minimize these deviations and prevent failure.

The upcoming sections introduce case studies on the system's closed and open loop responses to disturbances for 2-dimensional cases and 3-dimensional cases. For the feedback controller to be designed using LQR, the system must be linearized about its expected steady state equilibrium position discussed in this section.

The values for the equilibrium Euler angles of the elements $\theta_{0,j}$ and $\phi_{0,j}$ and the equilibrium element lengths $l_{0,j}$ can be calculated from the element's equilibrium coordinates, $x_{0,j}$ and $y_{0,j}$. These, along with the system's parameter values, can then be substituted into the mass, damping and stiffness matrices derived in the previous section. These can in turn be used to produce the state space matrices of the system required for LQR. Along with the state space matrices A and B, values for the input and state costs, R and Q respectively, are required to produce the system's closed loop feedback gain vector, K. The relative values of the costs are altered by trial and error to produce a controller that behaves in a feasible manner for a base motion input which could be conducted by a ship in reality.

9.7.1 Aims for the Implementation of Feedback Control

The aim of implementing a controller to the system is to generally reduce the system's deviation from its equilibrium state, as this reduces the likelyhood of the system's failure. A few of the potential aims when incorporating feedback control to the HATB system are discussed:

1. Reduce the balloon's deviation from its operational altitude.

   The main aim of the feedback controller for the HATB system is to reduce the balloon's deviation from its equilibrium altitude for which it was designed, as this is a crucial factor in the system's safe operation. Rising too high may cause the balloon to burst due to the increase in the differential pressure across its wall. Dropping too low may result in blow-over or a differential pressure that is too low causing the balloon to lose its tight spherical shape and therefore its aerodynamic properties. This is referred to as 'dimpling' and occurs when the dynamic pressure on the balloon's surface due to the wind exceeds the internal pressure of the balloon. As the balloon's altitude decreases, the wind velocity it is subjected to increases and its differential pressure decreases, increasing the risk of dimple formation. A blow-over occurs when temporary winds or other disturbances manage to push the balloon into regions of stronger winds at lower altitudes, leading to failure.

2. Reduce the maximum tension experienced by the tether.

   A potential benefit that may result from the reduced deviation of the system from its equilibrium state is the reduction of the magnitude of the maximum tension experienced by the tether, or the time for which it lasts. While a disturbance may not cause the cable to reach its breaking point or its yield strength, being subject to repeated high axial stresses can lead to fatigue or even creep depending on the durations. By acting

to reduce the magnitude of the axial stresses experienced by the tether as well as the exposure time, the introduction of feedback control may reduce the effects of creep and fatigue and increase the lifespan of the tethered balloon system.

3. Ensure that the controller is designed such that it produces an input that is feasible practically.

   It is important that the cost parameters are chosen such that the inputs to the system are realistic and feasible. A controller that is too cheap will produce a feedback input base motion that exhibits speeds and accelerations that can not be realistically achieved by ships, and is therefore useless for this application. A controller that is too expensive will not make significant improvements to the system's response and may therefore not be worth implementing. The Q and R values should be adapted from cases like these until a reasonable compromise is achieved, in which the inputs suggested are practically feasible, but drastic enough to make significant improvements to the system's performance under disturbances. A reasonable velocity limit applied to the base motion is 30 knots (around 56km/h) which is achievable by several types of ships. The large inertia of ships means that sudden changes in velocity are to be avoided as they are unfeasible. While the disturbances considered in the case studies are intentionally unrealistically extreme in order to highlight the benefits of the feedback controller and therefore result in larger distances being covered by the ship than what is expected in practise, it is useful to check that these have appropriate values. It is suggested that these be of the order of 10km to maintain practicality. A maximum power output of 110,000 hp or 82MW is selected as this seems to be a common value for a variety of types of ships and is therefore achievable. Dividing the selected power limit by the selected maximum speed (15m/s) gives a conservative value for the maximum input force of 5.4MN. This value is highly conservative, as the largest input forces are expected to occur at velocities significantly lower than the selected limit, meaning that larger forces would actually be feasible.

9.7.2 Cost Function Selection

In this section, a brief overview of the cost function selection process and the criteria behind it is provided. The impact of the cost values on the system's dynamic behaviour is highly dependent on the system's parameters, the base (ship) parameters and the choice of number of elements, so rather than giving actual values the thought process behind the value selection is given. A 3-dimensional system is assumed, as the same principles can be applied to a 2-dimensional system.

The input cost R was is normally given a unit magnitude to simplify the cost selection process. Since there are two inputs for the 3-dimensional cases (because the input is now a force vector with 2 degrees of freedom), the input cost parameter R is now a 2-by-2 matrix, corresponding to the force in the x direction and the force in the y-direction, F_x and F_y. Its diagonals are kept at 1, since it is logical for the two force components to have the same cost, and the values in the Q matrix are changed to alter necessary ratios.

$$R = \begin{bmatrix} 1 & 0 \\ 0 & 1 \end{bmatrix} \tag{9.33}$$

The state cost matrix Q contains costs for each state of the system in its corresponding diagonals. The diagonals of the state cost matrix are often given uniform values, such that it satisfies $Q = \rho I$. In this case, giving the states uniform costs is not ideal for reasons discussed later in this section. The different coordinates of the elements are grouped together however and given individual uniform costs, e.g. the angular deviations of the elements in the θ_j direction, u_j are given identical costs, q_u. The state cost mtrix Q therefore takes the following general form:

$$Q = \begin{bmatrix} q_{x_0} & & & & & & & & & & & \\ & q_{y_0} & & & & & & & & & & \\ & & [q_u I] & & & & & & & & & \\ & & & [q_v I] & & & & & & & & \\ & & & & [q_w I] & & & & & & & \\ & & & & & q_{\dot{x}_0} & & & & & & \\ & & & & & & q_{\dot{y}_0} & & & & & \\ & & & & & & & [q_{\dot{u}} I] & & & & \\ & & & & & & & & [q_{\dot{v}} I] & & & \\ & & & & & & & & & [q_{\dot{w}} I] & & \end{bmatrix} \tag{9.34}$$

Since the coordinates and velocity components of the base have no effect on the system's equilibrium and are more closely linked with the input, these are given unit costs.

$$q_{x_0} = q_{y_0} = q_{\dot{x}_0} = q_{\dot{y}_0} = 1 \tag{9.35}$$

The cost parameters of the coordinates u_j, v_j and w_j quantify relative the importance of minimising these values, and therefore act to minimise deviations in the system's equilibrium position. The parameters associated with their derivatives act to dampen out vibrations or

motion in their respective direction and are therefore useful in preventing oscillation and overshoot.

While minimising deviations of the Euler angles θ_j (and therefore u_j) and the element lengths l_j (and therefore v_j) are important in improving the system's safe operation, deviations in the ϕ_j coordinates of the elements are not. Deviations in θ_j have a direct impact on the altitude of the balloon and must be minimised in order to maintain a safe balloon altitude during operation. Deviations in l_j also have an impact on the balloon's altitude, as they involve the stretching and compression of the tether. They also have a direct impact on the axial stress experienced by the tether, which should be kept to a minimum to reduce the risk of the tether breaking and prolong its lifespan. Deviations in ϕ_j however merely result in the horizontal rotation of the system or parts of it, and pose no increased risk for the system's failure. In order to ensure that the controller prioritises the minimisation of the coordinates that do affect the system's safety, q_w and $q_{\dot{w}}$ are given very small values, of the order of 10^{-4}. This is very important because for the 3-dimensional cases in which out-of-plane disturbances are imposed on the system, the deviations of w_j and $\dot{w}_j$ are significantly larger in value than u_j and $\dot{u}_j$, so unless these are assigned very small cost values, the system will prioritise minimising these rather than acting to maintain the balloon's equilibrium altitude.

The cost parameters for the u_j and v_j coordinates and their respective derivatives must therefore be selected for the design of each controller. It is decided that the costs of states are to be the same as the cost of their derivatives as this is often the case in LQR cost selection and keeps the process simple.

$$q_{u_j} = q_{\dot{u}_j} \qquad q_{v_j} = q_{\dot{v}_j} \tag{9.36}$$

This leaves 2 degrees of freedom in the cost selection process. The largest value is selected for the costs associated with u_j as deviations in these are expected to have the biggest impact on the balloon's altitude. While the element extensions v_j do impact the balloon's equilibrium, and they are given significant costs, it is decided that for a tether of such a high stiffness the effects of rotations should be prioritised over extensions. The selection of the q_u value therefore has the biggest impact on the closed loop behaviour of the system, as it is highly significant in the controller's design. For the sections in which the effects of the controller's cost are investigated, it is the q_u (and therefore also $q_{\dot{u}}$) parameter that is altered to maintain simplicity.

9.8 SPICE Case Studies: 2-Dimensional Cases

Once the system is in its equilibrium position, its dynamic response to changes and disturbances can be observed, both with and without feedback control. For all of the case studies, all dynamic responses are produced by the nonlinear model to more accurately portray how the system is expected to behave, even for the closed loop system cases in which the controller was designed based on a linearized version of the model. This is because the amplitude of motion is not expected to stay small, and nonlinearities are expected to be present practically and should therefore be accounted for.

For the case of unidirectional wind, i.e. the wind direction does not vary with altitude, the tethered balloon system equilibrium will be planar. This section assumes unidirectional wind conditions and limits disturbances and motion to directions within this plane.

In this section, examples of possible changes in the wind velocity profiles and their effects on the system are considered. Changes in wind conditions are some of the most crucial and likely disturbances to affect the system, and how the system copes with these is a major factor in determining its feasibility. Wind changes for sustained periods of time (even of the order of minutes) can cause the balloon's altitude to be altered, which brings about failure risks, such as changes in the balloon's differential pressure, and the possibility of blow-over.

In the case studies, relatively extreme wind disturbances are considered to highlight the effects of feedback control on the system. The criteria used to quantify each response are the balloon's maximum deviation from its equilibrium altitude, and the maximum axial stress experienced by the tether, which includes dynamic stresses due to shock.

9.8.1 2D Case 1: In-Plane Wind Gust on Balloon

While the design wind speed of 55m/s acting along the system's length is extreme and mainly used to ensure that the system is able to tolerate strong sustained winds, it is actually possible that the balloon will have to tolerate strong winds of around 45m/s [30]. The steady state wind conditions do not account for gusts that may take place in the short term. In this case, a 25m/s wind velocity (resulting in a total wind speed of approximately 45m/s acting on the balloon) in the positive x-direction is applied to the balloon to mimic a gust, while the remainder of the velocity profile remains as normal. This gust is set to last for 500 seconds and then returns to its steady state wind velocity. The open loop response to these wind conditions is observed. Figure 9.14 shows the tether's planar shape as it varies with time.

For this case, the balloon is seen to drop to a minimum altitude of 19.1km.

A feedback controller is then designed and adapted using the linearized version of the model and then implemented into the nonlinear system model. Trial and error is used to

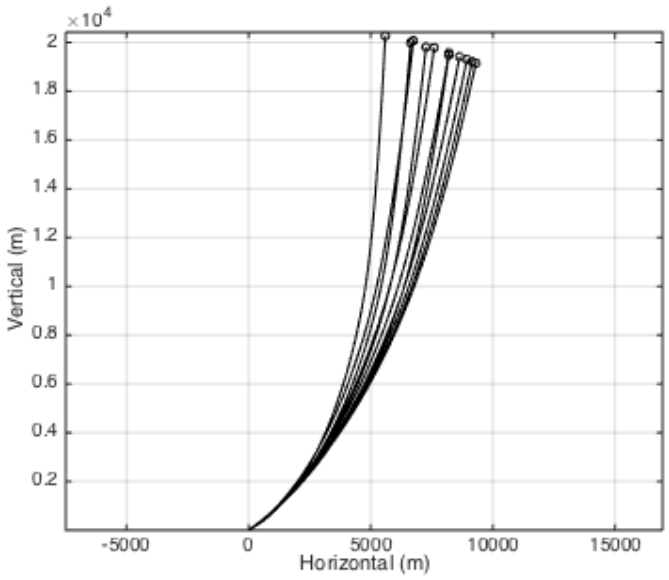

Fig. 9.14 HATB response to a horizontal in-plane wind gust on the balloon with a wind speed of 25m/s

find cost parameters that produce a suitable compromise in how 'expensive' the controller is. Figure 9.15 shows the vertical motion of equally spaced points along the system (the balloon and 20 equally spaced points along the tether), for both the open loop and closed loop systems. The closed loop response is plotted in black above the open loop response which is displayed in red.

In the open loop case, the points along the tether are seen to move downwards (and in the positive x-direction) with time in response to the gust and then stop and begin to return to their equilibrium when the gust stops at $t = 500s$. The closed loop response begins in the same way, but by about $t = 50s$, the system's response begins to deviate from the closed loop one. The tether's deviation from its equilibrium slows down before beginning to return at around $t = 200s$. Once the wind gust stops, the system exhibits some overshoot when returning to its equilibrium.

Figure 9.16 shows the variation of the system's shape over time for the two responses. The range of motion can be seen to have been reduced by the feedback controller.

A graph showing the balloon's change in altitude against time is also plotted in figure 9.17 for the open and closed loop system's for a comparison, since this is a crucially important parameter in the system's safe operation. The balloon's equilibrium altitude is displayed in a dashed line to highlight deviations from it. Although the closed loop response shows an increase in balloon altitude relative to the equilibrium that the open loop doesn't, the balloon appears to stay significantly closer to the equilibrium altitude on the whole.

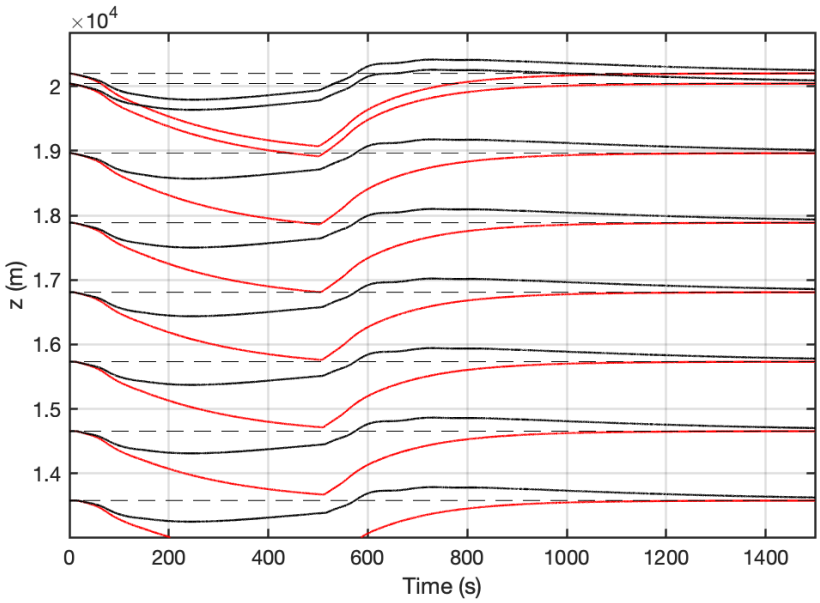

Fig. 9.15 Altitude variation of the balloon and the top 7 of 20 equally spaced points along the tether in response to an in-plane balloon gust of speed 25m/s acting on the balloon. The open loop response (red) and closed loop response (black) are plotted.

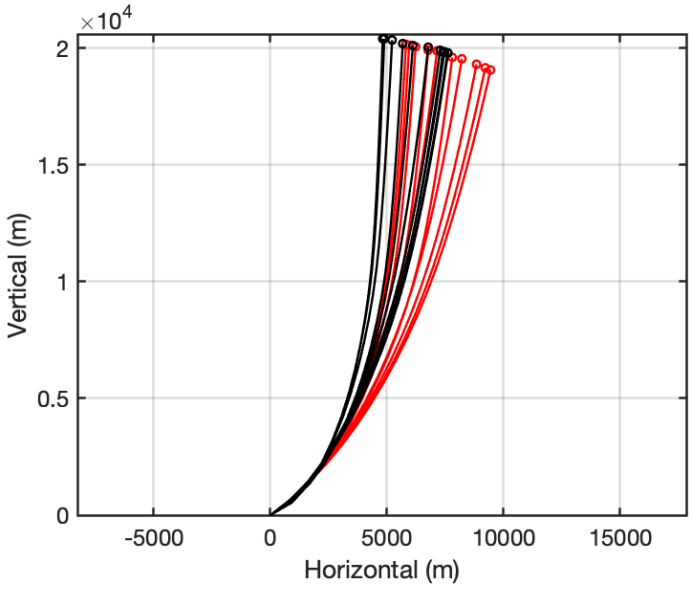

Fig. 9.16 Tethered Balloon shape variation for a superimposed 25m/s gust on the balloon for 500s, for closed loop system (black) and open loop system (red)

Table 9.4 displays a comparison of some important values obtained from the two responses. The balloon's altitude dropped by 5.6% for the open loop case to 19.1km, and

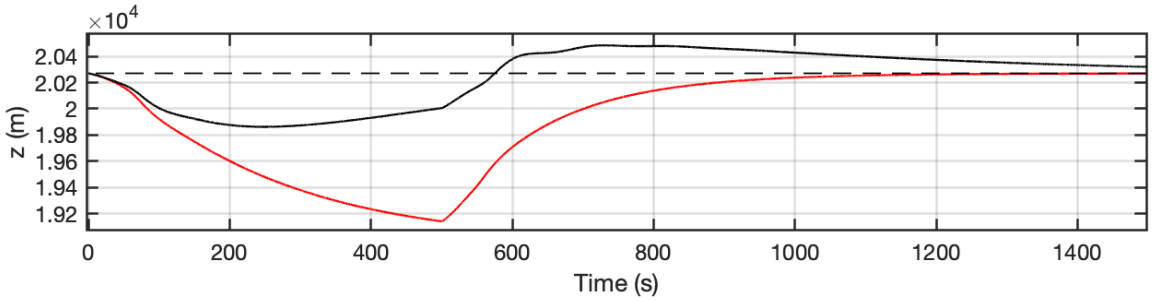

Fig. 9.17 Balloon Altitude against time for a 25m/s gust on the balloon for 500s, for closed loop system (black) and open loop system (red).

dropped by only 2.0% for the closed loop case t0 19.9km altitude, meaning that the implementation reduced the balloon's maximum altitude deviation by 64%.

There was also a significant improvement in the increase of the maximum longitudinal stress reached in the tether from the equilibrium case, increasing by 21.5% for the open loop system and 7.5% for the closed loop system. This is an improvement of 65%. For both cases the maximum stress reached by the tether is acceptable and significantly below the stress limits designed for the system.

Table 9.4 Comparison of Key Parameters of Response to 45m/s Balloon Gust for Open and Closed Loop Systems

Parameter	Open Loop	Closed Loop
Minimum Altitude Reached by Balloon	19.14km	19.86km
Altitude Drop from Eqm (%)	5.6%	2.0%
Maximum Altitude Reached by Balloon	20.27km	20.48km
Altitude Rise from Eqm (%)	0%	1.0%
Maximum Tension Experienced by Tether	13.9MN	12.2MN
Maximum Tether Stress	587MPa	519MPa
Increase in Maximum Tether Stress from Eqm (%)	21.5%	7.5%

These improvements in the system's response to the disturbance would be pointless if the base motion required to achieve them is unfeasible. The base motion produced by the controller that achieves the closed loop response described is presented in figures 9.18 and 9.19 which show the base displacement and velocity respectively as functions of time.

This response would require a maximum velocity of 14.2m/s, or 41.1km/h, which is less than 30 knot (55.6km/h) ship speed limit suggested. The velocity also changes smoothly, and the magnitudes of ships acceleration are very reasonable. The ship motion produced by the controller therefore appears to be practical and feasible, and results in a significant improvement to the system's response to the wind gust on the balloon.

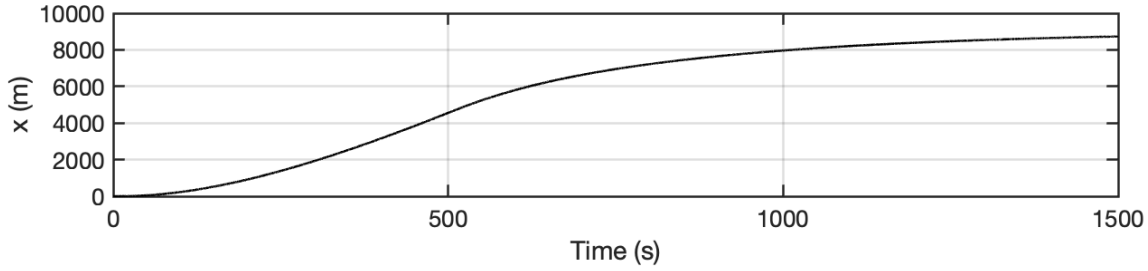

Fig. 9.18 Closed-loop base displacement for a 25m/s in-plane gust on the balloon for 500s

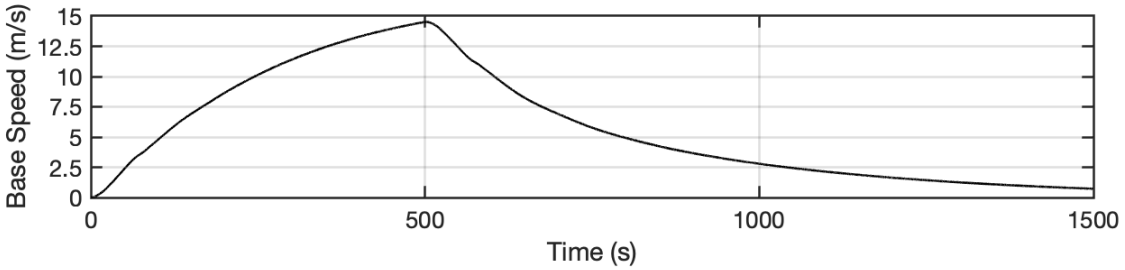

Fig. 9.19 Closed-loop base velocity for a 25m/s in-plane gust on the balloon for 500s

Table 9.5 Summary of the effects of the feedback controller on the system's response to a 45m/s wind gust disturbance on the balloon

Parameter	Improvement
% Reduction in Balloon Altitude Deviation	64%
% Reduction in Tether Stress Increase	65%

9.8.2 2D Case Study 2: 70% Increase in Wind Profile

In this case study the wind velocity along the entirety of the tether and balloon temporarily increases by a uniform factor. The wind velocity profile is assumed to increase to 1.7 times its normal value and then back down over a period of 500 seconds, in a sinusoidal manner. The equation for the ratio of the wind velocities to their normal value as a function of time is:

$$\frac{V_w}{V_{w,0}} = 1 + 0.7\sin(\frac{2\pi t}{T}) \qquad 0 < t < T/2 \tag{9.37}$$

The ratio of the wind speeds is equal to 1 outside of that time range. For this specific case, T is equal to 1000s. The change in wind over time relative to the steady state wind profile is plotted in Figure 9.20. This is an arbitrary example of a potential change in the wind conditions on the entire system.

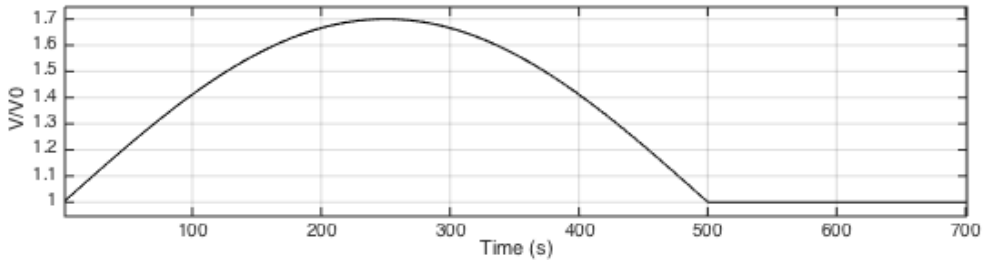

Fig. 9.20 Change in wind as a function of time

At each time step, the wind profile is multiplied by a factor that is calculated using the above equation, and the wind forces are calculated accordingly. The balloon altitude for the open and closed loop system responses is plotted in Figure 9.21.

It can be seen that the balloon's altitude drop is smaller for the closed loop system. While the open loop system balloon altitude drops by 3.8% down to 19.5km, implementing a feedback controller reduced this to 1.3%, to a 20.0km altitude. Applying feedback control to the system therefore reduced the balloon's maximum altitude deviation by around 66% for this case.

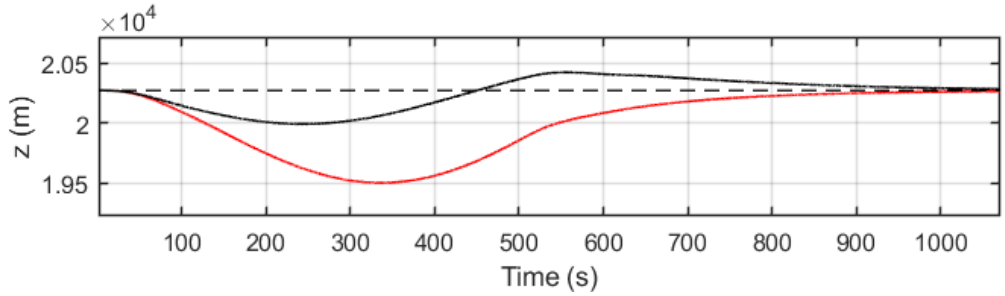

Fig. 9.21 Balloon altitude variation in response to a sinusoidally increasing wind profile (up to 70%) for the open-loop system (red) and closed-loop system (black).

Table 9.6 displays a summary of the important parameters reached by the system with and without a controller. The increase in tether stress was also seen to be reduced by 61% with feedback control.

The base motion as determined by the feedback controller that produced the closed loop response discussed is displayed in Figures 9.23 and 9.22 which show the base's displacement and velocity respectively, against time.

The maximum ship speed required for this response was 15.4m/s, which is just under 30 knots, which is the suggested speed limit to maintain practicality.

A summary of the improvements that resulted from the implementation of a feedback controller are summarised in Table 9.7.

Table 9.6 Comparison of Key Parameters of Response to a sinusoidally increasing wind profile up to 70% for Open and Closed Loop Systems

Parameter	Open Loop	Closed Loop
Minimum Altitude Reached by Balloon	19.50km	20.00km
Altitude Drop from Eqm (%)	3.8%	1.3%
Maximum Altitude Reached by Balloon	20.27km	20.42km
Altitude Rise from Eqm (%)	0%	0.7%
Maximum Tension Experienced by Tether	13.24MN	12.09MN
Maximum Tether Stress	561MPa	513MPa
Increase in Maximum Tether Stress from Eqm (%)	16.1%	6.2%

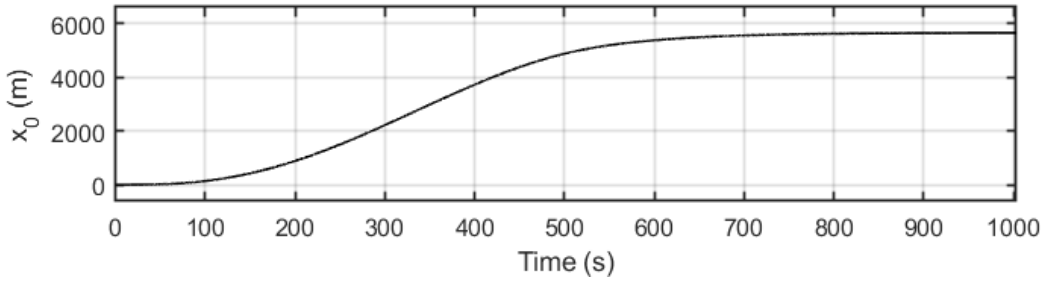

Fig. 9.22 Closed-loop base displacement for a sinusoidally increasing wind profile of up to 70%

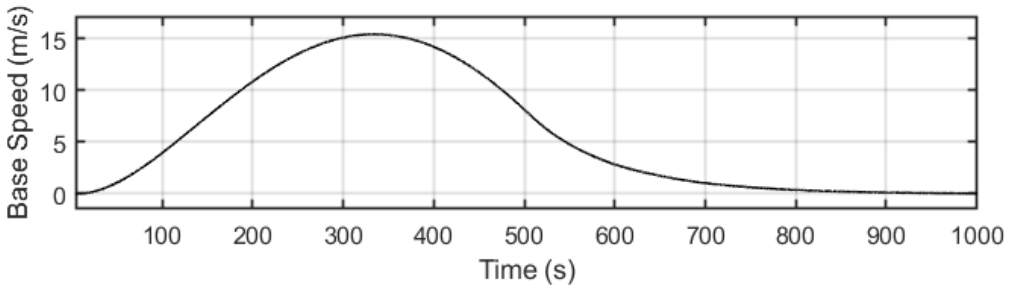

Fig. 9.23 Closed-loop base velocity for a sinusoidally increasing wind profile of up to 70%

Table 9.7 Summary of the effects of the feedback controller on the system's response to a 70% increase in the steady-state wind profile.

Parameter	Improvement
% Reduction in Balloon Altitude Deviation	66%
% Reduction in Tether Stress Increase	61%

9.8.3 2D Case Study 3: 50% Wind Drop

This case investigates the possibility of a drop in the steady state external wind conditions, which is expected to result in the balloon rising. As the balloon's altitude increases, so does

the differential pressure across its wall. The balloon is pressurized for its design altitude, so deviations from this must be kept minimal to avoid balloon failure. A 50% reduction in the wind velocity profile for a time duration of 500s was considered.

Feedback Control was implemented, and Figure 9.24 displays the resulting balloon altitude variation for the open and closed loop systems. Once again, the range of vertical motion exhibited by the balloon has been significantly reduced through the implementation of feedback control.

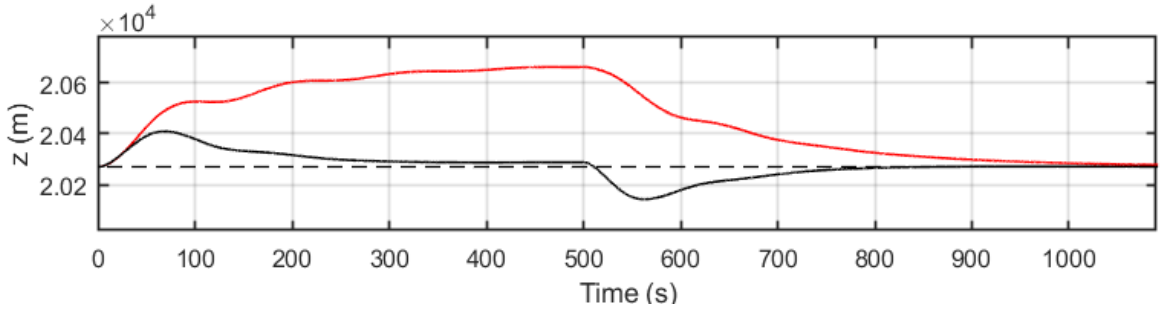

Fig. 9.24 Balloon altitude response to a 50% drop in the steady state wind conditions for the open-loop system (red) and the closed-loop system (black).

The response data is plotted in Table 9.8. The balloon rise due to the wind drop is reduced by 63% through the addition of feedback control.

Table 9.8 Comparison of Key Parameters of Response to a Wind Drop of 50% for 500 seconds for Open and Closed Loop Systems.

Parameter	Open Loop	Closed Loop
Minimum Altitude Reached by Balloon	20.27km	20.14km
Altitude Drop from Eqm (%)	0%	0.6%
Maximum Altitude Reached by Balloon	20.66km	20.41km
Altitude Rise from Eqm (%)	1.9%	0.7%

The tension data is not included in this case as a reduction in wind velocity is unlikely to result in an increase in tension, and tension values remained relatively constant in both models.

Figure 9.25 shows the base velocity that produced the response discussed.

The wind drop resulted in the base accelerating in the negative x-direction as expected. The maximum wind speed in this case is 13.51m/s and is therefore considered practically feasible.

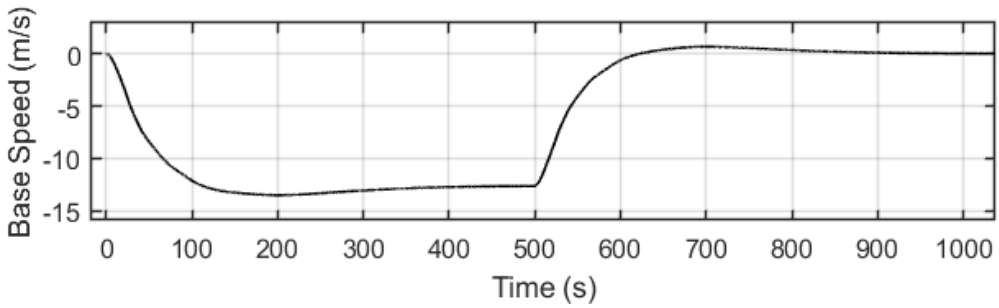

Fig. 9.25 Closed-loop base velocity for a 50% drop in the steady-state wind velocity profile.

9.9 SPICE Case Studies: 3-Dimensional Cases

In this section, disturbances and motion are no longer confined to the plane of the system, and full 3-dimensional motion is allowed. To account for unwanted motion in all directions, the feedback control is also extended to 3-dimensions, i.e. the control input is now a force on the base that can act in any direction in the horizontal plane, allowing for base motion in any direction on the plane. The input force can now be thought of as a vector rather than a scalar. Apart from that, the same process is applied as in the previous section; the system equilibrium is established under certain external conditions, and the system's open and closed loop responses to certain disturbances are observed and compared. A more detailed analysis of the controller's behaviour is included for the more complex 3-dimensional control. The effects of varying the cost function on the system's closed loop response are also studied in this section.

9.9.1 3D Case 1: Uniform Out-of-Plane Wind Disturbance

As in the 2-dimensional case, the effect of a change in the wind conditions is considered in this section. Since the model used in this section is 3-dimensional, the effects of changes in the equilibrium wind direction can also be considered.

The first case considered, is that in which a uniform wind speed of 25m/s acts all along the tether in the positive y-direction in addition to the equilibrium wind profile which acts in the x-direction. A uniform wind profile is practically unlikely and this is just used as an example to observe the system's closed and open loop responses to out-of-plane winds. The system begins at its equilibrium state, and the out of plane winds begin at $t = 0s$. After 700 seconds, the out-of-plane wind speed linearly decreases until it returns to zero at $t = 800s$. Figure 9.26 shows the magnitude of the uniform wind speed in the y-direction against time.

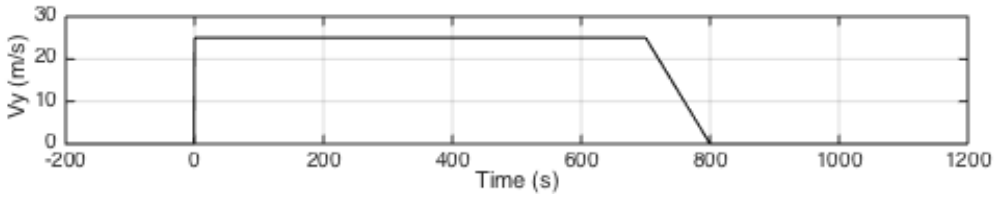

Fig. 9.26 Speed of uniform out-of-plane wind disturbance as a function of time.

At each time step, the wind velocity in the y-direction acting on the system can be calculated using the following expressions, which are independent of altitude in this case:

$$V_{y,j} = 25 \qquad 0 < t < 700 \tag{9.38}$$

$$V_{y,j} = -0.25t + 200 \qquad 700 < t < 800 \tag{9.39}$$

$$V_{y,j} = 0 \qquad t > 800 \tag{9.40}$$

Once the magnitudes of the x and y-direction wind speeds are computed for an element using expressions 9.1, 9.2 and 9.38-9.40, the relative wind velocity is found by subtracting the element's instantaneous velocity from these. Using this, the magnitude and direction of the instantaneous drag force experienced by the element can be calculated.

The system's open and closed loop responses to this out-of-plane wind disturbance are observed and compared. Since the system can now move and rotate in 3D space, a plot of the x-coordinates of the tether elements as functions of time do not give a good representation of the system's response, since the (approximate) vertical plane that the system exists in will be constantly varying. A plot of the altitudes or z-coordinates of 20 equally spaced points along the tether plus the balloon are plotted against time in Figure 9.27. The figure displays a close-up of the top 7 elements to make the changes in altitude more clearly visible, since these are small relative to the absolute altitudes of the points in question. The open loop system response is plotted in red, and the closed loop response is plotted in black.

In the open loop response, the additional wind is seen to cause a gradual drop in altitude of the points along the tether and the balloon, which begins to rise back up at around 700 seconds as expected. The closed loop system also shows an initial dip, but in this case the system begins to recover much faster, beginning to rise back up at around $t = 150s$ until it returns to its equilibrium. The system's closed loop response is analysed in more detail in section 9.9.2. Upon implementing feedback control, the altitude deviations of the points are seen to be significantly reduced, remaining relatively close to their equilibrium altitudes (plotted in black dashed lines) throughout the system's response.

Figure 9.28 shows just the balloon altitude's variation with time for the two systems for a clearer comparison. In addition to the balloon's altitude drop being significantly smaller

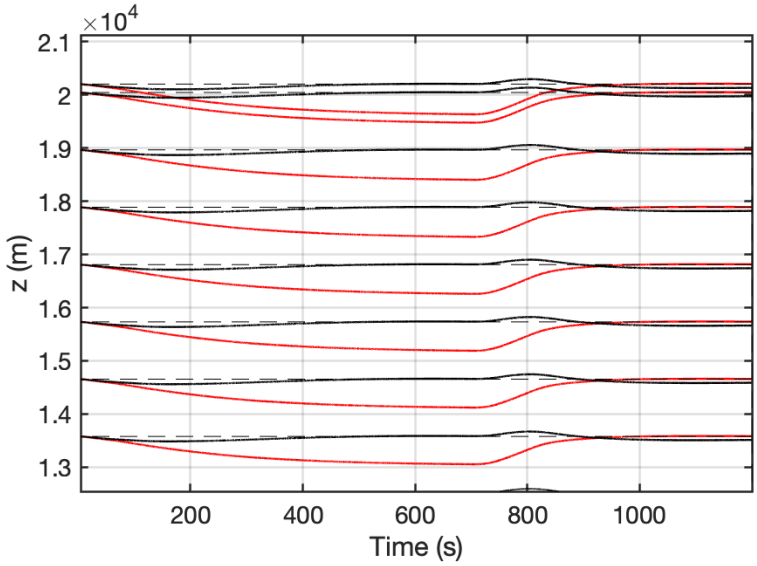

Fig. 9.27 Altitude variation of balloon and 20 equally spaced points along the tether in response to a uniform out-of-plane wind disturbance of 25m/s speed for the open-loop system (red) and the closed-loop system (black).

for the closed loop system, its rate of dropping appears to quickly reduce until around 150s where it ceases to drop any further, and begins to then rise back up towards its equilibrium altitude, while the open loop altitude is seen to continue to drop all the way until the out of plane wind speed begins to decrease. The open loop plot has a negative gradient immediately prior to $t = 700s$, indicating that the system was yet to reach its new equilibrium, and the altitude would have continued to drop even further if the wind disturbance was left unchanged. The balloon altitude is seen to drop by 2.8% to 19.70km without feedback control, and by only 0.4% to 20.19km with the feedback controller implemented. The introduction of the controller therefore resulted in an improvement of 86% in the balloon's maximum deviation from its design altitude. It is theoretically possible to improve this response further, at the cost of a larger control effort by implementing a cheaper controller, but this may become practically unfeasible and has disadvantages of its own. This will be discussed further in Section 9.9.3.

A visible disadvantage of using feedback control to reduce balloon drop for an increased wind disturbance is that, upon returning to its equilibrium altitude, the balloon becomes more susceptible to rising above its equilibrium altitude when the wind disturbance drops back down. In this case, the closed loop balloon altitude is seen to rise by 0.4% above its equilibrium because of this. In the open loop case, the balloon's altitude rises above its equilibrium by only 0.05% in a slight overshoot. Upon recovering from the rise above its equilibrium altitude, the balloon in the closed loop system exhibits a slight overshoot before

returning to its equilibrium state around the same time as the open loop system. Despite the increased maximum balloon altitude due to the controller, the balloon's deviations from its equilibrium altitude are greatly minimised on the whole, and the closed loop response is considered a significant improvement to the open loop response with respect to the balloon's altitude.

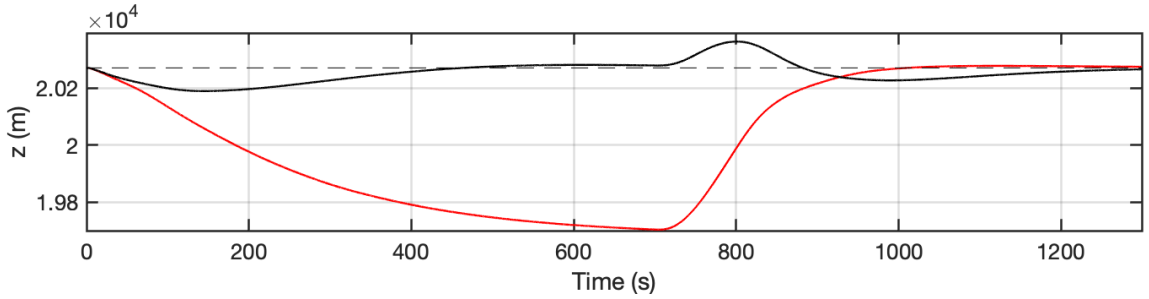

Fig. 9.28 Balloon altitude response to a uniform out-of-plane wind disturbance of 25m/s speed for the open-loop system (red) and the closed-loop system (black).

Figure 9.29 shows the motion of the closed loop system for the first 1200s of the response to scale to aid in the visualisation of how the controlled system achieves the improvements discussed above.

For a clearer visual of the system's deviation from its equilibrium state with time, Figure 9.30 shows the tether's planar shape relative to the base for 10 equally spaced time intervals for the closed (black) and open (red) loop systems. This diagram represents neither the view as an x-z plane projection or a y-z plane projection, but rather the planar image of the system at each time instant depicted. The x-axis of the graph therefore represents neither the x or the y-coordinates of the points, but the horizontal distance from a vertical axis going through the tether's base, to account for the 3-dimensional motion and rotation of the system. Although at each time instant the system is not necessarily completely planar, this is a good enough approximation to aid in the comparison of the deviated shape of the system with time for the closed and open loop systems. As expected, the open loop system shows a significantly wider range of deviated system shapes than the closed loop system which remains much closer to the equilibrium state throughout.

Table 9.9 displays a summary of some of the key parameters of the responses of the closed and open loop systems for comparisons. Besides minimizing the balloon's altitude variation, the other aim of implementing feedback control is to minimise the increased tether tension that may arise due to wind disturbances. For the wind disturbance considered in this case, the maximum tension in the tether increased by almost 11% for the open loop system and by just over 1% in the closed loop system. The implementation of the controller therefore

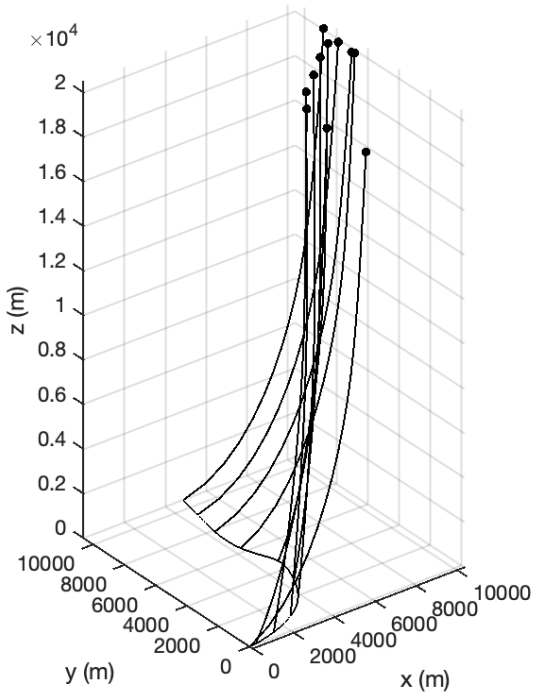

Fig. 9.29 3-Dimensional closed-loop system response to a uniform out-of-plane wind disturbance of 25m/s.

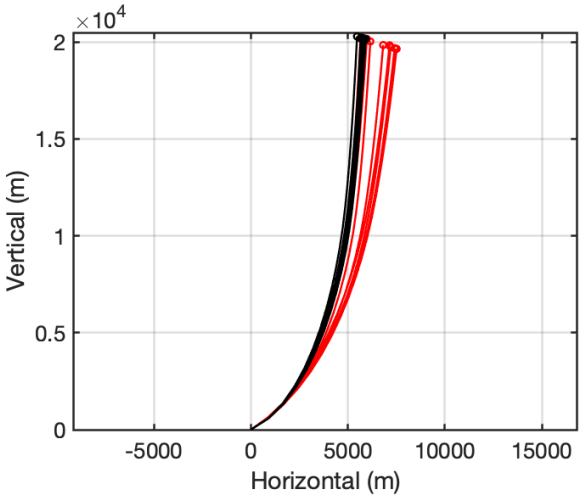

Fig. 9.30 System shape deflection response to a uniform out-of-plane wind disturbance of 25m/s speed for the open-loop system (red) and the closed-loop system (black).

resulted in an 89% improvement in reducing the increase in the tether's longitudinal stress, as well as the 86% reduction in the maximum deviation of the balloon's altitude.

Table 9.9 Comparison of Key Parameters of Response to a uniform out-of-plane wind disturbance of speed 25m/s for Open and Closed Loop Systems.

Parameter	Open Loop	Closed Loop
Minimum Altitude Reached by Balloon	19.70km	20.19km
Altitude Drop from Eqm (%)	2.8%	0.4%
Maximum Altitude Reached by Balloon	20.28km	20.36km
Altitude Rise from Eqm (%)	0.05%	0.4%
Maximum Tension Experienced by Tether	12.61MN	11.53MN
Maximum Tether Stress	535MPa	489MPa
Increase in Maximum Tether Stress from Eqm (%)	10.8%	1.2%

Similarly to the 2-dimensional cases, the base motion required for the closed loop system response is checked to ensure its practicality, and the cost function altered if necessary. For the 3-dimensional cases, the control input is no longer a scalar, but rather a vector, since the ship is now allowed to move in its horizontal plane. The direction of the base motion must now also be considered in addition to the base speed. Figure 9.31 shows a plan view of the trajectory of the ship as well as the trajectory of the balloon, in solid black lines (the base trajectory begins at the origin and the balloon trajectory begins further along the x-axis). The dashed lines linking these are the instantaneous plan views of the tether at 20 equally spaced time intervals. The circles linking these to the balloon's trajectory represent the balloon's position at these times, to scale. Figure 9.32 displays the magnitude of the base speed as a function of time. The maximum speed exhibited by the ship in this case is 13.9m/s which is approximately 27 knots, and therefore below the suggested speed limit of 30 knots. In addition to maximum speed, it is important that acceleration rates depicted by the closed loop model are also practically achievable, since this is limited by the large inertia of a ship that is sufficiently large to be used to anchor the system. It can be seen in Figures 9.31 and 9.32 that there are no dramatic changes in the speed or in the direction of the motion of the base that would be considered unfeasible.

The controller therefore appears to be practically applicable, and is shown to result in a big improvement in the system's dynamic response to the out of plane wind disturbance, by reducing the balloon's altitude deviation and the maximum stress reached by the tether, and therefore significantly decreasing the system's likelihood of failure under such a disturbance.

9.9.2 Analysis of Closed Loop System Behaviour

In this section, the response of the closed loop system is analysed and discussed in more detail. As mentioned in the previous section, Figures 9.31 and 9.32 display a plan view of

Table 9.10 Summary of the effects of the feedback controller on the system's response to a uniform out-of-plane wind disturbance of speed 25m/s.

Parameter	Improvement
% Reduction in Balloon Altitude Deviation	86%
% Reduction in Tether Stress Increase	89%

the system's trajectory with time and the base speed with time, respectively. These figures collectively portray the velocity of the base and therefore allow for the behaviour of the controller to be studied. The plots are labelled with numbers to indicate the approximate points at which the listed key occurrences take place. The closed loop balloon altitude is re-plotted in Figure 9.33 on its own, and is also labelled at the corresponding points.

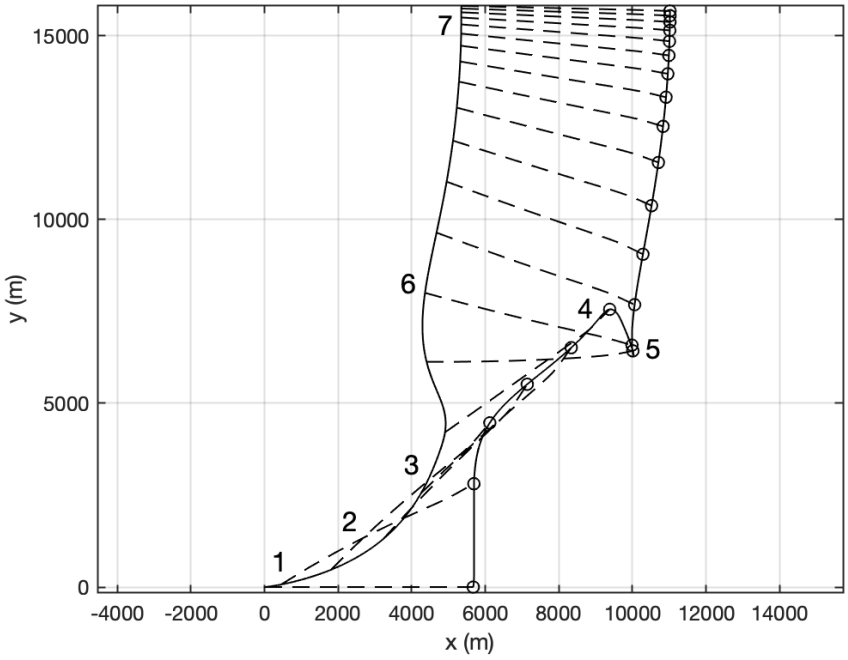

Fig. 9.31 Plan view of closed-loop system response to uniform out-of-plane wind disturbance of speed 25m/s. Black lines show the trajectory of the ship and the balloon (balloons displayed to scale) and the dashed lines are the plan views of the tether at equal time intervals.

Correlating to the numbers marked on Figures 9.31-9.33, the following list summarises the main occurrences of the closed loop system's response to the out-of-plane wind disturbance:

1. $t = 0 - 150s$ - The out of plane wind disturbance begins at time $t = 0$. The balloon begins to move in the positive y-direction relative to the stationary base, triggering

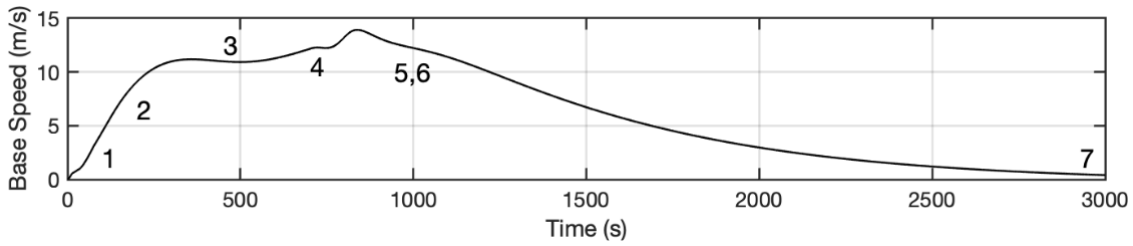

Fig. 9.32 Closed-loop base speed in response to a uniform out-of-plane wind disturbance of speed 25m/s.

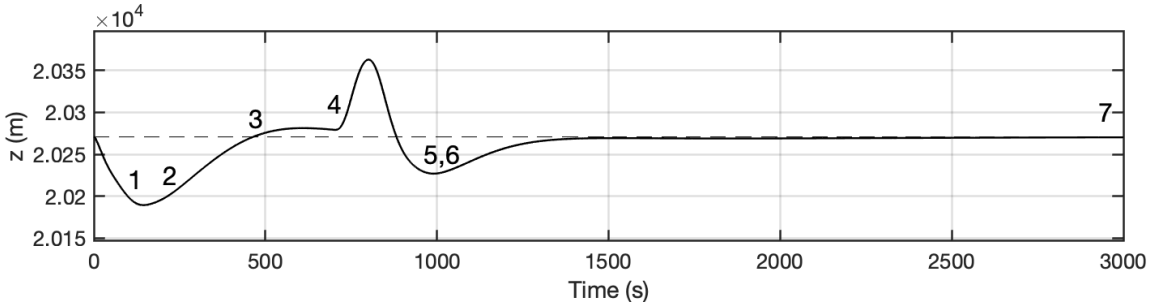

Fig. 9.33 Closed-loop balloon altitude variation in response to a uniform out-of-plane wind disturbance of speed 25m/s.

the controller into exerting a base force that causes the base to begin to accelerate. As the system's states deviate further from the equilibrium, the control input increases, and the base accelerates at a faster rate. Due to the large inertia of the base, and the input force being proportional to the extent of the reference error, the balloon will have already travelled by a significant amount before the base begins to make progress in its control. Once the base gets going, the rate at which the balloon descends can be seen to drop.

2. $t = 150 - 300s$ - To reduce the system's altered shape, the base travels in a direction that is approximately within the vertical plane of the system and towards the balloon, alleviating the tether's tension and reducing the rate at which the balloon travels away from its base. Figure 9.33 shows that the balloon height plateaus and then begins to rise again. As the system begins to return to its equilibrium state, the control input begins to decrease, and the rate of acceleration of the base begins to decrease.

3. $t = 400 - 750s$ - Once the base has 'caught up' and corrected the relatively large deviation that occurred due to the delay caused by its inertia, it begins to gently steer away from the direction towards the balloon, and towards the positive y-direction in order to maintain the corrected state under the wind disturbance forces acting in the

y-direction. Figure 9.33 shows the balloon reach its equilibrium altitude at around 500s and then exhibit a slight overshoot. The overshoot is also likely to have played a role in the base's steering away from the direction towards the balloon. At $t = 700s$, (a little bit prior to point 4 in Figure 9.31, the magnitude of the wind disturbance begins to decrease, and the balloon begins to decelerate in the y-direction. This causes the balloon's altitude to begin to rise, because the base still has a component of its velocity in the direction of the balloon.

4. $t = 750 - 900s$ - At $t = 750s$, the y-component of the balloon's velocity has decelerated to zero, before dropping below zero and starting to move in the negative y-direction. Due to its inertia, as well as the wind force in the x-direction, it maintains a velocity component in the positive x-direction. As the balloon rises further, the base begins to steer away from the direction towards the balloon faster to reduce this deviation, until the balloon begins to drop again at $t = 800s$. Since the controller input force is predominantly proportional to the to the deviations of the angles from the vertical in the direction away from the equilibrium, once the system begins to return back towards its equilibrium state, the force reduces and the base begins to decelerate.

5. $t = 900 - 1000s$ - Since the balloon and base are travelling in opposite y-directions, soon after, the tension begins to increase in the tether, until the base begins to pull the balloon back in the positive y-direction, as seen in Figure 9.31. This results in the balloon's altitude dipping below equilibrium once again.

6. $t = 1000 - 1500s$ - As the base continues to decelerate, the balloon's altitude begins to rise again. By around 1500s, the balloon's altitude has returned to being very close to its equilibrium value. With the wind acting purely in the positive x-direction at this point, the wind forces act to push the balloon such that its position relative to the base is also purely in the positive x-direction. With the base being further than the balloon in the y-direction, the balloon travels with a component in the positive y-direction to align its plane with the wind and return to its equilibrium state in which the Euler angles ϕ_j equal zero.

7. t=$1500 - 3000s$ - The base's rate of deceleration decreases as the system approaches its equilibrium position. At around t=3000s, the base velocity reaches 0m/s, and the tethered balloon system has aligned its plane with the direction of the wind. This occurred at a slow enough rate that no overshoot was observed. This is because the controller input is directly proportional to the magnitude of the deviations of the states

of the system, and so, as these approach zero, the base force also approaches zero, at which point the ship naturally decelerates as a result of drag.

9.9.3 Investigating the Effects of Varying the Cost Function

In this section, the effects of altering the parameter values of the cost function of the closed loop response are investigated. Since it is only the ratio of the costs that matters, the input cost matrix R is left unchanged. As discussed previously, the states w_j and $\dot{w}_j$ are assigned very small cost values of the order of 10^{-4} since their variation has no negative impact on the system's safe operation. While v_j and $\dot{v}_j$ do have an impact on the system's safety, the minimisation of the coordinates associated with u_j were given priority and therefore the largest cost parameter.

This section therefore focuses on the variation of the cost parameter values of the u_j and $\dot{u}_j$ states, as these are the states that pose the greatest risk to the HATB system in terms of balloon failure. As mentioned previously, the costs of these sets of coordinates are given the same value, q_u so in this section the value of only one parameter is altered.

In order to investigate the effects of varying the state costs relative to the input costs, two additional feedback controllers are designed using two different quadratic cost functions. Naming the controller used in the previous section Controller 1, the additional controllers are named Controllers 2 and 3.

The cost parameters of the expensive controller, Controller 2 relative to Controller 1 are:

$$\frac{(q_v/R)_2}{(q_v/R)_1} = \frac{(q_w/R)_2}{(q_w/R)_1} = \frac{(q_{\dot{v}}/R)_2}{(q_{\dot{v}}/R)_1} = \frac{(q_{\dot{w}}/R)_2}{(q_{\dot{w}}/R)_1} = 1, \quad \frac{(q_u/R)_2}{(q_u/R)_1} = \frac{(q_{\dot{u}}/R)_2}{(q_{\dot{u}}/R)_1} = 0.1 \tag{9.41}$$

The cost parameters of the cheaper controller, Controller 3 relative to Controller 1 are:

$$\frac{(q_v/R)_3}{(q_v/R)_1} = \frac{(q_w/R)_3}{(q_w/R)_1} = \frac{(q_{\dot{v}}/R)_3}{(q_{\dot{v}}/R)_1} = \frac{(q_{\dot{w}}/R)_3}{(q_{\dot{w}}/R)_1} = 1, \quad \frac{(q_u/R)_2}{(q_u/R)_1} = \frac{(q_{\dot{u}}/R)_2}{(q_{\dot{u}}/R)_1} = 100 \tag{9.42}$$

The ratios of the u_j and $\dot{u}_j$ state costs to the input costs are 10 times larger for Controller 1 (the controller analysed in the previous section) than for Controller 2, and all of the rest of the state costs are unchanged. These are 100 times larger for Controller 3 than for Controller 1. Controller 2 is therefore designed to be more 'expensive' than Controller 1, and Controller 3 is the cheapest controller.

Feedback control is implemented for both of these new cost functions separately, by producing an optimal gain matrix for each respective cost function and implementing it into the nonlinear system model. The closed loop systems' responses to the same wind disturbance are plotted in Figure 9.34 in the form of the balloon's altitude variation with time, since this

is one of the most important states to control, along with the tether's maximum stress. In this section, the response is plotted in black for Controller 1, in dark blue for Controller 2 and light blue for Controller 3. The system's open loop response to the disturbance is also plotted alongside these for reference, in red. It can be seen that all 3 of the controllers result in a significant improvement in the system's response to the disturbance, with the cheapest controller producing the best response of the three, at the price of a larger control effort. Controller 3 resulted in the best dynamic response as measured by the reduction in the system's deviation from its equilibrium, followed by 1 and then 2, as expected.

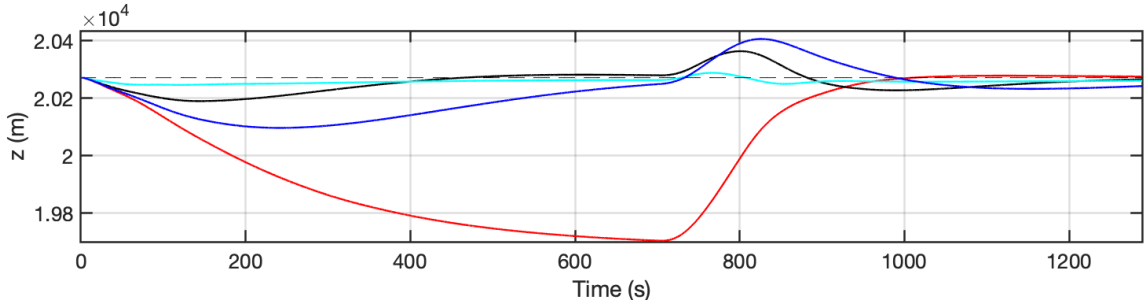

Fig. 9.34 Comparison of balloon altitude response for Controllers 1 (black), 2 (dark blue) and 3 (light blue) and the open-loop response is displayed for reference (red).

The way in which the controller's expensiveness translates into the system's feedback input can be observed in Figure 9.35 which shows the variation of the base's speed with time for the three closed loop system responses to the disturbance. While the three systems show similar patterns of speed changes with time, the maximum ship speed is seen to increase as the controller becomes cheaper. In addition to this, cheaper controllers are seen to exhibit more dramatic accelerations which require more energy than the gentle velocity changes produced by controllers designed for systems with expensive inputs. This is expected since larger accelerations require larger input forces, and the controller input is assigned the largest relative cost in the cost function of Controller 2. LQR works to minimise the cost function, and so Controller 2 was designed to produce smaller input forces than Controller 1 and 3 for the same deviation from the equilibrium. A compromise would therefore need to be made between the extent of the improvement of the system's response, and what is feasible both practically and economically when selecting the relative costs for the controller.

The variation of the plan view of the system with time is plotted for the responses of the two new controllers in Figure 9.36, since the magnitude of the speed is insufficient to describe the base motion for a 3-dimensional system, and directional changes also constitute accelerations. Again, the direction of the base's motion varies in a similar manner for the two cases, with more drastic velocity changes observed for the base of Controller 3 in terms of

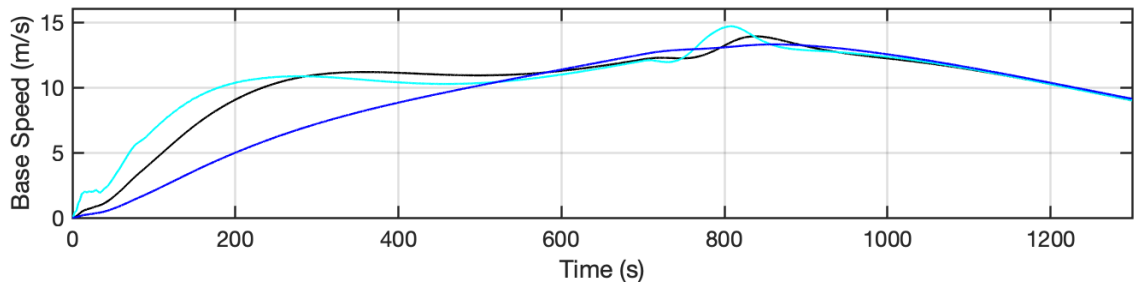

Fig. 9.35 Closed-loop base speed for Controllers 1 (black), 2 (dark blue) and 3 (light blue).

direction. A more dramatic change in base direction requires a larger input force, and since the input is assigned a larger cost value in Controller 2, a more gentle direction change is observed in the left hand side figure.

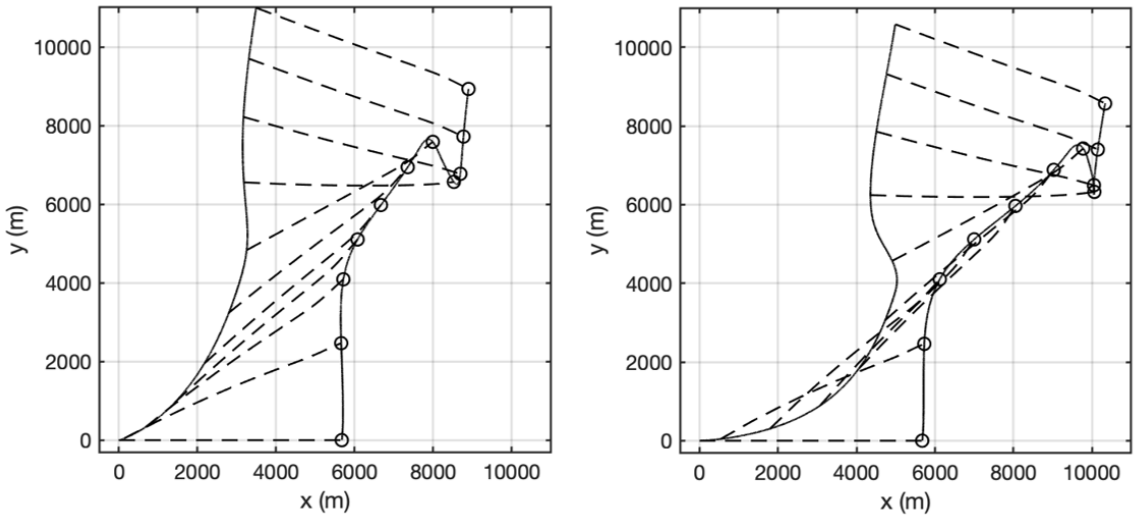

Fig. 9.36 Plan view of the the closed loop system trajectory for Controller 2 (left) and Controller 3 (right).

Table 9.11 summarises some of the key parameters of the responses of the two new closed loop systems as well as the open loop system for comparison. It can be seen that in addition to having reduced the deviations of the balloon's altitude more than Controller 2, Controller 3 also reduced the increase in the tether's stress more too, and therefore resulted in an overall better closed loop system response to the disturbance. This not only comes at the expense of a larger control effort, but is also expected to result in a less robust feedback control system in the face of time delays. The robustness of the feedback control systems in investigated in the next section.

Table 9.11 Comparison of Key Parameters of Response to a uniform out-of-plane wind disturbance of speed 25m/s for Open and Closed Loop Systems

Parameter	Open Loop	$(Q_{\dot{u}}/R)_2$	$(Q_{\dot{u}}/R)_3$
Min Altitude Reached by Balloon	19.70km	20.10km	20.25km
Altitude Drop from Eqm (%)	2.8%	0.8%	0.1%
Max Altitude Reached by Balloon	20.28km	20.41km	20.29km
Altitude Rise from Eqm (%)	0.05%	0.7%	0.1%
Max Tension Experienced by Tether	12.61MN	11.73MN	11.42MN
Max Tether Stress	535MPa	498MPa	485MPa
Increase in Max Tether Stress from Eqm	10.8%	3.1%	0.4%

The implementation of Controller 2 resulted in a 71% improvement in the maximum deviation of the balloon's altitude, compared to the 96% improvement produced by Controller 3. It shows an improvement of 71% in reducing the maximum stress experienced by the tether, compared to the 96% improvement of Controller 3. It produces base motions that are more gentle and gradual however, which would likely be cheaper to implement and more robust. Both of the controllers proved to significantly improve the system's response to out the out of plane wind disturbance, and reduce the likelyhood of the system's failure.

Table 9.12 Summary of the improvements to the dynamic response for controllers with different cost functions

Controller	$q_{u,i}/q_{u,1}$	Altitude Improvement	Tension Improvement
1	1	86%	89%
2	0.1	71%	71%
3	100	96%	96%

9.9.4 3D Case 2: Out-of-Plane Wind Gust on Balloon

In this section, a disturbance in the form of an out of plane gust on the balloon is considered as an example when investigating the effects of altering the cost values of said states. This out-of-plane wind gust acts in the positive y-direction with a constant speed of 30m/s and is superimposed onto the existing equilibrium wind profile which acts in the x-direction. This gust has a duration of 300s after which the wind velocity on the balloon in the y-direction returns to zero, and the wind conditions therefore return to the expected steady state conditions.

This case considers an out of plane gust acting on the balloon in the positive y-direction in addition to the equilibrium wind profile which acts in the x-direction. The speed of the wind in the y-direction is 40m/s, hence making the magnitude of the wind speed acting on the balloon around 45m/s, which is the speed that Davidson et al. said that the balloon may experience. The balloon gust lasts for a duration of 500s before returning to zero, as displayed in Figure 9.37.

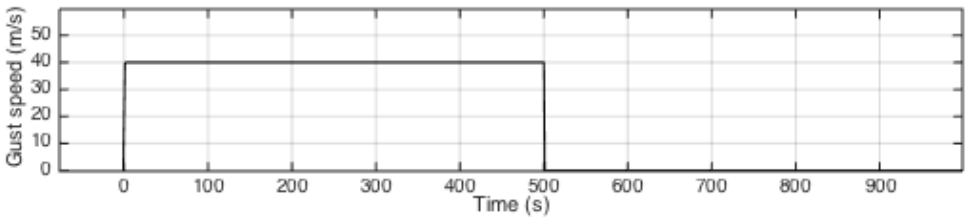

Fig. 9.37 Magnitude of the out-of-plane wind gust acting on the balloon as a function of time.

The open and closed loop responses to this out of plane balloon gust are displayed in Figures 9.38 and 9.39 in the form of the altitudes of equally spaced points along the tether against time, and a closeup of the balloon's altitude with time respectively. Similar qualitative observations can be made as in the previous case. Quantitatively, the open loop system shows a balloon drop in altitude of 3.8% to 19.5km while the closed loop system shows a balloon altitude drop of 1.8% to 19.9km. The controller therefore brought a 53% improvement in the balloon's maximum deviation from its equilibrium altitude.

In the same way as in the previous case, Figure 9.40 displays the variation in the planar shape of the tethered balloon system as time goes on for the open and closed loop systems. Once again, the implementation of the controller can be seen to reduce the amount of variation in the tether's shape.

Table 9.13 displays a comparison of the key parameters of the two responses. The controller introduces a 63% reduction in the increase of the tether's maximum stress during the response to the disturbance. Since this case considers quite a large gust speed on the balloon, greater deviations are observed in the system than in the previous case, however the percentage improvement in the response upon implementing feedback control appears to remain consistently good.

Once again, the base velocity is checked to ensure that the chosen controller is not too expensive and produces a feasible controller input. Figure 9.41 shows a plan view of the system at equally spaced time intervals in the same way as in the previous section. Starting from the origin, the ship trajectory can be observed in the bottom left corner. While this gives an idea of the direction of motion of the base, Figure 9.50 shows the magnitude of the speed of the base as a function of time. The maximum base speed observed in the response

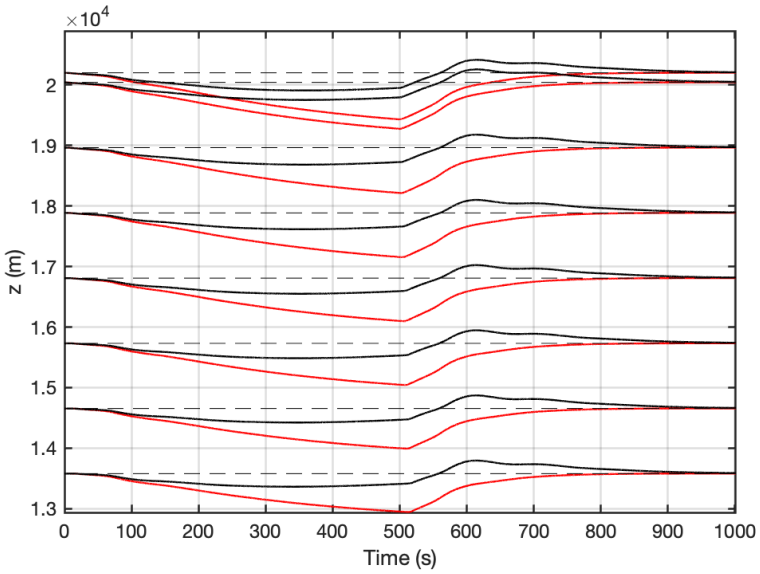

Fig. 9.38 Altitude variation of balloon and 20 equally spaced points along the tether in response to an out-of-plane wind gust of speed 40m/s acting on the balloon for the open-loop system (red) and the closed-loop system (black).

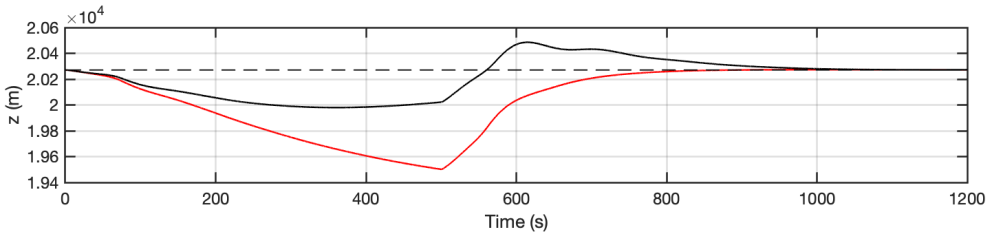

Fig. 9.39 Balloon altitude variation in response to an out-of-plane wind gust of speed 40m/s acting on the balloon for the open-loop system (red) and the closed-loop system (black).

Table 9.13 Comparison of Key Parameters of Response to an out-of-plane wind gust of speed 40m/s acting on the balloon for 500 seconds for Open and Closed Loop Systems.

Parameter	Open Loop	Closed Loop
Minimum Altitude Reached by Balloon	19.50km	19.98km
Altitude Drop from Eqm (%)	3.8%	1.4%
Maximum Altitude Reached by Balloon	20.27km	20.48km
Altitude Rise from Eqm (%)	0%	1.0%
Maximum Tension Experienced by Tether	13.1MN	11.9MN
Maximum Tether Stress	556MPa	505MPa
Increase in Maximum Tether Stress from Eqm (%)	15.1%	4.6%

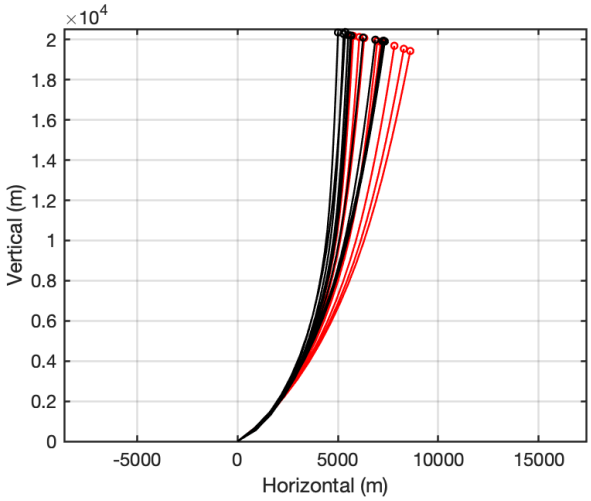

Fig. 9.40 Deflected system shape in response to an out-of-plane wind gust of speed 40m/s acting on the balloon for the open-loop system (red) and the closed-loop system (black).

is 13.3m/s (just under 26 knots) and the maximum acceleration observed is $0.12ms^{-2}$. A more expensive controller was used in this case than in the previous case, with the ratio of the state costs to the input costs doubled. This can be seen in the more dramatic speed and direction changes exhibited by the base. This controller's response still seems to be feasible, although it would be more expensive if implemented. The implications of the controller's expensiveness are discussed in more detail in the next section.

9.10 Practical Feasibility of Closed Loop HATB Systems

In Section 9.7.1, a list of practical constraints were imposed that ensure that the ship motion required to control the HATB system is practically achievable. In this section, the extent to which these were met in the results of the case studies is discussed.

It is important to keep in mind that the disturbances considered in the case studies were selected to be unrealistically large in order to both model the system's response in a worst case scenario and to highlight the benefits of the feedback controller. For this reason, the motion of the ship in these cases is on the extreme side, and is likely to be less dramatic under more common weather conditions.

1. Ship Speed

   A maximum ship speed constraint of 30 knots or 15.4m/s was selected. This constraint was met in every case study for the selected controller design.

2. Ship Acceleration

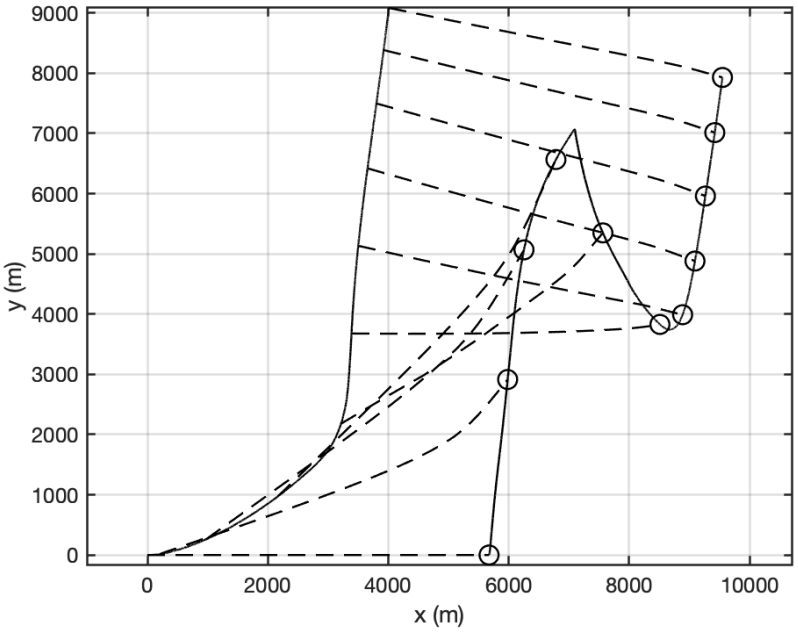

Fig. 9.41 Plan view of closed-loop system response to out-of-plane wind gust of speed 40m/s acting on the balloon. Black lines show the trajectory of the ship and the balloon (balloons displayed to scale) and the dashed lines are the plan views of the tether at equal time intervals.

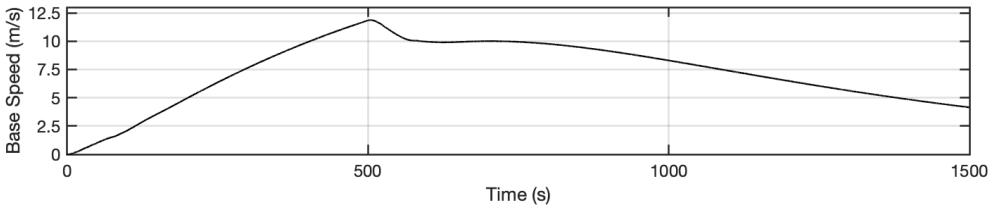

Fig. 9.42 Closed-loop base speed in response to an out-of-plane wind gust of speed 40m/s acting on the balloon.

Due to the ship's large inertia, large accelerations are unlikely to occur practically, both in terms of speed and directional changes. Maximum acceleration magnitudes in the different case studies did not exceed $0.12ms^{-2}$.

3. Distance Covered by Ship

   It was suggested that distances covered by the ship's motion not exceed the order of 10km which was achieved in the case studies, despite the extreme case scenarios.

4. Ship Output Power

A maximum ship power output of 110,000 hp or 82MW was selected. A conservative constraint for the maximum input force was then calculated by dividing the maximum power by the maximum allowable ship speed, giving a force limit of 5.4MN. The required input force for the ship's motion was significantly below that, remaining below 3MN in the range of case studies. The maximum ship output power therefore remained within practically achievable bounds.

The range of practical restrictions were therefore all met despite the extremeness of the selected disturbances of the case studies, implying that the great improvements in the responses achieved through the described feedback control methods should be practically feasible.

9.11 Robustness of Closed Loop HATB Systems

The introduction of optimal feedback control has proved to be theoretically effective in improving the system's response to harsh wind disturbances by reducing deviations from the equilibrium that may result in the system's failure. For all of the case studies investigated, feedback control significantly reduced the balloon's deviation from its equilibrium altitude as well as the maximum stress experienced by the tether. In all of these cases however, it was assumed that all of the parameters of the system are known and accurate, and that there are no time delays in the control system. When designing and incorporating feedback control into a system, it is essential that the closed loop system is not only stable, but also robust. It is important that the feedback controller is able to cope with errors and uncertainties within its design (which may come about as a result of inaccuracies in the system parameters) as well as time delays, without becoming unstable and without causing a substantial negative impact on the improved system response. In this section, the robustness of the controllers in the context of the SPICE HATB is investigated.

A robust controller is especially important for an application like the one in this research, where the external conditions vary significantly with both space and time, and it is therefore very difficult to keep track of these. It would be very expensive and unfeasible to monitor all of these at all times, and so estimates must be made when designing the controller for the system, and it is therefore vital that the closed loop system not be sensitive to errors of these estimations. This section investigates the effects of possible errors in the controller's design. Error and time delay margins specific to the system in question are looked into to establish the feasibility of incorporating feedback control to the system in question. The effect of cost function selection of the controller's robustness is also investigated.

The four main possible sources of error that may arise and should therefore be considered when investigating the system's robustness are the following:

1. Errors due to the nonlinearities exhibited by the system that are unaccounted for in the linearization and therefore controller design.

   The system model must be linearized about its equilibrium state in order to use optimal control to design a suitable feedback controller to implement. The controller is then implemented into the nonlinear system model, which differs from the linearized model it was technically designed for. In reality, the system is nonlinear, and is likely to exhibit large amplitude motion in which a linearized model is no longer a good approximation. This is a source of error in itself, and requires LQR to be robust even without the presence of parameter inaccuracies.

   This source of error is accounted for in all of the case studies described in this chapter through the application of the feedback controller to the nonlinear system model, and the use of the nonlinear model to simulate both the open and closed loop responses of the system. The linearized model was solely used to establish the optimal feedback controller. The closed loop nonlinear model responses produced in the Case Studies section proved that the controllers produced were robust enough to cope with the differences that arise due to the system actually being nonlinear.

2. Errors in the system's physical parameters

   This is an unlikely source of error, as the system's parameters can be measured to a high degree of accuracy and are unlikely to change significantly with time. The effects of potential parameter errors on the system's stability are considered in Section 9.11.1.

3. Errors in the external conditions

   Errors in external conditions, predominantly the steady state wind velocities that are used when designing the controller, are the most likely sources of error in the linearized system used to design the system's feedback controller. This is because these are likely to vary with both space and time are are therefore difficult and expensive to monitor and would need to be estimated. In the Case Studies section, the closed loop system proved to behave well under a wide range of wind disturbances occurring both in and out of plane, without losing stability. The controllers' sensitivity to errors in the equilibrium wind profile is also discussed in Section 9.11.1.

4. Time delays

One of the most important factors to consider when assessing the system's robustness is its sensitivity to time delays as these can have a large impact on the system's stability, and are very likely to be present for such a large scale system. Time delays are a different type of error that may lead to the closed loop system's loss of stability as these do not manifest as incorrect control gains, but rather, the correctly calculated control inputs are applied at incorrect times. The closed loop system's sensitivity to time delays is investigated in Section 9.11.2.

9.11.1 Closed loop system tolerance to parameter errors

It is important that the closed loop system is robust and able to cope with errors or changes in the system's parameter values or equilibrium external conditions used to design the controller. This section focuses on establishing the system's sensitivity to errors in its design. In order to test the system's sensitivity to parameter errors, the controller that is designed according to the assumed parameter values can be implemented into the system with the actual altered parameter values, and the closed loop response can be observed.

In linear terms, upon altering the system's parameter values, the state space matrices A and B are altered, but the feedback gain matrix K remains unchanged as it is designed according to the assumed parameter values. In doing this, the equivalent closed loop A matrix, $A_{CL} = A - BK$ will be altered, which leads to a shift in the closed loop poles of the system, since the following applies:

$$eig\,(A - BK) \neq eig\,(A_2 - B_2K) \tag{9.43}$$

With a large enough change to the parameter, these eigenvalues may eventually move to the right hand plane and the closed loop system becomes unstable. This assumes a fully linear system however.

Practically speaking, the system is nonlinear and is expected to exhibit motion that is not limited to small-amplitude vibrations about its equilibrium state. Using the system's linearized state space matrices to determine its robustness is therefore an oversimplification and is insufficient. To obtain a more realistic idea of the system's robustness in the face of errors in the system's parameters, the feedback controller can be applied to the mismatched nonlinear system model, and closed loop behaviour is observed for a variety of potential disturbances.

In reality, it is unexpected for there to be large errors in the measurable physical parameters of the HATB system, such as the tether's mass per unit length or stiffness or the balloon's diameter, although inaccuracies may be present. An example of a larger error

that may occur, is if the system's stratospheric particle injection operation ceases without the alteration of the feedback controller to account for the change. When not in operation, the fluid mass within the tether that is included in the controller's design is not present in the system. Another possible cause for a significant error in the controller's design is due to errors in the equilibrium external conditions assumed for the system, since these are more difficult to measure and keep track of. These potential causes for large errors in the controller's design are considered in this section.

Error in the Tether's Mass per Unit Length

During operation, the tether, which also acts as a pipe, is assumed to contain approximately 250 tonnes of fluid. In the case studies and in the design of the controllers, the operational mass of the tether was used, which includes the mass of the fluid it is expected to be carrying. One possible way to test the controller's robustness is to apply the unchanged controller designed using the combined pipe and fluid mass to the system while it is not under operation, and therefore contains no fluid. This effectively manifests as a reduction in the tether's mass per unit length by 24% in the system model. A reduction in the tether's mass affects in the system in multiple ways; the weight and inertia of the tether elements are reduced, and the equilibrium state of the system is altered, with the balloon now having an increased equilibrium altitude and the tether elements having larger equilibrium tensions. These changes are implemented into the nonlinear model, but the controller gains are kept unchanged.

The closed loop nonlinear system is observed to not only remain stable, but show a great improvement to the system's response relative to the equivalent open loop cases for a variety of disturbances. Controllers 1, 2 and 3 are used to ensure that robustness is maintained for controllers with a variety of cost functions. For the case of a uniform out of plane wind disturbance of 25m/s that lasts for 700s, the responses of the 3 closed loop systems are plotted alongside that of the open loop system (red), in the form of the balloon's altitude against time.

It can be seen that the balloon's equilibrium altitude is higher due to the system's reduced weight. Despite the significant change in the system and its equilibrium state, all 3 controllers significantly improved the HATB's response to the disturbance, with the errors in their design being unnoticeable.

Errors in the equilibrium wind profile

Another possible and likely change that may occur to the system, is a change in the external conditions, or more specifically the wind profile. While the physical parameters of the

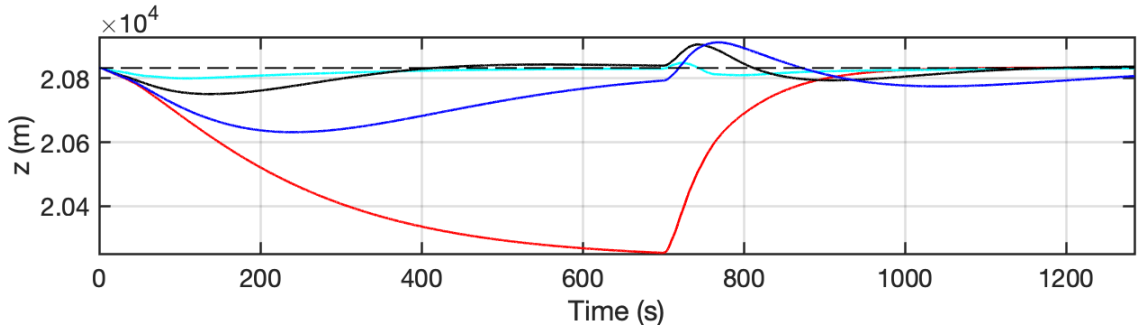

Fig. 9.43 Balloon Altitude response for a tether mass reduced by 24% to uniform out-of-plane wind disturbance of velocity 25m/s for no controller (red), and unchanged Controllers 1 (black), 2 (dark blue) and 3 (light blue).

HATB system can be measured accurately and are unlikely to change significantly with time, external conditions are not expected to be constant and so the system's robustness in the face of changes to these is crucial to its safe operation. While wind conditions can be monitored, the fact that they can change significantly with both space and time means that their values would need to be estimated and may be inaccurate at times.

It was found that, for a wide range of equilibrium wind conditions, the closed loop systems maintained their stability and still showed a great improvement in the system's response to disturbances to the new external conditions. This was tested for wind conditions of magnitudes up to 250% larger than those used in the controllers' design, and the mismatched controller maintained its stable performance. The response for this extreme case for the same wind disturbance as the previous section is plotted in Figure 9.44.

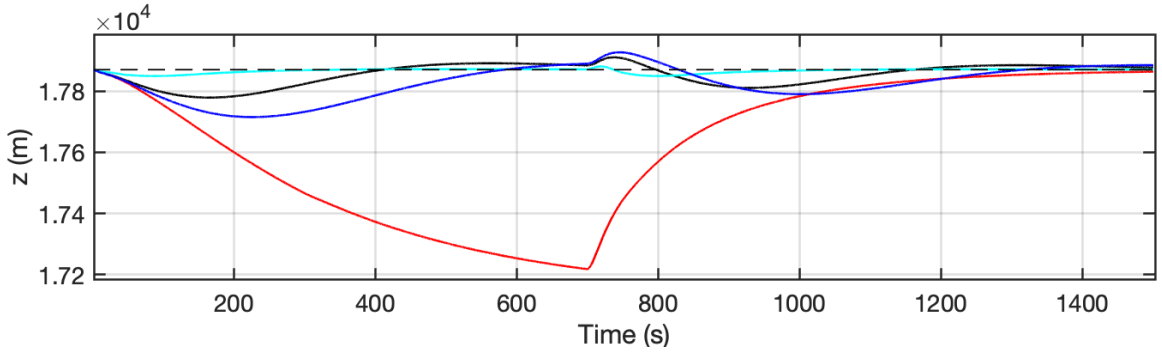

Fig. 9.44 Balloon Altitude response for an equilibrium wind profile increased by 250% to uniform out-of-plane wind disturbance of velocity 25m/s for no controller (red), and unchanged Controllers 1 (black), 2 (dark blue) and 3 (light blue).

The balloon's equilibrium altitude is seen to be significantly lower in this case, due to the larger wind drag forces acting on the tether and the balloon, but the controllers are still

seen to be stable and greatly improve the system's response despite being designed for a completely different wind profile.

While the controller is seen to cope well with a significant change in the magnitude of the wind velocity profile, it is not expected to cope as well with a large error in the wind's equilibrium direction. Intuitively, if the steady state wind was acting in the direction opposite to that with which the controller was designed, a deviation in the tether's approximate angle from the vertical would drive the base to move in the wrong direction, which would trigger a positive feedback loop and therefore be unstable. In order to lead to instability, the error in the wind direction would have to be larger than 90° however which is a very large error margin. Assuming that the tether's states can be measured to at least some degree of accuracy, the wind direction should never be that far off and so this is very unlikely to occur practically.

In conclusion, the optimal controllers designed using LQR are seen to have a low sensitivity to errors in both the system's physical parameters and the external conditions.

9.11.2 Introducing Time Delays

It's important to observe how well the closed loop feedback system copes with time delays, as they may be present in the real life situation. In these cases, the system's feedback input would be a function of a previous state rather than the current one. For no time delay (and a reference signal equal to zero), the closed loop input to the plant takes the following form:

$$\mathbf{u}(t) = -K\mathbf{x}(t) \tag{9.44}$$

Introducing a time delay alters the equation in the following way:

$$\mathbf{u}_{td}(t) = -K\mathbf{x}(t - t_d) \tag{9.45}$$

Here t_d is the time delay present in the system due to the sensor or actuator. This can be implemented into the closed loop nonlinear model by applying input forces at each time step that are dependant on the system's state at a time t_d ago. Whilst the Matlab *ode* functions are running, it is not possible to access states at previous time steps within the run as the functions go back and forth rejecting steps that do not meet the error limit. The data at a certain previous time step can therefore only be accessed once the entire *ode* run has been completed. For this reason, for cases with closed loop time delays, the *ode* integrator must be called in a loop. The time duration of each run is chosen to be equal to the length of the time delay, t_d.

That way, the previous states are established by a completed *ode* run. Force vectors for a time duration of t_d for the x and y-directions can then be calculated from the previous run and then applied as input force forces during the next run in the loop. The input force vectors are calculated using the negative feedback expression for the input but are continuously applied one loop late. Within the run, interpolation is used to calculate the input forces at each precise time instant. A summary of this process is provided in the flow diagram in Figure 9.45.

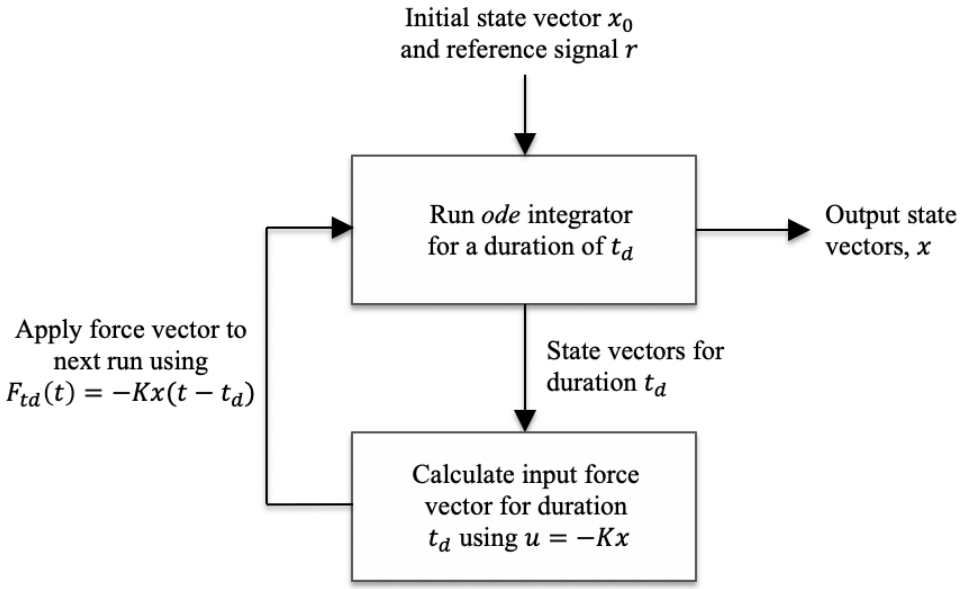

Fig. 9.45 Flow Chart for *ode* integrator loop used to implement closed loop time delays.

Introducing Time Delays to the SPICE Case Studies

Since errors in the system parameters are unlikely to be very large and since the closed loop system has already been seen to cope well with errors in both these and the external conditions the system is subjected to, time delays within the feedback system are likely to be the most important factors to consider when analysing the system's robustness. Practically speaking, a subset of the system's states would have to be measured by sensors (e.g. GPS or cameras), unmeasured states would have to be estimated, the control input needs to be calculated using the states, and then applied through the actuator, resulting in potential time delays between the state measurement and the corresponding input taking effect. The likely bottleneck step in this process would be between the measurement of the system's states and the transmission of this information to the controller at the system's base, due to the large distances involved for such a large scale system. In this section, the effects of these time

delays on the system's closed loop response are observed and compared for controllers of a variety of selected cost functions. Controllers 1, 2 and 3 from Section 9.9.3 are considered.

As an estimate of the maximum allowable time delays of the closed loop systems, Nyquist diagrams are plotted and time delay margins are obtained for each of these. This is done using the methods outlined in Section 6.5.2 and the values obtained are displayed in Table 9.14.

Table 9.14 Lower bounds for the maximum tolerable time delays for the different controllers deduced from the Nyquist plots

Controller	Time Delay
1	4.34s
2	6.81s
3	2.84s

As expected, the most expensive controllers, which exhibit the smallest control effort in response to deviations from the equilibrium, are able to tolerate the largest time delays. Cheap controllers which are quicker to respond to deviations are more sensitive to time delays.

While these time delay margins are useful lower bound measures to have for the systems, they do not accurately represent the maximum allowable time delays of the closed loop nonlinear models. This is because the linearized versions of the models, on which these values are based, do not include the effects of wind damping that opposes the balloon and tether's motion. This is because these values have a greatly reduced significance for small amplitude motion as they are proportional to the square of the elements' velocities. Damping reduces the rate at which systems oscillate about their equilibrium, and therefore reduces the system's natural frequencies. This in turn is expected to increase the maximum tolerable time delays of the closed loop systems, since shorter time delays initiate higher frequency oscillations. The following expression relates a system's undamped natural frequency ω_n to its damped natural frequency ω_d:

$$\omega_d = \omega_n \sqrt{1-\zeta^2} \tag{9.46}$$

Here, ζ is the damping coefficient, which is very large for a high-altitude tethered balloon system due to its huge surface area resulting in high wind damping which in turn results in greatly reduced natural frequencies than those predicted by the linearized model.

The effects of time delays on the nonlinear system's stability are investigated in the time domain. Time delays were incorporated using the loop described in Figure 9.45. Initially, Controller 1 is considered.

A uniform out-of-plane wind disturbance of speed 25m/s in the positive y-direction that lasts for 700s before dropping to zero is considered. A sudden drop in the disturbance is considered in this section, as this is expected to have a larger impact on errors caused by time delays. The closed loop system's robustness under the introduction of time delays is expected to vary depending on how expensive the controller is. The system is ran for the wind disturbance described, for the case of a 10 second time delay and a 30 second time delay. Although 30 seconds is quite an extreme time delay and unlikely to occur practically, it is plotted to show the extent of the system's robustness. The closed loop system's responses to these cases are plotted in the form of the balloon's altitude variation with time in Figure 9.46, alongside the closed loop response with no time delay present.

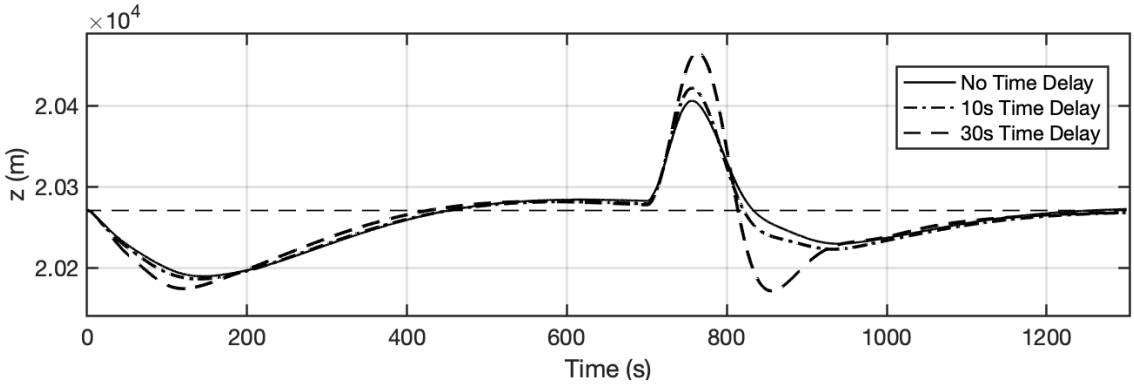

Fig. 9.46 Closed-loop balloon altitude responses to a uniform out-of-plane wind disturbance for Controller 1, with no time delay and with time delays of 10s and 30s.

Figure 9.47 displays the variation of the magnitude of the speed of the base with time for each of these cases.

For both of the time delay cases, the closed loop system not only remains stable, but maintains a significant improvement to the system's response compared to the open loop case. For both of these, there is a lag in the system's response to changes which results in larger amplitudes at the peaks of the response, which increase with the duration of the time delay as expected. The extent of the improvement of the closed loop response therefore decreases with the duration of the time delay, but not by very much at all for any likely time delays that may occur. Table 9.15 displays a summary of the important parameters of the responses for the time delays in question, alongside those of the equivalent open loop system and closed loop system with no time delay present for reference. Figure 9.48 shows a close-up of the plan view of the trajectory of the system, at a point where the base motion curves to show

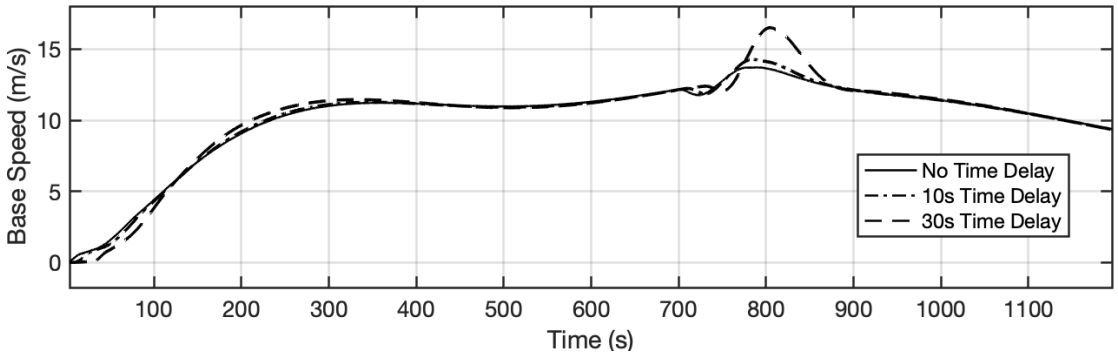

Fig. 9.47 Closed-loop base speed for a uniform out-of-plane wind disturbance for Controller 1, with no time delay and with time delays of 10s and 30s.

how the introduction of the time delays affects the base trajectory. At this point, the base of the no delay system is seen to curve to the left and then to the right. Upon introducing a time delay, there is a delay before the base begins to curve, which makes the curving angle larger in order to compensate (the delay in curvature would result in a larger deviation from the equilibrium which would result in a larger controller input force that acts to change the direction of the base).

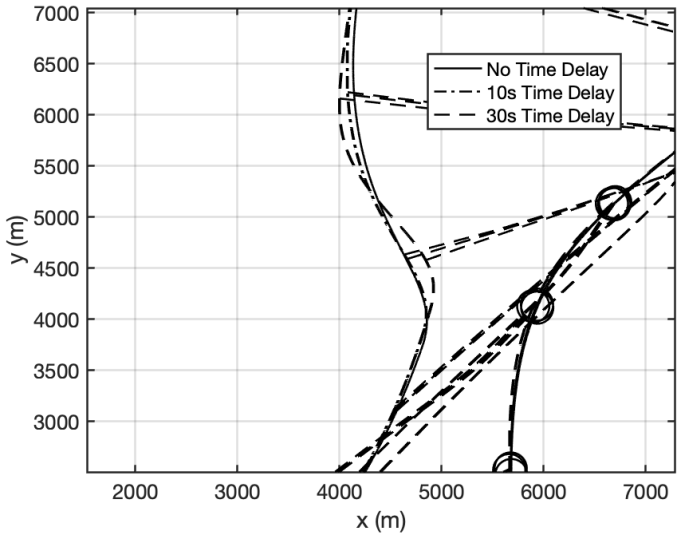

Fig. 9.48 Plan view closed-loop responses to a uniform out-of-plane wind disturbance for Controller 1, with no time delay and with time delays of 10s and 30s.

From Table 9.15, it can be seen that the 10 second time delay made a very minimal difference to the closed loop response compared to the case with no time delay present. Almost no changes were seen in the maximum and minimum balloon altitudes reached and

Table 9.15 Comparison of Key Parameters of Response to a uniform out-of-plane wind disturbance of speed 25m/s for varying time delays for Controller 1.

Parameter	OL	CL, $t_d = 0$	CL, $t_d = 10$	CL, $t_d = 30$
Min Balloon Altitude (km)	19.70	20.19	20.19	20.17
Altitude Drop from Eqm (%)	2.8%	0.4%	0.4%	0.5%
Max Balloon Altitude (km)	20.28	20.41	20.42	20.47
Altitude Rise from Eqm (%)	0.05%	0.7%	0.7%	1.0%
Max Tension in Tether (MN)	12.61	11.53	11.53	11.56
Max Tether Stress (MPa)	535	489	490	491
% Increase in Max Tether Stress	10.8%	1.2%	1.3%	1.6%

the percentage increase of the maximum tether stress from the equilibrium was only 0.1% larger than the no delay case. The introduction of a 30 second time delay had a slightly more negative impact on the system's response, with a maximum deviation from the balloon's equilibrium altitude of 1% compared to the 0.7% of the no delay case, and a 1.6% increase in the maximum tether tension compared to the 1.2% increase of the no-delay feedback controller. Considering these are quite significant time delays, the responses have changed very slightly and are still a significant improvement to the equivalent open loop case.

The feedback controller used in this case (Controller 1) is therefore able to cope well with time delays, producing a greatly improved response for time delays even as extreme as 30 seconds which are unlikely to occur practically. In fact, even for time delays of up to 70 seconds the response, although worse, remained stable. It is expected however, that a controller's robustness is highly dependant on how expensive it is, with cheaper controllers being less robust. This is because cheaper controllers respond more dramatically to system deviations and act faster to correct them, and this type of faster and more abrupt motion is expected to be more affected by time delays. This is investigated by introducing time delays to Controller 3, the cheapest controller used in Section 9.9.3.

The system's closed loop response to the same wind disturbance is plotted for time delays of 7, 8 and 9 seconds in Figure 9.49. The no-delay response of Controller 3 is once again plotted alongside these for reference.

For up to a 7 second time delay, the delayed closed loop response mostly remains close to the un-delayed response, with slightly larger amplitude at points of sudden changes in the motion of the base. For an 8 second time delay, both the base velocity and the system's response visibly oscillate about the un-delayed response but remain stable as the oscillations damp down and return to match those of the un-delayed response. For a 9-second time delay, oscillations of larger amplitude are observed in the response and in the motion of the base,

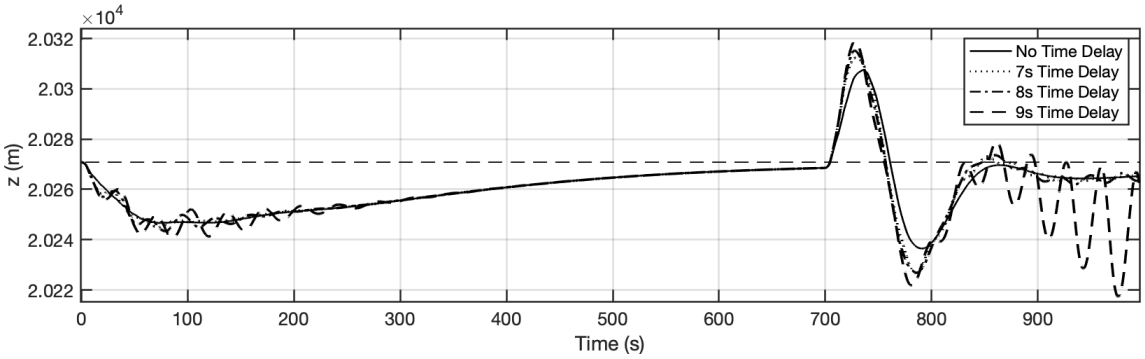

Fig. 9.49 Closed-loop balloon altitude responses to a uniform out-of-plane wind disturbance for Controller 3, with no time delay and with time delays of 7s, 8s and 9s.

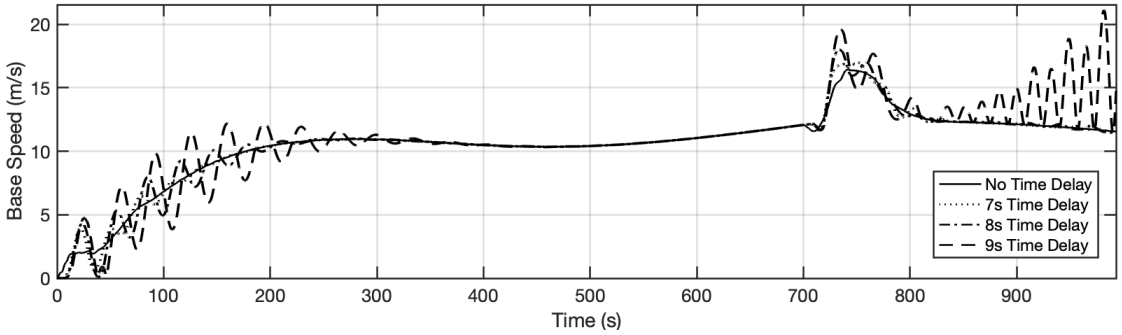

Fig. 9.50 Closed-loop base speed for a uniform out-of-plane wind disturbance for Controller 3, with no time delay and with time delays of 7s, 8s and 9s.

that are no longer stable. Following the drop in the wind disturbance, resonance is observed and the oscillations begin to increase in amplitude with time rather than settling, and the system has therefore become unstable.

The cheaper the feedback controller, the more sensitive the closed loop system is to potential time delays. Along with the costlier operation, the reduced robustness of the system is another factor that favours a more expensive controller. Once again, a compromise needs to made when selecting the controller's relative input cost, in the extent of improvement of the system's response and maintaining practicality and robustness. Controller 1 has proved to maintain robustness, while greatly improving the system's response to disturbances for this case.

Chapter 10

Conclusions and Recommendations for Further Work

An overview of the contributions of this research is presented in this chapter and compared to the initial objectives provided in Chapter 1. A summary of the findings is provided, as well as suggestions for potential further work that would build upon this research.

10.1 Conclusions

The primary aim of this research was to develop a full 3-dimensional nonlinear model to simulate the dynamics of tethered balloon systems, with the context of assessing the feasibility of VHATBs during their operation. The long-duration high-altitude platforms these systems are able to supply could be beneficial for a variety of different applications for which the findings presented could be useful.

A full 3-dimensional nonlinear model of a tethered balloon system was was developed using a discrete lumped mass cable model. In doing this, methods of translating the system's axial and bending properties into discrete parameters were derived. This model was validated using experimental data collected for hanging chains and a small-scale tethered balloon system [7]. A very good agreement was observed both qualitatively in the time domain response, and quantitatively in the frequency domain response. This experimental validation was very important, as it allows for the validation of the nonlinear motion of the system, which the theoretical validations do not.

A computationally efficient method of producing the linearized state space model of a tethered balloon system under any steady state wind loading was developed. To do this, general expressions for the entries of the system's mass, stiffness and damping matrix

were derived through the observation of patterns in the energy equations of the system's individual elements. These were validated by comparing the linearized models produced to the equivalent nonlinear model for small amplitude vibrations, and almost perfectly identical responses were observed.

Extensive theoretical validations were made for the linearized model discretized into 300 elements to more closely resemble a continuous system. Since the nonlinear and linear models produced very close responses for small amplitude vibration, the conclusions drawn from the validations were extended to the nonlinear model. Transient cable motion was validated by comparing the system's time domain impulse response to predictions made by wave propagation theory and excellent agreement was observed, with errors of 0.35% and less. The natural frequencies of the cable constrained as a hanging chain were compared against theory with a maximum percentage error of 0.07%. The cables discretized bending properties were validated against theory on continuous beams for two sets of boundary conditions, both with and without axial tensions, and very good agreement was seen in these as well. These validations resulted in a greatly increased confidence in both the linear and nonlinear models of the system, which could then be put to use in assessing the feasibility of VHATBs.

Appropriate parameters were selected for the VHATB with the stratospheric particle injection application in mind, and for an expected steady state wind profile the system was allowed to settle into its equilibrium position. The balloon's operational altitude was found to be close to that for which it was designed. The maximum axial stress along the tether's length was found and was well below the material's yield strength, including a safety factor. The system's operational steady state was therefore deemed feasible.

The system must also be able to endure more severe weather conditions in order to be suitable for long-duration operation. This poses failure risks to the system; deviations in the balloon's equilibrium altitude result in alterations to its differential pressure that may cause the balloon to burst or lose its aerodynamic spherical shape. There is also a risk of blow-over in which short term wind loading causes the balloon's altitude to dip into regions of stronger wind, resulting in failure. In addition to the balloon's altitude, the maximum tether stress is also considered a critical parameter in the system's response to disturbances.

The linearized version of the full scale VHATB under the steady-state wind loading was used to produce suitable feedback controllers with the aim of minimizing the deviations in these values, and therefore reducing the system's risk of failure. The optimal feedback gain matrices produced were implemented into the nonlinear model that more accurately portrays the dynamics of the system. The use of the motion of the ship as a feedback control input was investigated, and the benefits and practicality of such a feedback system were assessed.

It was found that for what were considered practically achievable control inputs (ship speeds less than 30 knots and power outputs less than 110,000 hp), the implementation of feedback control resulted in greatly improved dynamic responses to a range of quite extreme wind disturbances (both in plane and out of plane). Improvements in the critical parameters were of the order of 60% for in-plane disturbances and 90% for out-of-plane disturbances. The effects of cost function selection on the response were investigated, and the resulting compromises between better responses at the expense of larger control inputs were considered.

Once it was established that significant improvements to the system's safe operation could be made with practically achievable control inputs, it was important to consider the robustness of the controllers. The controllers were found to have excellent tolerance to both system parameter errors and errors in the assumed external conditions, maintaining both stability and a great improvement in the response compared to the open loop system. It was predicted and confirmed that time delays within the feedback cycle would be the most crucial source of error that could result in the system's loss of stability.

The closed loop system's sensitivity to time delays was found to be highly dependent on the design of the controller, as expected. Controllers designed to react faster and more abruptly to the system's deviations (cheap controllers) were found to be significantly more sensitive to time delays, which makes sense intuitively. Controllers that had been deemed hugely beneficial to the system's dynamic response as well as practically feasible, were found to have very large time delay margins of the order of 1 minute. This is obviously much larger than any time delays that would be practically present in the feedback system, and it was therefore concluded that the implementation of a feedback controller to reduce the system's risk of failure is feasible.

While Badesha et al. (2002) [10] conducted a feasibility study of a 20km altitude VHATB using a 2-dimensional model and Redi et al. (2011) [98] extended the model to 3-dimensions but studied a HATB of altitude 6km, this research provides a full 3-dimensional model of the 20km VHATB. In addition to this, the feasibility of the system for the specific application of Stratospheric Particle Injection, which caries its own unique risks due to the required geometry of the tether, was modelled and assessed. While the use of control to stabilise balloon altitudes has been done for smaller scale systems using reel-in pay-out methods with single and multiple tethers, this research conducted a preliminary assessment of the use of altitude control for the VHATB systems, which has not been conducted prior. With reel-in pay-out inputs and the use of multiple tethers [51] being considered impractical for the VHATB for the SPICE application, the use of base motion as a control input was investigated.

The potential use of this type of feedback control for this application and more generally, for VHATBs, has yet to have been investigated, and is introduced in this research.

While this research has positive conclusions about the potential use of feedback control to improve the safety of VHATBs during operation, further work would have to be done to solidify these conclusions more completely. This also applies for the statements about the general feasibility of the VHATB under operational conditions. Recommended work to further develop the simulation and therefore provide a more complete technical assessment of the feasibility of VHATB and the use of feedback control to improve its operational safety is provided in the next section.

10.2 Recommendations for Further Work

The VHATB case studies provided are a useful preliminary step in assessing both the feasibility of the of the system under operational conditions and the possibility of implementing feedback control as a means of making the system safer and more durable. It is not sufficient in itself however, and further developments of the model would provide a more complete picture of the system's dynamics, both with and without feedback control.

In this research, the potential effects of vortex-induced vibrations as well as turbulent air flow were ignored in the dynamic simulations of the system. Implementing these into the model would provide a fuller analysis of the system's dynamic behaviour under operational conditions and therefore a more complete feasibility assessment, as vortex-induced vibrations introduce an increased risk of cable fatigue.

While the small-scale experimentation [7] and various forms of theoretical validation played a big roll in verifying the accuracy of the model, it would be useful to conduct larger scale experiments. Furthermore, incorporating winds and base motion into the experimental validations could provide a more well rounded assessment of the aspects of the system model.

The feasibility study could also be expanded to account for the launch of the system rather than just its operation. The safety of the system's set-up is equally important to that of its operation, and modelling this process is vital in the overall assessment of the process.

In this research, full-state feedback was assumed. This is of course not feasible realistically and an observer would need to be implemented. Further work could be done on establishing practical methods of collecting sufficient state data for the system's control through sensor positioning and the design of an observer.

There is also scope for investigation of other potential inputs for the control of the system's altitude. While base motion was deemed the most appropriate for the application in question in this research, there is the potential of finding solutions that make other methods

suitable. The potential of using multiple tethers and/or a tether reel-in pay-out input for altitude control can be investigated.

The model of the VHATB used in this research also assumed a spherical balloon and a cylindrical pipe as the tether. It is known that the use of an aerodynamically shaped balloon as well as a streamlined cable would bring out benefits relating to the reduction of drag and vortex-induced vibrations. With the strong winds the system is expected to be subjected to this could be hugely advantageous, although these pose risks of there own [24]. Methods of introducing a streamlined outer wall of the tether's cross-section while maintaining a sufficient inner diameter for fluid flow and walls thick enough to withstand the hoop stress due to the fluid pressure would need to be considered. Once an appropriate and feasible tether geometry has been established, its effect on the system's dynamic behaviour can be determined with the necessary alterations of the system model. Altering the spherical balloon to a more aerodynamically shaped one could also be implemented into the model, and a feasibility assessment of the altered system can be conducted.

References

[1] Ablow, C. and Schechter, S. (1983). Numerical simulation of undersea cable dynamics. Ocean Engineering, 10(6), pp.443-457.

[2] Achenbach, E. (1972). Experiments on the flow past spheres at very high Reynolds numbers. Journal of Fluid Mechanics, 54(3), pp.565-575.

[3] Aglietti, G. (2009). Dynamic Response of a High-Altitude Tethered Balloon System. Journal of Aircraft, 46(6), pp.2032-2040.

[4] Aglietti, G., Markvart, T., Tatnall, A. and Walker, S. (2008). Solar power generation using high altitude platforms feasibility and viability. Progress in Photovoltaics: Research and Applications, 16(4), pp.349-359.

[5] Ali, H. (2014). Robust Stabilizing Controller Design for Inverted Pendulum System. Jurnal Teknologi, 71(1).

[6] Anderson, B. and Moore, J. (2014). Optimal Control. Newburyport: Dover Publications.

[7] Andrews, R. (2016). The Dynamics of a Tethered Balloon. M.Eng. University of Cambridge.

[8] Archer, D., Eby, M., Brovkin, V., Ridgwell, A., Cao, L., Mikolajewicz, U., Caldeira, K., Matsumoto, K., Munhoven, G., Montenegro, A. and Tokos, K. (2009). Atmospheric Lifetime of Fossil Fuel Carbon Dioxide. Annual Review of Earth and Planetary Sciences, 37(1), pp.117-134.

[9] Badesha, S. (2002). SPARCL: a high-altitude tethered balloon-based optical space-to-ground communication system. Free-Space Laser Communication and Laser Imaging II.

[10] Badesha, S. and Bunn, J. (2002). Dynamic Simulation of High Altitude Tethered Balloon System Subject to Thunderstorm Windfield. AIAA Atmospheric Flight Mechanics Conference and Exhibit.

[11] Badesha, S. S., Euler, A. J. & Schroeder, L. D. 1996 Very high altitude tethered balloon parametric sensitivity study. In Proc. 34th AIAA Aerospace Science Meeting, Reno, NV, 15–18 January 1996, AIAA-1996-0579

[12] Badesha, S. S., Euler, A. J. Schroeder, L. D. 1996 Very high altitude tethered balloon trajectory simulation. In Proc. AIAA Atmospheric Flight Mechanics Conf., San Diego, CA, 29–31 July 1996, AIAA-1996-3440

[13] Bahng, J., Danielson, J., Rogerson, J. and Schwarzschild, M. (1959). Sunspot photographs from the stratosphere. The Astronomical Journal, 64, p.323.

[14] Barrett, S. (2014). Solar Geoengineering's Brave New World: Thoughts on the Governance of an Unprecedented Technology. Review of Environmental Economics and Policy, 8(2), pp.249-269.

[15] Battisti, D., Blackstock, J., Caldeira, K., Eardley, D., Katz, J., Keith, D., Koonin, S., Patrinos, A., Schrag, D. and Socolow, R. (2009). Climate engineering responses to climate emergencies. IOP Conference Series: Earth and Environmental Science, 6(45), p.452015.

[16] Bely, P., Ashford, R. and Cox, C. (1995). High-altitude aerostats as astronomical platforms. Space Telescopes and Instruments.

[17] Belytschko, T. and Mindle, W. L. (1980). Flexural wave propagation behavior of lumped mass approximations. Computers and Structures, 12(6):805–812.

[18] Buckham, B. et al. "Dynamics And Control Of A Towed Underwater Vehicle System, Part I: Model Development". Ocean Engineering 30.4 (2003): 453-470. Web.

[19] Buckham, Brad, Frederick R. Driscoll, and Meyer Nahon. "Development Of A Finite Element Cable Model For Use In Low-Tension Dynamics Simulation". Journal of Applied Mechanics 71.4 (2004): 476. Web.

[20] Cao, L. and Caldeira, K. (2010). Atmospheric carbon dioxide removal: long-term consequences and commitment. Environmental Research Letters, 5(2), p.024011.

[21] Chucheepsakul, S. and Wongsa, S. (2001). Effect of axial stretching on large amplitude free vibration of a suspended cable. Structural Engineering and Mechanics, 11(2), pp.185-197.

[22] Colozza, A. and Dolce, J. (2005). High-Altitude, Long-Endurance Airships for Coastal Surveillance. NASA TM 2005-213427.

[23] Constantinescu, G. and Squires, K. (2004). Numerical investigations of flow over a sphere in the subcritical and supercritical regimes. Physics of Fluids, 16(5), pp.1449-1466.

[24] Costello, H. (2014). The Dynamic Behaviour and Stability of Streamlined Cables. Ph.D. University of Cambridge.

[25] Coulombe-Pontbriand, P. (2005). Modeling and experimental characterization of a tethered spherical aerostat. M.Sc., McGill University.

[26] Coulombe-Pontbriand, P. and Nahon, M. (2009). Experimental testing and modeling of a tethered spherical aerostat in an outdoor environment. Journal of Wind Engineering and Industrial Aerodynamics, 97(5-6), pp.208-218.

[27] Crill, B. P.; et al. (October 2003). "BOOMERANG: A Balloon-borne Millimeter Wave Telescope and Total Power Receiver for Mapping Anisotropy in the Cosmic Microwave Background". Astrophysical Journal Supplement Series. 148: 527–541.

[28] Crutzen, P. J. (2006). Albedo enhancement by stratospheric sulfur injections: a contribution to resolve a policy dilemma? Climatic Change, 77(3-4):211–220.

[29] Danielson, Robert E. “Project Stratoscope.” American Scientist, vol. 49, no. 3, 1961, pp. 370–398.

[30] Davidson, P., Burgoyne, C., Hunt, H. and Causier, M. (2012). Lifting options for stratospheric aerosol geoengineering: advantages of tethered balloon systems. Philosophical Transactions of the Royal Society A: Mathematical, Physical and Engineering Sciences, 370(1974), pp.4263-4300.

[31] Davidson, P., Hunt, H. E. M. Burgoyne, C. J. 2011 Atmospheric delivery system. Patent application no. GB 2476518.

[32] de Azevedo, B., Góes, L. and Azinheira, J. (2017). Tethered Aerostat Stabilization in Turbulent Wind Using Actuated Fins. Journal of Guidance, Control, and Dynamics, 40(12), pp.3290-3298.

[33] DELAURIER, J. (1972). A Stability Analysis for Tethered Aerodynamically Shaped Balloons. Journal of Aircraft, 9(9), pp.646-651.

[34] Deshler, T., Liley, J., Bodeker, G., Matthews, W. and Hoffmann, D. (1997). Stratospheric aerosol following Pinatubo, comparison of the north and south mid latitudes using in situ measurements. Advances in Space Research, 20(11), pp.2089-2095.

[35] Dreyer, T. and Murray, D. (1985). Pre-elimination approach to the modelling of segmented representations of cable shape with application to the positioning of a towed sensor. Applied Mathematical Modelling, 9(3), pp.163-169.

[36] Dreyer, T. and Van Vuuren, J. (1999). A comparison between continuous and discrete modelling of cables with bending stiffness. Applied Mathematical Modelling, 23(7), pp.527-541.

[37] Driscoll, F.R., R.G. Lueck, and M. Nahon. "Development And Validation Of A Lumped-Mass Dynamics Model Of A Deep-Sea ROV System". Applied Ocean Research 22.3 (2000): 169-182. Web.

[38] Egner, S., Masciadri, E. and McKenna, D. (2007). Generalized SCIDAR Measurements at Mount Graham. Publications of the Astronomical Society of the Pacific, 119(856), pp.669-686.

[39] Elliott, S. D., McKay, J. M., and McKee, R. B. (1965). Tethered aerological balloon system. Technical report, U.S. Naval Ordnance Test Station, China Lake.

[40] Engineeringtoolbox.com. (2019). U.S. Standard Atmosphere. [online] Available at: https://www.engineeringtoolbox.com/standard-atmosphere-d_604.html [Accessed 21 Nov. 2019].

[41] Euler, A. J., Badesha, S. S., and Schroeder, L. D. (1995). Very high altitude balloon feasibility study. In 11th Lighter-than-air Systems Technology Conference, pages 46–51, Clearwater Beach, Florida.

[42] Federal Aviation Administration, Policy FAA-P-8110-2 (1995). Airship Design Criteria.

[43] Fesen, R. and Brown, Y. (2015). A method for establishing a long duration, stratospheric platform for astronomical research. Experimental Astronomy, 39(3), pp.475-493.

[44] Friedland, B. (1986). Control System Design : An Introduction to State-Space Methods. McGraw-Hill, New York ; London.

[45] Fuss, S., Canadell, J., Peters, G., Tavoni, M., Andrew, R., Ciais, P., Jackson, R., Jones, C., Kraxner, F., Nakicenovic, N., Le Quéré, C., Raupach, M., Sharifi, A., Smith, P. and Yamagata, Y. (2014). Betting on negative emissions. Nature Climate Change, 4(10), pp.850-853.

[46] Giannopoulos, I. and Burgoyne, C. (2009). Stress limits for aramid fibres. Proceedings of the Institution of Civil Engineers - Structures and Buildings, 162(4), pp.221-232.

[47] Govardhan, R. and Williamson, C. (1997). Vortex-induced motions of a tethered sphere. Journal of Wind Engineering and Industrial Aerodynamics, 69-71, pp.375-385.

[48] Grant, D. and Rand, J. (1996). Dynamic analysis of an ascending high altitude tethered balloon. 34th Aerospace Sciences Meeting and Exhibit.

[49] Grosenbaugh, M. (2007). Transient behavior of towed cable systems during ship turning maneuvers. Ocean Engineering, 34(11-12), pp.1532-1542.

[50] Guo, S., Bluth, G., Rose, W., Watson, I. and Prata, A. (2004). Re-evaluation of SO2release of the 15 June 1991 Pinatubo eruption using ultraviolet and infrared satellite sensors. Geochemistry, Geophysics, Geosystems, 5(4), p.n/a-n/a.

[51] Gupta, S., Duttagupta, S., Vachhani, L. and Mitra, M. (2019). Attitude control of LTA platform for generation of a non-oscillatory solar power. Solar Energy, 189, pp.131-150.

[52] Haan Y.M., Sluimer G.M.: Standard linear solid model for dynamic and time dependent behaviour of building materials. Heron 46(1), 49–76 (2001)

[53] Hamilton, C. (2013). Earthmasters. Crows Nest: Allen Unwin.

[54] Hartsuijker, C., Welleman, J. W. (2007). Engineering Mechanics. Volume 2: Stresses, Deformations, Displacements. Springer, Dordrecht, Netherlands.

[55] Hembree, B. and Slegers, N. (2010). Efficient tether dynamic model formulation using recursive rigid-body dynamics. Proceedings of the Institution of Mechanical Engineers, Part K: Journal of Multi-body Dynamics, 224(4), pp.353-363.

[56] Hembree, B. and Slegers, N. (2011). Tethered Aerostat Modeling Using an Efficient Recursive Rigid-Body Dynamics Approach. Journal of Aircraft, 48(2), pp.623-632.

[57] Hembree, B. and Slegers, N. (2016). Comparison of experimental and simulated motion for discrete tether models. Multibody System Dynamics, 41(3), pp.233-258.

[58] Herse, M. (1979). High resolution photographs of the sun near 200 nm. Solar Physics, 63(1), pp.35-60.

[59] Hover, F., Grosenbaugh, M. and Triantafyllou, M. (1994). Calculation of dynamic motions and tensions in towed underwater cables. IEEE Journal of Oceanic Engineering, 19(3), pp.449-457.

[60] Huang, S. (1994). Dynamic analysis of three-dimensional marine cables. OceanEngineering, 21(6), pp.587-605.

[61] Hulme, M. (2014). Can science fix climate change? A case against climate engineering. Cambridge: Polity.

[62] Irvine, H. M. (1981). Cable Structures. MIT Press, Cambridge, Massachusetts.

[63] Irvine, H. M. and Caughey, T. K. (1974). The linear theory of free vibrations of a suspended cable. Proceedings of the Royal Society A: Mathematical, Physical and Engineering Sciences, 341(1626):299–315.

[64] Irvine, P., Kravitz, B., Lawrence, M. and Muri, H. (2016). An overview of the Earth system science of solar geoengineering. Wiley Interdisciplinary Reviews: Climate Change, 7(6), pp.815-833.

[65] Irvine, T. (2011). Natural Frequencies of Beams Subjected to a Uniform Axial Load, Revision C.

[66] Jones, S. and Schroeder, L. (2001). Nonlinear Dynamic Simulation of a Tethered Aerostat: A Fidelity Study. Journal of Aircraft, 38(1), pp.64-68.

[67] Jones, S. P. and Krausman, J. A. (1982). Nonlinear dynamic simulation of a tethered aerostat. Journal of Aircraft, 19(8):679–686.

[68] Kamman, James W. and Ronald L. Huston. "Modeling Of Variable Length Towed And Tethered Cable Systems". Journal of Guidance, Control, and Dynamics 22.4 (1999): 602-608. Web.

[69] Kamman, J. and Huston, R. (2001). Multibody Dynamics Modeling of Variable Length Cable Systems, 5(3), pp.211-221.

[70] Kang, W. and Lee, I. (2009). Analysis of Tethered Aerostat Response Under Atmospheric Turbulence Considering Nonlinear Cable Dynamics. Journal of Aircraft, 46(1), pp.343-348.

[71] Keith, D. (2013). A case for climate engineering. Cambridge, MA: The MIT Press.

[72] Koh, C. G., Y. Zhang, and S. T. Quek. "Low-Tension Cable Dynamics: Numerical And Experimental Studies". J. Eng. Mech. 125.3 (1999): 347-354. Web.

[73] Kuo, K. and Hunt, H. (2015). Isothermal pumping analysis for high-altitude tethered balloons. Royal Society Open Science, 2(6), p.140468.

[74] Lambert, C. (2006). Dynamics and Control of a Multi-Tethered Aerostat Positioning System. Ph.D. McGill University, Montreal.

[75] Lambert, C. and Nahon, M. (2003). Stability Analysis of a Tethered Aerostat. Journal of Aircraft, 40(4), pp.705-715.

[76] Lambert, C. and Nahon, M. (2008). An Aerostat Positioning System with Cable Control. IFAC Proceedings Volumes, 41(2), pp.779-784.

[77] Lambert, C., Nahon, M., Buckham, B. and Seto, M. (2003). Dynamics and control of towed underwater vehicle system, part II: model validation and turn maneuver optimization. Ocean Engineering, 30(4), pp.471-485.

[78] Lambert, C. M. (2002). Dynamics modeling and conceptual design of a multi-tethered aerostat system. M.Sc., University of Victoria.

[79] Lambert, C., Nahon, M. and Chalmers, D. (2007). Implementation of an Aerostat Positioning System With Cable Control. IEEE/ASME Transactions on Mechatronics, 12(1), pp.32-40.

[80] Lambert, C., Nahon, M., and Chalmers, D. (2006). Study of a multitethered aerostat system: experimental observations and model validation. Journal of Aircraft, 43(4):1182–1189.

[81] Lambert, C., Saunders, A., Crawford, C. and Nahon, M. (2003). Design of a one-third scale multi-tethered aerostat system for precise positioning of a radio telescope receiver. In: CASI Flight Mechanics and Operations Symposium. Montreal.

[82] MacTavish, C. J.; et al. (August 2006). "Cosmological Parameters from the 2003 Flight of BOOMERANG". Astrophysical Journal. 647: 799–812.

[83] Maxworthy, T. (1969). Experiments on the Flow Around a Sphere at High Reynolds Numbers. Journal of Applied Mechanics, 36(3), pp.598-607.

[84] McClellan, J., Sisco, J., Suarez, B. Keogh, G. 2010 Aurora Flight Sciences Corporation geoengineering cost analysis final report, no. AR10-182, prepared under contract to the University of Calgary

[85] Miller, J. and Nahon, M. (2007). Analysis and Design of Robust Helium Aerostats. Journal of Aircraft, 44(5), pp.1447-1458.

[86] Minx, J. C., Lamb, W. F., Callaghan, M. W., Fuss, S., Hilaire, J., Creutzig, F., et al. (2018). Negative emissions—part 1: research landscape and synthesis. Environmental Research Letters, 13(6), 063001.

[87] Moriyama, R., Sugiyama, M., Kurosawa, A., Masuda, K., Tsuzuki, K. and Ishimoto, Y. (2016). Erratum to: the cost of stratospheric climate engineering revisited. Mitigation and Adaptation Strategies for Global Change, 23(1), pp.145-146.

[88] Nahon, M. (1999). Dynamics and control of a novel radio telescope antenna. Modeling and Simulation Technologies Conference and Exhibit.

[89] Nahon, M., Gilardi, G. and Lambert, C. (2002). Dynamics/Control of a Radio Telescope Receiver Supported by a Tethered Aerostat. Journal of Guidance, Control, and Dynamics, 25(6), pp.1107-1115.

[90] Nahon, M., Howard, A., Frenette, E. and Pullen, D. (2007). Experimental Testing of an Aerostat with Actuated Tail Fins. AIAA Balloon Systems Conference.

[91] NASA. (2018). NASA Balloon Mission Captures Electric Blue Clouds. [online] Available at: https://www.nasa.gov/feature/goddard/2018/nasa-balloon-mission-captures-electric-blue-clouds [Accessed 7 Nov. 2018].

[92] Newland, D. E. (1989). Mechanical Vibration Analysis and Computation. Dover Publications Inc., Mineola, New York.

[93] Palo, P., Meggitt, D. and Nordell, W. (1983). Dynamic Cable Analysis Models. Offshore Technology Conference.

[94] Pidgeon, N., Parkhill, K., Corner, A. and Vaughan, N. (2013). Deliberating stratospheric aerosols for climate geoengineering and the SPICE project. Nature Climate Change, 3(5), pp.451-457.

[95] Preston, C. (2012). Ethics and geoengineering: reviewing the moral issues raised by solar radiation management and carbon dioxide removal. Wiley Interdisciplinary Reviews: Climate Change, 4(1), pp.23-37.

[96] Rajani, A., Pant, R. and Sudhakar, K. (2010). Dynamic Stability Analysis of a Tethered Aerostat. Journal of Aircraft, 47(5), pp.1531-1538.

[97] Redi, S., Aglietti, G. S., Tatnall, A. R., and Markvart, T. (2010). An evaluation of a high altitude solar radiation platform. Journal of Solar Energy Engineering, 132(1):011004.

[98] Redi, S., Aglietti, G., Tatnall, A. and Markvart, T. (2011). Dynamic Response to Turbulence of Tethered Lighter-Than-Air Platforms. Journal of Aircraft, 48(2), pp.540-552.

[99] Robock, A. (2000). Volcanic eruptions and climate. Reviews of Geophysics, 38(2), pp.191-219.

[100] Robock, A. (2016). Albedo enhancement by stratospheric sulfur injections: More research needed. Earth's Future, 4(12), pp.644-648.

[101] Robock, A., Marquardt, A., Kravitz, B. and Stenchikov, G. (2009). Benefits, risks, and costs of stratospheric geoengineering. Geophysical Research Letters, 36(19).

[102] Sanderson, B., O'Neill, B. and Tebaldi, C. (2016). What would it take to achieve the Paris temperature targets?. Geophysical Research Letters, 43(13), pp.7133-7142.

[103] Schwarzschild, M. (1973). An Upper Limit to the Angular Diameter of the Nucleus of NGC 4151. The Astrophysical Journal, 182, p.357.

[104] Shepherd, J.G. , Working Group on Geoengineering the Climate (2009) Geoengineering the climate: science, governance and uncertainty (RS Policy document, 10/29) London, GB. Royal Society 98pp.

[105] Smith, P., Davis, S., Creutzig, F., Fuss, S., Minx, J., Gabrielle, B., Kato, E., Jackson, R., Cowie, A., Kriegler, E., van Vuuren, D., Rogelj, J., Ciais, P., Milne, J., Canadell, J., McCollum, D., Peters, G., Andrew, R., Krey, V., Shrestha, G., Friedlingstein, P., Gasser, T., Grübler, A., Heidug, W., Jonas, M., Jones, C., Kraxner, F., Littleton, E., Lowe, J., Moreira, J., Nakicenovic, N., Obersteiner, M., Patwardhan, A., Rogner, M., Rubin, E., Sharifi, A., Torvanger, A., Yamagata, Y., Edmonds, J. and Yongsung, C. (2015). Biophysical and economic limits to negative CO2 emissions. Nature Climate Change, 6(1), pp.42-50.

[106] SPICE Project (2014). SPICE: Stratospheric particle injection for climate engineering. www.spice.ac.uk. Accessed: April 9 2014.

[107] Srinil, Narakorn, Giuseppe Rega, and Somchai Chucheepsakul. "Three-Dimensional Non-Linear Coupling And Dynamic Tension In The Large-Amplitude Free Vibrations Of Arbitrarily Sagged Cables". Journal of Sound and Vibration 269.3-5 (2004): 823-852. Web.

[108] Stanney, K. and Rahn, C. (2006). Response of a tethered aerostat to simulated turbulence. Communications in Nonlinear Science and Numerical Simulation, 11(6), pp.759-776.

[109] Stilgoe, J., 2015. Experiment Earth: Responsible Innovation In Geoengineering. New York: Routledge.

[110] TCOM L.P. (2011). TCOM Aerostat Systems. www.tcomlp.com/aerostat-platforms/. Accessed: April 4 2013.

[111] Tilmes, S., Sanderson, B. and O'Neill, B. (2016). Climate impacts of geoengineering in a delayed mitigation scenario. Geophysical Research Letters, 43(15), pp.8222-8229.

[112] Tjavaras, A. A., Zhu, Q., Liu, Y., Triantafyllou, M. S., and Yue, D. K. P. (1998). The mechanics of highly-extensible cables. Journal of Sound and Vibration, 213(4):709–737.

[113] Tuveri, Marco, Alessandro Ceruti, and Pier Marzocca. "Added Masses Computation For Unconventional Airships And Aerostats Through Geometric Shape Evaluation And Meshing".International Journal of Aeronautical and Space Sciences 15.3 (2014): 241-257. Web.

[114] Vinodh Kumar, E. and Jerome, J. (2013). Robust LQR Controller Design for Stabilizing and Trajectory Tracking of Inverted Pendulum. Procedia Engineering, 64, pp.169-178.

[115] Walton, T. and Polachek, H. (1960). Calculation of transient motion of submerged cables. Mathematics of Computation, 14(69), pp.27-27.

[116] Winget, J.M. and R.L. Huston. "Cable Dynamics—A Finite Segment Approach". Computers Structures 6.6 (1976): 475-480. Web.

[117] Woolf, N., Schwarzschild, M. and Rose, W. (1964). Infrared Spectra of Red-Giant Stars. The Astrophysical Journal, 140, p.833.